CD28 AND TCR IN-SITU BIOPHYSICAL ANALYSES INFORM T CELL IMMUNITY MECHANISMS

A Dissertation
Presented to
The Academic Faculty

by

Aaron Michael Rosado

In Partial Fulfillment
of the Requirements for the Degree
Doctorate of Philosophy in the
Department of Biomedical Engineering
The Wallace H. Coulter Department of Biomedical Engineering at Emory University and Georgia Tech

Georgia Institute of Technology
December 2021

CD28 AND TCR *IN-SITU* BIOPHYSICAL ANALYSES INFORM T CELL IMMUNITY MECHANISMS

Approved by:

Dr. Cheng Zhu, Advisor
Department of Biomedical Engineering
Georgia Institute of Technology

Dr. Arash Grakoui
Department of Medicine, Division of Infectious Diseases
Emory University School of Medicine

Dr. Susan Thomas
Department of Mechanical Engineering
Georgia Institute of Technology

Dr. Michelle Krogsgaard
Department of Pathology
NYU School of Medicine

Dr. Michael Davis
Department of Biomedical Engineering
Georgia Institute of Technology

Date Approved: August 19, 2021

I dedicate this work to my parents Gladys and Rafael Rosado who through countless sacrifices gave their children a chance for higher education and empowered me to pursue my interests in medicine, science, and engineering. Without their love and patience, I would not have the opportunity to pursue my childhood dream.

ACKNOWLEDGEMENTS

Many people contributed to the work documented within this thesis. Dr. Cheng Zhu provided constant guidance and support as a thesis advisor. Dr. Zhu's mathematical modeling, data analytical, sophisticated understanding of physical and biological systems enabled resolving through biophysical analysis the complex immunological processes presented within this work. Dr. Zhu contributed most significantly to the work presented in this thesis.

Dr. Fangyuan Zhou supported this thesis work significantly by contributing the cell trap calcium flux data and analysis demonstrating functional differences between CD28 ligands. Jintian Lyu provided initial CD28 molecular tension probe data and supported the data contained within this thesis. Dr. Fengzhi Jin contributed to all P14 anatomic compartmentalization experiments by providing all CD8+ T cells used experimentally and conducting flow cytometry for determining 2D effective affinity. Dr. Michael Benner provided expertise and guidance towards developing the chimeric proteins used in all CD28 work.

Dr. Yunfeng Chen, Dr. William Rittase, and Dr. Prithiviraj Jothikumar provided significant training in biophysical instrumentation for 2D Kinetics and bond lifetime under force measurements involving the micropipette adhesion frequency assay, biomembrane force probe, and horizontal atomic force microscope.

Dr. Zhou Yuan and Dr. Kaitao Li provided essential insights and knowledge. Dr. Yuan and Dr. Li helped immensely by providing knowledge related to purifying T cells,

working with T cells in experiments, conducting data analysis, and interpreting findings. Dr. Yuan offered the most support in improving presentations related to this work.

Dr. Kavitha Sthanam provided helpful advice related to biology and cell culture that improved protein expression and purification.

Larissa Doudy supported many experiments by offering her time and assistance purifying T cells. As a lab manager, Larissa provides essential support to all experiments occurring within Dr. Cheng Zhu's laboratory.

Finally, the thesis committee for this work provided essential guidance and support towards developing the final product. Anatomic compartmentalization findings presented in this work come from a collaboration between Dr. Cheng Zhu and Dr. Arash Grakoui. Dr. Arash Grakoui's and Dr. Michelle Krogsgaard research contributions in immunology inspire this work heavily. Dr. Susan Thomas's and Dr. Michael Davis's biomedical engineering knowledge and work provide inspiration towards utilizing engineering in studying disease and developing therapeutics.

This work would not be possible without the Emory University Medical Scientist Training Program, Georgia Institute of Technology and Emory University Wallace H. Coulter Department of Biomedical Engineering, and the National Institutes of Health Diversity Supplements Program Managed by the National Cancer Institute.

TABLE OF CONTENTS

LIST OF FIGURES

LIST OF SYMBOLS AND ABBREVIATIONS

μM	Micromolar
μm	Micrometer
1D	One-dimensional
2D	Two-dimensional
3D	Three-dimensional
AcKa	2D affinity
AIRE	Autoimmune regulator
APC	Antigen presenting cell
APTES	(3-Aminopropyl)triethoxysilane
BAP	Biotin acceptor peptide
BFP	Biomembrane force probe
BLAST	Basic local alignment search tool
BSA	Bovine Serum Albumin
BTLA	B-and-t-lymphocyte attenuator

C	Celsius
CAR-T	Chimeric antigen receptor T cells
CD	Cluster of differentiation
cSMAC	Central supramolecular activation cluster
CSV	Comma separated value
CTLA-4	Cytotoxic T-lymphocyte-associated protein 4
Da	Dalton
DFS	Dynamic force spectroscopy
DMEM	Dulbecco’s modified eagle medium
DNA	Deoxyribonucleic acid
DNase	Deoxyribonuclease
DR3	Death receptor 3
d-SMAC	Distal supermolecular activation cluster
E. Coli	Escherichia coli
ER	Endoplasmic reticulum
FACS	Flow Activated Flow Cytometery

FOXP3	Forkhead box P3
Fyn	Proto-oncogene tyrosine-protein kinase
GITR	glucocorticoid-induced TNFR-related-protein
HDF	Hierarchical Data Format
HEK	Human embryonal kidney
HSC	Hematopoietic stem cells
HVEM	Herpesvirus entry mediator
ICD	Immune checkpoint blockade
IFN	Interferon
Ig	Immunoglobulin
ILK	Integrin-linked kinases
IPTG	Isopropyl β-D-1-thiogalactopyranoside
ITAM	Immunoreceptor tyrosine-based activation motif
iTreg	Induced regulatory T cells
LB	Luria Bertani
L-BFGS	Limited memory Broyden- Fletcher-Goldfarb-Shanno

Lck	Lymphocyte-specific protein tyrosine kinase
LFA-1	Lymphocyte function-associated antigen 1
Mac-1	Macrophage-1 antigen
MAFA	Micropipette adhesion frequency assay
MAL	Maleimide
mDC	Myeloid dendric cells
MgCl	Magnesium chloride
MHC	Major Histocompatibility Complex
mM	Millimolar
MPTMS	(3-Mercaptopropyl)trimethoxysilane
MWCO	Molecular Weight Cutoff
NaCl	Sodium Chloride
NEB	New England biolabs
NIH	National Institutes of Health
nm	Nanometer
NTA	Nitrotriacetic acid

nTreg	Natural regulatory T cells
OD	Optical density
Pa	Adhesion probability
PBS	Phosphate Buffered Saline
pDC	Plasmacytoid dendritic cells
PEG	Polyethylene glycol
PEI	Polyethylenimine
PES	Polyethersulfone
pMHC	Peptide major histocompatibility complex
pN	Piconewton
pSMAC	Peripheral supramolecular activation cluster
RBC	Red blood cell
RICM	Reflection Interference Contrast Microscopy
RMSD	Root mean square deviation
SA	Streptavidin
SDS-PAGE	Sodium dodecyl sulphate-polyacrylamide gel electrophoresis

SGA	Succinimidyl glutaramide
TCR	T cell receptor
TEV	Tobacco envelope virus
Tfh	T follicular helper
TNF	Tumor necrosis factor
UART	Universal asynchronous receiver-transmitter

SUMMARY

This work investigated two receptors on T lymphocytes that shape immunity, the T cell receptor (TCR) and cluster of differentiation 28 (CD28). T cells coordinate adaptive immunity, but how signaling via TCR and CD28 interactions with peptide-major histocompatibility complex (pMHC) and B7 family ligands on antigen presenting cells govern T cell activation, function, and differentiation remains poorly understood. Towards illustrating how TCR and CD28 receptor biophysics influenced receptor-ligand interactions this work explored 2D kinetics, receptor-ligand interaction memory, and molecular catch bond presence, a counter intuitive phenomenon where force prolongs bond lifetime rather than shortening (molecular slip bonds). *In-situ* biophysical receptor-ligand measurements on live CD8+ T cell surfaces suggested B7 family ligands form monomeric bonds with CD28 and exhibit molecular catch bonds. Although TCR–pMHC catch bonds on splenic T cells represent an established TCR mechanosensing mechanism, the same interaction on hepatic T cells showed slip bonds that correlated with an activated state among liver T cells. CD28 and TCR memory analyses examined how receptor interactions with their ligands impacted future interactions on shorter (seconds) and longer time scales (minutes) within binary, discrete-time adhesion sequences. Moreover, analyzing influences on future receptor-ligand interactions revealed spatial and temporal dynamics governing future TCR and CD28 interactions. Memory analyses showed TCR and CD28 interactions with their ligands increased subsequent test adhesion probability within binary, discrete-time sequences. Memory analyses exploring how adhesion events effected future proceeding tests promoted splenic T cell TCR internalization, a consequence of TCR

triggering and activation. Differences in bond lifetime under force measurements acquired in the first and last 100 bond lifetime tests demonstrated TCR ligation encouraged slip bond formation. This work suggests biophysical instrumentation employed *in-situ* can reveal information about feedback systems regulating immunological receptor signaling. The findings within this work provide insights into mechanistically how TCR and CD28 biophysics could influence receptor signaling. Additionally, this work shows similarities between TCR and CD28 biophysics that correlated with their overlapping localization and function. These insights provide a foundation for future investigations examining CD28 and TCR feedback systems and how those systems shape receptor crosstalk. Employing insights within this work in clinical diagnostics and therapies enhance clinical outcomes.

CHAPTER 1. INTRODUCTION

T cells play important roles in adaptive immunity. Within immunology, research investigations continuously seek a deeper understanding of how T cells function within adaptive immunity. T cells exist in many different subsets distinguished by their immunologic functions, but many questions remain about how T cells sense antigens, coordinate their immunologic functions, and support future antigen responses. Processed antigens and other immune receptor ligands located at APCs and T cell interfaces shape antigen sensing, cell function, and memory development. Although its well understood perturbing immune receptor-ligand interactions and signaling machinery impacts immune responses, mechanistically the physical processes mediating receptor signaling remain poorly understood.

Cell-cell interactions play key roles in CD8+ T cell immunity. This thesis focuses on two key T cell surface receptors functioning within adaptive immunity, the T cell receptor (TCR) and co-stimulatory receptor CD28. As immunoglobulins super family (IgSF) receptors present on T cell surfaces, TCR and CD28 cooperatively influence T cells through co-stimulation, a signal integration occurring within immune synapses (1). Co-stimulation signal integration occurs mechanistically because both receptors co-localize on cell surfaces and engage overlapping signaling machinery (2). Early investigations into TCR and CD28 signaling highlighted co-stimulation necessity through the two-signal model whereby without concurrent CD28 and TCR stimulation T cells would not activate and instead became anergic (3). Moreover, early TCR investigations yielded insights demonstrating somatic TCR gene rearrangement could enhance interactions between TCR

and presented peptide fragments within major histocompatibility complex (MHC) grooves, an essential process influencing T cell development and function through TCR signaling (4). CD28 and TCR signaling shape CD8+ T cell immunity and either increasing or decreasing their signaling enables clinical immunosuppression and immunotherapy. Given their immunological and clinical relevance, CD28 and TCR receptor biophysical measurements could provide insights elucidating a deeper understanding of their contributions to adaptive immunity.

Given the lack of phosphorylation sites on TCR, TCR signaling occurs through the TCR complex, a multimeric structure formed by TCR and CD3 subunits. TCR ligation by peptide major histocompatibility complex (pMHC) induces signaling responses ranging from agonism to antagonism. TCR agonism and antagonism relates with TCR 2D kinetics and mechanosensitivity (Figure 1). Larger 2D affinity and 2D dissociation rates correlate with pMHC agonism. Additionally, molecular catch bond presence and strength associates with pMHC agonism. Inversely, smaller 2D affinity and 2D dissociation rates as well as catch bond absence complements pMHC antagonism. Given correlations between 2D kinetics and mechanosensitivity, this thesis work employed *in-situ* live-cell biophysical instrumentation towards studying TCR and CD28 biophysics.

CD28 signaling involves interactions between its cytoplasmic tail and signaling machinery. Concurrent TCR and CD28 signaling results in T cell activation enabling T cell development and differentiation. CD28 receptors interact with two expressed on APC surfaces, CD80 and CD86. CD80 and CD86 expression on APCs changes after APC activation. CD80 and CD86 demonstrate different interaction kinetics with CD28 and the co-inhibitory receptor cytotoxic T-lymphocyte associated protein 4 (CTLA4). CD28

cytosolic domains bind diverse signaling machinery enabling CD28 signaling pathways that influence cell activation, development, differentiation, and metabolism (5). Although the CD28 signaling results from signaling machinery interactions with CD28 cytoplasmic tails, mechanistically how CD28 ligation drives diverse signaling outcomes remains poorly defined. Researchers examining CD28 mechanosensitivity previously failed to demonstrate mechanosensitivity without concurrent TCR signaling (6, 7), a surprising finding given CD28's published impact on cytoskeletal rearrangement (8). This thesis work examined CD28 biophysics using 2D kinetics and mechanosensitivity measurements towards showing possible biophysical contributions to CD28 signaling.

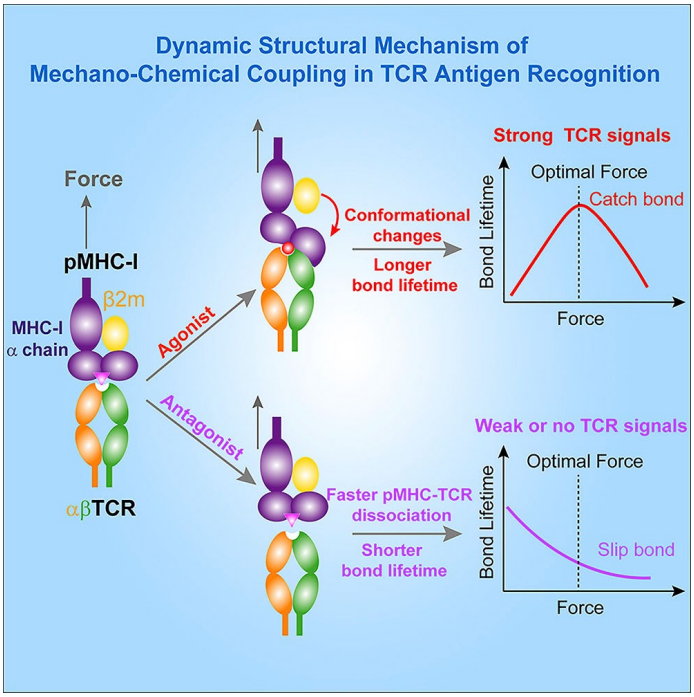

Figure 1 - Previous Publication Graphical Abstract Illustrating Mechanosensing Differences Between pMHC Agonists and Antagonists. A previous publication explored relationships between mechanosensitivity and pMHC function using 2C transgenic TCR mice specific for H2-K^b pMHC. Publication authors performed BFP experiments measuring agonist R4 and antagonist EVSV bond lifetime under force. Strong agonists induced molecular catches (increasing bond lifetime under force until moderate force) while antagonist measurements showed a molecular slip

bond (decreasing bond lifetime under force). Reprinted from Molecular Cell, Volume 73, Issue 5, Wu P, Zhang T, Liu B, Fei P, Cui L, Qin R, Zhu H, Yao D, Martinez RJ, Hu W, An C, Zhang Y, Liu J, Shi J, Fan J, Yin W, Sun J, Zhou C, Zeng X, Xu C, Wang J, Evavold BD, Zhu C, Chen W, Lou J., Mechano-regulation of Peptide-MHC Class I Conformations Determines TCR Antigen Recognition, Pages No. 1015-27, Copyright 2019, with permission from Elsevier. (9)

Both TCR and CD28 receptors inspire different questions about how receptor ligation mediates T cell responses. Interactions between TCR and CD3 induced by ligation trigger downstream signaling events allowing antigen responsiveness, but additional insights into how physiologic and pathophysiologic processes shape antigen responsiveness could enhance immunologic models relied upon in both research and medicine. Physiologically, T cells must remain inactive, protect against self-reactivity, and mount adaptive responses towards eliminating pathogens and cancer. Pathophysiologically, T cells can mediate destructive processes that mount inappropriate immune responses against non-threatening antigens (allergy) and self-antigens (autoimmunity) eventually manifesting as end stage organ disease without clinical treatment. Many research studies suggest T cells respond differently to presented antigens depending on their subtype, but generally measuring antigen responsiveness relies upon functional studies that capture cytotoxic function or cytokine expression levels. Consequently, such experimental methods employed require analyzing large cell populations and exaggerating stimuli beyond their natural presence within physiologic and pathophysiologic processes limiting their statistical sensitivity and specificity. This thesis work employed biophysical measurements towards distinguishing similarities and differences between CD28 and TCR receptors, comparing microenvironmental and T cell subset influences on TCR-pMHC interactions, and developing metrics related to receptor activation in single T cells. Collectively, the findings illustrated *in-situ* biophysical

measurement sensitivity and specificity for characterizing single receptor-ligand interactions and their consequences not possible within many *in-vitro* and *in-vivo* assays.

The rationale for correlating receptor-ligand biophysical measurements with receptor signaling stems from the idea that receptor-ligand interaction induced conformational states shape interactions between receptors and other cellular components. Physically, investigating conformational changes proves challenging given structural analysis methods lack resolution for large, assembled protein complexes under physiologically relevant conditions (10-12). Moreover, imaging methods involve modifications that can impact proteins (13) through altered conformational dynamics (14), function (15), and cell localization (16, 17). Through focusing on TCR and CD28 receptor-ligand interactions this thesis contributes biophysical and mechanobiological insights towards understanding physical processes shaping T cell activation signals.

A major concept explored within this thesis work includes microenvironment induced impaired TCR mechanosensing. As previously discussed mechanosensing relates with pMHC agonism enabling antigen discrimination towards conducing physiological functions. Several processes contribute to forces between T cells and APCs including microenvironment-induced morphological changes (18) as well as movement under fluid flow in blood (19) and lymph (20). Investigating TCR and CD28 receptor-ligand interactions using surface bound receptors and ligands without considering force offers limited insights into physiological and pathological signaling. Likewise, investigating ligand-receptor interactions outside their natural signaling contexts offers limited insights into signaling. Conformational changes in proteins can shape both biophysical and mechanobiological process associated with signal transduction (21-23). As a result, signal

transduction integrates mechanical force waveforms occurring naturally within cell-cell interactions (mechanotransduction) (24). This thesis aims to understand TCR and CD28 biophysics and mechanobiology in model physiologic contexts as well as adapt those findings into developing biophysical metrics and signaling models.

By focusing on both TCR and CD28, this work contributes biophysical insights that could be exploited in immunotherapy and immunosuppression. Immunotherapy and suppression aim to alter natural immune responses towards suppressing or supporting immunological function, respectively. The main modalities currently used in clinical immunotherapy focus on controlling signaling by enhancing CD28 co-stimulation (immune checkpoint blockade, ICB) (25) as well as genetically modifying CD8+ T lymphocytes to express chimeric antigen receptors (CAR-T) featuring domains that specifically bind surface antigens and transduce signals through CD28's transmembrane and intracellular domains to CD3 domains present in the TCR complex (26, 27). Moreover, more recent advances in vaccines utilizing expressed mRNA towards supporting both B and T cell immunity highlight an appreciation for CD8+ T cell activation and differentiation (28). Providing biophysical insights into CD28 and TCR receptor-ligand interactions will yield foundational knowledge for immunology research, immunotherapy, and vaccine development.

This thesis work utilized dynamic force spectroscopy (DFS) using biomembrane force probe (BFP) biophysical instrumentation towards characterizing CD28 and TCR on CD8+ T cell surfaces. Specifically, *in-situ* live-cell measurements described CD28 and TCR 2D kinetics and bond lifetime under force. Within this work, CD28 on CD8+ T cell surfaces displayed ligand-specific 2D kinetics and mechanosensitivity. Additionally, this

work explored correlations between CD8+ T cell subsets as well as spleen and liver microenvironments demonstrating both subtype and microenvironments shape TCR biophysics. Through *in-situ* live-cell biophysical characterization, this thesis work shows TCR and CD28 ligation can influence biophysical measurements correlating with molecular and cellular changes associated with signaling and activation. Collectively, *in-situ* live-cell measurements provide additional perspectives into immune receptor signaling models suggesting similar intracellular processes shape CD28 and TCR signaling. Possibly, overlapping feedback mechanisms contributed to observed similarities.

These insights provide evidence that biophysics shape co-stimulation and provide the basis for further characterizing co-stimulation and co-inhibition receptor biophysics towards a more comprehensive immune signaling model. Moreover, this work illustrates the power for biophysical instrumentation to provide information pertinent to understanding receptor signaling, activation, and their consequences at a receptor and cellular level. This work establishes a foundation for utilizing biophysical instrumentation to ascertain mechanistic information about T cell immunity. This work hopefully will encourage utilizing biophysical measurements towards understanding T cell immunity and immune responses. Moreover, employing the insights and metrics developed within this work could improve clinical outcomes by providing diagnostic information and therapeutic strategies for enhancing or inhibiting immunity.

CHAPTER 2. BACKGROUND

2.1 The Role of CD8+ T cells in Adaptive Immunity

2.1.1 T cells in the Context of The Immune System

The immune system protects the body from dysfunction resulting from neoplasms and pathogens. At the highest level, the immune system responds synergistically through conserved processes mediated by recognizing patterns in abnormal cells or foreign substances (innate) as well as evolving processes involving maturing sensitivity and specificity through differential responses to processed proteins (adaptive). Within natural adaptive immune response, the immune system builds responses by producing proteins that neutralize foreign substances (humoral) as well as cell activation dependent processes that support pathogen and abnormal cell destruction through cytokine secretion, phagocytosis, and cytotoxin release (cell-mediated) (4).

To accomplish the diverse functions required to protect the body from dysfunction by immunosurveillance, a process enabling continuously evaluating self and non-self-antigens towards mounting immunologic responses against neoplasms and pathogens. In order to accomplish immunologic functions, different immune cells subtypes exist distinguished by their developmental lineage from multipotent hematopoietic stem cells (HSC) (29) and capacity for professional antigen presentation (30). Developmentally circulating immune cells come from two distinct hematopoietic lineage lines, myeloid and lymphoid (31). Myeloid immune cells include mast cells (32), granulocytes like eosinophils (33), basophils (34), and neutrophils (35), as well as monocytes that can

develop into macrophages (36) and myeloid dendritic cells (mDC) (37). Lymphoid cells include natural killer cells (38), T and B lymphocytes (39, 40), as well as plasmacytoid dendritic cells (pDC) (41). Functionally, all except basophil myeloid lineage cells can professionally present antigens through phagocytosis with neutrophils, macrophages and mDCs function driven mainly by phagocytic capacity (30). In the lymphoid lineage professional antigen presenting cells (APC) include B cells (42) and pDCs with B cell professional antigen presenting mainly occurring through endocytosis (43). Non-phagocytic lymphoid lineage cells function in adaptive immunity by cell-mediated processes (44, 45) and supporting humoral immunity (4). Humoral immunity occurs through the antibody production by cells derived from B cell. Secreted antibodies can functionally neutralize pathogens and encourage their phagocytosis. Cell-mediated immunity functions primarily to drive pathogen and abnormal cell clearance. Cell-mediated immunity involves cell activation dependent mechanisms driven by antigen recognition by surface receptors. Cell activation in response to antigen recognition supports several mechanistic processes that involve phagocytosis, cytokine, and cytotoxin release. Cell-mediated and humoral immunity influence each other during adaptive immunity (4).

Adaptive immunity largely relies upon T cells that display cytotoxic capacity (46) and helper T cells that functionally support both humoral and cytotoxic T cell responses (47). CD4 or CD8 cell surface expression distinguish helper T and cytotoxic T cells respectively after thymic development (19). Professional APCs activated after phagocytosis can migrate to lymph nodes where they present antigens to developed T and B cells (48). Antigen recognition, cell-cell interactions, and cytokine signaling drive naïve

CD4+ and CD8+ T cells in lymph nodes to differentiate into many different T helper subtypes that play different roles in immunity (49). Differentiated T cells migrate into other lymph nodes and tissues where they can functionally influence adaptive immunity (20). Differentiated CD4+ T helper cells that migrate into tissues can promote inflammation or tolerance (50). Differentiated CD8+ T cells that migrate into tissues can eliminate infected or abnormal cells (51). Collectively T cell driven immunological processes contribute to both health and disease. Adaptive immunity functionally can eliminate pathogens and abnormal cells, but also drive undesirable hypersensitivities like allergy and autoimmunity.

2.1.2 T Cell Development in the Thymus

Immune cells primarily circulate in the body in both the circulatory and lymphatic system. Immune cells developmentally arise from the bone marrow where multipotent HSCs differentiate into myeloid progenitors and lymphoid progenitors (hematopoiesis) (52). Cytotoxic cell-mediated immunity arises from lymphoid progenitors that can differentiate into natural killer cells and thymocytes. Thymocytes exiting the bone marrow must undergo maturation into lymphocytes (thymopoiesis) in a specialized lymphatic tissue termed the thymus located in the anterior superior mediastinum in front of the heart (53-55). Throughout thymopoeisis in the thymus lymphocytes undergo somatic recombination (V(D)J recombination) (56, 57).

Lymphocyte development in the thymus must delicately balance reactivity to self and non-self to enable functional antigen discrimination essential in immunity. Antigen discrimination involves processes by which self and non-self-antigens processed by APCs

on special protein complexes called major histocompatibility complex (MHC) (58). Physiologically, most cells present antigens through proteolysis where different processes exist to both process self-antigens and phagocytosed non-self-antigens. MHC Class I molecules function through presenting processed peptide sequences produced endogenously within cells. MHC Class II molecules function through presenting processed peptide sequences produced from phagocytized particles (59). Within the thymus T cell development specialized epithelial and dendritic cells present self-antigens through both MHC class I and II molecules (60).

During thymopoesis thymocytes differentially express CD4 and CD8 which functionally relate a TCR's capacity to discriminate antigens presented through MHC class I and class II respectively. Stages within thymopoesis involve transitioning from lacking CD4 and CD8 (double negative) to acquiring CD4 and CD8 (double positive) expression and eventually results in mature lymphocytes expressing either CD4 or CD8 (single positive) (61). Double negative cells undergo positive selection whereby developing T cells through recombination activating genes 1 and 2 (RAG1 and RAG2) expression undergo V(D)J recombination resulting in genetically divergent TCRs that interact with different strengths against presented self-antigens (62). During positive selection T cells develop with varying self-reactive strength resulting maturation eventually leading to double positive T cells, but unreactive cells become anergic and undergo apoptosis. Double positive cells undergo negative selection where cells that interact strongly with self-antigens can be eliminated or become natural regulatory T cells (nTreg) (61, 63). The transcription factor autoimmune regulator (AIRE) enables thymic APCs to express proteins from many different tissues (64). Double positive cells that successfully undergo negative

selection become either naïve CD4+ or CD8+ T cells. Naïve T cells express functional TCRs that can react specifically with presented antigens (19).

2.1.3 T cell Subsets and their Functions

CD4+ and CD8+ T cells developed in the thymus can differentiate into several different subtypes that shape immunity. Experimentally, differences in surface expression, transcription factors, and cytokine production distinguish T cell subtypes. Differences between T cell subtypes enable them to play different immunological roles, but T cells collectively help shape immune system responses (65).

CD4+ T cells diverge into T helper cells and regulatory T cells. CD4+ T regulatory cells called induced regulatory T cells (iTreg) can also develop within lymph nodes (66). CD4+ T regulatory cells protect against host autoreactivity by releasing anti-inflammatory cytokines after activation (67). CD4+ T regulatory cells are distinguished by forkhead box P3 (FOXP3) transcription factor expression (68). CD4+ T helper cells subtypes include T helper (Th) 1, Th2, Th17, and T follicular helper (Tfh). CD4+ T helper subtypes support humoral and cell-mediated immunity by secreting different cytokines and providing specific cell-cell ligands. Certain T helper cells like Th1 and Th17 enhance cell-mediated immunity by secreting interferon-γ (IFNγ) and interleukin (IL) 17, respectively. The Th2 subtype enhance parasitic immunity by stimulating and recruiting basophils and eosinophils as well as encouraging immunoglobulin (Ig) H production in B cells. T helper cells encourage B cell-based humoral immunity through antibody class-switching mediated by CD40-CD40L co-stimulation and cytokine signaling. Tfh cells promote antibody production by creating anatomic structures within lymph nodes called germinal

centers (69). In lymph nodes, germinal centers feature mature B cells that proliferate, differentiate, and shape antibody affinity through somatic hypermutation (70).

CD8+ T cells play key roles in cell-mediated immunity by destroying infected and genetically abnormal cells through antigen-specific mechanisms. Naïve CD8+ T cells can differentiate into regulatory, follicular, and effector subsets (71). Regulatory CD8+ T cells suppress immunity and enhance tolerogenic responses by cytokine secretion, supporting tolerogenic APC formation, and cytotoxic activity against CD4+ T cells (72). CD8+ T follicular cells regulate B cells within germinal centers and suppress auto-antibody production (73, 74). Effector CD8+ T cells exist in several subtypes distinguished by their effector function and cytotoxic potential. Effector CD8+ T cell subsets include T cytotoxic (Tc) 1, Tc2, Tc9, Tc17, and Tc22 (71). Tc cell subsets largely resemble cytokine profiles within the T helper subsets previous described. Tc1 fits the most classical T effector cell definition by secreting IFNγ and TNFα and cytotoxic function (75, 76). The Tc2, Tc9, Tc17 and Tc22 diverge from the classical T effector cell definition by expressing different effector cytokines. Only Tc2 and Tc22 cells retaining cytotoxic function (71).

CD4+ and CD8+ T cells also diverge into different subsets within a spectrum defined by memory and effector function. Self-renewal capacity and *in-vivo* longevity define memory T cell subsets (77). Cytokine production and cytotoxic activity define effector functionality in CD4+ and CD8+ T cells (78). Naïve CD8+ and CD4+ T cells differentiate into different cells within the memory and effector spectrum, but mechanistically the differentiation process remains poorly understood. Several models exist attempting to explain memory and effector cell lineages that focus on T cell antigen specific activation and differentiation state. In the on-off-on model activation through TCR result in a large

clonal effector cell population that after antigen clearance can become memory cells randomly or by superior specificity. Moreover, memory cells resemble naïve CD8+ T cells more and through antigen specific activation again form a larger effector clonal T cell population (79). In the developmental differentiation model naïve T cells become differentially activated with more highly activated cells undergoing apoptosis after antigen clearance (80, 81). In this model, memory T cells form from less activated cells with lower TCR affinity (82). Analyzing cell division by telomere length supports the developmental differentiation model given effector cells that presumably became more activated exhibited shorter telomeres compared to memory cells (83).

Research on CD8+ T cell subsets focuses on the memory and effector spectrum in the conventional Tc1 cells. CD8+ T cells within the memory and effector spectrum shape future cell-mediated immune responses and cytotoxic activity against infected and abnormal cells. Surface marker expression distinguishes CD8+ T cell memory and effector subsets. CD8+ T stem cell memory (T_{SCM}) cells can self-renew and differentiate into other CD8+ memory and effector subsets (84). CD8+ central memory T (T_{CM}) cells also retain self-renewal capacity and can differentiate into other CD8+ memory and effector subsets (85). CD8+ T_{SCM} and T_{CM} occupy different microenvironments with T_{SCM} identified within diseased tissues like tumors (84) and T_{CM} cells residing in lymph nodes (86). CD8+ T effector memory (T_{EM}) retain more cytotoxic activity and less self-renewal capacity than CD8+ T_{SCM} and T_{CM}, but exist primarily within the peripheral circulation and tissues (86). CD8+ T effector cells produced by naïve or memory CD8+ T cell differentiation exist primarily within the peripheral circulation and tissues and undergo robust contraction (87). The CD8+ memory and effector T cell spectrum plays an

important role in immune surveillance by retaining cytotoxic cell-mediated immunity after immune mediated pathogen or abnormal cell clearance (88).

2.2 T cell Signalling

2.2.1 The Immunological Synapse

The immunological synapse (immune synapse) refers to an interface that forms between lymphocytes and APCs (Figure 2). The supramolecular activation cluster (SMAC) refers to concentric rings formed structurally at immune synapses. The SMAC can be further divided into concentric rings forming the central (cSMAC), peripheral (pSMAC), and distal SMAC (dSMAC) on lymphocytes. In a T cell context, TCR, protein kinase C θ (PKCθ), CD2, CD4, CD8, CD28, and lymphocyte-specific protein tyrosine kinase (Lck), and proto-oncogene tyrosine-protein kinase (Fyn) localize within cSMAC. Lymphocyte function-associated antigen 1 (LFA-1) and talin localize within pSMAC. CD43 and CD45 exist within the dSMAC. Localization within the SMAC influences lymphocyte activation, pMHC transfer from APCs to lymphocytes (trogocytosis), as well as cytokine and cytotoxin secretion (89).

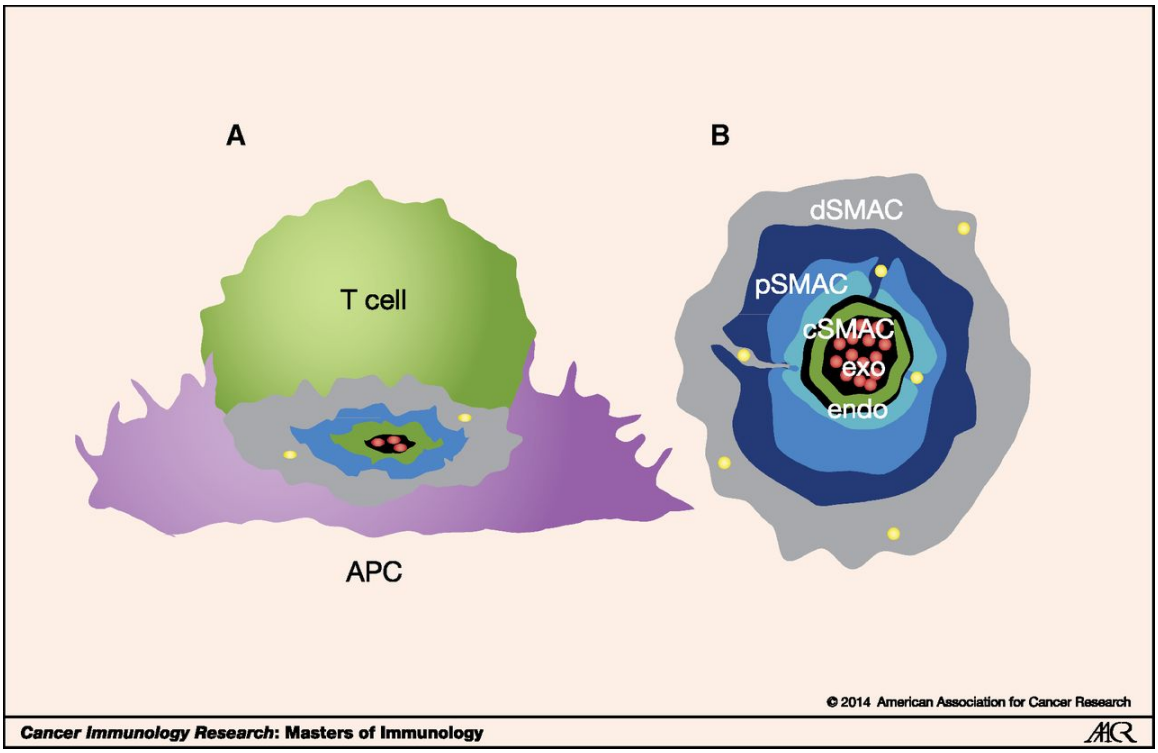

Figure 2 - Graphical Depiction of Immune Synapse Organization. Previous publications using various microscopy techniques captured an organization structure that developed between T cells and APCs termed the immunological synapse. The immunological synapse contained multiple regions defined by cell membrane protein organization. Immune synapse organizational structures included central, peripheral, and distal SMAC (cSMAC, pSMAC, and dSMAC respectively). Reprinted from Cancer Immunology Research, Volume 2, Issue 11, Dustin ML, The immunological synapse, Pages No. 1023-33, Copyright 2014, with permission from Elsevier. (89).

Immune synapses form between cells by dynamic surface protein segregation. In the kinetic segregation model, CD45 phosphatase must segregate away from the TCR complex otherwise its phosphatase activity would prevent TCR phosphorylation. Moreover, receptors on T cell surfaces segregate in a size-dependent fashion between T cell and APC. In a close-contact zone formed between T cells and APCs the smaller T cell receptors mediating T cell activation aggregate together excluding larger surface receptors such as CD45 (90). Physically, the kinetic segregation model's focus on molecular interaction

kinetics between surface proteins on T cells and APCs provides a robust model for how randomly distributed signaling machinery could form complex and regulated signaling complexes shaping T cell activation (91). Kinetics strongly influence immunological synapse characteristics with pMHC-TCR interaction strength and density strongly correlating with TCR segregation from ICAM-1 (92).

Since demonstrating these important considerations driving immune synapse structure arising from molecular interactions, cytoskeletal changes shape immune synpase receptor and signaling machinery segregation. Mechanistically, the SMAC formation involves a stepwise morphological change within T cells driven by actin cytoskeleton dynamics that segregate receptors into domains that favor T cell activation signaling (93). Initially, TCR triggering causes sub-micron clusters (microclusters) driving F-actin nucleation through downstream adaptors (94). Synapse formation occurs at the micro scale involving organizational receptor structures. Initially, T cell spreading encourages actin enrichment within the dSMAC (95), actomyosin enrichment in the pSMAC , and actin depletion within the cSMAC (96). After spreading, actin retrograde flow towards the cSMAC and pSMAC actomyosin contraction. During contraction, actomyosin dynamics drive microcluster movement towards the cSMAC (97).

2.2.2 The T Cell Receptor Complex

The TCR complex forms on T cells through interactions between TCR and CD3 chains. The TCR exists as a heterodimer formed from either α and β chains (TCRαβ) (98) as well as γ and δ chains (TCRγδ) (99). Thymopoesis refers to T cell development occurring within the thymus. Thymopoesis results in naïve T cells expressing either

TCRαβ and TCRγδ which respectively get referred to as either αβ or γδ T cells, respectively (100). TCRαβ interacts antigen with class I or class II pMHC (101). TCRαβ antigen recognition results in signalling through CD3 chains (91). CD3δ, CD3ε, CD3γ, and CD3ζ chains form CD3γε, CD3δε, and CD3ζζ heterodimers enclosing transmembrane TCR in an open barrel (Figure 3). TCR chains contain a transmembrane region with a short cytosolic tail (22). CD3 chains contain immunoreceptor tyrosine-based activation (ITAM) motifs that function in intracellular signalling (102). This thesis work focuses on TCRαβ and abbreviates TCRαβ as TCR.

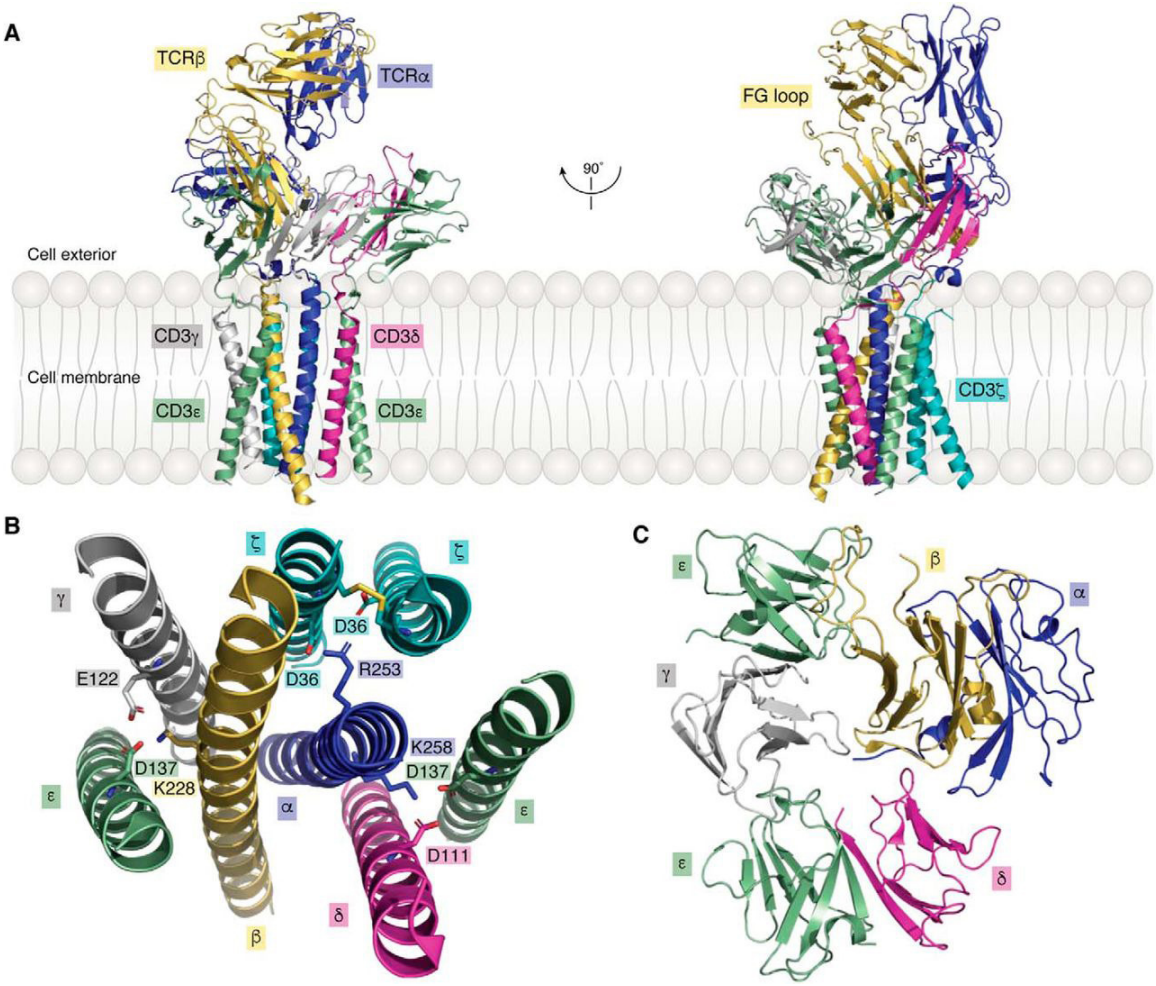

Figure 3 - Structural Diagram of TCRαβ Complex. Previous structural characterization of TCRαβ and CD3 subunits (PDB 6JXR) enabled constructing a ribbon representation for the TCRαβ complex. TCRαβ complex composition includes CD3δ, CD3ε, CD3γ, and CD3ζ chains that interact to form CD3γε, CD3δε, and CD3ζζ heterodimers. Reprinted from Journal of Biological Chemistry Reviews, Volume 295, Issue 4, Mariuzza RA, Agnihotri P, Orban J, The structural basis of T-cell receptor (TCR) activation: An enduring enigma, Pages No. 973-988, Copyright 2019, distributed under the Creative Commons CC-BY license. (103).

TCR gene V(D)J recombination enables the formation genetically diverse TCR heterodimers that can differentially interact with pMHC. V(D)J recombination, a form of somatic recombination, occurs within developing T and B cells shaping TCR and B cell receptor (BCR) by combining variable V, D, and J genetic elements (104). TCRαβ expressing thymocyte development results in first D-to-J β-chain recombination,

subsequently V-to-DJ rearrangement, and finally VDJ rearrangement with the constant domain resulting in full length TCR β-chain. Full length TCR α-chain results from just V-J recombination alone (105). The main enzymes enabling V(D)J recombination include recombination activating genes (RAG) 1 and 2, terminal deoxynucleotide transferase (TdT), and artemis nuclease. Recombination enzymes mediate DNA breaks, DNA repairs, template-independent polymerization, exonuclease enabled stochastic degradation and joining, as well as ligation towards additional recombined domains interfacial diversity (106).

2.2.3 T cell Co-stimulation and Co-inhibition Receptors

Lymphocyte co-stimulation and co-inhibition receptors exist within immune synapses where they enhance or inhibit immune responses, respectively. A prominent signalling model involves acquiring two stimuli for a fully active immune response within T and B lymphocytes (107). In the two-signal model for T cells, APCs provide the first signal through TCR interacting with selective pMHCs and a second non-specific co-stimulatory signal (108). Co-inhibitory receptors work by either competitively preventing ligand binding or producing co-stimulatory antagonistic signals (109). Co-stimulatory and co-inhibitor receptors on T cells exist in two families: tumor necrosis factor receptor superfamily (TNFRSF) and immunoglobulin superfamily (IgSF). T cell co-stimulation and co-inhibition in the IgSF superfamily occur through CD28 family receptors and B7 family ligand interactions. CD28 family members include co-stimulatory receptors CD28 and ICOS as well as co-inhibitor receptors b-and-t-lymphocyte attenuator (BTLA), cytotoxic-T-lymphocyte-associated protein 4 (CTLA-4), and programmed cell death protein 1 (PD-1) (110). TNFRSF superfamily members include co-stimulatory receptors

OX40, 4-1BB, CD30, glucocorticoid-induced TNFR-related-protein (GITR), tumor necrosis factor receptor 2, death receptor 3 (DR3) as well as a receptor with both co-stimulatory and co-inhibitory signalling herpesvirus entry mediator (HVEM) (111).

2.2.4 CD28 Receptor and Ligand Structure

The human CD28 receptor gene features four exons encoding for 220 amino acids that form a glycosylated, 44 kDa disulfide-linked homodimer (112). In addition to expression on developing thymocytes and T cells, bone marrow stromal cells (113), plasma cells (114), eosinophils (115), and neutrophils (116). CD28 expression on human T cells varies throughout life. Almost all T cells express CD28 early in life while at age 80 around 10-15% CD4+ T cells and 50-60% CD8+ T cells lack CD28 (117). Human and mouse CD28 amino acid sequences overlap with a 277 max basic local alignment search tool (BLAST) score (68.90% identical). In thymopoesis, CD28 expression differs during thymocyte developmental stages with its highest on double negative and lowest on double positive thymocytes. Cell activation on both thymocytes and T cells upregulates CD28 expression (118). Like other IgSF superfamily proteins, CD28 monomers feature a ligand binding domain and Ig-like V-type extracellular domains. A disulfide linkage connects two Ig-like V-type extracellular domains with CD28 homodimers. CD28 monomers also contain transmembrane and cytosolic tail components containing signalling motifs (119).

CD28 receptor ligands include B7 family members B7-1 (CD80) and B7-2 (CD86). The human CD80 and CD86 features 7 and 8 exons respectively. Human CD80 and CD86 exons encode for 288 and 309 amino acids respectively. Human and mouse CD80 and CD86 sequences overlap with max BLAST scores 220 (46.30% identical) and 280 (58.9%

identical). CD80 and CD86 can also interact with the co-inhibitory receptor CTLA4 where competition with CD28 drives co-inhibition. CD80 interacts much more strongly with CTLA4 than CD86 (120). CD86 interacts more with CD28 that CD80 (121). As IgSF family members, CD80 and CD86 contain Ig-like V-type and Ig-like C2-type extracellular domains. CD80 and CD86 mutagenesis of the GFCC'C"β-sheet in the Ig-like V-type domain and ABED β-sheet face in the Ig-like-C2-type domain impacts CD28-Ig and CTLA-Ig binding (122). Both CD80 and CD86 contain transmembrane and cytosolic domains. Cytoplasmic CD80 and CD86 tails associate with cytoskeletal and signalling proteins. Cytoplasmic signalling in CD86 occurs through prohibitin-1 (Phb1) and prohibitin-2 (Phb2) adaptor binding resulting in PLCγ2 and PKCα/β_2 phosphorylation mediated NF-κB nuclear translocation (123). Cytoskeletal interactions occur through a conserved motif on CD86 cytoplasmic tails called K4 that plays a role in CD86 polarization in the immune synapse (124). Analogously, the CD80 cytoplasmic tail shapes localization on cell surfaces. CD80 cytoplasmic tail truncation results in CD80 immune synapse accumulation with decreased co-stimulation capacity (125). Non-specific to either CD80 or CD86, CD80/CD86 ligation using CD28-Ig induces NF-κB signalling in an PI3K and AKT dependent way (126). CD80 and CD86 expression occurs on APCs, but CD80 can also be found on FoxP3+ T regulatory cells (127). CD80 on APCs exists primarily as a homodimer, but also in a monomeric form. CD86 constitutively expressed on APC surfaces occurs as a monomer (128). Upon stimulation APCs upregulate both CD80 and CD86 expression (129). CD86 upregulation occurs earlier than CD80 upregulation (130). The CD28 work within this thesis focuses on CD28 expressing murine T cells and their ligands.

2.2.5 Antigen Processing and Presentation

Antigen presentation refers to cellular processes that result in presenting molecules on cell surfaces that can be discriminated against using an antigen sensing receptor. Processed presented antigens can include peptide fragments on MHC class I and class II (pMHC) (59). MHC class I molecules exist on all nucleated cell surfaces enabling peptide fragment presentation from intracellular proteins (131). Only APCs express MHC class II molecules on their surface that present peptide fragments from phagocytized protein (132).

Antigen sensing refers to the process by which interactions between a surface receptor and antigens trigger intracellular signalling processes that encourage cell activation. Antigen sensing through the TCR and BCR involves somatic recombination. TCRs recognize antigens presented on both CD1 and pMHC (133, 134). BCR complexes form from membrane-bound immunoglobulin of any isotype with a membrane domain and a signal transduction heterodimer called Ig-α and Ig-β. Somatic hypermutation enables increased immunoglobulin affinity maturation and class switching in B cells (135). BCR recognizes antigens without processing that exist extracellularly and secreted immunoglobulins (antibodies) functionally neutralize antigens and aid in APC phagocytosis and cell activation through Fc receptors (136). This thesis focuses on antigen sensing by interactions between TCRαβ and MHC class I molecules.

Antigen presentation involves processing steps. APCs load antigen presenting molecules with their antigen payloads within the cell prior to external presentation. Antigen presentation with MHC molecules occurs through proteolytic processing within cells. Proteolytic processing results in peptide loaded MHC molecules with peptides in a

specialized groove. MHC class I molecules on nucleated cells form cytosolic proteolytic degradation resulting in peptides that get translocated into the endoplasmic reticulum (ER), become associated with folded MHC class I molecules, subsequently shuttled through the Golgi apparatus, and finally integrated into the plasma membrane for antigen presentation (131). Given presentation results from proteolytic degradation in the cytosol, MHC class I molecules display many self-antigens as well as intracellular pathogens. MHC class II molecules on APCs fold within the ER with an invariant chain, traffic within the Golgi apparatus to the plasma membrane, undergo clathrin mediated endocytosis, get transported within early endosomes into intraluminal vesicles or multivesicular bodies where sequential invariant chain proteolysis causes class II-associated invariant chain peptide (CLIP) formation in the MHC class II molecule grove, CLIP removal by HLA-DM enzyme, and peptide incorporation into MHC class II molecules that get subsequently trafficked back to the plasma membrane by transport vesicles from antigen processing compartments (132). MHC class II antigen presentation mediates CD4+ T cell responses against self-antigens and extracellular pathogens. Additionally cross-presentation enables APCs to present phagocytized proteins in MHC class I molecules with dendritic cells having the highest efficiency. Cross-presentation involves phagosome proteolytic degradation and antigen export into the cytosol from phagosomes for proteasomal degradation and subsequent MHC class I molecule loading in phagosomes. Antigen cross-presentation can occur during infections, cancer, allogenic immune responses, and homeostatic tolerance maintenance (137). Within this thesis work, we explore antigen recognition using murine MHC class I molecule featuring peptides generated *in-vitro.*

2.2.6 TCR Complex Signalling

The TCR complex contains the TCR as well CD3 heterodimers that enable signalling. ITAMs located within CD3 intracellular domains enable signalling with CD3δ, CD3ε, and CD3γ containing one ITAM and each CD3ζ chain containing three ITAMs resulting in 10 total TCR complex ITAMs. TCR signalling occurs when the TCR heterodimer engages a presented antigen. In the context of TCRαβ signalling, TCR engages processed peptide fragments within MHC class I and class II molecules. TCR engagement with cognate pMHC triggers Lck recruitment to the TCR complex by CD4 or CD8 co-engagement with pMHC and co-localization enabling Lck to phosphorylate ITAM signalling motifs within the TCR complex. ITAM phosphorylation enables SH2 domain mediated Zeta-chain-associated protein kinase 70 (Zap70) binding preventing Zap70 autoinhibitory mechanisms by localization near the plasma membrane. Zap70 recruitment and activation drive TCR complex signalling events through linker for activation of T cells (LAT) phosphorylation mediating SH2 domain-based docking for downstream signalling. Downstream signalling through LAT involves PLCγ1, GRB2 and GADS, as well as SOS and SLP-76 adaptors that trigger Ras, Rac, and Rho GTPase activation (91).

2.2.7 CD28 Signalling: Integration and Independent

The human CD28 intracellular tail contains distinct signaling motifs that enable diverse, multifunctional signaling both independently and concurrently with TCR. Without intrinsic enzymatic activity, CD28 relies upon adaptor proteins and kinases during intracellular signaling. Human CD28's cytoplasmic tail contains motifs that associate adaptors and kinases featuring SH2 and SH3 domains (138). Human CD28 contains two main motifs, YMNM (139) and PYAP (140). YMNM, CD28's most cross-species conserved motif, mediates interactions with PI3K (139, 141), GRB2, and GADS (142-

144), signaling proteins involved in cell growth, proliferation, differentiation, and survival. CD28 shares the PI3K interaction enabling YXXM motif with CTLA-4 and ICOS. CTLA-4 and ICOS do not retain GRB2 and GADS interactions potentially accounting for signaling differences between CD28 family receptors (145). The PYAP motif enables PDK1 and PKCθ activation through Lck (140). PKCθ signaling mediates cytokine production and survival through NF-κB (146), AP-1 (147), and NFAT transcription factors (148). NFAT transcription factor activation shapes cytokine production and survival (149). CD28 can independently invoke actin cytoskeletal rearrangement without TCR signaling through the small Rho GTPase cell division control 42 homolog cdc42 (150). GRB2 binding recruits Vav1 for Rho GTPases activation mediated changes in actin cytoskeleton (151). Vav1 binding to talin and vinculin can mediate actin cytoskeletal changes to the cell membrane (152). Phosphatidylinositol-4-phosphatase-5-kinase α (PIP5α) can influence CD28-mediated actin polymerization (153). PIP5α kinase generates the PLCγ1 substrate phosphatidylinositol 4,5-bisphosphate (PIP2) secondary messenger (154). Actin cytoskeletal forming lipid microdomains and signalling recruitment also can also be mediated by PxxPP motif and filamin-A interactions (155).

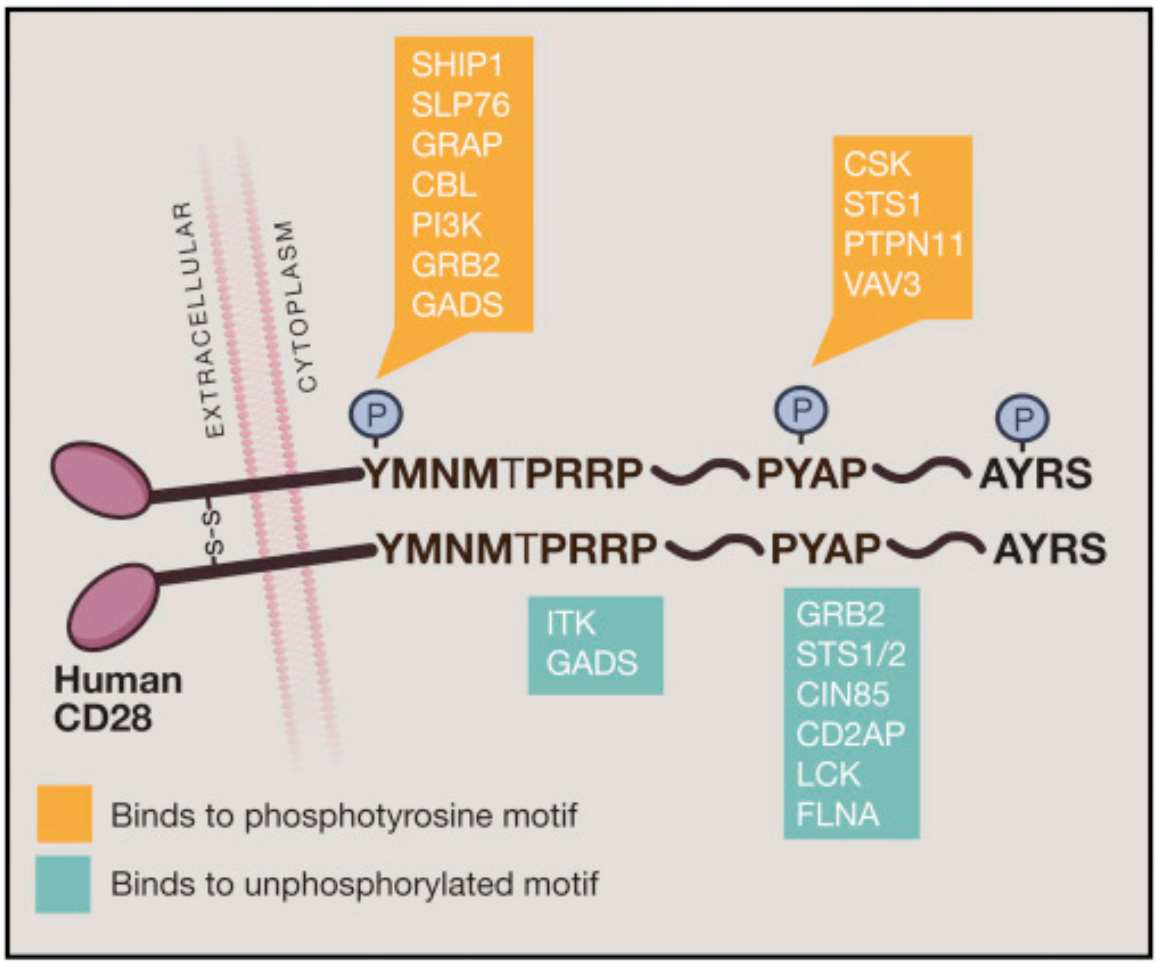

Figure 4 - CD28 Cytosolic Tail Signaling Machinery Interactions. Human CD28 contains multiple intracellular signalling machinery binding domains that bind different signalling proteins depending on phosphorylation state. Interactions between CD28 cytosolic tails and signalling machinery enable diverse signalling outcomes. Reprinted from Immunity, Volume 44, Issue 5, Esensten JH, Helou YA, Chopra G, Weiss A, Bluestone JA, CD28 Costimulation: From Mechanism to Therapy, Pages No. 973-988, Copyright 2016, with permission from Elsevier. (5).

CD28 signalling potentiates T cell activation as a co-stimulatory receptor during TCR dependent signalling (156). CD28 signalling at the immunological synapse contributes to CD28's co-stimulatory function (157). CD28's location at the cSMAC place it proximal to the TCR receptor, co-receptor (CD4 or CD8), PKCθ, Lck, and capping protein regulator and myosin 1 linker 2 (CARMIL2) (96). Without localization in the immune synapse,

CD28 does not retain co-stimulatory capacity given the signaling overlap existing between the CD28 and TCR complex (158). Co-stimulation requires the mechanosensitive actin filament cross-linker filamin-A for cytoskeletal rearrangement and PKCθ signaling (159). Additionally, within thymocytes Csk kinase signaling potentiates full TCR signaling through actin cytoskeletal remodeling (160).

2.2.8 TCR Sensitivity, Specificity, and Antagonism Within Immunity

On T cells, the TCR-pMHC interactions enable T cells to mount antigen specific responses. TCR-pMHC interactions must be both sensitive and specific for T cells to effectively coordinate immunity. TCR triggering refers to mechanistic processes mediating sensitive and specific TCR dependent activation through biochemical changes to CD3 cytoplasmic domains (161). Specific pMHC scarcity on APCs and target cell surfaces requires TCR sensitivity (162). Both CD4+ and CD8+ T cells can respond to between 1-10 pMHCs among 10^5-10^6 irrelevant pMHCs (162, 163). The need for TCR specificity stems from the same MHC molecule used during T cell development potentially presenting different peptides that must be reacted against specifically while supressing undesirable activation (164). A TCR should distinguish between peptides with single amino acid substitutions presented by MHCs (162), but also demonstrate cross-reactivity through recognizing more than one pMHC (165). Moreover, TCR antagonists exist that although specific for ligands fail to mediate T cell proliferation in-vivo and activation despite reaching steady-state internalization (166, 167).

Specificity and cross-reactivity shapes TCR reactivity towards supressing autoimmunity during molecular mimicry and neoplasm specific responses. During

molecular mimicry, conserved structural features between pathogens and humans can potentially drive immune self-reactivity (168). Neoplasms by their nature present antigens resulting from genetic modifications within cells (169) favouring cell proliferation, survival, and metastasis (170). Antigens presented during pathogen and neoplasm immune responses must be specific enough to supress off-target autologous immunity (171). Cross-reactivity also plays an important role within immunity whereby immunological responses mounted against antigens must be robust against potential variants (172, 173). In viral illnesses, viruses stochastically change genetically during error prone nucleotide sequence replication, a process enabling viruses to evade immune responses (174). Cross-reactivity between TCR and pMHC featuring peptides from different viral genetic variants enhances anti-viral immunity (175).

Antigen specificity and sensitivity can occur at many different levels including TCR itself, cell, and immune cell population (162). TCR kinetics shape specificity and sensitivity. TCR-pMHC interactions display decreased affinity and faster dissociation kinetics compared to affinity-matured antibodies (176, 177). The CD8 co-receptor can also stabilize TCR-pMHC interactions by decreasing dissociation rate (178). The serial engagement model describes how a single agonist pMHC can occupy TCRs on T cells. Specifically, the model describes how single pMHC can trigger ~200 TCRs by looking at TCR complex downregulation after peptide pulsed APC specific TCR stimulation (179, 180). Serial engagement explains sensitivity given TCR lower affinity and faster dissociation. Disagreement in the field resides over whether or not affinity or dissociation contributes to specificity (162) although this author believes both shape sensitivity and specificity under force.

The kinetic proofreading model focuses on how interactions trigger downstream signalling. The TCR complex itself does not signal without interactions between the TCR and other signalling proteins such as Lck and Zap70. Within the kinetic proofreading model, TCR-pMHC interactions must exist for a time before mediating T cell activation otherwise upon dissociation the TCR would revert to an inactivated state (91). The kinetic proofreading model does not explain TCR antagonism given that antagonistic pMHCs fail to mediate ZAP70 activation requiring a modification for an incomplete signal (181). Kinetic proofreading does not describe potential ITAM phosphorylation diversity (162), a process important for optimal T cell receptor signalling and thymocyte development (182). Kinetic proofreading explains TCR specificity in that downstream signalling regulation at the TCR complex would shape TCR-dependent activation and integrates other signalling mediators. TCR complex activation mediated by pMHC interactions also involves feedback mechanisms impacting T cell activation temporally (162). Lck regulation occurs through feedback pathways such a trans-autophosphorylation (positive) and CD45 and SHP-1 phosphatases (negative) with Lck also activating SHP-1 (162, 183). Spatial reorganization during TCR signalling changes local Lck concentrations in an activated Lck threshold dependent mechanism (184, 185).

2.3 Immune Receptor Mechanosensing and Mechanotransduction

2.3.1 Cell Receptors and Forces

Cells retain the capacity to differentially respond to environmental stimuli. Environmental stimuli interpretation involves cell surface receptors. Cell surface receptors can mediate signal transduction through conformational changes that open ion channels or

cause internal enzymatic changes. Receptor conformational changes can promote or inhibit interactions between receptors and other molecules. Conformational changes enable interactions between receptors and internal kinases and adaptors that propagate signalling (186). Any physical process involving a physical body's change in momentum over time relates to a directly proportional force (Newton's second law). Receptors and ligands undergo physical processes like diffusion and advection (187). Diffusion refers to a physical process whereby particles disperse along a concentration gradient. Advection results from mass transport along a fluid's bulk motion. In the context of the body, diffusion occurs within body fluids, along cell surfaces, and inside cellular fluids. Fluid flow within cells (188-191) and externally drive advection (187). Advection resulting from blood and lymph flow contribute physically to many physiologically important cell-cell interactions. Constrained diffusion, lateral diffusion constrained within cell membranes, influences surface embedded receptors and ligands (192). Given receptors and ligands have mass, interactions between the two resulting in a momentum change corresponds with force with force magnitudes shaped by ligand mass and presentation. This thesis work focuses on forces on a piconewton (pN) level forces influencing singular immunological cell surface embedded receptor and ligand interactions.

In addition to advection and diffusion, receptors and ligands embedded within cell surfaces can also undergo motion resulting from morphological changes. Cell-cell interactions occur under forces generated simultaneously by cells propelled along fluid flow, traversing through tissue microenvironments, and resulting from morphological changes. Cytoskeleton refers to structural proteins within cells. Cytoskeleton components include actin microfilaments, intermediate filaments, and tubulin microtubules. Actin

microfilaments provide structural support for cells enabling cells to bear tension. Actin generates force on cell membranes through dynamic polymerization that pushes against the cell membrane. Specialized protein motors called myosin attach to actin polymers and can walk along actin. Actin polymerization drives formation and maintenance of cell membrane structures such as the cortex, filopodia, and lamellipodia (186). Collectively actin and myosin can work towards enabling muscle contraction (193), cell movement, intracellular trafficking, cell shape maintenance, cytokinesis (186), and cytoplasmic streaming (intracellular cytoplasm advection) (194). The deformable coiled-coil lamin intermediate filaments provide structural support for the nuclear envelope. Lamin plays a role in signalling, transcription, and chromatin organization (195). Hollow microtubule cylinders dynamically aid in intracellular transport (196), cilia and flagella movement (197), and mitotic spindle function (198).

Cell surface receptors can interact with actin cytoskeleton. Cell surface proteins such as integrins link to actin cytoskeleton through many different mechanisms. The most well studied receptor actin interactions occur within the integrin family. Integrin ligand interactions drive actin filament clustering and recruitment at integrin cytoplasmic domains. Given their linkage to actin cytoskeleton, integrin signalling shapes cell polarization, directed-migration, growth, and survival. Integrins can shape actin-based cell structures like stress fibres, lamellipodia, and filopodia. Other receptors can also interact with actin cytoskeleton through adaptor proteins and signal through actin cytoskeleton. Connections between receptors and actin cytoskeleton involve adaptor proteins like integrin-linked kinases (ILK), α-actinin, talin, and filamin. Adaptor proteins facilitate

signal transduction through receptors giving linked receptors the capacity to influence actin cytoskeleton-based cellular processes (199).

2.3.2 Dynamic Force Spectroscopy

Dynamic force spectroscopy (DFS) refers to biophysical methods employed towards measuring biomolecular interaction force-induced changes. DFS applies different physical principles towards measuring force transduction generally by resolving optical signals. Optical signals can involve determining bead or cylinder displacement by computer vision or laser deflection by photosensitive diodes. The atomic force microscope (AFM) involves a reflective cantilever acting as a spring whereby force bends cantilevers changing a cantilever's laser reflection position resolvable by photosensitive diode or resistor (200). An optical tweezer or optical trap (OT) involves trapping a bead within a focussed laser beam resulting in a spring where measured bead displacement provides a force readout (201). Magnetic tweezers (MT) operate by a similar principle whereby a magnetic field operated on superparamagnetic beads or ferromagnetic nanowires generate forces measurable by bead displacement (202). The biomembrane force probe (BFP) utilizes an assembled force transduction probe resulting from a micropipette aspirated red blood cell (RBC) with an apex affixed glass bead (203).

Given their different physical principles, these DFS biophysical instrumentation setups retain different strengths and weaknesses for studying various molecular interactions. Strengths and weaknesses result from differences in experiment preparation, procedures, force transducer physical constraints, and resolved force signal features. OT, MT, and AFM excel at precise force transducer for molecular interaction measurements

mediating anywhere between femtonewton (fN) (204) to nanonewton (nN) resolution (205). OTs can detect the smallest displacements (0.1-2 nm), operate with 10 KHz temporal resolution, achieves stiffnesses ranging from 0.005-1 pN/nm, generally involves 0.25-3 μm probes, and measures probe displacements between 0.1-10^5 nm. MTs can achieve similar temporal resolution as OTs (10 KHz), provides less spatial resolution than OTs (2-10 nm), operates at stiffnesses ranging from 10^{-3}-10^{-6} pN/nm, involves probes ranging from 0.5-5 μm, and involves displacement measurements between 5-10^5 nms. AFMs achieve lower temporal resolution (1 KHz), demonstrates spatial resolution ranging from 0.5-1 nm, operates in stiffnesses ranging from 10-10^5 pN/nm, involves 100-250 μm probes (cantilevers), and measures displacement from 0.5-10^4 nm. Therefore, for DFS measurements AFMs best handle high force interactions while OTs and MTs excel in lower force measurements with MTs being the most versatile force-wise. OT operation involves strong concentrated electromagnetic radiation risking molecule photodamage and heating that could adversely impact molecular measurements (205).

Investigating single receptor-ligand interactions involve forces between 1 pN to 1 nM (206). Single molecule resolution protein-protein interaction experiments involve immobilized proteins. In single molecule interaction experiments, DFS probes featuring immobilized receptors or ligands pull on complementary proteins immobilized on another surface. In single molecule interaction experiments immobilized ligands on DFS probes interact with complementary receptors on cell surfaces. DFS instrument signals generate force measurements during contact cycles between surfaces. Protein immobilization occurs through covalent binding, physical adsorption, as well as strong non-covalent interactions such as streptavidin-biotin. To favour single molecule interactions during

instrument contact cycles, experimentally controlling protein surface densities increase single protein-protein interaction probability. Practically, at around 20% adhesion probability contact cycles produce an overall 18% single-molecule adhesion event probability. Moreover, such conditions leave an overall 2% multiple bond adhesion event probability (207).

Given these important experimental constraints, BFP instrumentation enables resolving single molecule resolution protein-protein interactions with measurable forces ranging between 0.1 pN to 1 nN and force loading rates ranging between 1-10^6 pN (208). BFP experiments involve DFS probes generated by using micropipettes to precisely control probe positions during both probe assembly and DFS force measurements. BFP experiments utilize a minimum of two pipettes whereby one pipette holds an RBC-based probe coated with immobilized receptors or ligands and another pipette featuring complementary immobilized proteins on a bead or cell. Resolving forces from probe displacement in the BFP employs a mathematical model describing probe stiffness as a function of micropipette radius, aspirated RBC radius, contact disk radius between the RBC and bead, bead radius, and aspiration pressure (203). Experimentally, assembling a targeted probe stiffness between 0.1-0.3 pN/nm requires RBC aspiration, measuring probe component radii, and subsequently readjusting pipette aspiration towards achieving a targeted probe stiffness. Probe quality influences measurement quality and accuracy with the most accurate measurements involving precisely placed apical beads and 1 μm sized radii pipettes with aspirated RBC tails ≈ pipette radius (209). DFS data within this thesis employed BFP instrumentation exclusively. BFP instrumentation provided an ideal DFS

setup for measuring single molecule live-cell receptor-ligand interaction biophysics and biomechanics under physiologically relevant forces.

2.3.3 Receptor Mechanotransduction and Mechanosennsing

Cells must respond to external physical influences while mediating physiological processes. Mechanotransduction refers to the process by which a mechanical (mechano-) energy gets transduced into another energy (-transduction). In the context of cell receptors, mechanotransduction refers to a physical external cue being transduced into biochemical signals within the cell (210). During mechanotransduction, a receptor must be presented with a ligand to enable tension on a molecular bond between a ligand and the receptor (mechano-presentation). During the process of mechanoreception, conformational changes induced by force can stabilize molecular bonds between receptors and their ligands aiding in applying tension along the molecular bond. Following mechanoreception, force propagates from the molecular bond towards the receptor's transmembrane domain and eventually the receptor's cytosolic tail (mechano-transmission). Finally, at the cytosolic tail force propagated along the receptor can support biochemical signal generation within the cell (mechanotransduction). Force propagating through receptors can also apply tension to other proteins within the cell such as kinases and adaptor proteins (211). In integrins, adaptor proteins like previously mentioned can mediate tension to cytoskeletal structures within cells.

Force transmission occurring during receptor mechanotransduction involves receptor mechanosensitive changes. Mechanosensitive mechanisms include deformation, relative displacement, hinge movement, unfolding/unmasking, translocation/rotation, and cluster

rearrangement (211). Deformation causes receptor global shape changes in response to mechanical force and/or hydrophobic effects (211, 212). Pore-forming membrane ion channels and transient receptor potential (TRP) channels can open and close in response to membrane tension. Such processes within TRP channels mediate pain responses within lightly and unmyelinated peripheral nervous system neurons (213).

Relative displacement resulting from mechanical forces can destabilize interactions between external structures to mediate channel opening and closing (211). Relative displacement in mechanoelectrical transducer (MET) mediated by displaced tip link connections within hair cells results in MET channel opening (214). MET channel opening mediates the electrochemical signal translating auditory information into propagated electrochemical signals within the central nervous system during channel opening (213).

Hinge movement manifests within integrins where globular domains connected by a hinge can undergo force-induced conformational changes mediating transition from a bent to extended conformation during hinge opening (211, 215). Integrin hinge opening plays an important role in increasing integrin affinity for ligands, a process that can enhance cell adhesion (216). Cell adhesion plays a role in many essential physiologic processes including platelet aggregation and cell transmigration (217, 218).

Unfolding and unmasking occurring from mechanical force transmitted along a receptor can expose through conformational change domains for cleaving, binding, or enzymatic modification. An example of unfolding occurs in GPIbα and von Willebrand factor (VWF) interactions where unfolding generated by a pulling on VWF causes domains within GPIbα to unfold during signal transduction (219).

Translocation occurs within molecular motors such as myosin and kinesin. Myosin and kinesin ATP hydrolysis mediates unbinding within a subunit and binding within another subunit generating forces that facilitate movement along actin filaments (211, 220). Myosin-related actin cytoskeletal changes shape receptor localization within immune synapses as previously described (97). Rotation motion occurs within ATP synthase where rotation within the F_1 gamma subunit mediated by H+ protons moving from the F_O region causes ADP conversion into ATP (221, 222). Without this mechanical rotation within gamma subunit supporting ATP synthesis within mammalian mitochondria the energy required for many fundamental physiological processes would be substantially limited.

Cluster rearrangement occurs when forces applied on receptors located within organized cell surface units called clusters can mediate interactions between receptors and lateral components within the plasma membrane (211). Integrin cluster rearrangement plays a role in integrin function where high affinity integrin interactions can encourage focal integrin localization within cells (223). Focal integrin localization can distribute cell adhesion forces and promote specific integrin-mediated signalling processes (224-226).

2.3.4 Catch and Slip Bonds

Understanding receptor-ligand interactions occurring at cell-cell interfaces requires both biophysical and biological measurements to develop physiologically relevant models for receptor-ligand engagement and signal transduction. Describing receptor-ligand interactions under force provides biophysical information relevant to understanding physiological receptor function. Relationships between applied force on molecular bonds and bond lifetime can be resolved by DFS to describe force-dependent dissociation rates,

also known as an off-rate. Force and off-rate receptor-ligand interaction relationships generally involve two conserved trends termed molecular catches and slips. During molecular catches increasing tension on bonds causes measurably longer bond lifetimes, associated with a slower off-rate, until force researches an intermediate value. Molecular slips involve the opposite trend demonstrating increasing off-rate under increasing force measured through shorter bond lifetimes (227). Experimentally, DFS measurements under controlled force enable bond lifetime measurements that resolve molecular catches and slips. The resulting bond lifetimes interpreted using survival analysis enable resolving dissociation rates through exponential decay fitting (228). Catch bonds exist within many immunologically relevant receptor-ligand interactions including ICAM-1 (229), TCR (9, 230-232), and macrophage-1 antigen (Mac-1) (233). Catch bonds form the molecular basis for mechanosensing enabling biomechanical transduction into biochemical signals (228).

2.3.5 Immunoreceptor Mechanotransduction and Mechanosensing

Immunoreceptors refers to cell surface receptors that function within an immune system context driving important signalling events that drive key immunological cell functions. In the context of many immunoreceptors within the immune synapse, many immunoreceptors interact with ligands presented on cell surfaces potentially mediating signal translation upon receptor engagement. Forces on T cells occur during circulatory and lymphatic T cell trafficking, migration (234), triggering (235), as well as immunological synapse and kinapse formation and stabilization (236-238). Specifically, this thesis focuses on receptor interactions that occur within the cSMAC.

Several physical processes occur during immune synapse formation and stabilization within secondary lymphoid organs that exert forces on interactions between T cells and APCs including lymph flow as well as cytoskeletal rearrangements within both T and APCs (236). Cytoskeletal changes in both T cells and APCs control receptor localization and morphological cell changes impacting receptor engagement. Mechanosensitive mechanisms shape many cell-cell contacts between T cells and APCs including integrins like LFA-1 and CD2 (LFA-2) and the TCR complex mediating interactions with ICAM-1 and CD58 (LFA-3) respectively (236, 238, 239). Mechanosensitive mechanisms for integrins such as LFA-1 and CD2 resemble other integrins like previously described (229, 240, 241) with segregation within the immune synapse shaped by integrin molecular sizes (242, 243).

2.3.6 TCR Mechanosensing and Mechanotransduction

Findings surrounding TCR mechanosensing and mechanotransduction provide essential information for understanding TCR signalling within immune synapses and illustrates biomechanical cues can mediate TCR triggering. The earliest models attempting to mechanistically describe TCR sensitivity and specificity integrate TCR-pMHC interaction kinetics as well as signal transduction processes and molecular segregation occurring within immune synapses as described previously. TCRs form catch bonds with strong agonists and slip bonds with weak agonist and antagonists. CD8 co-receptor binding can facilitate trimolecular catch bonds with implications shaping thymic negative and positive selection (232). In trimolecular catch bonds CD8 co-receptor interactions mediate Lck-dependent dynamic catches by facilitating catch bonds in what would otherwise be slip bonds when involving biomolecular interactions between TCR and pMHC (232, 238).

Mechanistically, tension applied along a TCR-pMHC results in complex length increases that enhance interactions formed between TCR and pMHC (9). Collectively these findings suggest molecular catches and slips formed between TCR and pMHC contribute mechanistically to TCR sensitivity and specificity (238).

DFS-based measurements provided experimental techniques that could resolve mechanosensitivity and molecular catches formed between TCR and pMHC. Initially, OT measurements applying sinusoidal force tangentially along bead-cell interactions featuring pMHC or anti-CD3 resulted in calcium flux (244). Separately BFP experiments demonstrated tension along TCR-pMHC directed normally could induce calcium flux in a catch bond dependent manner (235). Furthermore, OT experiments involving stepwise probe movements both tangentially and normally could both generate calcium flux (245). DFS measurements conducted with OT and BFP instrumentation demonstrate TCR mechanosensing through visualizing downstream signalling through calcium flux. Moreover, mechanistically forces applied on TCR-pMHC bonds could facilitate mechanical waveforms interpreted within T cells potentially mediating more complex, distinct downstream signalling events (238).

CHAPTER 3. EXPERIMENTAL MATERIALS AND METHODS

3.1 Biophysical Instrumentation and Data Analysis Software

BFP instrumentation within Dr Cheng Zhu's laboratory enabled biophysical experiments. BFP instrumentation involves utilizing computer vision techniques to determine RBC-bead edge position in subpixel resolution from images recorded by

machine vision cameras at high framerates (>1000 frames per second (FPS)) to achieve high spatial and temporal precision. BFP experiments involved a program written in the Labview programming language that interfaced with a 1D piezoelectric actuator through a universal asynchronous receiver-transmitter (UART) serial communications bus to control pT cell positions while simultaneously interpreting bead displacement. The resulting subpixel resolution signal output reflects an instrument cycle interpreted by another Labview or Python analysis program. Analysis programs enable event annotation and specifying key positions within the instrument cycle reflecting impingement relaxation, forces associated with bond lifetime or rupture events, and bond lifetime durations. Analysis programs output created comma separated value (CSV) or hierarchical data format (HDF) 5 files that could be interpreted through python scripts or Graph Pad Prism.

3.2 Protein Engineering and Biochemistry for DFS Experiments

3.2.1 Custom Protein Engineering Software

We developed a software library written in python using the BioPython library to access NCBI sequences for murine CD80 and CD86 and produce chimeric protein sequences *in-silico* (GitHub @amrosado, Artic Vault Contribution). The UniProtKB enabled determining amino acid sequences corresponding to CD80 and CD86 extracellular domains and genetic sequence translation validation. NCBI sequences for AJ278965.1 (*Mus Musculus* CD80) and AK079513.1 (*Mus Musculus* CD86) provided genetic sequences searchable for translational elements. Appending N-terminal secretion sequence and C-terminal biotin acceptor peptide (BAP/AviTag), tobacco envelope virus (TEV) cleavable sequence, and 6x poly-histidine (HIS) sequence elements permitted secreted

translated protein purifiable by nickel-nitrilotriacetic acid (Ni-NTA) modifiable by enzyme chemistry for optimal streptavidin (SA) immobilization. Appended restriction enzyme sequences for NheI and EcoRI at the 5' and 3' sequence ends respectively allowed restriction enzyme-based plasmid subcloning. GenScript subcloned DNA sequences into pCDNA3.1+ (Invitrogen) multiple cloning site (MCS). GenScript produced plasmids used during transient mammalian protein expression.

3.2.2 Plasmid Preparation for Protein Expression

DH10B-T1 phage resistant *Escherichia coli* (*E. coli*) purchased from ThermoFisher Scientifc enabled plasmid production as directed by the manufacturer. To prepare sufficient plasmid DNA for transient transfections, 200 mL scale *E. coli* fermentations at 37 Celsius (C) using 100 μg/mL ampicillin in Luria Bertani (LB) broth produced bacterial optimal for plasmid purification (246). After fermentation culture, PureLink HiPure Maxiprep plasmid purification kits purchased from ThermoFisher Scientific and used as directed by the manufacturer produced transfection grade plasmid DNA.

3.2.3 Bacterial Protein Expression

BL21 (DE3) competent *E. coli* bacteria purchased from New England Biolabs (NEB) enabled bacteria protein expression. BL21 (DE3) component *E. coli* transformed with pET21a-BirA from Addgene (#20857) deposited by Dr. Alice Ting (247) allowed isopropyl β-D-1-thiogalactopyranoside (IPTG) induced protein production. Plasmid transformations as specified by NEB provided inducible protein expression bacteria containing our expression pET21a-BirA plasmid. A 500 mL scale fermentation at 37C with 100 μg/mL ampicillin facilitated plasmid selection and maintenance. Bacterial

protein expression involved adding 400 μM IPTG after achieving an optimal bacterial growth rate resolved by 600 nm optical density (OD) 0.4-0.8.

3.2.4 Mammalian Protein Expression

Transient mammalian protein expression using embryonal kidney (HEK) 293T clone 17 cells from American Type Culture Collection (ATCC) produced murine CD80 and CD86 with physiologically relevant glycosylation. HEK293T/17 cells expressing SV40 large T antigen, an oncogene involved in viral genome replication, facilitated plasmid replication within cells upon transfection. Linear polyethylenimine (PEI) transfection of plasmid DNA into HEK293T/17 cells generated cells transiently secreting protein into culture supernatant. The performed PEI transfections largely resembled previously published methods (248) with histone deacetylation inhibitors addition (249). For all transfections, Dulbecco's modified eagle medium (DMEM) with 4.5 g/L glucose, L-glutamine, and sodium pyruvate supplemented with additional non-essential amino acids (NEAA) and L-glutamine provided culture conditions necessary for 4-5 day secreted protein expression.

3.2.5 Bacterial Protein Purification

Lysing IPTG induced BL21 (DE3) *E. coli* for protein purification began by centrifuging cultures for 10 minutes at 4000 relative centrifugal force (RCF) to extract cell pellets. Cell pellets frozen at -20C overnight provided optimal pellets for enzymatic lysing. To lyse cell pellets enzymatically, treatment with 1 mg/mL lysozyme, 20 μg/mL deoxyribonuclease (DNase) I, and Pierce protease inhibitor tablets (as directed by manufacturer) dissolved into 1x phosphate buffered saline (PBS) buffer at pH 6.8 yielded

a lysed solution for native condition affinity protein purification. Ni-NTA polyhistadine affinity tag purification resin purchased from Cube Biotech and used as directed by the manufacturer generated protein bound resin that could be eluted by imidazole gradients. Imidazole gradients ranging from 20-1000 millimolar (mM) in 1x PBS buffer at pH 6.8 eluted resin bound proteins loaded into disposable affinity chromatography columns purchased from Bio-Rad Laboratories. sodium dodecyl sulphate-polyacrylamide gel electrophoresis (SDS-PAGE) with Coomassie blue staining visualized eluted proteins towards selecting fractions for further processing. A Macrosep advanced centrifugal device with a 10 kDa molecular weight cutoff (MWCO) operated as directed by Pall Corporation at 3000 RCF simultaneously exchanged and concentrated samples into 1x PBS at pH 7.0 (necessary for protein stability).

3.2.6 Mammalian Protein Purification

Protein purification from harvested transfection cell culture media employed polyhistidine affinity chromatography. Centrifugation at 150 RCF for 15 minutes and subsequent supernatant filtering with 0.45 μm pore size polyethersulfone (PES) membranes yielded clarified supernatants. After clarification, dissolved Pierce protease inhibitor tablets purchased from ThermoFisher Scientific prevented proteolytic degradation. Clarified supernatants dialyzed with a 1x PBS dialysate supplemented with 150 mM sodium chloride (NaCl) and 10 mM imidazole at pH 7.6 overnight at 4C using 12-14 kilodalton (kDa) molecular weight cutoff (MWCO) regenerated cellulose purchased from Carolina Biological Supply Company enabled native condition affinity purification. Supernatants incubated with Ni-NTA resin purchased from Cube Biotech overnight at 4C produced protein bound resin. Solutions containing 20-1000 mM imidazole in 1x PBS

supplemented with 150 mM eluted protein from resin loaded into disposable affinity chromatography columns purchased from Bio-Rad Laboratories. SDS-PAGE with Coomassie blue staining identified protein elution fractions containing the target protein. Macrosep advanced centrifugal devices with 10 kDa MWCO membranes purchased from Pall Corporation allowed simultaneous buffer exchanging and concentration into 1x PBS at pH 7.4 before subsequent post-purification processing.

3.2.7 Post-Purification Mammalian Protein Processing Steps

Enzymatic modifications produced protein suitable for BFP biophysical experiments. Prior to enzymatic modification, 280 nm absorbance measurements using a NanoDrop spectrophotometer enabled quantifying protein yield and concentration. Concentration estimation involved applying the Beer-Lambert law using protein excitation coefficients obtained online from the Expasy ProtParam tool. Enzymatic post-processing utilized TEV protease purchased from MilliporeSigma and BirA provided recombinantly in bacteria as previously described. TEV protease-based affinity tag cleavage involved adding 200 units TEV protease and incubating the enzymatic reaction overnight at 4C with gentle agitation. Subsequently, BirA ligated the purified protein's BAP tag by adding concentrated BirA enzyme at a 1:15 molar ratio based on initial purified protein concentration, 20 uL 200 mM adenosine triphosphate (ATP), 20 uL 10 mM D-biotin, 10 uL 1M magnesium chloride (MgCl), and 1x PBS at pH 7.0 to achieve a 1 mL final enzymatic reaction volume (250). After incubating BirA containing enzymatic reactions at 4C with gentle agitation for 6 hours, adding BirA using the same amount previously determined by molar ratio into the enzymatic reaction and overnight incubation at 4C with gentle agitation ensured complete biotin ligation. A final overnight incubation at 4C with Ni-NTA resin in excess captured

cleaved His tags, non-enzymatically processed protein, as well as BirA and TEV protease enzymes. Centrifugation of resin and enzymatic reaction solution in a centrifugation affinity chromatography column separated the remaining protein in solution from the resin. Macrosep advanced centrifugal devices with a 10 kDa MWCO used as directed by the Pall Corporation concurrently concentrated and dialyzed enzymatically processed proteins separated from the resin. Macrosep processing removed residual biotin and buffer exchanged target protein into 1x PBS at pH 7.4. Finally, SDS PAGE gel electrophoresis and 280 nm absorption quantified enzymatic processing steps for determining final product quality.

3.3 Bead Preparation

BFP probes required surface silanizating glass standard beads around 2.0 μm ± 0.4 μm purchased from ThermoFisher to functionalize glass surfaces with thiol groups for subsequent covalent maleimide (MAL) labelled SA linking. A 30-minute incubation in Piranha solution cleaned and hydroxylated purchased glass standard beads. After Piranha solution cleaning, washing three times with filtered deionized water removed residual Piranha solution and subsequent washing three times with 100% ethanol dehydrated hydroxylated beads. Incubating hydroxylated glass beads with 3% (3-Mercaptopropyl)trimethoxysilane (MPTMS) in ethyl alcohol for 2 hours produced glass surfaces uniformly coated with MPTMS. Washing with 100% ethanol three times to remove residual MPTMS and baking beads in glass vials at 100C for 2 hours covalently linked MPTMS onto hydroxylated surfaces. Incubating MPTMS coated beads with an excess of MAL labelled streptavidin in phosphate buffer at pH 6.8 overnight at room temperature with gentle incubation generated covalently immobilized SA surfaces. To

store beads for prolonged periods, washing beads with phosphate buffer and later with 1x PBS with 2% bovine serum albumin (BSA) formed a SA bead stable for a month.

Protein immobilization on SA beads involved incubating beads with biotinylated receptor ligands at varying concentrations. Experiments involving studying TCR interactions utilized the murine P14 TCR system cognate pMHC (gp33) and the murine OT-1 TCR system cognate pMHC (OVA) acquired from the NIH Tetramer Core Facility (TCF) located at Emory University. All pMHCs acquired from the featured human beta-2 microglobulin for additional stability. For P14 TCR experiments, a mutation ablating CD8 pMHC interactions limited observed interactions to those formed only by TCR and pMHC. All murine CD28 experiments used recombinantly expressed murine CD28 ligands (murine CD80 or CD86) as documented previously. Biotinylated ligand incubations at room temperature for 2 hours with gentle agitation in 1x PBS + 2% BSA produced ligand coated beads. After incubations, washing beads with 1x PBS + 2% BSA and storing ligand immobilized beads in the same buffer on ice removed residual ligands and prepared beads for experimental use.

3.4 Cell Isolation

3.4.1 Murine CD8+ T Cell Isolation and Culture

Experiments utilized negative purification to acquire CD8+ T cells from mouse spleens and livers. EasySep CD8+ T cell negative selection kits purchased from StemCell Technologies enabled isolating CD8+ T cells mechanically digested by forcing tissue through 70 μm pore size mesh filters. Purifying CD8+ T cells from spleens involved following the protocol supplied by StemCell Technologies. To minimize the influence of

having cells outside their host, only CD8+ T cells isolated the same day within 6 hours post isolation provided immobilized cell surface receptors investigated experimentally. Flow cytometry and microscopy ensured cell quality post isolation.

3.4.1.1 CD28 Experiment Isolations

BFP experiments investigating CD28 receptor-ligand binding biophysics used C57BL/6 mice. Given CD28 expression varies during organism lifespan, we preferably used younger mice (~3 months old) for CD28 experiments. Procuring CD8+ T cells from mouse spleens utilized the Easy Sep CD8+ T cell isolation kit specified previously.

3.4.1.2 P14 TCR Experiment Isolations

P14 TCR receptor-ligand biophysical measurements involved both BFP and micropipette adhesion frequency assay experiments. Experiments utilized RAG knockout transgenic mice that express P14 TCR specific for lymphocytic choriomeningitis (LCMV) gp33 antigen . Humanely sacrificed P14 mice provided spleen and liver tissues for CD8+ T cell isolation. Portal vein perfusion before tissue surgical excision ensured the isolation of tissue resident cells. After surgical excision we mechanically digested spleens and livers using the same methodology specified in the EasySep product documentation. Subsequently after mechanical digestion, Percoll (GE Healthcare) density-based separation selected for non-parenchymal cells. Negative selection using an EasySep Murine CD8+ T cell isolation kit (memory and effector memory cells) or EasySep Murine naïve CD8+ T cell isolation (antigen inexperienced cells) sepearted CD8+ T cells as specified by the manufacturer's (StemCell Technologies) protocol.

3.4.1.3 Flow Activated Cell Sorting (FACS) for CD8+ T cell Memory Subsets

Two-dimensional effective affinity measurements for different murine CD8+ T cell memory subsets required flow activated cell sorting (FACS) CD8+ cells from LCMV-armstrong (Arm) resolved infection mice. Adoptively transferred P14 TCR transgenic T cells (Thy1.1^{+} or CD45.1^{+}) into C57BL/6 (Thy1.2^{+} or CD45.2^{+}) mice 1 day before LCMV-Arm infection enabled an acute LCMV infection with cells that could be subsequently separated using FACS at least 30 days after a resolved acute infection. FACS separation involved antibodies against Thy1.1 or CD45.1, CD8, KLRG-1, and CD127. Resolving effector memory from central memory CD8+ T cells involved gating for adoptively transferred CD8+ T cells expressing CD127^{hi} KRLG-1^{lo} (central memory) and CD127^{lo} KLRG-1^{hi} (effector memory) based on their relative expressions as determined by fluorescence. Purity FACS sorting ensured maximum specificity for effector and central memory CD8+ T cells.

3.5 Surface Density Measurements

Calculating molecular surface densities involved flow cytometry with phycoerythrin (PE) calibration beads manufactured by BD Biosciences. Incubating beads and cells with 10 μg/mL PE conjugated antibodies ensured saturating epitope binding sites for correlating PE fluorescence with molecular surface densities. Monoclonal antibodies conjugated with PE specific for ligand and receptor epitopes enabled determining molecular surface densities. Subtracting non-specific antibody binding signal from cells utilized a similar incubation with an isotype control PE conjugated antibody. Subtracting non-specific antibody binding signal from beads featuring immobilized ligands involved using the same

PE conjugated antibody specific for the ligand incubated with an SA bead without ligand. To ensure a comparable signal between SA beads incubated with the same antibody and ligand coated beads incubated with an isotype, we initially investigated the staining florescence between several ligand coated beads with the appropriate isotype to demonstrate a negligible difference in florescence.

3.5.1 Specific Monoclonal Staining Procedures for Cells and Beads

On T cells, receptor surface density measurement utilized monoclonal antibodies H57-597 and E18 against TCR and CD28, respectively. On ligand coated cells and beads CD80, CD86, and gp33mt ligands quantification involved clones 16-10A1, GL-1, and KH95, respectively. For background subtraction, samples with isotype controls for TCR and CD28 (mouse IgG2bκ and clone MPC-11 respectively) provided non-specific binding signals. For background subtraction for beads, incubating SA beads with the same antibody used for ligand staining as previously discussed provided non-specific binding signals. Incubating beads and cells at 4° Celsius (C) for 30 minutes using 10 μg/mL (well beyond saturation) with 10^5 cells or prepared beads in 100 uL volumes ensured each antibody bound a single epitope with minimal surface density changes during staining. A PBS + 2% FBS cell staining buffer minimized non-specific stating in cell samples. A PBS + 2% BSA antibody bead staining buffer minimized non-specific staining in cell samples and prevented biotinylated ligand dissociation given FBS would feature physiologic biotin concentrations. Washing beads and cells twice with 200 uL of their respective staining buffers before resuspending beads or cells in 100 uL of staining buffer removed residual antibody unbound to surface epitopes. Fixating cells by adding 200 uL of PBS + 0.7% paraformaldehyde (PFA) ensured sample stability before flow cytometry quantification.

3.5.2 Flow Cytometry Instrument Data Acquisition and Surface Density Extrapolation from Flow Cytometry Fluorescence Data

Flow cytometry measurements using BD Accuri C6 and LSR II instruments maintained at the Georgia Institute of Technology Cellular Analysis and Cytometry Core (CD28 experiments) and Yerkes National Primate Research Center at Emory University (P14 experiments) supplied flow cytometry standard (FCS) data analysed in Flow Jo version 10.5 software (BD Biosciences). Standard curve generated from log base 10 transformed geometric means versus log base 10 PE molecular density enabled extrapolating molecular densities in Office 365 Microsoft Excel. The determined molecular amount for the whole cell or bead surface enabled us to calculate surface densities by then dividing by bead or cells surface area. For beads and cells, assuming a spherical shape provided a surface area estimate provided cell and bead radii (equation for surface area = $4\pi R^2$). Bright field microscopy enabled measuring mean radii for beads, murine CD8+ T cells, and human RBCs: 2 μm, 6 μm, and 7 μm respectively.

3.6 Micropipette Adhesion Frequency Assay (MAFA)

3.6.1 RBC Biotinylation and Ligand Immobilization

The micropipette adhesion frequency assay (MAFA) enabled determining 2D receptor-ligand interaction kinetics. Biotinylated RBCs using an NHS-based linker chemistry from Sigma Millipore (Biotin-X-NHS) at varying molar concentrations ranging from 0.1-500 micromolar (μM) in EAS45 buffer provided RBCs for SA based biotinylated ligand immobilization as previously described (251). To validate surface biotinylation quality prior to ligand coating, SA-PE staining with saturating amounts provided surface

biotinylation density estimates as previously discussed in Section 3.5.2. On the day of experiments, coating RBCs with 1mg/mL SA in EAS45 buffer at room temperature for 20 minutes provided SA immobilized surfaces. After SA coating, washing RBCs twice with 200 uL EAS45 and subsequently incubated SA coated RBCs with 20 μg/mL biotinylated gp33mt (gp33 H2-D^b with ablated CD8 binding) acquired from the tetramer core facility (TCF) at Emory University produced gp33mt coated surfaces with appropriate biophysical characterization orientation. Washing RBCs again twice with 200 uL of EAS45 buffer before resuspending RBCs in 10 uL EAS45 buffer ensured only ligands immobilized by surface SA could produce measurable interactions between bead and cell pairs.

3.6.2 MAFA Chamber Assembly

Acquiring MAFA data required assembling a thermodynamically stable chamber not reliant upon carbon dioxide gas exchange for buffering. MAFA chambers assembled using a modified microscope stage with magnetic strip featuring aluminium L brackets for supporting a 5 mm thick channels created an experimental setup that could pair liver and spleen cells with the same gp33mt coated RBC. Chamber assembly involved cutting 60 mm long by 24 mm wide rectangular 1 oz coverslips in half lengthwise and using vacuum grease to hold coverslips in place. Carefully assembling a L15 chamber media (L15 culture media + 2% BSA + 5 mm HEPES) channel along both L brackets provided the experimental environment used in MAFA experiments. Mineral oil chamber sealing ensured thermodynamic stability during experiments.

Pairing between anatomic compartments required carefully assembling the experiment within the chamber. After chamber assembly, gently adding cells into the

chamber and placing cells spaced out from each other prevented sample mixing and ensured chosen cells represented the appropriate experimental groups. Chamber cell placement involved putting the RBCs in the center and CD8+ T cells from spleen or liver above and below the RBCs. MAFA experiments also utilized micropipettes forged from borosilicate glass tubes at < 1.6 μm for RBCs and between 2-3 μm for CD8+ T cells. Pressure control columns with filtered DI water controlled fluid pressure within pipettes to gently aspirate RBCs and CD8+ T cells. During experiments we aspirated RBCs and CD8+ T cells by carefully controlling pipette pressure. CD8+ T cells from the liver required very low negative pressures and optimal pipette sizes to prevent shear mediated cell death. Holding CD8+ T cells from the spleen with the same rigorous aspiration technique provided comparable measurements between anatomic compartments.

3.6.3 MAFA Anatomic Compartmentalization Experimental Procedure

Pairing CD8+ T cells from anatomic compartments increased statistical power and reduced cofounder effects. Pairing CD8+ T cells from different anatomic compartments involved using the same ligand coated RBC when conducting contact cyles. Alternating between assessing spleen or liver CD8+ T cells prevented a contact cycle mediated RBC effect. Replacing RBCs after finishing both spleen and liver CD8+ T cell contact cycles provided unique paired anatomic compartment data. Contact cycles involved piezoelectric actuation to control RBC position relative to the tested CD8+ T cell. During contact cycles, targeting a 2 μm contact diameter between cell-cell pairs provided a sufficient impinged RBC surface area with minimal variability contact cycle variability. Contact cycles also required a uniform 14 μm/s piezo velocity for impingement and retraction based upon prior anatomic compartment experiments. A 2s contact duration between cell pairs enabled

measurements that reflect binding equilibrium between gp33mt and P14 TCR. Only using an assembled chamber for 2 hours ensured measurements reflected the cells as close to their physiologic state after isolation.

3.6.4 Mathematical Modelling Bernoulli Process Towards Deriving 2D Effective Affinity

MAFA adhesion frequency measurements involved 50 contact cycles between cell-cell pairs. Adhesions between cell-cell bead pairs during contact cycles required visualizing RBC deformation resulting from clear focal adhesions along the RBC surface during retraction. Non-adhesion events lacked RBC deformation during retraction. Contact cycles resulted in binary discrete-time sequences assumed to reflect a Bernoulli process. Interpreting 2D effective adhesion frequency utilized a mathematical model interpreting an adhesion event as a contact cycle involving any number of bonds. Adhesion frequency calculations reflected the number of adhesion events over non adhesion and adhesion events summed (Equation 1). A probabilistic adhesion kinetics model (Equation 2) transformed adhesion frequency into the average number of bonds. The kinetic model assumed a single-step reversible kinetic process involving a first-order reverse interaction and second order forward interaction (Equation 3). Experimentally controlled contact time (t_c), receptor (m_r) and ligand (m_l) surface densities enabled resolving kinetic parameters using non-linear least squares fitting. Simplifying our 2D affinity model by assuming binding equilibrium occurred at t_c = 2s generated a 2D effective affinity (Equation 4).

Equation 1 - Adhesion Frequency

$$P_a = \frac{n_a}{n_a + n_{na}} \tag{1}$$

Equation 2 - Relationship Between Average Bond Number and Adhesion Frequency

$$P_a = 1 - \exp\left(-\langle n \rangle\right) \tag{2}$$

Equation 3 - Kinetic Model Relating Average Bond Number to Kinetic Parameters

$$\langle n \rangle = m_r m_l A_c K_a \left[1 - exp\left(-k_{off} t_c\right)\right] \tag{3}$$

Equation 4 - 2D Effective Affinity from Simplified Kinetic Model

$$A_c K_a = \frac{\langle n \rangle}{m_r m_l} \tag{4}$$

3.7 Biomembrane Force Probe (BFP)

3.7.1 BFP Instrumentation

Biomembrane force probe (BFP) instrumentation required a specialized bright field microscopy instrumentation setup with a magnification reflecting a high spatial and temporal resolution to provide measurements characterizing a single bond's duration. BFP experiments utilized a calibrated force transducer assembled from an RBC and silica bead

pair for measuring interactions between receptors and ligands. BFP instrumentation involved utilizing a high-speed CCD camera (Prosilica GE680) connected to a computer by a GigE camera connection to determine bead displacement at subpixel resolution. The BFP instrumentation software recorded bead displacement over time during contact cycles that involved controlled cell placement relative to the BFP probe. BFP probes assembled from biotinylated red blood cells (RBC) treated with nystatin enabled displacement measurements that reflected probe spring constants between 0.1-0.3 pN/nm.

3.7.2 BFP RBC Preparation

Generating BFP probes required biotinylated RBCs with stiffnesses that reflected the mathematical model employed within our instrumentation setup. RBC biotinylation involved N-hydroxysuccinimide (NHS) chemistry using 3500 Da biotin polyethylene glycol (PEG) succinimidyl glutaramide (SGA) linkers purchased from JemKem Technology USA. NHS chemistry on RBC surfaces using isosmotic carbonate bicarbonate buffer at pH 8.5 for 30 minutes at room temperate with gentle agitation provided biotinylated RBC surfaces for bead immobilization. Washing biotinylated RBCs with 5% N2 buffer and subsequently treating with varying nystatin concentrations produced RBCs with variable, temporally dependent stiffnesses that lasted between 1-4 weeks. Storing RBCs at 4C in N2 5% buffer ensured RBC stability by reducing metabolic demand and providing the minimal metabolic resources required for maintaining RBC membrane stability.

3.7.3 BFP Chamber Preparation

Assessing *in-situ* interactions between cell surface receptors and immobilized ligands required a thermodynamically stable chamber supplying metabolic resources essential for CD8+ T cell homeostasis. BFP chambers employed aluminium L brackets held together by a metallic arm. Cutting 22 mm x 40 mm glass coverslips into two rectangular portions along the long end provided a translucent surface compatible with bright-field microscopy. Placing coverslips on L brackets with 2 mm thickness L-brackets using vacuum grease held the coverslips stationary. Adding L15 chamber media with 2% BSA between the coverslips created channels subsequently sealed from the environment using mineral oil to ensure thermodynamic stability. After chamber sealing placing BFP RBCs and beads to assembled chambers and waiting at least 5 minutes for particles fall to glass surfaces ensured chambers mounted onto the microscope stage maintained locations within the chamber for experimental components selection. Inserting micropipettes for BFP probes, T cells, and beads into the chambers at angles conducive for touching the chamber bottom enabled assembling both probes and probe-cell pairs for instrument contact cycles.

3.7.4 BFP Probe Assembly

BFP probe assembly required a careful calibrated instrument whereby RBC aspiration for the probe would reflect a configurable negative pressure to generate BFP probes with stiffnesses ranging from 0.1-0.3 pN/nm. Initially, determining probe pipette zero pressure involved altering water pressure column height until fluid flow from the pipette would not change RBC position within the BFP chamber. Column height adjustments occurred in larger increments until finally providing a 0.1 mm resolution zero pressure. BFP probe assembly comprised aspirating prepared RBCs using a micropipette between 1.8-2.2 μm diameter and then used a small pipette (0.8-1.4 μm diameter) to

position 2.0 μm diameter beads on aspirated RBC apexes. Selected RBCs within a proper stiffness range demonstrated a RBC tail within the pipette between 1-2 μm in length. A mathematical model developed by Evans et. al. (203) provided the optimal aspiration pressure for RBC stiffnesses from 0.1-0.3 pN/nm for subsequent water column height adjustment for pressure control. Mathematical model parameters used for determining aspiration pressure included pipette, RBC, contact disc, and bead radius.

3.7.5 Micropipette Adhesion Frequency Assay Using BFP

Producing 2D kinetics with high temporal off-rate resolution employed utilizing BFP instrument data with the same mathematical model previously described for the MAFA (Equation 3). BFP instrumentation for 2D kinetics involved using the BFP in a bond rupture mode. MAFA BFP measurements utilized a 0.3 pN/nm probe stiffness. BFP in a bond rupture mode employed a controlled probe impingement and retraction to a force well-beyond possible single molecular bond strength. Specific BFP instrument parameters included a 20 pN activation force, 15 pN impingement force, 1000 pN clamp force, and a 1000 pN/s (3333.33 nm/s) piezo velocity for all piezo movements. Varying contact times provided multiple conditions essential for non-linear fitting the 2D kinetic model. Each probe-cell pair generated at least 75 contact cycles. Specialized software interpreting instrument raw data enabled resolving if contact cycles involved a molecular interaction between probe-cell pairs.

Determining specific contributions to interpreted adhesion events performed using the BFP instrument involved isolating receptor-ligand interactions from non-specific contributions. Determining non-specific binding contributions involved conducting

similar instrument contact cycles with SA coated beads without any ligands. Conducting contact cycles with varying contact times ranging from 0.1 to 5s generated data representing non-specific adhesion contributions with the same contact time range as the investigated ligand. Utilizing the non-specific adhesion frequency model specified in Equation 6 with our non-specific contribution data enabled non-linear fitting to define parameters *a* and *b*. Defining the contact time dependent non-specific adhesion contribution enabled subtracting non-specific signal from ligand-specific adhesion frequency measurements (Equation 7). Assuming the adhesion frequency measurements corresponded to one molecular interaction between receptor and ligand simplified our model for use in non-linear fitting 2D kinetic parameters (Equation 8).

Equation 5 - Specific Adhesion Frequency

$$P_s = \frac{P_T - P_N}{1 - P_N} \tag{5}$$

Equation 6 - Model for Non-Specific Adhesion Frequency

$$P_N = 1 - exp(-a(1 - e^{-bt})) \tag{6}$$

Equation 7 - Model for Specific Molecular Interaction Contributions To Total Adhesion Frequency

$$P_T = 1 - exp\left(-a(1 - e^{-bt}) - \sum_{i=1}^{N} \langle n_i \rangle\right) \tag{7}$$

Equation 8 - Simplified Specific Molecular Interaction Equation For One Molecular Interaction

$$P_T = 1 - exp(-a(1 - e^{-bt}) - \langle n \rangle) \quad (8)$$

3.7.6 Force Clamp Bond Lifetime Measurements

Generating bond lifetime under force measurements required using the BFP instrumentation setup utilizing an assembled BFP force transducer for measuring force placed on a molecular bond and bond dissociation. BFP bond lifetime measurements utilized the BFP in a force clamp mode where retracting the probe a certain distance produces a tensile force on a molecular bond related to probe stiffness. Assembling 0.3 pN/nm probes and subsequently performing contact cycles generated raw instrument data quantifying bond tensile force and lifetime. Specific instrument settings for BFP force clamp experiment contact cycles included a 20 pN activation force, 15 pN impingement force, varying clamp forces (5-50 pN), and a 1000 pN/s (3333.33 nm/s) piezo velocity. Minimizing non-specific bond lifetime measurements required optimal ligand surface densities targeting 20% with a 0.1 s contact duration. Evaluating cell-bead pairs involved 200 instrument contact cycles before assembling a new cell-bead pair. Careful attention to probe stability ensured force measurement accuracy. Analysing signals involved interpreting bead displacement with specialized software after experiments.

3.7.7 BFP Signal Interpretation

Post experimental signal analysis involved interpreting raw BFP instrument bead displacement data. Raw displacement data corresponded to different phases based on piezo

position throughout a contact cycle. Evaluating raw signal for bond tensile force and a clear bond dissociation enabled resolving adhesion from non-adhesion events. Characterizing bond dissociations required a rapid release of force (force clamp assay) or a shift in signal standard deviation back to baseline (thermal fluctuation). Bond lifetime measurements only included instrument cycles with a clear singular dissociation. Recording within the signal where impingement relaxation starts, impingement relaxation reaches 0 pN, and resulting tensile forces generated during a bond lifetime or rupture ensured force clamp raw signal interpretation quality. Using mean tensile force signal during a bond lifetime event ensured comparable measurements during potential actin mediated membrane changes. Bond lifetime duration corresponded to tensile force period before bond dissociation. Thermal fluctuation bond lifetimes demonstrated a significantly decreased signal standard deviation within a defined measurement window.

3.7.8 Molecular Stiffness Analysis

Molecular stiffness analysis enabled resolving different bond interaction states relating to receptor valency and multimeric bond formation. Interpreting instrument signals generated during BFP clamp force contact cycles produced temporal changes in force corresponding with probe, cell, and molecular bond stiffnesses. Determining raw signal loading rates during impingement relaxation (below 0 pN, $k_{system\ below}$) and tensile force generation (above 0 pN, $k_{system\ above}$) generated force versus time signals used for calculating stiffnesses. A robust Huber linear regression quantified loading rates ($\dot{F}_{loading}$) for both phases. A Huber linear regression offered more robust signal interpretation less susceptible to signal fluctuations. System loading phases reflected the 1000 pN/s (relative to the probe stiffness 3333.33 nm/s) piezo velocity (Equation 11). Calculating stiffnesses

(k) from loading rates using Equation 12 provided the necessary stiffnesses for determining k_{cell} and k_{probe} from Equation 9 and Equation 10. Discarding negative k values reflecting probe shifting and non-ideal force loading ensured stiffness accuracy. Generating a histogram from the determined stiffnesses and subsequently conducting gaussian fits assuming one or more distributions provided evidence for evaluating multimeric bond types.

Equation 9 - Stiffness Relationship for Cell

$$\frac{1}{k_{system\ below}} = \frac{1}{k_{probe}} + \frac{1}{k_{cell}} \tag{9}$$

Equation 10 - Stiffness Relationship for Molecular Bond

$$\frac{1}{k_{system\ above}} = \frac{1}{k_{probe}} + \frac{1}{k_{cell}} + \frac{1}{k_{bond}} \tag{10}$$

Equation 11 - Velocity of the Piezo From Instrument Settings

$$v_{piezo} = k_{probe}\dot{F}_{piezo} \tag{11}$$

Equation 12 - Relationship Between System Stiffness and Mechanical Loading

$$k_{system} = \frac{\dot{F}_{loading}}{v_{piezo}} \tag{12}$$

3.7.9 Cell Bead Thermal Fluctuation

Generating bond lifetimes at forces below 2 pN required resolving bond lifetimes under force by thermal fluctuation. Thermal fluctuations utilized the BFP in a clamp force mode, but without fully retracting cells if probe displacement lacked bond tensile force. Assembled BFP probes with a 0.1 pN/nm stiffness provided a difference in probe fluctuation dramatic enough to ensure accurate bond lifetime measurements. Adjusting instrument contact cycle parameters towards the same displacements as force clamp experiments ensured thermal fluctuation measurements correlated with force clamping experiments. Using a 333 pN/s (3333 nm/s) piezo velocity prevented probe deformation during contact cycles. Likewise, a 5 pN activation and impingement force with a 0.1 s contact time ensured probe stability during measurements. A 1 pN force clamp placed cell-bead pairs close enough together for 0.1 pN/nm probe thermal fluctuations that could clearly differ during bond formation. Closely monitoring experimental cell-bead pairs enabled retracting cells if ligand stimulation generated morphologic changes that visually displaced beads. A 100-sample standard deviation window for our ~1800 Hz thermal fluctuation signal allowed identifying bond formation and dissociation. Interpreting thermal fluctuation measurements required developing a customized python-based signal analysis program given large contact cycle signal lengths. A previous publication from our laboratory influenced our methodology (252), but the methodology within this work required tweaking for live cell analysis involving receptor-ligand signals that profoundly impact actin cytoskeletal reorganization. Non-linear fitting a bond survival analysis for

thermal fluctuation bond lifetime measurements with forces between -1 to 0 pN using a constrained one-phase dissociation model (Equation 13) estimated off-rates at 0 pN.

Equation 13 - Constrained One-Phase Dissociation Model

$$P_S = \exp\left(-k_{off} * t_{lt}\right) \tag{13}$$

3.8 Statistical Analysis and Curve Fitting

Accurately performing statistical and fittings required using computational tools given data volume and complexity. Graph Pad prism 9.1.0 in a Windows 10 64-bit environment and python based numerical and scientific analysis tools enabled statistical analysis and curve fitting using. The 64-bit Python 3.8 native package manager consistently deployed with NumPy 1.20.1, SciPy 1.6.1, and StatsModels 0.12.2 packages during statistical analysis. The MKL version of NumPy provided by Christopher Gohlke at the Laboratory for Fluorescence Dynamics at the University of California, Irvine allowed high-performance basic linear algebra subprograms (BLAS) optimized for Intel processor architectures. All statistical comparisons shown graphically in figures used Graph Pad prism. Graph Pad Prism linear and non-linear fitting generated 2D kinetic and molecular stiffness Gaussian mean parameters. SciPy non-linear fitting provided parameters for memory and irreversibility analyses. The python StatsModels package facilitated non-parametric kernel regressions using NumPy and SciPy packages. Careful attention to data attributes ensured choosing the most rigorous statistical tests applying corrections for differences in standard deviation, sample sizes, and multiple comparisons. All statistical

analyses used the most rigorous corrections unless differences between experimental group size prevented appropriate multiple comparisons. Each figure and section references specific statistical methods, sample sizes, and experiment quantity when appropriate.

3.9 Antibody Blocking

Demonstrating receptor and ligand interaction specificity required demonstrating receptor antibody blocking would statistically resemble conditions lacking ligand. Antibody blocking experiments involved producing L15 + 2% BSA containing chamber media with 10 μg/mL blocking antibody or isotype controls. Previous work illustrated anti-CD28 clone E18 antibody ablated interactions between CD28 and its ligands (253). Previous work also identified anti-CTLA-4 clone 9H10 antibody ablated interactions between CTLA-4 and its ligands (254). Experiment isotype controls reflected monoclonal antibody isotypes murine IgG2b, κ and Syrian hamster IgG for clone E18 and 9H10, respectively.

3.10 Cell Trap Experiments and Calcium Flux Analysis

3.10.1 Capturing Intracellular Calcium Concentration Changes Upon Receptor Stimulation

Characterizing single cell calcium fluxes resulting from CD28 receptor signalling enabled evaluating a potential receptor signalling consequence. Measuring single cell calcium fluxes employed a microfluidic cell trap device. The cell trap calcium assay methodology development involved a collaboration between Dr. Cheng Zhu's and Dr. Hang Lu's laboratory facilitated by a previous student, Dr. Loice Chingozha (255). Dr.

Fangyuan Zhou conducted microfluidic cell trap experiments for resolving single cell calcium fluxes. Microfluidic device fabrication utilized cross-linked PDMS deposited on silicon wafers with cell trap features formed through photolithography. Plasma treating glass surfaces and PDMS mould feature sides enabled strong surface bonding suitable for protein adsorption. Treating plasma cleaned glass surfaces with 2 mg/mL biotin-BSA, 2 mg/mL 2 mg/mL SA, and then ligands or antibodies at appropriate concentrations for experiments generated experiment surfaces. Washing with 1x PBS between protein treatment steps ensured protein surface immobilization reflected biotinylated ligands with the correct orientation for receptor engagement. Loading CD8+ T cells with Fura-2-acetoxymethyl ester (Fura-2-AM) allowed imaging intracellular calcium flux using fluorescence. Imaging with 340 nm and 380 nm wavelength excitations resolved local intracellular fluxes by ratio. A customized MATLAB image analysis program interpreted single cell calcium fluxes from confocal microscopy image sequences. The MATLAB analysis program tracked when cells occupied positions within cell trap arrays and their subsequent calcium fluxes upon stimulation. Normalizing signals to the first frame allowed measuring relative intracellular cellular calcium signal associated with image sequences generated during experiments.

3.10.2 Calcium Signal Analysis

Raw normalized intracellular calcium signal using python NumPy and SciPy packages allowed smoothening calcium signals and quantifying metrics reflecting differences in calcium signal characteristics that distinguished co-stimulation from ligand independent stimulation. Savitzky-Golay filtering using a first order polynomial with a 11 window size smoothed raw normalized calcium signals allowing for computational feature

derivation. Derived metrics corresponded to signal intensity (cumulative calcium flux), robustness (peak number and cell percentage sustained above 50% maximum calcium flux), and speed (time to reach 50% or 90% the maximum calcium signal). Cumulative calcium flux calculations involved trapezoidal rule signal integration to derive area under curves (AUC). Peak detection resolved calcium signal changes using a requirement that peaks exceed 1 normalized fluorescence unit prominence. Iterating through signals identified the amount of frames calcium signal exceeded 50% signal maximum as well as if when calcium signal exceeded 50% or 90% maximum signal thresholds. Requiring that the thresholds exceed the first frame prevented non-responding cells from contributing to metrics. Python analysis generated HDF5 files that could be evaluated in GraphPad prism for further statistical analysis.

3.11 Molecular Tension Probe

Molecular tension probes (MTP) provided another dimension for characterizing signalling resulting from receptor stimulation through cellular generated tension. Molecular tension probe (MTP) experiments visualized tension applied by live cells on receptor-ligand bonds upon receptor engagement. MTP experiments involved surface treatments that immobilized MTP probes for presenting biotinylated ligands or antibodies. A protocol provided by Dr. Khalid Salaita's lab and previously published methodology (256) enabled generating MTP functionalized surfaces for biotinylated ligands.

Glass surface salinization using (3-aminopropyl)triethoxysilane (APTES) produced amine functional groups for chemical cross-linking. Cross-linking with 2 kDa mPEG-succinimidyl ester (SC) and 3.4 kDa lipoic acid (LA) PEG with subsequent sulfo-NHS

acetate passivation created surfaces that bound gold nanoparticles. MTP probe components included a 4.7 pN hairpin loop strand, a thiol containing strand with black hole quencher 2 (BHQ2), and biotinylated strand with Cy3B. MTP probe assembly occurred through a DNA denaturing and annealing reaction. Surface bound gold nanoparticles covalently bound MTP probes through thiol. MTP functionalized surfaces subsequently immobilized SA for optimal biotinylated ligand presentation. Imaging surfaces using total interference reflection fluorescence (TIRF) microscopy visualized probe tension through Forster resonance energy transfer (FRET) loss. Reflection interference contrast microscopy (RICM) demonstrated surface contact between cells and MTP functionalized surfaces. A MATLAB program analysed images generated during experiments as well as provided a workflow for evaluating surface and image quality. Image acquisition utilized a 60x Nikon TIRF objective and Nikon Ti eclipse microscope within Georgia Tech's imaging core facility.

3.12 Memory Analysis

Adhesion memory analysis allowed characterizing how receptor ligation immediately influenced subsequent interactions by modelling deviation from a Bernoulli process. Adhesion memory modelling involved applying a previously published mathematical model featured in Zarnitsyna, et. al. 2007 (257). Adhesion memory analysis modelling implies that binary, discrete-time sequences generated experimentally during 2D kinetic experiments can deviate from a Bernoulli sequence defined by consistent adhesion probability. A python program interpreted binary, discrete-time sequences and generated memory model parameters by direct (transition probability) and fit (cluster analysis) methods. Binary, discrete-time sequences generated during lifetime analyses

provided memory analysis input. The python program interpreted analysis program annotations and created binary, discrete-time sequences corresponding to single cell-bead pairs. Binary, discrete-time sequences then provided input for further analysis. Limiting analysed sequences to those with 150 contact cycles produced the most consistent adhesion memory analysis between direct and fit methods comparable between experimental systems.

3.12.1 Running Adhesion Frequency and Scaled Event Graphs

Visualizing adhesion memory graphically required plots that demonstrated consecutive adhesion or non-adhesion events within Bernoulli sequences. Determining running P_a involved iteratively determining P_a throughout an entire sequence (Equation 18). Additionally, scaled adhesion event plot generation utilized a sequence's last adhesion frequency value towards scaling adhesion event outcomes. Running P_a plots graphically demonstrated adhesion event clustering through periods of consistent increases in P_a. Likewise, scaled adhesion event plots illustrated sequence periods with adhesion clustering through consecutive adhesions.

Using both the cluster analysis and counting contact cycle results based on prior contact cycle results we determined memory parameters p and Δp. The parameter p represents what P_a should be if prior adhesion contact cycles did not influence adhesion probability for a cycle. The parameter Δp represents the influence a prior adhesion contact cycle has on the following cycle.

3.12.2 Direct and Fit Memory Modelling

Adhesion memory modelling with direct and fit methods characterized deviations from a Bernoulli sequence using parameters *p and Δp* first documented Zarnitsyna et. al. 2007 (257). The parameter *p* represented adhesion probability for contact cycles. The parameter *Δp* related to adhesion probability for a proceeding contact cycle. If adhesions lacked an influence on subsequent contact cycles then $\Delta p = 0$ corresponded with a Bernoulli process where $p = P_a$. If adhesions influenced subsequent contact cycles a positive *Δp* or negative *Δp* increased or decreased proceeding adhesion probably after an adhesion event, respectively.

Memory analysis using cluster fitting involved quantifying clusters by iterating through binary, discrete-time sequences and assigning every adhesion event to a unique cluster. Cluster size (*m*) corresponded to consecutive adhesion event quantity. The memory index M_m (Equation 16) represented cluster number for a cluster size *m* to occur within a binary sequence with length *n* give memory parameters *p* and *Δp*. A non-linear least squares fit using sequence cluster analysis produced fit parameters *p* and *Δp*. Direct memory analyses also utilized the same binary, discrete-time sequences but determined *p* and *Δp* based on transitions alone. Initially, classifying events into groups reflecting transitions between an event and the previous event enabled calculating direct adhesion memory model parameters. Direct adhesion memory model calculations involved determining transition counts denoted by $n_{i,j}$ with *i* and *j* representing the prior and following contact cycle results, respectively. Direct *p* (Equation 14) and *Δp* (Equation 15) calculations utilized all transitions within a sequence.

Equation 14 - Direct *p*

$$p \approx \frac{n_{01}}{n_{00} + n_{01}} \tag{14}$$

Equation 15 - Direct Δ*p*

$$p \approx \frac{n_{01}}{n_{00} + n_{01}} \tag{15}$$

Equation 16 - Memory Model (M_M)

$$M_M(m, n, p, \Delta p) = \begin{cases} p \cdot (p + \Delta p)^{m-1} \cdot \left[1 - p\frac{1 - \Delta p^{n-m}}{1 - \Delta p} + (1 - p - \Delta p)\left(n - m - \frac{p}{1 - \Delta p}(n - (m+1) - \Delta p\frac{1 - \Delta p^{n-(m+1)}}{1 - \Delta p}\right)\right] \\ p(p + \Delta p)^{n-1} \end{cases} \tag{16}$$

3.13 Irreversibility Analysis

Characterizing adhesion influences on all proceeding events required a mathematical model describing long-term changes to an adhesion probability. The irreversibility model described irreversible changes resulting from molecular bonds that aggregated over contact cycles resulting. Binary, discrete-time sequences from annotated lifetime data provided data for non-linear fitting irreversibility parameters. After generating binary discrete time sequences, minimizing χ^2 reduced chi-squared statistic (Equation 17) or the mean square weighted deviation (MSWD) enabled non-linear fitting to derive irreversibility model parameters $<n>$ and I_m. The MSWD fitting approach minimized differences between running adhesion frequency (f_i) (Equation 18) and the irreversibility model (F_i) (Equation 19) featuring parameters $<n>$ and I_M. Within our model $<n>$ represented average bond number and I_M irreversibility within our binary, discrete time sequences resulting from adhesion events.

The minimize tool within SciPy's optimization and root finding library using the limited-memory Broyden-Fletcher-Goldfarb-Shanno algorithm with bounds (L-BFGS-B) method constraining for a positive $<n>$ and 100 max iterations produced fitted irreversibility model parameters. During our fitting, initial parameter values for $<n>$ reflected average bond number given the last running adhesion frequency value. Providing an initial $I_M = 0$ value assumed binary, discrete-time sequences reflected a Bernoulli sequence. Figure 35A represents hypothetical F_i given $I_M = 0.1$, $I_M = 0$, or $I_M = 0.1$ and a $<n>$ value representative experimental groups featured in CHAPTER 6. Positive I_M values indicated an irreversible decrease to the adhesion probability resulting from contact cycles. Negative I_M values demonstrated an irreversible increase to the adhesion probability resulting from contact cycles. A zero I_M illustrated the outcome if adhesion probability remained consistent throughout contact cycles. An additional commentary on irreversibility provided in CHAPTER 6 further discusses the irreversibility's biologic relevance.

Equation 17 – Mean Square Weighted Deviation (MSWD)

$$\chi^2 = \sum_{i=1}^{k} \frac{(F_i - f_i)^2}{\sigma^2} \tag{17}$$

Equation 18 - f_i for Irreversibility Analysis

$$f_i = \frac{1}{i}\sum_{j=1}^{i} P_{a,j} \tag{18}$$

Equation 19 - F_i for Irreversibility Analysis

$$F_i(i, < n >, I_M) = 1 - \frac{1}{i}\sum_{j=1}^{i} exp\left(-\langle n\rangle(1 - \langle n\rangle I_M)^{j-1}\right) \tag{19}$$

Equation 20 - σ^2 for Irreversibility Analysis

$$\sigma_i^2 = \frac{1}{i^2}\sum_{j=1}^{i} exp\left[-\langle n\rangle(1 - \langle n\rangle I_M)^{j-1}\right]\left[1 - exp\left(\langle n\rangle(1 - \langle n\rangle I_M)^{j-1}\right)\right] \tag{20}$$

CHAPTER 4. BIOPHYSICAL CHARACTERIZATION OF CD28 AND CORRELATION WITH STIMULATION AND CO-STIMULATION

4.1 Introduction

T cells integrate extracellular signals to coordinate their immunological functions. Among contexts critically shaping immune responses include T cell development (19), activation (258), and differentiation (259). T cells originate from thymocytes in the thymus that undergo selection to ensure reactive T cells without autoreactivity. T cells emerging from the thymus fall into two major groups based on whether their developed TCR recognize MHC class I or class II molecule presented peptides. After thymic development, the TCR enables T cells to recognize antigens and antigen recognition drives T cell mediated immunity (19). CD28 signalling profoundly influences T cell immunity, but CD28's signalling remains poorly understood despite several therapies modulating or exploiting CD28 signalling. Utilizing biophysical instrumentation and single cell signalling analysis this work investigates CD28 on murine CD8+ T cells providing a physiologically relevant characterization foundational for understanding immunotherapy success and challenges. Moreover, this work demonstrates CD28 mechanosensitivity suggesting mechanical force influences T cell-APC signalling warranting further studies into immune receptor mechanical force integration. Collectively, these insights suggest exploiting CD28 mechanics in immunotherapies could improve therapeutic outcomes.

4.1.1 The Immunological Relevance of CD28 Signalling

T cell development, activation, and differentiation result from interactions between T cells and APCs. At the interface between T cells and APCs exists several different cell-cell signalling molecules critically influencing antigen responses. Among those cell-cell signalling molecules, the co-stimulatory receptor CD28 plays a prominent role in shaping T cell antigen responses. CD28's importance in immunity began when researchers theorized a two-signal mechanism regulated adaptive immune responses (260). After the proposition of the two-signal model, researchers discovered CD28 (previously called Tp44) and demonstrated through antibody-based co-stimulation that CD28 signalling prevented T cell anergy (112). Since then, research into CD28 co-stimulation revealed complex intracellular signalling dynamics enabling CD28 to mediate signalling machinery phosphorylation (261-265), transcription (266, 267), metabolism (268), cytokine and chemokine production (269), proliferation (270), as well as survival signals (271). Moreover, independently CD28 signalling also involves pathways divergent from TCR signalling especially in actin remodelling and transcriptional processes (5, 150).

Given CD28's diverse signalling consequences, many questions remain about mechanistically how CD28 coordinates so many complex, yet important processes within T cells. Possibly explaining this diversity, CD28 receptors ligate two different ligands (CD80 and CD86). APCs constitutively express CD28 ligands and vary their respective concentrations during maturation and activation (272). CD80 exists in both monomeric and dimeric forms on APC surfaces while CD86 exists solely in monomeric forms (128). The co-inhibitory receptor CTLA-4 antagonizes CD28 signalling with proposed mechanisms including ligand competition, inhibiting CD28 signalling, and increased T cell mobility (273). Upon stimulation, APCs upregulate both CD86 and CD80 expression with

CD80 expression rising later (274). Ubiquitous APC expression reflects CD28's contribution to facilitating T cell immunity through multiple signalling pathways.

4.1.2 Prior Kinetic Studies and the Need for a Physiologically Relevant CD28 Characterization

Previous kinetic characterizations using SPR suggested that CD28 preferentially binds CD86 with a stronger affinity and faster off-rate than CD80 (120, 121) and CTLA-4 binds CD80 with a significantly higher affinity and lower off-rate enabling competitive inhibition (120, 121). Within our laboratory, *in-situ* 2D kinetic measurements showed comparable relative differences between CD80-CD28 and CD80-CTLA-4 interactions using CD80 expressing CHO cells and human CD28-Fc as a control for characterizing PD-1 interactions with its ligands (275). However, these previous 2D kinetic measurements between recombinant human CD28 and CHO surface expressed CD80 lacked non-specific binding controls illustrating binding specificity between CD28 and CD80 and presented neither receptor nor ligand on a physiological cell surface. Evaluating 2D kinetics using murine CD8+ T cells expressing CD28 provides a physiological representation for native CD28 receptor signalling. CD28's low surface density compared to CD80 and CD86 expressed on APC surfaces could favour specific interactions not observed among other relative surface densities. Moreover, *in-situ* kinetic measurements on CD8+ T cell surfaces provide a physiological recapitulation of native T cell intracellular signalling machinery, spatial organization within signalling clusters, and potential lateral interactions between receptors. Given these factors could profoundly influence CD28 biophysics, our studies focused on characterizing murine CD28 on CD8+ T cell surfaces. As a foundational work, utilizing murine animal models could provide the most flexible and physiologic system for

studying antigen-specific immune receptor signal integration surpassing traditional approaches involving the human Jurkat T cell line.

4.1.3 CD28 as a Focal Point for Immune Signal Integration

PD-1 signalling studies revealed ligation induced phosphatase activity preferentially targeted CD28 phosphorylation (276) highlighting the need for investigating lateral interactions between CD28 and other immune receptors. Moreover, additional studies found cis-dimers formed between PD-L1 and CD80 trigger CD28 while repressing PD-1 and CTLA-4 inhibitory pathways (277). These studies demonstrate that complex mechanisms influence CD28 signalling providing motivation for utilizing *in-situ* kinetics towards more sophisticated studies examining how concurrent ligation and signalling shape signal integration among immune receptors. Clearly, APCs shape CD28 signalling by controlling relative surface expression of multiple B7 family ligands and those relative changes influence whether an activating or inhibitory influence predominates a T cell's signalling response, but mechanistic questions remain about how and why this occurs.

Many immune receptor signalling models focus on spatial and temporal constraints influencing feedback mechanisms that regulate immune cell activation and potentiate immune cell functions. Among well studied immune receptor mechanisms, the TCR complex utilizes sophisticated feedback systems for sensitive and specific TCR triggering. In TCR triggering, TCR mediated Lck activation must overcome CD45 phosphatase activity to phosphorylate ITAM residues in the TCR complex (161). Lck's interaction with other immunoglobulin superfamily (IgSF) members including CD2, CD4, CD8, CD28, and ILT2 suggests mechanistic processes regulate Lck's spatial proximity to other immune

receptors and kinase activity influences antigen-specific immune responses. Previous studies demonstrated CD4 and CD28 cooperate to induce Lck autophosphorylation during APC stimulation (278). Another study showed CD4 and CD8 coreceptors bind Lck restricting Lck mobility and activity (279). Physiologically relevant biophysical CD28 investigations could elucidate important physical constraints surrounding CD28 signalling and provide the basis for a model describing how IgSF receptors work concurrently towards regulating and shaping T cell responses.

Given inhibitory IgSF receptors function through modulating CD28 signalling, CD28 functions as a major focal point for immune receptor signalling. Among IgSF receptors, CD28 interacts with the most diverse signalling machinery components enabling CD28's previously mentioned varied functionality. CD28 signalling machinery components overlap considerably with linker of activated T cells (LAT) (280) and lymphocyte cytosolic protein 2 (SLP-76) (281) including GRB2, GADS, GRAP, and interlukin-2-inducible T-cell kinase (ITK). CD28 interacts with integrin signalling machinery like CD2-associated protein (CD2AP) and filamin A (FLNA). CD28 also interacts directly with kinases such as C-terminal Src kinase (CSK) and Casitas B-lineage lymphoma (CBL) and phosphatases including Src homology region 2 domain-containing phosphatase-2 (SHP-2) and Src homology 2 domain containing inositol polyphosphate 5-phosphatase 1 (SHIP1). CD28 cytoplasmic domain also contains additional phosphorylation and ubiquitination sites, but they remain poorly understood (5). As an intersectional receptor between several signalling pathways, conducting *in-situ* measurements provides a perspective about ligation mediated signalling events potentially revealing lateral interactions between receptors and their signalling machinery. *In-situ*

studies characterizing CD28 interactions with its ligands provide a foundation for future studies perturbing intersectional signalling pathways towards elucidating mechanistically how immune receptor signalling integration occurs within T cells.

4.1.4 The Rationale for Investigating CD28 Mechanosensitivy

Although kinetic measurements provide useful information about how immunoreceptors work, mechanosensing investigations also provide important insights. Immunoreceptor mechanosensing investigations revealed mechanosensing shapes immune cell function and differentiation. Mechanosensing experiments involving DFS instruments demonstrated force exerted on the TCR (with or without co-receptor) elicits catch bonds with pMHCs biological activity but slip bonds with low biological activity (9, 230). Combining DFS instrumentation with concurrent live calcium flux cell imaging revealed mechanical force on the TCR could trigger calcium flux influenced by bond quality (catch versus slip bonds), force waveform (clamped vs ramped force), and force direction (tangential versus normal to cell surfaces) (235, 244). Additionally, DNA-based molecular tension probes demonstrated T cells could exert endogenous force on the TCR-pMHC bonds shaped by coreceptor, proximal TCR signalling, as well as actin cytoskeletal and myosin motors (256). Forces on TCR induced conformational changes in TCR-pMHC bonds influencing molecular catch or slip behaviour (9, 282, 283). Possible mechanosensitive mechanisms shaping CD28 signalling include molecular catches, unfolding, unmasking, and cluster rearrangement. As an IgSF family member with similar kinase interactions and additional interactions with cytoskeletal adaptors, logically CD28 should also demonstrate mechanosensitivity with signalling outcomes influenced by force.

4.1.5 Summary of Chapter Findings

Motivated to develop a more comprehensive understanding about receptor signalling at interfaces between T cells and APCs this chapter focused on biophysical interactions. Specifically, BFP instrumentation measured interactions between CD28 featured on murine CD8+ T cells and recombinant murine CD80 and CD86 ligands. BFP instrumentation provided the most sensitive and specific *in-situ* receptor-ligand interaction measurements with exceptional spatial and temporal precision among biophysical instrumentation techniques. Measuring 2D kinetics and bond lifetime under force revealed unique 2D kinetics among CD28 ligands and CD28 mechanosensitivity through catch bonds. BFP measurements lacked evidence demonstrating multimeric bond formation between CD28 and its ligands. Attempting to demonstrate CD28 signalling could elicit tension on CD28 ligand bonds showed close to negligible tension suggesting potential limitations towards studying murine CD28 on CD8+ T cells using molecular tension probes. Moreover, single cell calcium flux experiments revealed synergistic interactions between CD28 and TCR with altered dynamics. Collectively, these findings expand upon known CD28 biology highlighting how mechanical forces could contribute to CD28 signalling function. Through providing a biophysical perspective on CD28-ligand interactions that shape T cells this work provides motivation for further studies into how mechanical force influences signal integration among receptors at T cell-APC interfaces.

4.2 Background

4.2.1 CD28's Impact on Human Disease

Many disease processes involve beneficial or harmful antigen-specific immune responses. In infections and cancer, T cells must coordinate eliminating abnormal cells presenting infectious or neoplastic antigens. In autoimmune disease and transplant rejection, T cells pathologically contribute to tissue damage contributing to organ dysfunction and eventually organ failure. CD28 shapes T cell immune responses and accordingly associations between CD28 genetic variants and many diseases exist including rheumatoid arthritis (RA) (284), multiple sclerosis (285), sporadic breast cancer (286), cervical cancer (287), and diabetic kidney disease (288). Although the genetic disease associations do not imply a direct association, many genetic variants possibly result in CD28 loss of function and function loss would certainly impact immune response quality. Interestingly, acquired CD28 mutations found in cancers could increase CD28 ligand binding (289) and CTLA4-CD28 gene fusions exist within angioimmunoblastic T-cell lymphoma that could contribute significantly to T cell lymphomas (290). Moreover, many genetic variants associated with disease exist in CTLA-4 (291) and CARMIL2 (292) that indirectly influence CD28 signalling causing human primary immune deficiencies (293).

4.2.2 CD28 as a Therapeutic Target: Success and Failures

4.2.2.1 Fusion Proteins and Immune Checkpoint Blockade (ICB)

Considering lateral immune receptors such as PD-1 and CTLA-4 function primarily by influencing CD28 signalling, investigating physiologic CD28 signalling contributes relevant knowledge for therapeutic strategies targeting T cell signalling. Therapeutic interest in CD28 signalling stems from a desire to modulate immune responses. Therapeutic agents targeting CD28 both augment and discourage immune responses. In

organ transplantation, CTLA-4-Fc/Ig therapy (abatacept/belatacept) blocks CD28 signalling by ligand competition enabling extended graft survival and limiting standard immune-supressing drug toxicity (294). In oncology, antibodies against PD-1 and CTLA-4 block their inhibitory effects to help immune responses against cancer overcome immune suppression (295). Immune checkpoint blockade (ICB) profoundly influenced cancer therapeutics becoming some of the most widely prescribed anticancer therapies often as single agents or combined with chemotherapies (296).

4.2.2.2 Chimeric Antigen Receptor (CAR) T Therapy

Other prominent oncological immunotherapies also utilize CD28 signalling such as chimeric antigen receptor (CAR) T cell therapy. Chimeric antigen receptors (CAR) featuring transmembrane and intracellular CD28 domains enable targeted cytotoxic activity against haematological cancer. Interestingly, comparing CD28/CD3ζ and 4-1BB/CD3ζ CAR-T receptors revealed CD28/CD3ζ CAR-T receptors cause faster and larger dynamic changes in protein phosphorylation correlating with effector T cell-like phenotype and function despite activating similar signalling intermediates (297). Moreover, CD28/CD3ζ and 4-1BB/CD3ζ CAR-T receptors demonstrated differing clinical efficacy with 4-1BB/CD3ζ CAR-T receptors associated with better clinical performance against B cell non-Hodgkin's lymphoma (298). Collectively, research into CAR-T signalling suggests that immune receptors retain mechanistic functions that amount to more than their individual signalling domain components necessitating more sophisticated signalling studies that elucidate how co-stimulatory receptors achieve distinct signalling outcomes and how such distinct outcomes influence T cell fate.

4.2.2.3 CD28 Superagnoist Monoclonal Antibody TGN1412

CD28 superagonist immunomodulatory monoclonal antibody TGN1412 also attempted to modulate CD28 as a cancer immunotherapeutic. TGN1412 preferentially activated CD28 on regulatory T cells causing their activation and proliferation in the absence of TCR co-stimulation. Given this preferential activation, researchers believed TGN1412 could prevent autoimmune diseases. After being well-tolerated in cynomolgus monkeys with 100% homologous CD28 receptors a randomized phase I clinical trail shockingly revealed in eight healthy male volunteers that volunteers developed dramatic symptoms including headache, back pain, migraines, vomiting, hypertension, and extreme fever within the first hour. Moreover, the volunteer's health continued to decline eventually progressing to multiple organ failure and severe cytokine release syndrome (CRS) necessitating the need for immunosuppressants (299). TGN1412's failure impacted the immunotherapeutic field significantly promoting additional safeguards to define immunotherapeutic risks, more through toxicity investigations, and protect patients from poorly characterized immunotherapies (300). Investigations into alternative approaches in modulating CD28 signalling could prove useful in therapies targeting increasing or decreasing T cell responses. A more comprehensive model understanding CD28 signalling could elucidate alternative approaches.

4.2.2.4 Bispecific and Trispecific CD28 Antibodies

Immunotherapy's success motivated other approaches to immune modulation involving CD28 modulating antibodies. Investigations by pharmaceutical companies expanded into bispecific and trispecific antibodies. Engineering mutlispecific antibodies

with binding specificity for multiple receptors enabled novel therapeutic strategies with potential cancer efficacy resembling CAR-T therapies. Bispecific antibodies against tumor specific antigens (TSA) and CD3 demonstrate antitumour reactivity that can be enhanced by another bispecific antibody against TSAs and CD28 (301). Trispecific antibodies developed against myeloma featuring reactivity against CD38, CD3, and CD28 demonstrated efficient T cell stimulation, T cells directed against myeloma, and myeloma growth inhibition within an humanized mouse model (302). Interestingly, bi-specific and tri-specific antibodies that engage native T cell receptors show potential beyond CAR-T therapies in treating solid tumour malignancies (303). Multispecific antibody successes motivate the need for a more comprehensive T cell signalling model given approaches modulating signalling provide profound therapeutic potential.

4.2.2.5 Common Immune Modulating Drug Adverse Effects

Although immune modulating therapies retain less toxicity than their chemotherapeutic or traditional immunosuppressive counterparts, immune modulating therapeutic sequela also adversely impact patient care. CTLA-4 fusion protein drugs such as belatacept serious adverse events include post-transplant lymphoproliferative disorder and progressive multifocal leukoencephalopathy. ICB therapies potentially induce immune-related adverse events (irAEs) that resemble autoimmune responses. Autoimmune-like irAEs result in colitis, encephalitis, myocarditis, myositis, pneumonitis, and multiple organ failure (304). CAR-T therapies also result in adverse toxicities that influence patient care outcomes. CAR-T therapy damage occurs to non-cancerous cells expressing the same tumor-associated antigen targeted by the CAR-T therapy. CAR-T therapy damage could also result from CAR-T receptor cross-reactivity against an antigen expressed on normal tissue.

CAR-T therapy can also potentially induce CRS resulting in organ dysfunction and can progress to multiple organ failure (305). Such serious adverse therapeutic effects motivate investigations into more tuneable CD28 immunomodulation with less off-target effects. More precise control over CD28 signalling would improve immune modulating therapy clinical outcomes.

4.2.3 The Limitations of Using Stimulatory Antibodies for Studying CD28 Receptor Signalling

Previous investigations into CD28 signalling primarily used antibodies against surface CD28 to elicit its signalling. Antibodies functionally can activate and inhibit receptors through mechanisms influenced by receptor biology and antibody epitope. Although CD28 ligation can facilitate signalling, developing a more comprehensive model for CD28 signalling necessitates investigations utilizing CD28's native ligands. From a biophysical perspective, interactions between receptors and ligands often do not resemble interactions between antibodies and epitopes. Antibody-epitope interactions generally demonstrate higher affinities and slower off-rates that receptor ligand interactions with high affinity antibodies demonstrating 3D association rates around 2×10^7 M^{-1} sec^{-1} and dissociation rates around 0.02 sec^{-1} (306). In the simplest case, ligation inducing similar cytosolic tail conformations would favour different signalling states. Receptors with many signalling machinery would favour signalling mediators that bind stably although other signalling machinery with faster kinetics could mediate early signalling events. In such instances, receptor-ligand kinetics could mediate different signalling outcomes. Such biophysical constraints could explain why CAR-T receptors despite similar intracellular

signalling domains fail to elicit the same signalling pathways as their receptor counterparts (Section 4.2.2.2).

Moreover, high-affinity IgG antibodies commonly used in signalling studies bind two similar epitopes spatially constraining receptors in ways that influence signalling. Many receptors such as cytokine receptors mediate signalling through ligand-induced receptor dimerization (307). Although some receptors natively induce signalling through receptor dimerization, monovalent, dimeric receptors such as CD28 interact with monomeric ligands. Monomeric ligands could spatially constrain receptor signalling in ways that would differ from monoclonal signalling antibodies. Spatial constraints could explain how trispecific antibodies (Section 4.2.2.4) with reactivity towards both CD3 and CD28 demonstrate distinct signalling outcomes compared similar antibodies with CD3 or CD28 binding ablation (302). Moreover, such spatial constraints could explain why superagnoistic antibody TGN1412 inducing CRS during its phase I clinical trial (Section 4.2.2.3) correlated with differences in CD4+ T cell CD28 expression between species (308). TGN1412's clinical trial failure illustrated complexities surrounding modulating receptor signalling through antibodies and how even immobilization strategies could substantially influence outcomes (308).

Moreover, thermodynamic differences also distinguish antibody-epitope and receptor-ligand interactions. The Gibbs free energy, a thermodynamic potential describing chemical equilibrium, differs between antibody-epitope and receptor-ligand interactions. Binding enthalpy reflects the formation of noncovalent interactions at binding interfaces with heat effect relating to interactions formed and disrupted within the system. Entropy changes relate to increases or decreases in system freedom shaped by protein

conformational freedom and solvent released from surface burial (309). Given thermodynamic constraints, receptor-ligand interactions retain unique thermodynamic potential resulting from different interaction kinetics and influences on chemical equilibrium achieved upon receptor ligation.

4.2.4 Functional and Signalling Differences Between CD80 and CD86

Research comparing CD28 engagement CD80 and CD86 reveal different signalling and functionality outcomes. CD86 knockout mice show deficient class switching and germinal center formation after immunization without an adjuvant while CD80 knockout mice can (310). Blocking CD86 alone on APCs inhibited TCR-dependent T cell proliferation and cytokine production (130). In-vivo studies using knockout models revealed potential differences between CD80 and CD86, but the differences remain hard to interpret given APC dynamically alter CD80 and CD86 expression based on factors like toll like receptor (TLR) activation (311) and cytokines (312). Experimental limitations in knockout and blocking studies prevent researchers from elucidating dynamic responses specifically related to CD80 and CD86 that could differentially influence T cells

Studies comparing signalling differences using CHO cells expressing CD80 or CD86 demonstrated much higher PLC-γ1 stimulation for CD80 stimulated in both human peripheral CD4+ T cells and Jurkat cells. In the same study, CD80 produced more robust tyrosine phosphorylation compared to CD86 and this correlated with PI3K association with CD28 (313). CD80 and CD86 blocking differentially influenced early cytokine production with CD86 blocking causing reduced IL-4 and IFNγ expression while CD80 blocking showing no effect (314). Although these studies provide motivation for further

investigations elucidating mechanistic reasons for signalling differences, signalling observed using CD80 and CD86 expressed on CHO cells could reflect other signalling processes mediated by co-culturing cells and thus lacks specificity conferred by immobilizing recombinant proteins.

4.2.5 Prior Investigations Characterizing Relationships Between CD28 and Force

Given the many investigations characterizing actin cytoskeletal changes mediated by CD28 signalling, many studies also attempted to define force generation or stabilization facilitated by CD28. Experiments involving polyacrylamide gels presenting anti CD3 and anti CD28 antibodies revealed varying surface stiffness could shape T cell activation (6). In another study, researchers investigated mechanosensing through surface spreading on different stiffness surfaces and determined CD28 did not influence TCR mechanosensing (315). Further characterization of traction forces using elastomer pillar arrays showed greater traction forces with anti CD28 and anti-CD3 together (7). The inability to identify CD28 mechanosensitivity within these studies could be multifactorial ranging from investigations using antibodies that would not resemble ligand ligation and cells with low CD28 expression.

4.3 Results

4.3.1 Mammalian Recombinant Protein Expression of Murine CD28 Ligands Optimized for In-situ Biophysical Characterization

Investigating *in-situ* CD28 biophysics in a manner that could elucidate receptor function required developing an optimized recombinant ligand for biophysical

characterization. Given the limited CD28 signalling research using recombinant ligands, at the time murine recombinant ligands lacked commercial availability and an appropriate format for biophysical characterization. CD80's and CD86's smaller molecular weight necessitated avoiding covalent linking strategies utilizing NHS chemistry that could produce a non-ideal molecular orientation or potentially damage N-terminal receptor binding domains. Designing a recombinant protein sequence featuring CD80 or CD86 extracellular domain with an N-terminal secretion signal and C-terminal enzymatic biotinylation peptide sequence (biotin acceptor peptide), TEV protease cleavable peptide, and polyhistidine purification tag (Figure 6A) produced protein constructs for biophysical investigations. The idealized protein constructs contained features enabling native purification from transient transfection supernatants, removing purification tags that could influence biophysical measurements, and enzymatic biotinylation for immobilization on SA coated surfaces. DNA sequences corresponding to CD80 and CD86 ligands designed *in-silico* from NCBI sequences allowed GenScript to synthesize pCDNA3.1+ transient mammalian protein expression vectors for desired protein constructs.

Initially, pCDNA3.1+ transient mammalian vector expression optimization required exploring different DNA to PEI ratios using a published protocol on mammalian protein expression using PEI as a guide (316). Investigating optimal DNA to PEI ratios revealed a similar ratio (1:3 DNA to PEI) as the published protocol produced the highest transient protein expression although experiments involved similar suggested screening ratios. Western blotting supernatants from transfection optimization experiments with polyclonal antibodies against CD86 demonstrated a single band around 45 kDa in (Figure 6B).

Western blotting supernatants from CD80 transfections using optimized transfection conditions showed a similar single band (data not shown).

Protein chromatography involved batch NTA resin incubations after extensive dialysis to remove chelating substances within transfection supernatants. Dialysing into a 10 μM imidazole containing buffer increased resin binding specificity for the transiently expressed protein. Eluting with imidazole gradients between 15-800 μM generated protein containing elutants. SDS PAGE gel electrophoresis verified chromatography elutants contained the target protein for subsequent dialysis and enzymatic modification. A representative Coomassie stained SDS PAGE gel for CD80 chromatography showed strong bands in 50 to 200 μM imidazole elutants (Figure 6C). Chromotography for CD86 transfectants produced similar Coomassie stained SDS PAGE gels (data not shown). ProtParam with designed polypeptide sequences predicted molecular weights for the full length CD80 (30.9 kDa) and CD86 (32.1 kDa). Observed molecular weights related with significant glycosylation as well as correlated with previous publications (120) and manufactured human ligands.

Enzymatic modifications first removed polyhistidine purification tags using purchased TEV protease. After proteolytic tag removal, biotin ligase produced in purified from *E. coli* enabled enzymatically adding biotin to the biotin acceptor peptide. An additional NTA resin incubation cleaned up TEV protease, biotin ligase, cleaved polyhistidine tags, as well as non-enzymatically modified proteins. SDS PAGE electrophoresis and western blotting with streptavidin HRP verified enzymatic modifications and the desired polypeptide sequence (data not shown). Verifying proper protein conformation and suitability for biophysical experiments required immobilizing

final products on SA beads and confirming staining with PE conjugated monoclonal antibodies against CD80 (clone 16-10A1) and CD86 (clone GL-1) (Figure 6D-E). Flow cytometry revealed narrow peaks consistent with other biotinylated ligands and effective antibody staining.

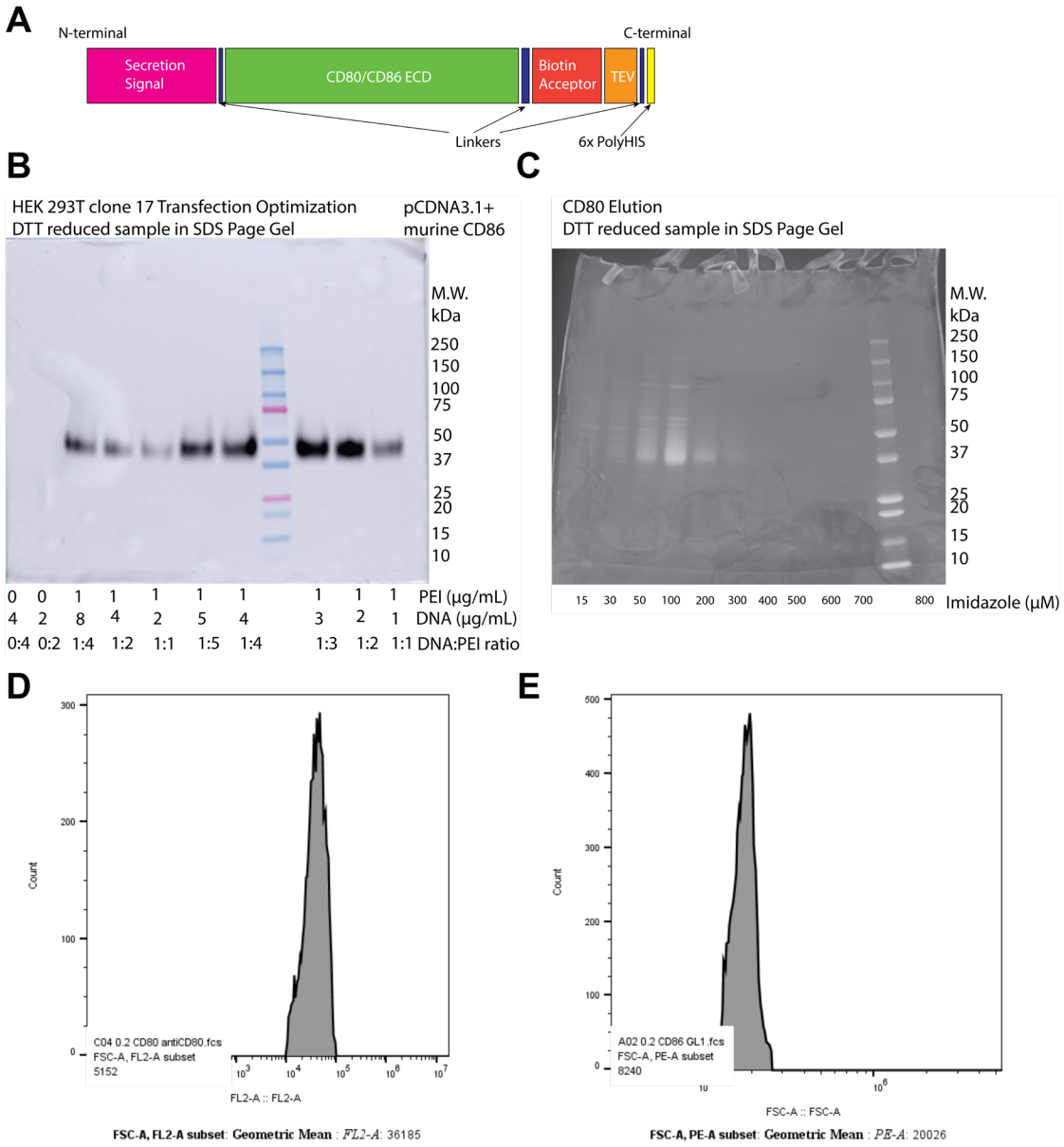

Figure 5 - CD28 Ligand Protein Expression, Purification, and Validation Protein engineering enabled CD80 and CD86 constructs for biophysical characterization. CD80 and CD86 extracellular domains (ECD) featuring N-terminal secretion signal and C-terminal enzymatic biotinylation, enzymatic cleavage, as well as polyhistidine sequences biophysical characterization experiments. A representative schematic for the linear polypeptide sequences generated for CD80 and CD86 protein constructs depicted fusion protein design (A). A transfection optimization experiment verified proper sequences and ensured optimal expression conditions for transient protein expression vectors containing desired CD80 and CD86 inserts (pCDNA3.1+) purchased from GenScript. Western blot using polyclonal antibodies for CD86

verified protein polypeptide sequences and showed a 1:3 DNA to PEI ratio produced the highest transient mammalian protein expression in HEK293T clone 17 cells with singular bands around 45 kDa (B). SDS PAGE gel electrophoresis and subsequent Coomassie blue staining imidazole gradient elutions ranging from 15-800 µM verified elutants from NTA resin incubations with dialyzed supernatants contained target CD80 with strong bands in elutants with 50 to 200 µM (C). Enzymatic modifications using dialyzed elutants produced biotinylated proteins without promiscuous polyhistidine affinity purification tags. Flow cytometry verified biotinylated CD80 (D) and CD86 (E) immobilization on SA coated beads showing narrow fluorescence peaks with PE conjugated antibodies clones 16-10A1 and GL-1, respectively.

4.3.2 Experimental System Used in CD28 Biophysical Investigations

Sensitive and specific biophysical interaction measurements for 2D kinetics, bond lifetime under force, and thermal fluctuation experiments utilized BFP live-cell DFS instrumentation. Measurements using murine CD80 and CD86 and murine CD8+ T cell surface CD28 required an instrumentation setup where CD8+ T cells could be closely monitored throughout experiments. BFP experiments involved assembling an RBC-based force transducer calibrated to specific spring constants with a previously published mathematical model (203). The BFP instrumentation illustrated in Figure 7A shows an assembled BFP probe and CD8+ T cell aspirated in glass micropipettes. Subpixel bead displacement quantification through computer vision methods enabled quantifying force over time. Altering CD8+ T cell position during measurements with piezoelectric actuation allowed controlling cell impingement and tensile bond force.

Acquiring biophysical measurements involved immobilized biotinylated recombinant proteins presented by BFP probes. Incubating streptavidin (SA) coated beads with biotinylated ligands produced ligand-coated beads for probe assembly. Purifying CD8+ T cells from young mouse spleens for each experiment ensured consistent surface

CD28 expression for experiments. Cell isolation with a magnetic bead based negative selection kit purchased from StemCell Technologies ensured minimally perturbed cells.

A schematic for the experimental system in Figure 7B illustrates experimental surfaces. Experiments used beads coated with only CD80 or CD86, but the schematic shows both CD80 and CD86 on the same surface. The schematic attempts to depict CD28 and its ligands at their relative scales. Monoclonal E18 antibody blocked CD28 from interacting with ligands in binding specificity experiments.

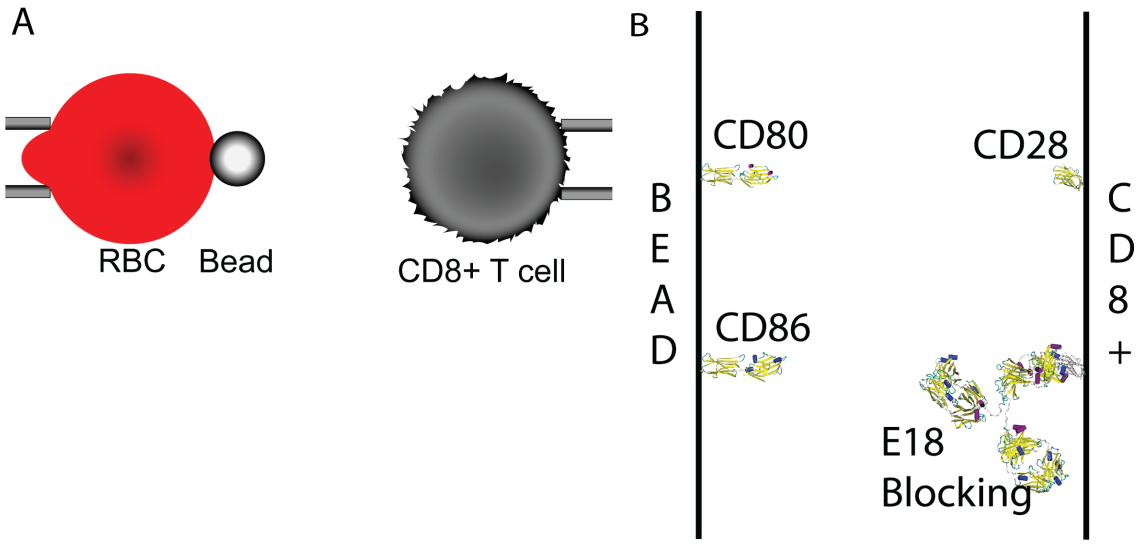

Figure 6 - Experimental System Used in Characterizing CD28 Biophysics. The BFP measured 2D kinetics and bond lifetime under force. BFP instrumentation involved assembling an RBC based tension probe featuring glass beads with streptavidin (SA) immobilized ligands, holding CD8+ T cells with micropipettes, and controlling CD8+ T cell position by piezoelectric actuation (A). BFP experiments involved CD28 receptors on murine naïve CD8+ T cells and immobilized murine CD28 ligands (CD80 and CD86) on glass beads (B). Monoclonal antibody against CD28 (clone E18) blocked CD28 during binding specificity experiments. Root mean-square deviation (RMSD) measurements made using visual molecular dynamics (VMD) with protein data bank (PDB) files for CD80 (1DR9), CD86 (1NCN), and CD28 (1YJD) allowed depicting receptor, ligand, and antibody relative sizes.

4.3.3 Binding Specificity Between CD28 and CD80 or CD86 Ligands

Biophysical characterization required specific measurements probing at interactions between CD28 and its ligands. Ensuring measurement specificity also validated recombinantly expressed proteins. Measurements using the rupture mode BFP generated an adhesion frequency (P_a) for bead-cell pairs under different experiment conditions. P_a represented a bead-cell pair's adhesion frequency (Equation 1) interpreted after the experiment by analysing contact cycle signal.

Demonstrating binding specificity required observing specific interactions between CD28 ligands and cell surface CD28. BFP measurements used SA beads coated with and without CD80 or CD86. Given CTLA-4 could contribute to P_a measurements by either being present on cell surfaces or trafficked to the membrane upon CD28 ligation, experiments also probed at potential interactions between cell surface CTLA-4 and CD28 ligands. CD28 and CTLA-4 blocking antibodies ablated potential interactions between receptors and CD28 ligands. Isotype controls for blocking antibodies illustrated effect specificity as positive controls. SA beads without CD28 ligands served as negative controls. Antibody blocking conditions utilized chamber media containing 10 µg/mL blocking (anti-CD28 and/or anti-CTLA-4) or isotype control antibodies (murine IgG2b isotype or Syrian hamster IgG isotype) to our chamber media. Brown-Forsythe and Welch One-way ANOVA tests with Dunnett's T3 multiple comparisons analysis produced statistical comparisons between experimental groups with SA negative controls.

P_a measurements with anti-CTLA-4, mIgG2b isotype, or Syrian hamster IgG isotype displayed statistically higher P_a for experiments featuring murine CD80 (Figure 8A) or CD86 (Figure 8B) coated beads. P_a measurements with anti-CD28 blocking antibody (anti-CD28 and anti-CD28/anti-CTLA-4) did not demonstrate statistically

significant differences from the negative control for both CD80 and CD86 ligand beads. Statistical comparisons confirmed that only conditions where CD28 and its ligands could interact rejected the null hypothesis. Binding specificity experiments lacked evidence that CTLA-4 interactions contributed to observed adhesions.

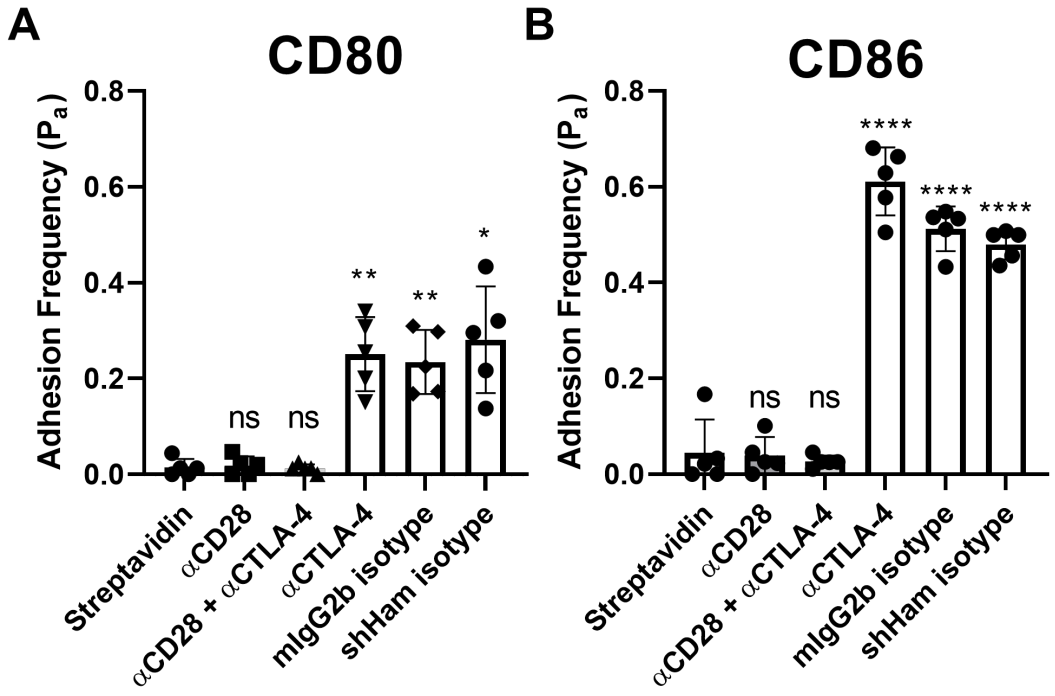

Figure 7 - Murine CD8+ T cells Form Specific Bonds with CD28 Ligands Through CD28. An adhesion frequency (P_a) assay demonstrated binding specificity between recombinant murine CD80 (A) and CD86 (B) and CD28 expressed on murine CD8+ T cell surfaces. Biotinylated CD80 or CD86 immobilized on streptavidin (SA) coated beads interacted with CD28 expressing cells to produce P_a measurements. SA beads without CD28 ligands served as negative controls. BFP chamber media containing 10 µg/mL isolated receptor interactions by blocking CD28 and CTLA-4. Antibodies isotypes served as additional controls for specific binding (mIgG2b isotype for anti-CD28 and Syrian hamster (sh) IgG for anti-CTLA-4). Brown-Forsythe and Welch One-way ANOVA tests with a Dunnett's T2 corrected multiple comparisons statistically compared experimental groups with the SA negative control. Anti-CTLA-4, mIgG2b isotype, and sh IgG isotype demonstrated higher P_a than the negative control CD80 (A) and CD86 (B) experiments. Anti-CD28 conditions (anti-CD28 and antiCD28+anti-CTLA-4) for CD80 and CD86 coated beads lacked statistically significant differences from negative controls. Each

symbol represented an P_a measurement from a single cell-bead pair. Bar height represents the mean P_a value and error bars represent the standard error of the mean (SEM). Plotted data included 5 bead-cell pairs (n=5) for each condition.

4.3.4 CD80 and CD86 Demonstrated Different 2D Affinity

Demonstrating binding specificity enabled further biophysical measurements between CD28 and its ligands. *In-situ* 2D kinetic measurements characterized interactions between CD28 and its ligands. *In-situ* 2D kinetic measurements enabled comparisons with previously published findings and potentially correlated with functional differences between the ligands. The 2D kinetic parameters described interactions between receptor and ligand coated surfaces that occur only when surfaces contact each other. 2D kinetic parameters differ from 3D kinetic parameters derived from SPR measurements. *In-situ* 2D kinetic measurements involved determining P_a using rupture mode BFP for bead-cell pairs featuring either CD80 or CD86.

Determining 2D kinetic parameters describing 2D affinity and bond dissociation required non-linear least squares fitting a published mathematical model that isolated species specific contributions (317). P_a measurements under varying contact times (Figure 9A) generated using at least 75 contact cycles produced data corresponding to non-specific and species-specific interactions. Initially, modelling non-specific contributions from negative control experiments enabled mathematically recognizing specific interactions between CD28 and its ligands acquired experimentally. P_a measurements provided the model's dependent variable. Non-linear least squares fitting our $<n>$ measurements over varying contact times (independent variable t_c) with Equation 6 (Figure 9A black line) produced non-specific interaction parameters a and b.

After modelling non-specific contributions, additional non-linear fitting transformed P_a measurements into 2D kinetic modelling parameters. P_a measurements provided data for non-linear least squares fitting Equation 8. Plotting $<n>$ normalized by receptor and ligand surface densities ($m_R * m_L$) versus contact times (Figure 9B) demonstrated longer contact times reached an equilibrium between bonds formed and broken. Determining surface densities involved extrapolating flow cytometry fluorescence measurements with a standard curve acquired using manufactured calibration beads. Saturating antibody concentrations ensured fluorescence signals corresponded with antibodies binding singular receptors.

Non-linear least squares fitting generated 2D affinity (A_cK_a) and dissociation rate (k_{off}) for CD80 (Figure 9B red line) and CD86 (Figure 9C blue line). Fitted A_cK_a values described binding equilibrium kinetics between CD28 interactions and its ligands. Comparing non-linear fitted A_cK_a and k_{off} showed statistically higher A_cK_a value for CD28-CD86 interactions (Figure 9C), but no statistically significant difference in k_{off} (Figure 9D). Observed differences between the ligand A_cK_a values correlated with previously published data, but not k_{off} (120, 121).

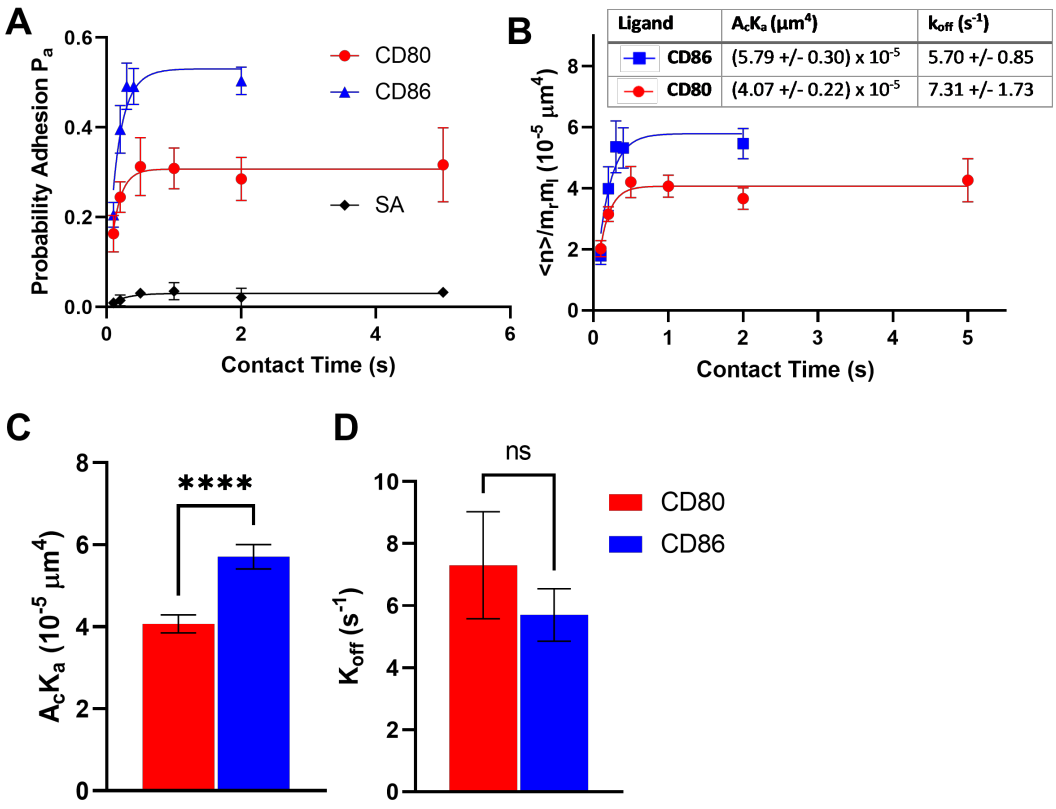

Figure 8 - CD80 and CD86 Interactions with CD28 Demonstrate Different 2D Affinity. P_a measurements with varying contact times allowed determining 2D affinity for both CD80 (red) and CD86 (blue) interactions with CD28 on CD8+ T cells through non-linear least squares fitting. BFP rupture mode measurements provided P_a at varying contact times for CD80 or CD86 ligand coated beads (A). SA beads without ligands (black) served as a non-specific binding control. Fitting the P_a data acquired over different contact times enabled non-linear least squares fitting non-specific interaction parameters a and b in Equation 6 (black line in A). Utilizing Equation 8 with species specific P_a and non-specific interaction parameters enabled non-linear least squares fitting 2D kinetic parameters A_cK_a and k_{off}. Plotting $<n>$ normalized by receptor and ligand surface densities showed receptor-ligand interactions reached equilibrium (B). Superimposed table for B represented non-linear parameter fitting results for both CD80 (red line) and CD86 (blue line) ligands. A Welch's two-tailed t test statistically compared fitted A_cK_a (C) and k_{off} (D) parameters for CD28 ligands. CD86 demonstrated a statistically significant higher 2D affinity than CD80. Statistically comparing k_{off} lacked significant differences between ligands. Ligands required different contact times to resolve k_{off} after determining both ligands exhibited fast dissociation rates: CD86 (0.1s, 0.2s, 0.3s, 0.4s, 0.5s, 2s) as well as CD80 and SA (0.1s, 0.2s, 0.5s, 1s, 2s, 5s). Symbols on A and B illustrated the mean P_a and normalized $<n>$ from 5 bead-cell pairs with error bars for the SEM. P_a versus contact time measurements involved one experiment for

CD80 and two experiments for CD86. Bar height corresponded with fitted parameter value and error bars for fitting error. Statistical comparison symbols featured included: ns (not significant) and ** ($p < 0.0001$).**

Previous research documenting surface CD80 exists in monomeric and dimeric forms on APC surfaces (318, 319) as well as studies suggesting dimeric CD28 bivalency upon TCR ligation (320) encouraged additional experiments probing at relationships between surface densities and 2D effective affinity. Moreover, defining 2D effective affinity at different receptor densities validated 2D affinity values calculated from varying contact time. Using a consistent contact time (t_c=2s) beyond the time needed for receptor-ligand interactions to reach binding equilibrium produced P_a measurements for extrapolating into 2D effective affinity by combining species specific $<n>$ from Equation 8 with Equation 4.

BFP rupture mode measurements generated P_a values related to our species specific $<n>$. Acquiring $<n>$ using beads with varying ligand concentrations allowed visualizing how ligand density influenced receptor-ligand interactions. Plotting $<n>$ versus the receptor-ligand surface density product ($m_R m_L$) revealed linear relationships for CD80 (Figure 10A) and CD86 (Figure 10B). A simple linear regression constraining the y-intercept through the origin provided slopes representing $A_c K_a$ (linear equations on graphs). The $A_c K_a$ determined from linear regression closely resembled values calculated by varying contact time (Figure 9). Statistically they also demonstrated higher $A_c K_a$ for CD86 than CD80 (Figure 10C).

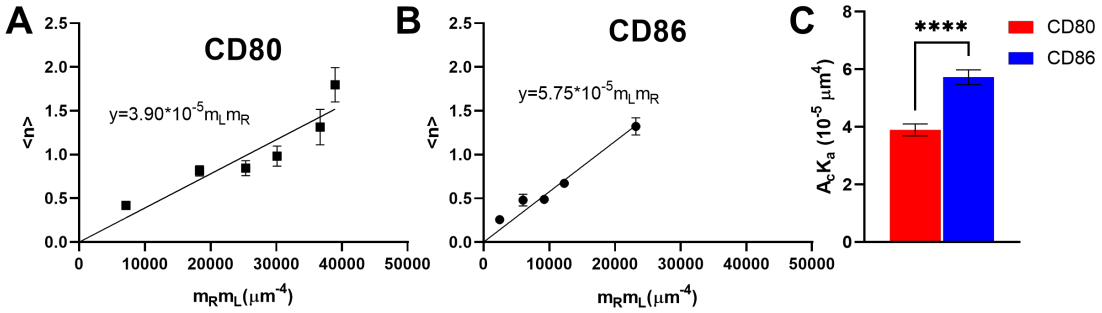

Figure 9 - Differences in 2D Affinity Under Varying Ligand Coating. Varying ligand surface densities provided P_a measurements for identifying relationships between surface densities and observed receptor-ligand interactions. BFP rupture mode P_a measurements at equilibrium contact times CD80 and CD86 (2s) enabled determining $\langle n \rangle$ using Equation 8. Plotting $\langle n \rangle$ versus receptor-ligand surface density products ($m_R m_L$) demonstrated linear relationships for CD80 (A) and CD86 (B). Fitting $\langle n \rangle$ versus $m_R m_L$ data with a simple linear regression constrained to the origin enabled resolving $A_c K_a$ for CD80 and CD86 from slopes ($y = A_c K_a * m_R m_L$). Slope values resembled previously determined $A_c K_a$ in Figure 9. Linearity suggested interactions between surface CD28 and CD80 or CD86 resulted from CD28 monovalency. Statistically comparing the fitted slope parameters from CD80 and CD86 using a Welch's two-tailed t test revealed a statistically significantly higher 2D affinity for CD86 (C) correlating with Figure 9. Plotted symbols in A and B represent the mean $\langle n \rangle$ for 5 bead-cell pairs (n=5) with error bars representing SEM. Plotted bar graph values represent fitted $A_c K_a$ parameter values with error bars representing fitting error. Data shown represents a representative experiment after conducting two separate experiments for CD80 and CD86. Statistical comparison symbols shown included: ** ($p < 0.0001$).**

4.3.5 CD80 and CD86 Demonstrated Different Dissociations

Fast dissociation kinetics identified in Section 4.3.4 motivated acquiring live-cell thermal fluctuation measurements to accurately define receptor-ligand dissociation kinetics. The thermal fluctuation method more rigorously defined dissociation between CD28 and its ligands using bond lifetimes measurements. BFP thermal fluctuation measurements for CD28 and its ligands required a BFP signal that sensitively resolved binding through changes in signal fluctuation. Live-cell thermal fluctuation measurements

built upon previously published work for non-live cells (252) and live cells (251), but required specialized methodology addressing fast receptor-ligand interaction kinetics and ligand induced morphological changes. To achieve the most sensitive signal, experiments used BFP probes assembled with a 0.1 pN/nm spring constant. BFP probes and CD8+ T cells brought close together formed bonds during probe thermal fluctuation. Closely monitoring distances between bead-cell pairs ensured measurements occurred during conditions conducive for probe fluctuation changes. Identifying drastic changes to probe position induced by cell morphology changes allowed aborting measurements and attempting more thermal fluctuation measurements.

Thermal fluctuation measurements produced bond lifetimes with a large force range given CD28 ligation with its ligands stimulated profound cell morphological changes. Segregating thermal fluctuation bond lifetime measurements into force bins allowed analysing bond lifetimes around 0 pN. Ordering bond lifetimes according to their length and determining a bond's survival probability based on its position within an ordered sequence enabled constructing bond survival curves for both ligands. Plotting bond survival analysis produced trends for extrapolating dissociation rate by non-linear least squares fitting a one phase exponential decay (k_{off}) (Figure 10A). Comparing fitted parameters with a Welch's two-tailed t test showed a statistically significant higher k_{off} for CD80 than CD86 (Figure 11B). The fitted parameters remained within the error from previous fitted k_{off} calculations in Figure 9D.

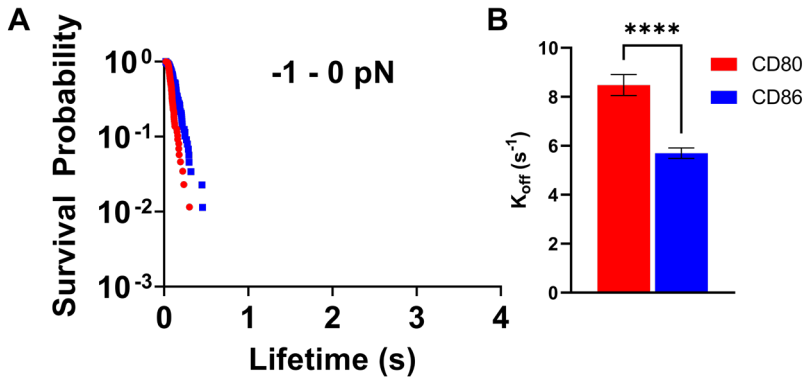

Figure 10 - CD80 and CD86 Display Different Dissociation Rates. Utilizing BFP instrumentation for thermal fluctuation experiments enabled calculating dissociation rates for CD28 and its ligands. BFP thermal fluctuation experiments measured bond lifetimes under varied forces. Segregating bond lifetime measurements within force bins produced a -1 to 0 pN force bin with a mean force approximately 0 pN. Ordering bond lifetimes according to their length rendered an ordered sequence for deriving bond survival probability. Plotted survival analyses for CD80 (red, n=87) and CD86 (blue, n=88) showed trends representing dissociation rates (k_{off}). A non-linear least squares fitting using a constrained one phase exponential decay model (Equation 13) generated k_{off} parameters for both CD80 (red) and CD86 (blue) (B). Determined dissociation parameters resembled values previously obtained. Statistical comparison using a Welch's two-tailed t test demonstrated CD80 dissociates faster than CD86. Bar height illustrated the fitted parameter value with error bars for the fitting error. Data shown represented data from one single cell-bead pair from an individual experiment for each ligand. Statistical comparisons symbols shown included: ** ($p < 0.0001$).**

4.3.6 CD80 and CD86 Observed Different Force-Dependent Dissociation Kinetics

Reported CD28 interactions with actin cytoskeleton adapter proteins and overlapping signalling with the TCR complex encouraged CD28 mechanosensitivity investigations. BFP instrumentation enabled measuring bond lifetime under force using the BFP in a force clamp mode. Operating the BFP in a force clamp mode involved retracting enough to produce tensile force on a molecular bond formed during a contact cycle. Retraction distance controlled computationally produced measurable bond lifetimes and tensile

forces. BFP bond lifetime under force measurements elucidated the influence of tensile force on bond dissociation.

Using the same recombinant murine CD28 ligands, BFP bond lifetime under force measurements characterized CD28 mechanosensitivity during receptor-ligand interactions. Acquiring accurate bond lifetime under force measurements at low forces required incorporating bond lifetime data from thermal fluctuation measurements. Grouping bond lifetime under force data generated through thermal fluctuation and force clamp experiments produced distributed bond lifetime under force measurements that described the relationship between bond tensile force and lifetime. Binning bond lifetime under force data according within different force bins showed a monotonically increasing bond lifetime with increased force for CD28 and its ligands until a peak force bin (Figure 12A). Subsequent force bins after peaking showed monotonically decreasing bond lifetime with increased force. The visualized relationship suggested tensile force could increase bond stability until reaching a threshold (molecular catch).

Identifying a potential molecular catch for CD28 and its ligands motivated validating the potential molecular catch using statistical methods not influenced by human biases. Non-parametric kernel regression offered a potential solution for transforming measurements into a model describing the relationship between bond lifetime and tensile force. Plotting non-parametric kernel regressions for CD80 (Figure 12C) and CD86 (Figure 12D) validated force bin findings. Resolving molecular catches involved dividing bond lifetime distributions into ascending (catch) and descending (slip) phases corresponding to the highest lifetime peak in our kernel regression model for CD80 (5.74

pN and 0.327 s) and CD86 (9.70 pN and 0.363 s). Examining the model revealed poor performance at higher forces lacking bond lifetime measurement quantity.

Ordinary least squares linear regression on catch and slip phases allowed determining if slopes statistically differed from a hypothetical 0 s/pN value and comparing ligand slopes (Figure 12B). CD80 and CD86 observed statistically significantly larger than 0 s/pN slope and catch phases as well as lower than 0 s/pN slope slip phases. Comparing slopes using a Welch's two-tailed t test showed a statistically higher CD80 catch slope than CD86, but no statistical difference between slip phase slopes. Collectively, our analysis suggests that CD80 and CD86 formed molecular catches with surface expressed CD28 indicative of a mechanosensitive receptor.

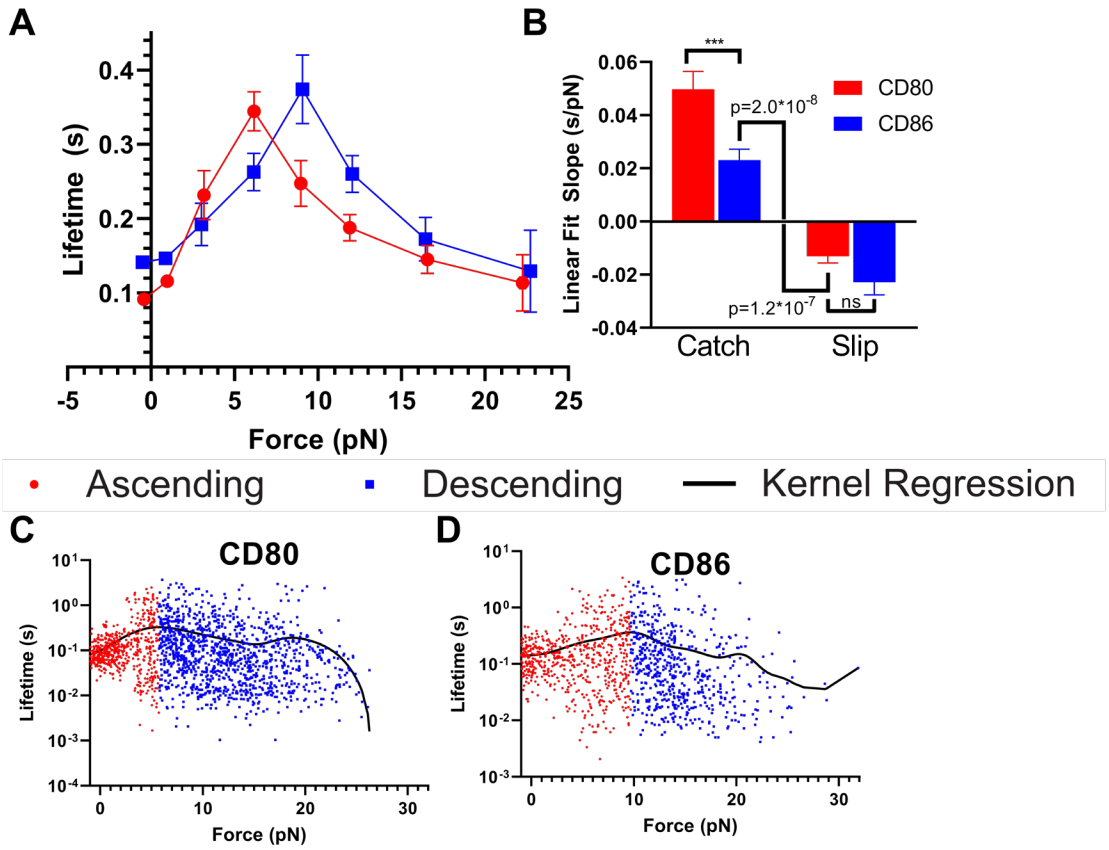

Figure 11 - CD80 and CD86 Display Different Force-Dependent Dissociation. BFP bond lifetime under force measurements enabled under force influences CD28 receptor interactions with its ligands CD80 (red, n=1731) and CD86 (blue, n=1197). Combining BFP bond lifetime measurements from force clamp experiments and thermal fluctuation experimental data generated measurements within the desired force range. Force binning the combined bond lifetime under force measurements generated CD80 and CD86 curves (A). Force binned data demonstrated force-dependent bond lifetime enhancement as a monotonically ascending trend in bond lifetime under force followed by monotonic descending trends. CD80 displayed bond lifetime enhancement under a smaller force range resulting in an earlier peak before a descending bond lifetime under force relationship. Nonparametric kernel regression validated findings from force binning on bond lifetime under force data for both CD80 (C) and CD86 (D). Nonparametric kernel regression modeled the relationship between bond lifetime and force within our data (black line). CD80 demonstrated a lower force peak in bond lifetime (5.74 pN and 0.327 s) than CD86 (9.70 pN and 0.363 s) validating our force bins accurately reflected the relationship between bond lifetime and force. Dividing bond lifetime under force data into ascending (red circles) and descending (blue squares) using nonparametric kernel regression model peak allowed statistically comparing ascending (catch) and descending (slip) phase slopes. Fitting catch and slip phases with an ordinary least

squares linear regression calculated slopes for statistical analysis. Catch and slip phases deviated significantly from a hypothetical 0 s/pN fit value using a one sample t test (p values represented on B). A Welch's two-tailed statistical comparison revealed a statistically larger slope for CD80 than CD86 as well as no statistically significant difference between slip slopes. Each symbol in A represented the mean bond lifetime with error bars showing SEM. For C and D, each symbol corresponded to one bond lifetime measurement. Bar height in B illustrated ordinary least squares linear regression slopes with error bars for fitting error. Data shown depicted multiple experiments for CD80 (12) and CD86 (8). Statistical comparisons shown on the figure correspond to: ns (non-significant) and * ($p < 0.001$).**

4.3.7 CD80 and CD86 Presented Using Monovalent or Tetravalent Streptavidin Observed Similar Force-Dependent Dissociation Kinetics

Additional experiments immobilizing ligands with monovalent and tetravalent streptavidin (SA) provided additional evidence supporting the observed interactions between CD28 monovalency when interacting with its ligands. SA streptavidin naturally exists as a tetramer with capacity to bind four biotintylated proteins. Engineered SA subunits with ablated biotin binding (dead = D) assembled with wild-type subunits (alive = A) generated SA multimers with altered valency. Controlling stoichiometry ratios for alive and dead subunits produced monovalent (A1D3) and wild-type tetravalent (A4D0). A1D3 enabled presenting CD28 ligands absent of possible dimers. Comparing CD28 ligands presented with A1D3 and A4D0 allowed distinguishing if ligand dimers contributed to bond lifetime measurements where bivalent CD28 interacting with dimeric ligands should mediate longer bond lifetimes.

Additional BFP force clamp experiments with CD28 ligands produced bond lifetime measurements within priorly determined peak force ranges. Binning bond lifetime under force measurements performed with A4D0 and A1D3 corresponded with prior peaks for

CD80 (4 to 9 pN) and CD86 (9-14 pN) (Figure 13). Binned lifetime data allowed conducting bond survival analysis as previously discussed (4.3.5). Overlapping values between our A4D0 and A1D3 data illustrated similar trends for CD80 and CD86 in both force bins. Collectively the data suggested SA valency did not shape prior bond lifetime under force measurements and additional evidence supporting CD28 monovalency.

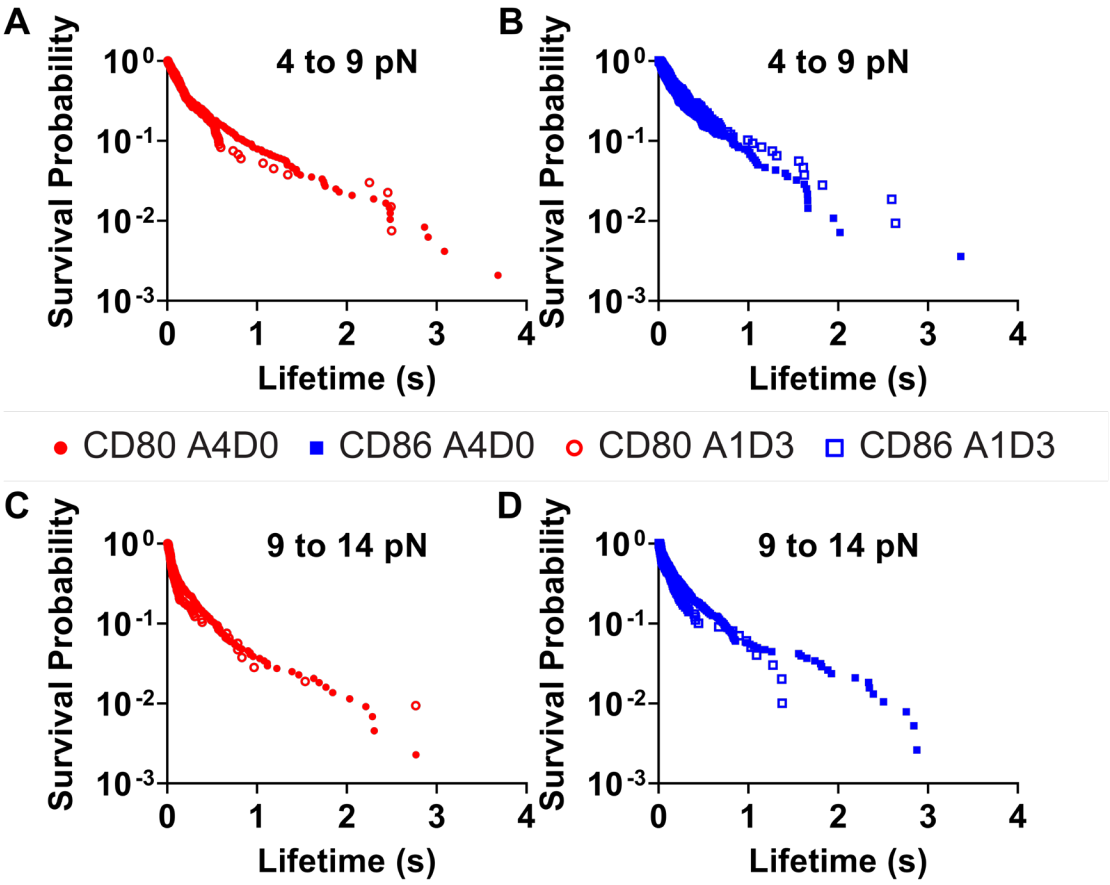

Figure 12 – Bond Survival Analysis Revealed Similarity Between Bond Lifetimes Acquired with Monovalent (A1D3) and Tetravalent (A4D0) Streptavidin (SA). Additional lifetime measurements using A1D3 SA for either CD80 (red, left) or CD86 (blue, right) provided evidence supporting prior bond lifetime under force measurements represented CD28 ligands interactions with monovalent CD28. Acquiring bond lifetime measurements within ranges overlapping with resolved molecular catches enabled determining if CD28 bivalency contributed to longer lifetimes. Plotting bond survival analyses in a 4-9 pN (top) and 9-14 pN (bottom)

allowed visualizing similarities between acquired bond lifetimes under force. Survival analyses revealed overlapping values between A4D0 (closed shapes) and A1D3 (open shapes) for both CD80 and CD86 in both force bins. Each plotted bond survival analyses symbol corresponded with a single bond lifetime under force measurement. Sample sizes displayed graphically for the 4-9 pN force bin representations: CD80 A4D0 (n=480), CD80 A1D3 (n=133), CD86 A4D0 (n=278), and CD86 A1D3 (n=107). Sample sizes displayed graphically for the 9-14 pN force bin: CD80 A4D0 (n=438), CD80 A1D3 (n=381), CD86 A4D0 (n=106), and CD86 A1D3 (n=99). Bond lifetime measurements shown consisted of previously discussed experiments and two additional experiments for both ligands presented with A1D3.

4.3.8 CD80 and CD86 Presented on Tetravalent and Monovalent Streptavidin Demonstrate Similar Molecular Stiffnesses

Leveraging bond lifetime under force and rupture bond measurements also provided additional experimental evidence for evaluating CD28 valency. Bond lifetime under force measurements acquired using CD28 ligands presented with either A1D3 or A4D0 contained bond lifetime and rupture events with BFP signals that describing contact cycle tensile force loading. Raw BFP data contained two phases following bead-cell contact describing loading rates for impingement relaxation and tensile force generation on molecular bonds. Impingement relaxation occurred after an established bead-cell contact (negative to zero force) while tensile force loading transpired (zero to positive force). Molecular stiffness (k_{bond}) calculations involved using Huber robust regression on both phases and inferring cellular (Equation 9) and molecular (Equation 10) stiffnesses from loading rates in both phases (Equation 12). Considering only positive stiffnesses ensured measurements represented stable probes. Histograms from determined molecular stiffnesses illustrated molecular stiffness distributions that relating to observed molecular binding states. CD28 bivalently binding dimeric CD80 would show greater molecular

stiffnesses given calculated molecular stiffnesses relate to cis-interactions (at the same cell-cell interface) between receptors and other molecular species.

Calculating k_{bond} for all bond lifetime data enabled plotting normalized histograms for CD80 A4D0 (Figure 14A), CD86 A4D0 (Figure 14B), CD80 A1D3 (Figure 14C), and CD86 A1D3 (Figure 14D). Non-linear least square Gaussian fitting normalized histograms provided assessments of different multimeric bonds formed between CD28 and its ligands. Attempting multi-mode Gaussian fitting revealed that multi-mode Gaussian fitting (> 1 mode) poorly described molecular stiffness distributions suggesting molecular stiffness data lacked higher order multimeric bonds. Statistically comparing single mode Gaussian fitting means using a Brown-Forsythe and Welch one-way ANOVA test showed no statistically significant difference between molecular stiffnesses acquired with A1D3 or A4D0 for the same ligand (Figure 14E) further supporting a lack of evidence in support of higher order multimeric bonds between CD28 and its ligands.

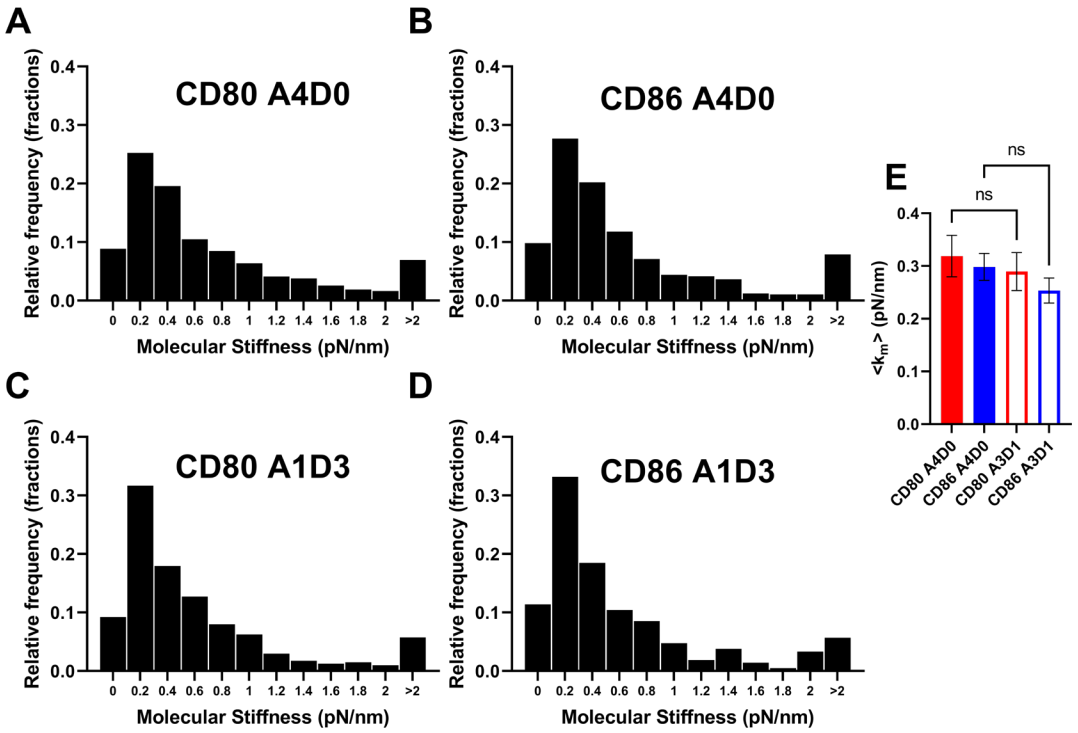

Figure 13 - Tetravalent or Monovalent Presentation Resulted in Indistinguishable Molecular Stiffnesses for CD80 and CD86. Molecular stiffness analyses using BFP rupture and bond lifetime measurements for CD80 or CD86 presented by tetravalent (A4D0) or monovalent (A1D3) SA provided molecular stiffness distributions that related to multimeric structures formed during molecular bonds. Dividing BFP signals into two ascending phases correspond to cell impingement relaxation and applying tensile force on molecular bonds generated loading phases that could be interpreted computationally to derive system stiffnesses. Robust Huber linear regressions for loading phases allowed calculating system stiffnesses during phases (Equation 12). Stiffnesses determined from phases mapped to cellular stiffness (k_{cell}, Equation 9) and molecular bond stiffness (k_{bond}, Equation 10). Plotting k_{bond} calculations using normalized histograms for CD80 A4D0 (A, n=334), CD86 A4D0 (B, n=1154), CD80 A1D3 (C, n=402), and CD86 A1D3 (D, n=212) illustrated potential molecular species with different molecular stiffnesses. Graphically, normalized histogram distributions resembled each other. Non-linear least squares multi-mode (> 1) Gaussian distribution fitting failed to describe observed molecular species. Non-linear least squares Gaussian single mode fitting calculated mean molecular stiffnesses for each experimental group (E). Statistical comparisons using Brown-Forsythe and Welch one-way ANOVA multiple comparison tests between ligands presented with A4D0 and A1D3 lacked statistical difference. Collectively, experimental evidence suggested presenting CD28 ligands with A4D0 and A1D3 did not influence observed stiffnesses. Molecular stiffness histograms (A-D) bar height represented the relative frequency of a molecular

stiffness measurement within 0.2 pN/nm wide bins. Gaussian fit parameter comparisons (E) bar height showed fit parameter value with error bars showing fitting error. Statistical symbols shown: ns (not significant).

4.3.9 CD8+ T Cells Initially Pushed on CD28 Ligand Bonds and Subsequently Pulled on CD28-CD80 Bonds

During experiments CD28 ligation caused profound CD8+ T cell morphological changes most likely related to previously published downstream actin cytoskeletal changes that operate independent of TCR signalling (150, 321, 322). Such actin cytoskeletal changes made recording bond lifetimes under force difficult given they influenced force stability. However, thermal fluctuation experiments uniquely provided opportunities to examine how CD28 ligation influenced a CD8+ T cell's morphology over several minutes. Although BFP instrumentation lacked functionality for tracking bead displacement when cells rotated beads, recorded thermal fluctuation bond lifetimes under force existed within a large force range representing cytoskeletal changes induced by ligation. Cells initially extended and pushed on probes (Figure 15A). After reaching a maximum extension (fully polarized) stimulated cells rotated around micropipette base appearing to extend in a direction away from probes (Figure 15B).

Experiments attempting to stimulate cells with anti-CD3 before stimulating with CD80 revealed similar morphological changes that corresponded with experimental observations, but quickly reproduced the polarization effect. Cells bound to anti-CD3 beads retained a spherical shape without morphologic change (Figure 15C). Cells bound to anti-CD3 beads quickly extended out towards anti-CD3 beads upon stimulation with CD80 (Figure 15D). Observations aligned with polarization achieved after repeated

stimulation with CD28 ligands, but clearly demonstrated polarization focality through bead position.

Dividing the bond lifetime events into two phases defined by lifetime accumulation illustrated the dynamic morphological changes that occurred over minutes of mechanical stimulation. Periods before and after 10 s accumulated lifetime showed polarization and redirection, respectively. Before and after 10 s accumulated lifetime revealed CD8+ T cells pushed (negative force) and then pulled (positive force) on CD28 receptor bonds (Figure 15D). Brown-Forsyth and Welch one-way ANOVA multiple comparisons with Games-Howell correction showed a statistically significant force increase for CD80 and CD86 ligands after 10 s accumulated lifetime. CD80 and CD86 before 10 s lifetime accumulation lacked a statistically significant difference. Comparing CD80 and CD86 after 10 s lifetime accumulation demonstrated a statistically greater force for CD80 than CD86. The large difference between before and after experimental groups provided experimental evidence that an association between bond lifetime accumulation and force exists for both CD80 and CD86.

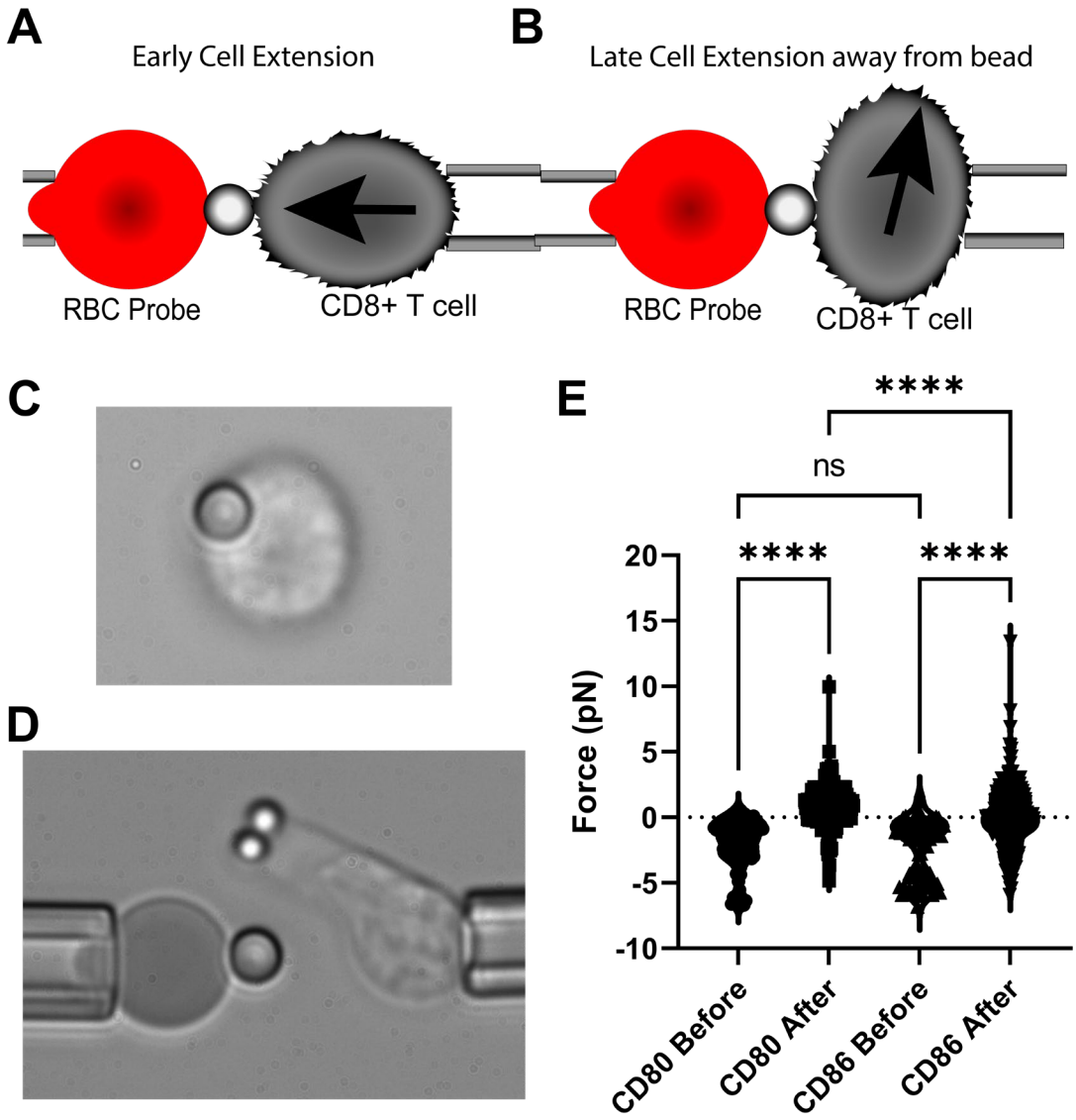

Figure 14 - CD8+ T Cells Pushed on CD28 Receptor-Ligand Bonds and Pulled on CD28-CD80 Bonds. CD8+ T cells during thermal fluctuation experiments observed morphological changes in response CD28 interactions with its ligands. During thermal fluctuation experiments cells extended towards ligand coated beads (A, negative) until reaching a certain point and subsequently extended the same polarized component away from the bead while rotating around the micropipette base (B, positive). Anti-CD3 bound cells stimulated with CD80 clearly showed polarization effect. Cells interacting with anti-CD3 beads retained a spherical shape without apparent polarization (C). Mechanically stimulating anti-CD3 bound cells with CD80 caused rapid cell extension of anti-CD3 bound membrane (D).

Capturing the dynamic morphological changes during lifetime measurements required dividing bond lifetime data into before and after 10 s accumulated lifetime. Statistical comparisons with a Brown-Forsythe and Welch one way ANOVA multiple comparison with Games-Howell correction demonstrated a statistically significant increase in force after 10 s lifetime accumulation for CD80 and CD86. CD80 and CD86 before 10 s lifetime accumulation lacked a statistically significant difference. Comparing after lifetime accumulation revealed a statistically significant increase for CD80 over CD86. Statistical symbols graphically represented: ns (not significant) and ** ($p < 0.0001$). Sample sizes for groups shown: CD80 before (n=93), CD80 after (n=305), CD86 before (n=85), and CD86 after (n=288). Data shown corresponded to the same thermal fluctuation experiments shown in Figure 11 and Figure 12.**

4.3.10 CD8+ T Cells Applied Tension Through Anti-CD28, but Inconclusively Applied Tension on CD28 Ligand Bonds

After demonstrating mechanosensitivity through catch bonds, molecular tension probes (MTP) enabled exploring CD28 mechanosensing with its ligands. MTP experiments involved a collaboration with Jintian Lyu and Yuesong Hu in Dr. Khalid Salaita's using MTP technology developed in Dr. Salaita's laboratory. MTPs experiments potentially corroborated previous findings by demonstrating CD28 ligation induced cells tensile force production on CD28 bonds. MTPs utilized a force-deformable DNA hairpin loop where Forster resonance energy transfer (FRET) loss between Cy3B and black hole quencher 2 (BHQ2) demonstrated tension. MTP surface preparation involved glass treatment, gold nanoparticle immobilization, and subsequent covalent probe linkage on treated glass surfaces. Within work presented data, the author prepared the MTP surfaces, conducted the experiment, and analysed the data. Prior to this experiment, Jintian Lyu performed multiple experiments using author supplied CD8+ T cells and proteins obtaining similar results with less statistical power. This work featured data from the most thoroughly conducted experiment containing the most analysed cells.

Incubating MTP surfaces with SA provided valent binding sites for biotinylated ligand or antibody immobilization. Immobilizing biotinylated BSA provided a negative control for experiments. Antibodies against CD3 and TCR previously documented to induce tension generation allowed evaluating MTP surface quality as positive controls. Experimental conditions consisted of anti-CD28, CD80, and CD86. Assembling experimental group MTP surfaces into imaging chambers with a 1x hanks buffered saline solution (HBSS) generated conditions compatible live CD8+ T cell imaging. Cells incubated on surfaces for around 30 minutes with total interference reflection fluorescence (TIRF) microscopy and reflection interference contrast microscopy (RICM) created images for interpreting tension as FRET loss and surface contact area, respectively. Using the term surface contact area instead of surface spreading area reflected the more dynamic nature of interactions between cells and surfaces that lacked stability in CD80, CD86, and BSA experimental groups. Capturing accurate CD80, CD86, and BSA images required carefully analysing cells that contacted surfaces and avoiding non-contacting cells that could not be accurately analysed by software. Image analysis software processed images to calculate tension through single cell FRET loss with subtracted local background and contact area in pixels for post-analysis conversion into micron using a calibration scale. Matlab image analysis used in analysis featured usability modifications of the original software supplied by Jintian Lyu.

Figure 16 contained results from the experiment with the highest statistical power. Plotting results for surface contract area demonstrated an influence shaped most profoundly by surface molecular density (Figure 16A). Statistical comparisons between experimental groups using a Brown-Forsyth and Welch one-way ANOVA multiple comparisons test

with Games-Howell correction showed the highest statistically significant increases in contact areas over the BSA negative control for positive controls anti-CD3 and anti-TCR. Comparing anti-CD28 with the negative control revealed a statistically significant difference, but smaller effect size. The most minimal effect observed through statistical analysis between CD86 and BSA surprisingly showed significant decrease in contact area. CD80 lacked statistically relevant differences from the BSA negative control. A histogram created from contact area experimental data also illustrated differences observed among experimental groups (Figure 16C).

Graphing normalized tension also enabled visualizing molecular tension differences between experimental groups (Figure 16B). Statistically comparing normalized molecular tension for experimental groups using a Kruskal-Wallis non-parametric multiple comparisons test with Dunn's correction revealed a statistically significant increase over the SA negative control in positive control groups anti-CD3 and anti-TCR. Comparing anti-CD28 with the negative control showed cells applied tension on CD28. CD86 demonstrated a statistically significant increase in normalized tension over the BSA negative control, but with a small effect. CD80 lacked any statistical difference from the BSA negative control. CD80 and CD86 experimental groups did not differ from each other statistically. A histogram created from data also illustrated differences between experimental groups (Figure 16D). Close inspection of individual cells within BSA, CD80, and CD86 experimental groups (Figure 16B) elucidated that the BSA experimental group featured two populations with a lower tension primary population as well as CD80 and CD86 single populations elevated above BSA's primary population.

Collectively experiments suggested that cells applied tension on CD28 when ligated by anti-CD28, but experimental evidence for tension generation mediated by CD28 and CD28 ligand bonds remained inconsistent. A lack of tension in other MTP experiments reflected their lack of statistical power primarily resulting from small sample sizes ($n < 50$) especially small sample sizes for BSA negative controls. Small negative control sample sizes failed to elucidate non-specific tension signal from the primary negative control population observing the lowest normalized tension signal. Moreover, the contact dependence of signal and its image processing required excluding cells without surface contact. The observed effect strength in CD28 related signals also related to lower surface receptor density (CD28 ~11-12 molecules per μm^2) and considerably fast ligand dissociation kinetics (5-8 molecules per second) than antibodies.

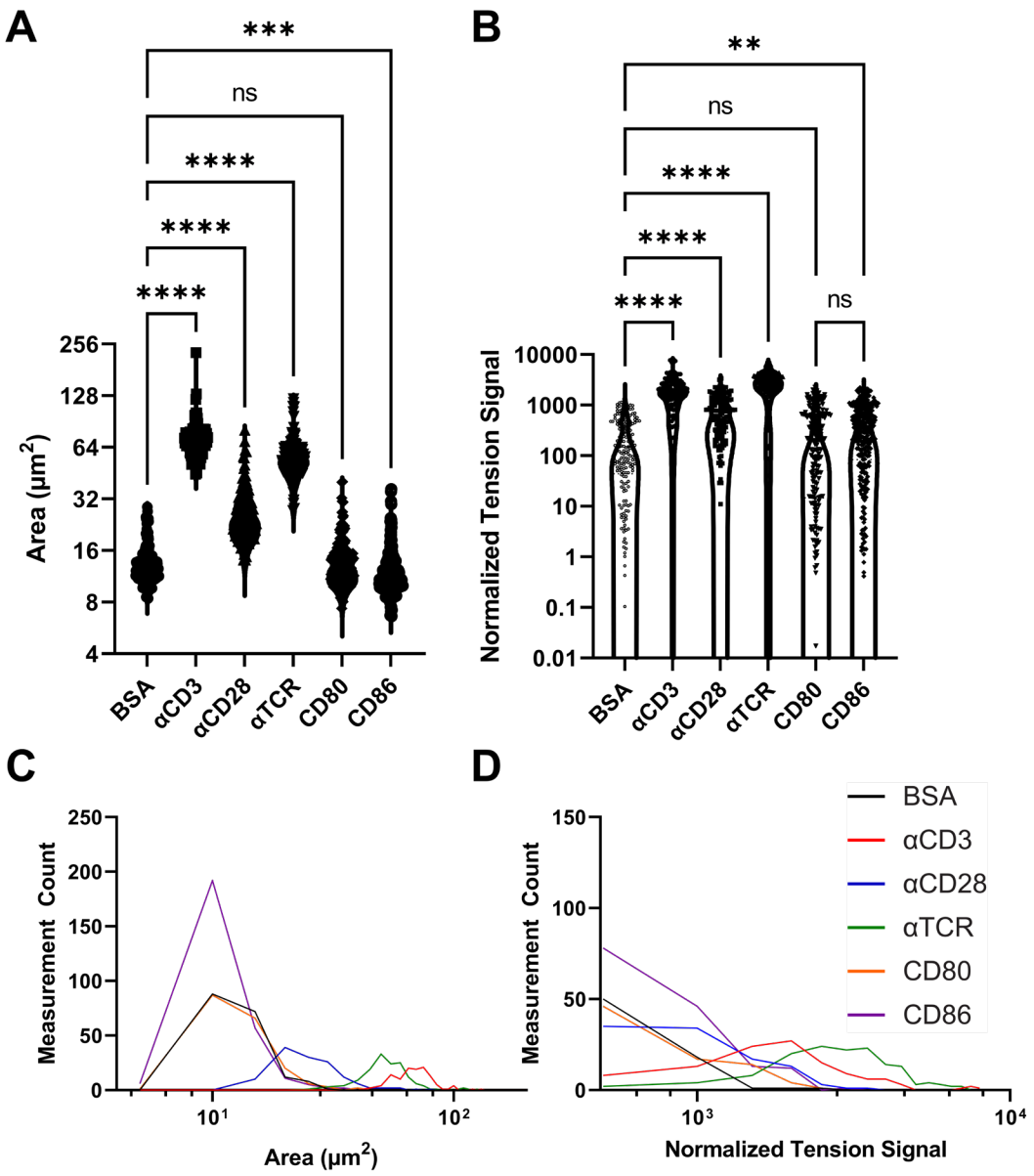

Figure 15 - Molecular Tension Probes Showed Pulling Force on CD28 Upon Anti-CD28 Ligation. Molecular tension probes (MTPs) measured receptor pulling forces upon ligation with antibodies or CD28 ligands. MTPs quantified cell generated tension on receptors through FRET loss mediated by force-sensitive DNA hairpin loop deformation. Immobilized MTPs on glass surface gold nanoparticles allowed presenting ligands or antibodies via SA. MTP surfaces mounted within imaging chambers enabled live-cell imaging CD8+ T cells on MTP surfaces. After incubations, reflection interference contrast microscopy (RICM) and total interference reflection fluorescence (TIRF) microscopy produced images for computational image analysis. RICM microscopy quantified cell MTP surface

contact area (A). TIRF microscopy determined normalized MTP tension by capturing FRET loss and local FRET background signal (B). Experimental groups featured: BSA (negative control), anti-CD3 (positive control), anti-TCR (positive control), anti-CD28, CD80, and CD86. Statistical comparisons involved a Kruskal-Wallis non-parametric multiple comparisons test with Dunn's correction and Brown-Forsythe and Welch's one-way ANOVA multiple comparisons test with Games-Howell correction for normalized tension signal and contact area, respectively. Positive controls controls (anti-CD3 and anti-TCR) induced significantly higher contact area than our negative control (BSA). Anti-CD28 also showed a statistically significant increase surface contact over the BSA negative control, but not as large as anti-CD3 and anti-TCR. Statistical comparisons between CD86 and the BSA negative control revealed smaller surface contact, but with a small effect not replicated in other experiments. Normalized tension signal also displayed similar statistical differences with anti-CD3 and anti-TCR both with higher tension compared BSA. Anti-CD28 observing moderately increased tension statistically compared to BSA. CD86 displayed statistically higher tension than BSA, but a small observed effect not replicated in other experiments. CD80 lacked a statistically significant difference from BSA, and an additional statistical comparison between CD86 and CD80 missed significance. Histograms from experimental data for surface contact area (C) and normalized tension signal (D) also illustrated differences between groups. Each symbol in A and B corresponded to a single analyzed cell. Featured data within figure corresponded to one experiment with the highest statistical power. Experiments with less statistical power failed to show differences between negative controls and CD28 interactions with its ligands. Experimental groups featured: BSA (black, n=181), anti-CD3 (red, n=117), anti-CD28 (blue, n=133), anti-TCR (green n=147), CD80 (orange, n=185), and CD86 (purple n=275). Statistical comparison symbols shown corresponded to: ns (not-significant), ** ($p < 0.01$), * ($p < 0.001$), and **** ($p < 0.0001$).**

4.3.11 CD28 Ligation Mediated Calcium Flux Independent and Concurrently with TCR Signalling

4.3.11.1 Calcium Flux Investigation Collaboration

Demonstrating differential 2D kinetics and mechanosensitivity between CD28 and its ligands through catch bonds motivated investigating if such differences also contributed to calcium signalling differences. Resolving single cell differences in calcium signalling required previously published specialized cell trap microfluidic devices (255). Dr. Fangyuan Zhou, a post-doctorial researcher within Dr. Cheng Zhu's laboratory, conducted

all cell trap calcium flux experiments using OT-1 CD8+ T cells and recombinant proteins and antibodies. The author constructed all graphical data representations and analyses contained in this work from raw data supplied by Dr. Fangyuan Zhou. Original dynamic patterns found by Dr. Zhou provided the basis for the author generated calcium flux signal analysis. Utilizing computational signal processing techniques allowed resolving single-cell calcium flux dynamics.

4.3.11.2 Cell Trap Experiments for Resolving Calcium Flux Responses

Cell trap experiments utilized polydimethylsiloxane (PDMS) devices generated from photolithography defined features on a silicon wafer. Biotin BSA protein adsorption generated surfaces for biotinylated ligand or antibody immobilization using SA. Loading isolated OT-1 CD8+ T cells with Fura-2-acetoxymethyl ester (Fura-2AM) provided a ratiometric calcium indicator capable of accurately measuring calcium flux despite variations in local concentrations or cell thickness. Imaging cells at 340 and 380 nm excitation flowed into cell trap arrays provided raw imaging data for subsequent ratiometric (340/380) calcium flux analysis. An image analysis tool utilized masking towards deriving representative ratiometric calcium indication during experiments. Identifying initial frames where cell trapping occurred allowed estimating cell stimulation duration. Quantifying calcium fluxes involved normalizing ratiometric calcium indication to the initial trapped frame whereby increases in the ratiometric calcium indicator signal indicated cell responses.

Utilizing Savitzky-Golay filtering (first order polynomial with a 11 window size) with raw normalized ratiometric calcium indicator signals generated smoothened signals

with interpretable peaks (323). Initially, graphing filtered signals within heat maps visualized experimental condition responses inspiring the development for metrics to quantifying signal strength, robustness, and dynamics (Figure 17). Determining the area under curves (AUC) for filtered signals using the composite trapezoidal rule generated cumulative calcium indicator fluorescence during T cell treatment responses (Figure 18A). Peak detection given a 1 normalized fluorescence unit minimal prominence on filtered calcium indicator signals produced testable peaks. Counting true peaks identified for cells allowed identifying if cells responded to experimental conditions and cyclical patterns within responses (Figure 18B). Iteration through calcium indicator signals generated additional metrics for comparing experimental conditions. Cell percentage sustained above 50% their maximum calcium flux indicated signal response robustness (Figure 18C). Iterating through calcium signals until maximum observed signals and determining when the signal exceeded 50% (Figure 18D) or 90% (Figure 18E) the maximum signal provided a response speed metric. Excluding times where the first frame satisfied threshold conditions minimized non-responder influences.

4.3.11.3 Validating Calcium Fluctuation Experimental Conditions

Exploring CD28 dependent calcium fluctuation responses required establishing conditions conducive for observing co-stimulation and comparing co-stimulation with independent contributions. The OT-1 transgenic TCR system allowed characterizing TCR signalling using $OVA^{257-264}$ $H2\text{-}K^{b}$ (OVA), an established agonist pMHC for OT-1 TCR. To control relative amounts of presented ligands each condition featured a 10 μM total ligand concentration. The 3.L2 transgenic TCR agonist Hb^{64-76} $I\text{-}E^{k}$ pMHC (class II) served as a negative control to show observed response specificity to TCR signalling. Conditions

with two components featured equal molar (5 μM) ligand or antibody incubated devices. Antibodies against anti-CD3, anti-CD28, as well as anti-CD3 and anti-CD28 served as positive controls for TCR agonist signalling and TCR agonist co-stimulation. Antibodies against human IgG illustrated antibody presence alone did not contribute to observed signal. Conditions with CD28 ligands and class II or OVA and class II enabled resolving if observed co-stimulation influence on calcium fluctuations surpassed their individual component contributions. Experimental trials optimized observed co-stimulation conditions (OVA + CD80 or OVA + CD86) and required three experiments. Included data from analyses stemmed from two experiments with similar conditions and observations. Plotting heat maps for experimental conditions allowed quickly distinguishing features within experimental condition responses while also exposing potential co-stimulation specific metrics characterizing signal strength, robustness, and dynamics (Figure 17).

Heat maps clearly showed that class II alone produced little changes in calcium indicator signal over time effectively characterizing experimental system background noise. Likewise, co-stimulation condition (OVA + CD80 and OVA + CD86) heat maps demonstrated robust increases in signal with many cells showing sustained calcium release compared to non-co-stimulation experimental conditions. CD28 ligand conditions (CD80 + class II and CD86 + class II) featured low level calcium flux signals with several non-responding cells. Identifying frame number within cell signal sequences signals appeared close to cell maximums show that many cells responded quickly after becoming trapped within devices.

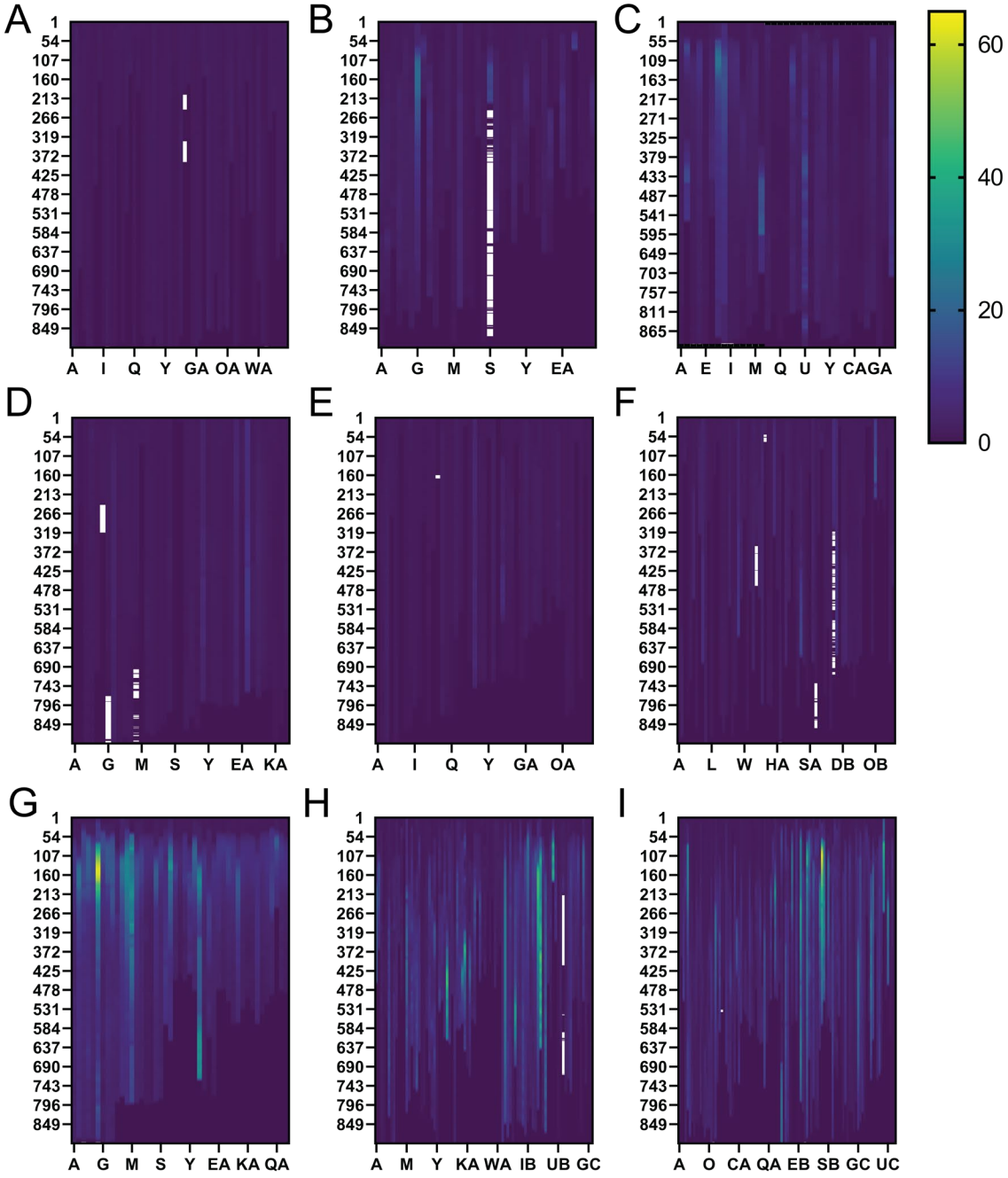

Figure 16 –Filtered Calcium Indicator Signal Heat Maps for Experimental System Validation. Ratiometric calcium indicator dye quantified changes in intracellular calcium during cell trap experiments. Visualizing data using heat maps offered perspectives into response strength, duration, and dynamics. OT-1 CD8+ T cells flowed within devices responded differentially to immobilized ligands or antibodies once trapped allowing for imaging-based response quantification. OT-1 TCR agonist $OVA^{257-264}$ $H2\text{-}K^{b}$ (OVA) allowed measuring TCR specific signal. The 3.L2

transgenic TCR agonist Hb^{64-76} $I\text{-}E^{k}$ pMHC (class II) offered a negative control. All conditions featured a 10 μM total molar concentration to control relative concentrations between co-stimulation components. All conditions with two components represented equal molar (5 μM) ligand or antibody. Experimental conditions included: class II (A), OVA + class II (B), anti-CD3 + anti-human IgG (C), anti-CD28 and anti-human IgG (D), CD80 (E), CD86 (F), anti-CD3 + anti-CD28 (G), OVA + CD80 (H), and OVA + CD86 (I). Heat map viridis color scale from black to yellow represented a continuum of normalized filtered signals from 0 to 65, respectively. The color white illustrated signal values outside the set ranges (below and near zero). Columns corresponded with analyzed, trapped cell signal (x-axis) in 1 s frames from 1 to 901 (y-axis). Heat maps showed dramatic differences in filtered signals from co-stimulation conditions (OVA + CD28 ligand or anti-CD3 + anti-CD28). Heat maps also elucidated cells responded differentially to conditions either rapidly reaching a maximum filtered signal or potentially a sustained filtered signal elevation from the first frame.

Computational signal analysis using previously specified metrics allowed comparing experimental conditions statistically (Figure 18). Differences in sample sizes necessitated using Brown-Forsythe and Welch one-way ANOVA multiple comparison tests without corrections (unpaired Welch's two-sided t tests) for statistical comparisons. As expected in all metrics co-stimulation conditions (OVA + CD80 and OVA + CD86) observed statistically significant increases compared to the negative control (class II). Comparing OVA + class II with co-stimulation conditions showed statistically significant increases for co-stimulation conditions in non-response speed metrics (signal AUC, peak count, sustained signal). Statistically significant increases in CD86 + class II over CD80 + class II experimental groups existed for signal AUC, peak count, sustained signal, and time to 90% signal maximum. Observed statistical significances between co-stimulation and CD28 ligand conditions highlighted effectiveness in identified metrics in describing co-stimulation calcium indicator changes. Validating differences between CD80 and CD86 with class II experimental groups required additional experiments, but calcium signal heat maps illustrated clear CD28 dependent responses for both ligands although with a small

effect compared to both OVA + class II and OVA + CD28 ligand experimental groups likely reflecting dramatic differences in surface densities (CD28 ~ 11-12 molecules/um^2 and TCR 133-145 molecules/um^2)(251).

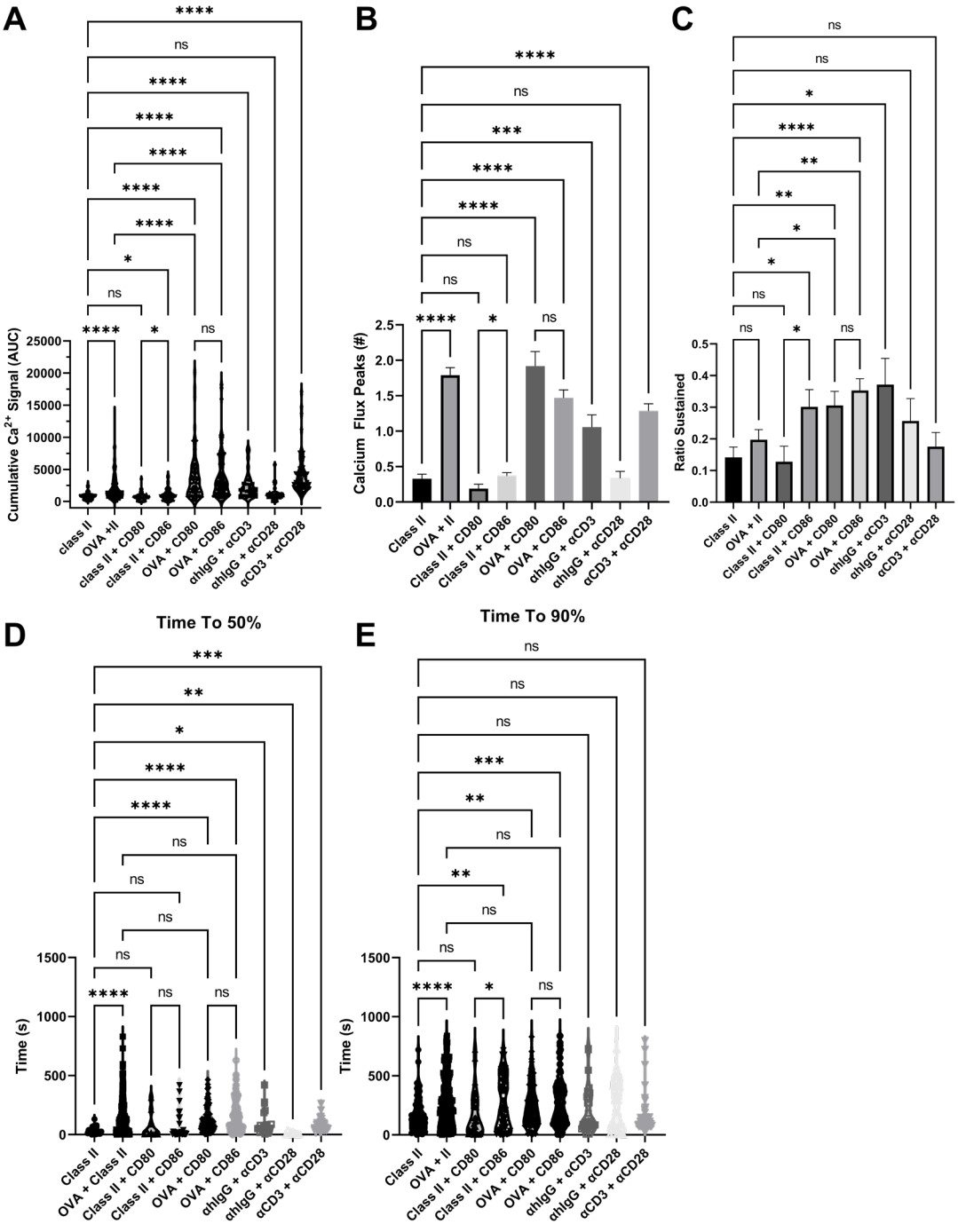

Figure 17 - Statistical Comparisons of Filtered Signal Analysis for Establishing Co-stimulation Conditions. Observed patterns in Figure 17 heat maps inspired developing programmatic metrics for comparing experimental conditions. Filtered signals generated input for trapezoidal rule integration towards calculating area under curves (AUC) representing cumulative calcium signal (A). Peak detection using a minimal 1 normalized signal prominence on filtered signal peaks indicated true signal peaks without contributions from non-responding cells while also identifying cells with true oscillations in calcium flux (B). Iterating through filtered signal sequences for cells with true calcium peaks allowed identifying if signals sustained above 50% for more than half acquired signal frames (C). Iterating through filtered signals until the observed maximum signal towards identifying when signals exceeded 50% (D) or 75% (E) the maximum signal enabled quantifying dynamics. Plotted data included all experimental conditions from Figure 17: class II (n=132), OVA + class II (n=244), anti-CD3 + anti-human IgG (n=35), anti-CD28 and anti-human IgG (n=39), CD80 (n=47), CD86 (n=73), anti-CD3 + anti-CD28 (n=35), OVA + CD80 (n=172), and OVA + CD86 (n=204). Data shown represented two aggregated experiments representing three experimental attempts with similar findings. Brown-Forsythe and Welch one-way ANOVA multiple comparisons without correction tests (unpaired Welch's two-sided t test) created statistical comparisons shown between experimental groups. Statistical comparison symbols graphed: ns (not significant), * ($p < 0.05$), ** ($p < 0.01$), * ($p < 0.001$), and **** ($p < 0.0001$). Statistical differences between co-stimulation conditions (OVA + CD80 or OVA + CD86) illustrated developed signaling metric effectiveness in describing unique co-stimulation features.**

4.3.11.4 Co-stimulation Response Time Differences Between CD28 Ligands

Identifying metrics showing clear distinctions between co-stimulation conditions and non-co-stimulation conditions motivated additional experiments to elucidate potential differences between CD80 or CD86 co-stimulation. Previous findings within the literature documenting APCs vary CD28 ligand expression upon activation encouraged investigating if CD28 ligand to pMHC ratios shaped co-stimulation calcium signals. Additional experiments incorporated previously established metrics in Section 4.3.11.3 with the same OT-1 CD8+ T cells, but varied CD28 ligand to OVA ratios (9:1, 3:1, 1:1, 1:3, 9:1) for CD80 and CD86. Like previous experiments, all conditions featured a constant 10 μM total concentration and independent components varied in concentration from 1 to 9 μM.

Given the multitude of conditions evaluated, analyzed data featured three independent experiments with different CD28 ligand to OVA ratios accumulated together.

Plotting calculated metrics for each ligand given ratio metric calculations generated graphical representations that could illustrate ratio-dependent trends (Figure 19). Peak counts, ratio sustained, and cumulative calcium signal metrics failed to demonstrate different trends between CD80 and CD86 co-stimulation (Figure 19C, D, and G). Co-stimulation response times as determined by time to 50% or 90% maximum signal intensity thresholds showed opposing trends for CD80 and CD86 (Figure 19E-F). Increasing CD80 to OVA ratio rendered an increasing trend for both 50% and 90% maximum signal thresholds. Increasing CD86 to OVA ratios decreased response times calculated by 50% and 90% maximum signal thresholds. Statistical comparisons between CD80 and CD86 experiment groups at 3:1 and 9:1 ligand to OVA ratios revealed statistically significant increased response times with both thresholds. Interestingly, comparing cumulative calcium signals between CD80 and CD86 experimental groups also identified a statistically greater cumulative calcium signal for CD80, but the lack of a ratio-dependent trend suggested a need for additional experiments to validate observed differences. A heat map graphically showed the dramatic differences in co-stimulation at 9:1 CD28 ligand to OVA ratios (Figure 19A-B).

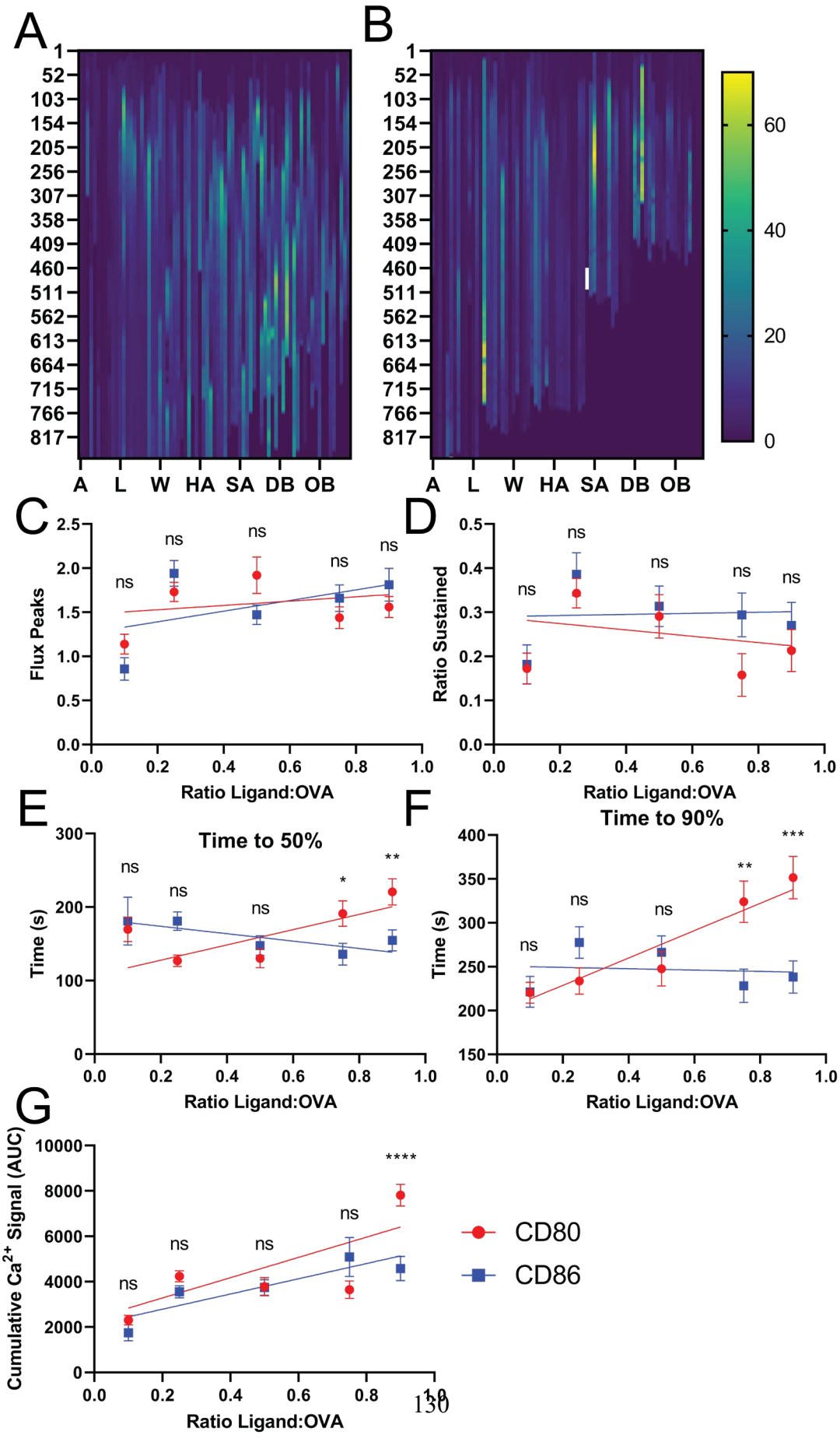
A
B
1
52
103
154
205
256
307
358
409
460
511
562
613
664
715
766
817
A L W HA SA DB OB
60
40
20
0
C
Flux Peaks
Ratio Ligand:OVA
D
Ratio Sustained
Ratio Ligand:OVA
E
Time to 50%
Time (s)
Ratio Ligand:OVA
F
Time to 90%
Time (s)
Ratio Ligand:OVA
G
Cumulative Ca2+ Signal (AUC)
Ratio Ligand:OVA
ns
*
**
***
****
CD80
CD86

Figure 18 - CD80 and CD86 Observe Differential Calcium Flux Dynamics in A Co-stimulation Context. Elucidating co-stimulation differences between ligands required additional experiments varying relative CD28 ligand to OVA ratios. All conditions featured a constant 10 μM total concentration of OVA and CD28 ligand with independent components varying from 1 to 9 μM. For CD80 and CD86 molar ratios (CD28 ligand to OVA) included: 1:9 (0.1) , 1:3 (0.25), 1:1 (0.5), 3:1 (0.75), and 9:1 (0.9). All experimental conditions involved signal analysis as previously specified in Section 4.3.11.3 (Figure 18). Heat maps from 9:1 CD80:OVA (A) and 9:1 CD86:OVA (B) graphed filtered signals with viridis color scale varying from black to yellow for 0 to 70, respectively. Columns corresponded with analyzed, trapped cell signal (x-axis) in 1 s frames from 1 to 851 (y-axis). Heat maps showed clear differences in signal strength and dynamics between co-stimulation with CD80 or CD86. Using the same metrics previously explored to show co-stimulation features in Section 4.3.11.3 (Figure 18) identified ratio dependent co-stimulation effects. Graphing metric results using scatter plots visualized ratio dependent trends using simple linear regressions (CD80 red lines and CD86 blue lines). Trends within CD28 ligand to OVA ratio plots for flux peak count (C), sustained signal ratios (D), and cumulative signal (G) failed show completing trend differences between ligands. However, response times reported as times to 50% and 90% maximum signal showed opposing trends between CD80 or CD86 co-stimulation. CD80 increased in response times (50% and 90%) with increasing CD80:OVA ratios while CD86 demonstrated an opposite trend (50%, E) or minimally decreasing trend (90%, F) with increasing CD86:OVA ratios. Statistical comparisons using a Brown-Forsythe and Welch one-way ANOVA multiple comparisons test without corrections (unpaired Welch's two-sided t test) found a statistically significant greater response time for CD80:OVA at 3:1 and 9:1 over CD86:OVA. Likewise, comparing 9:1 CD80:OVA with CD86:OVA identified a greater cumulative signal for CD80:OVA. Graph symbols illustrated metric mean ± SEM for CD80 (red) and CD86 (blue). Experimental groups included: 1:9 OVA:ligand (CD80 n=116, CD86 n=77), 3:1 OVA:ligand (CD80 n=201, CD86 n=101), 1:1 OVA:ligand (CD80 n=86, CD86 n=102), 3:1 OVA:ligand (CD80 n=57, CD86 n=85), and 9:1 OVA:ligand (CD80 n=75, CD86 n=74). Statistical comparison symbols shown illustrated: ns (not significant), * ($p < 0.05$), ** ($p < 0.01$), * ($p < 0.001$), and **** ($p < 0.0001$). Graphs featured data accumulated from three experiments using different OVA:ligand ratios.**

4.4 Discussion

The co-stimulatory receptor CD28 plays an important role in T cell physiology delivering essential signals impacting the T cell activation strength (324), proliferation (270), metabolism (268), survival (271), development (325), and differentiation (326-328). For many years since its identification, the immunological field regarded its signalling as

an essential component in a two-signal process mediating T cell activation along with the TCR (3). Since then, studies into T cell activation revealed the process occurred more dynamically involving other co-stimulatory and co-inhibitory receptors that work to enhance or supress T cell activation through signalling and competitive mechanisms (272). Several drugs targeting supressing or enhancing co-stimulation to influence T cell immunological function (295, 329). Despite its success as a therapeutic target, many questions regarding mechanistically how the receptor works remain especially when the receptor appears to enhance immunity or induce tolerance in different contexts (330-332).

4.4.1 Physiological Significance

Investigations into mechanistically how CD28 receptors worked involved characterizing downstream signalling events often elicited through stimulatory antibodies and in a co-stimulatory context with TCR complex binding antibodies. Kinetically, stimulatory antibodies do not resemble interactions between receptors and ligands. Although antibodies can induce conformational changes that result in receptor signalling, dynamics resulting from binding and unbinding play important roles in other immunological receptors such as the TCR enabling feedback mechanisms shaping the overall integrated signal. Building a more comprehensive understanding of the dynamic interactions occurring between receptors and ligands at T cell and APC interfaces offers valuable nights into mechanistically how receptors work. Here we perform live-cell DFS with the BFP towards characterizing 2D kinetics and force-dependent dissociation offering the most comprehensive biophysical analysis of CD28 and ligand interactions to date. This work sought to characterize CD28 on murine CD8+ T cell surfaces towards a foundation for future work investigating signalling crosstalk between T cell immune receptors.

Previous research from our laboratory indicated environmental and cellular factors influence TCR 2D effective affinity during an acute infection model (333), but it remains possible that other immune receptors like CD28 also display altered 2D kinetics. *In-situ* live-cell biophysical analysis produces unique measurements under potential circumstances influencing interactions between immune receptors and their ligands including post-translational modifications, receptor surface organization and localization, as well as cis-immune receptor and signalling machinery interactions. Among possible factors influencing CD28 signalling within different physiologic and pathophysiologic contexts include Lck regulation, previous investigations found CD4 and CD28 cooperate to regulate Lck activity (278). Moreover, recent evidence produced within our laboratory established a cross-junctional Lck-dependent heterodimer formed between TCR complex, CD8, pMHC, and Lck that regulated observed dynamic catch bonds (232). Unfortunately, Lck dysregulation prominence in lymphoproliferative disorders and neoplasias (334) suggests immune receptor signalling studies produced within Jurkat cell lines provide limited insight into physiologic signalling.

Within the scope of this work, observed co-stimulation differences in calcium indicator signal response times demonstrates that differences in TCR and CD28 ligand surface densities can influence immune receptor signalling integration. Physiologically, antigen presentation mediated by MHCs lacks dominant composition from a single peptide as APCs commonly present different proteolytically processed self and non-self-proteins. Constitutive APC CD28 ligand expression suggests that CD28 ligation predominates interactions between T cells and APCs especially under circumstances with scarce APC presented pMHC agonists. The co-stimulation signalling studies presented here reinforce

insights from previous investigations suggesting an essential synergy between CD28 and TCR signalling, but importantly distinguish that relative ligand and receptor surface densities shape co-stimulation dynamics especially with larger relative concentrations in CD28 over pMHC ligands. Moreover, CD28 ligand composition on APC surfaces may mediate co-stimulation response differences shifting intracellular calcium flux speed, intensity, and duration. Differences in intracellular calcium signalling dynamics would influence both TCR complex and CD28 signalling by disrupting ionic cytoplasmic domain interactions with cell membranes (335, 336). Previous research gnomically profiling activated T cells suggested increased CD28 signalling sensitivity in memory T cells (337) highlighting that revealed calcium signalling dynamics investigated within this work likely shape memory T cell development although additional experiments into AP1 mediated transcriptional changes within devices would provide the most insight into potential co-stimulation differences between ligands given either observed signalling pattern could differentially regulate transcriptional changes.

4.4.2 CD28 Induced Cytoskeletal Changes and Potential Physiological Relevance

Another major consideration poorly investigated in other CD28 signalling investigations involves actin mediated cytoskeletal changes. During this work we observed dynamic CD28 receptor-ligand interactions stimulated actin cytoskeletal changes with evidence suggesting cells altered CD28 interactions as cells appeared polarized during thermal fluctuation measurements as they extended towards BFP probes featuring CD28 ligands ultimately appearing to rotate around the micropipette base. T cell morphological changes made BFP measurements difficult given mechanical receptor stimulation induced cytoskeletal changes influencing bond tensile force during both force clamp and thermal

fluctuation measurements. However, during thermal fluctuation measurements forces determined during bond lifetime measurements demonstrated forces that clearly distinguished themselves from potential signal drift with recognizable force transitions during dissociations.

Anecdotally, the T cells appeared to be actively searching for antigens upon CD28 receptor ligation as indicated by morphological changes, but it remained difficult to map BFP bond lifetime measurements with morphological changes especially when cells seemingly extended their pseudopodia to touch beads sometimes necessitating probe replacement. The observed cytoskeletal changes mapped well with reported cytoskeletal changes within the literature interestingly with one report investigating inducible costimulator engagement (ICOS) (338-340). Thermal fluctuation measurements presented a consistent CD28 stimulus allowing T cells to recognize the bead as a potential APC and direct morphological changes accordingly. Consequently, thermal fluctuation instrumentation offered a better platform for characterizing these observations. Observed force differences after 10 s total lifetime accumulation illustrated how CD28 ligand signalling alone could cause cytoskeletal changes that could accumulate forces on CD28 and potentially other mechanosensitive receptors such as the TCR with similar localization. Unfortunately, current BFP instrumentation measures normal forces on probes and this constraint impeded observing more complex relationships than pushing and pulling on CD28 bonds. Potentially BFP instrument software enhancements could enable measuring forces along additional dimensions capturing probe rotations induced by morphological changes with similar temporal and spatial accuracy. Additional instrumentation enhancements could capture morphological changes and correlate such changes with bond

lifetime measurements. Such improvements would be essential when conducting co-stimulation BFP measurements given morphological changes observed experimentally with anti-CD3 beads (Figure 15Figure 16D).

It is important to consider how interaction kinetics between CD28 and its ligands might contribute to unique signalling observations. Within raw thermal fluctuation data, many binding and unbinding events could occur before measured bond lifetime suggesting that dynamic bond formation and dissociation plays a physiologic role in propagating CD28 signalling potentially shaping feedback mechanisms in immune receptor signal integration. Constraining CD28 receptors with immobilized antibodies could prevent recognizing these distinct dynamic changes mediated by CD28 ligands especially when CD28 receptor-ligand kinetics differ so substantially from commonly used monoclonal signalling antibodies. This consideration in addition to low level CD28 expression on naïve T cells likely prevented previous researchers from recognizing CD28 mechanosensitivity in experiments involving altering surface stiffness (6).

A potential explanation for why T cell CD28 ligand stimulation might differentially modulate actin cytoskeleton lies in the dynamic process underlying T cell migration through lymph nodes where APC stimulation shapes T cell activation and fate. CD28 ligand induced polarization would initiate more surface contact between T cells and APCs while concurrently directing future APC-T cell contacts a sufficient antigen search. Anti-CD3 beads effectively induced uropod formation while CD28 stimulation with CD80 directed cell extension towards pseudopodia (Figure 15C-D). This dynamic cytoskeletal process could explain how T cells overcome stronger adhesions formed between APCs and T cells while migrating through lymph nodes. This work's findings correlate with previous

T cell lymph node migration investigations characterizing T cell movement within lymph nodes (341).

4.4.3 Significance of Biophysical Measurements Given Previous In-Situ and SPR Measurements

An explanation for the diverse behaviours resulting from CD28 signalling comes from differential interactions with two its ligands, signalling integration with other receptors and scaffolds, and its cytosolic tail's capacity to bind many different kinases and adaptors necessitating conducting *in-situ* measurements on murine CD8+ T cell surfaces. Previous live-cell *in-situ* measurements using recombinant human CD28 and human CD80 CHO cells used the micropipette adhesion frequency assay (MAFA) to determine CD28 receptor-ligand 2D kinetics, but it remains difficult to contextualize those results given the primary work focused on PD-1 receptor-ligand interactions and thus lacked CD28 and CTLA-4 blocking controls (275). Furthermore, MAFA lacks the spatial and temporal resolution offered by BFP instrumentation making it difficult to interpret faster dissociation rates. During MAFA experiments keeping surface contact area consistent and accurately judging bond dissociation upon instrument retraction by eye introduce human bias especially during more rigorous testing at lower contact times (t_c < 0.5 s) and affinity interactions. Furthermore, this work extended BFP instrumentation towards characterizing near zero force (Figure 11) and force-dependent off-rates (Figure 12) associated with CD28 receptor-ligand interactions. In previous investigations rigorously defining TCR-pMHC dissociation rates required thermal fluctuation measurements (251) and this work further illustrated that thermal fluctuation measurements provided higher dissociation rate resolution especially for the higher CD28 and CD80 dissociation rate. Furthermore,

differences between this work's murine *in-situ* 2D kinetics measurements and human also correlated with previous published data showing greater 2D affinity in human PD-1-ligand interactions.

Distinguishing biophysical differences in CD28 receptor-ligand interactions in physiologically relevant circumstances remains essential for understanding receptor signalling. Unfortunately, SPR CD28 receptor-ligand measurements involved both freely dissociating and surface immobilized receptors or ligands preventing observing cell-dependent effects . This work validated previous SPR 2D kinetics findings that CD28-CD86 interactions display higher binding affinity (Figure 9 and Figure 10) (120, 121). However, thermal fluctuation measurements demonstrated CD28-CD80 bonds dissociate faster than CD28-CD86 bonds differing from previous SPR measurements (Figure 11). CD80 produced within this work resembled CD80 documented in previous SPR CD28-CD80 interaction measurements, so likely both studies involved monomeric CD80 interactions with dimeric CD28 (human CD28-Fc in SPR and previous *in-situ* measurements).

4.4.4 CD28 Valency Observed During Biophysical Measurements

BFP measurements suggested that CD28 displays a predominantly monovalent interaction with a bivalent CD28 dimer validating pervious structural analysis modelling differences between CD28 and CTLA-4 (121), although potentially also representing a small number of multimeric bonds. Varying CD80 and CD86 surface densities offered little support for an increased avidity between CD28 and dimeric CD80 upon cytosolic tail extension that would be initiated by applying tension on a CD28-CD80 bond (320).

Moreover, this lack of support aligned with similar published CD28-CD80 interaction experiments (342). A predominantly linear relationship between CD80 and CD86 ligand density and average bond number suggested ligand immobilization at surface densities surpassing SA molecular density did not influence observed 2D affinity (Figure 10). Bond survival analysis showed similar bond lifetime data between CD80 and CD86 presented by tetravalent or monovalent SA (Figure 13). Additionally, molecular stiffnesses calculated for CD28 ligands presented on either tetravalent or monovalent SA lacked statistically significant differences (Figure 14). This work's findings supported previous structural analysis findings suggesting steric hindrance prevents multimeric bonds. Moreover, this work contributed a perspective into CD28 interactions with monomeric ligands, a relevant topic given previously published work demonstrating effective CD28 monovalency regulated CD28 co-stimulation (253).

4.4.5 CD28 Mechanosensitivity and Its Potential Implications

This work's bond lifetime under force data suggested CD28 receptor interactions with monomeric CD80 and CD86 display different force-dependent kinetics, but both CD80 and CD86 form molecular catches with CD28 on CD8+ T cell surfaces (Figure 12). Other research groups published conflicting results regarding CD28 mechanosensitivity. One study investigated CD28 mechanosensitivity using antibodies against CD3 and CD28 immobilized within materials with alterable stiffnesses and showed increased stiffness enhanced traction force (6). Another study into CD28 mechanosensitivity suggested CD28 did not contribute to TCR mechanosensing because surfaces featuring anti-CD3 and anti-CD28 did not enhance surface spreading (315). Additionally, using antibodies on force pillars arrays to engage CD28 and TCR demonstrated higher traction forces compared with

force pillar arrays with antibodies against CD3 and CD28 alone (7). Unfortunately, these studies lack immunologic context for CD28 given endogenous CD28 engagement does not involve antibodies but does offer evidence that downstream signalling mediates significant forces that could influence interactions at T cell and APC interfaces. Specifically, this work focused on investigating if CD28 receptor-ligand interactions displayed mechanosensitivity.

The tremendous amount of research work investigating functional outcomes from CD28 signalling mediating important actin cytoskeletal changes that influence T cell activation provided considerable support for investigating CD28 mechanosensitivity (150, 343). Moreover, CD28 exhibits multiple mechanisms that influence actin cytoskeletal changes with Vav1 overlapping with both TCR and LFA-1 (344), but more importantly occurring outside a co-stimulatory context (150). Single molecule level measurements suggested CD28 exhibits mechanosensitivity at the molecular level. Interestingly, within this work anti-CD28 mediated cell spreading independent of antibodies against CD3 or TCR and CD28 engagement induced force on CD28 receptor-ligand interactions conflicting with previous mechanosensitivity investigations (Figure 16). Differences in methodology, immobilization strategies, and cell handling could account for the observed differences between this work and previous studies.

CD28 mechanosensitivity potentially enables mechanosensing through CD28 receptor-ligand interactions. Current evidence within this work did not strongly support CD28 mechanosensing. MTP experiments inconclusively showed a statistically significant tension on CD28 receptor-ligand bonds. Showing a statistically significant tension on CD28-CD86 bonds required more statistical power than previous experiments that failed

to demonstrate a similar effect. Interestingly, CD28 receptor ligation with anti-CD28 produced a statistically significant tension signal suggesting that MTP experiments lacked sensitivity for measurements involving low receptor expression and fast receptor-ligand dissociation kinetics. Additional MTP experiments using a locking DNA strand and cells with higher CD28 expression (thymocytes) could potentially offer MTP measurements overcoming current MTP measurement limitations (345). MTP results acquired with the locking DNA and thymocytes strand might resemble thermal fluctuation pulling findings where with lifetime accumulation T cells pulled more on CD80 than CD86 bonds despite lower observed lifetime.

Demonstrating the integration of mechanical information through mechanosensing within this work remained a major goal throughout experiments. Differential CD28 mechanical information integration through CD28 ligands could explain the diverse downstream signalling consequences surrounding co-stimulation. CD28 dimer ligation causes cytoplasmic domain release from the plasma membrane mediated by basic residues (BRS) that associate with Lck causing CD28 phosphorylation and stabilize CD28's signalling complex (346). Currently, force clamp and thermal fluctuation bond lifetime measurements provided the most compelling evidence for mechanical information integration necessitating additional investigations focused on CD28 mechanosensing. Given CD28 ligation did not robustly induce calcium indicator signal, integrating actin cytoskeleton visualization concurrently with BFP instrumentation potentially could reveal if cells differentially modulate actin cytoskeleton in response to CD28 mechanical stimulation. Moreover, monovalent interactions might dynamically engage dimeric CD28

through both receptor binding domains correlating with previous investigations into the Lck driven signalling mechanisms that required specifically CD28 dimers (346).

Hypothetically, CD28 could provide information about the APC it is interacting with through mechanosensing mechanisms that mediate differential actin cytoskeletal changes. Actin cytoskeletal changes might effectively place forces on TCR-pMHC bonds enahcing TCR specificity and sensitivity. Previous research investigating expression dynamics revealed that on B cells, Ig receptor engagement would drive rapid CD86 induction on the cell surface (347). Conversely, LPS or anti-IgD-dextran induced both CD80 and CD86 expression although CD80 expression remained significantly less than CD86 (130). Given these dynamic processes regulating CD80 and CD86 expression on APCs, many theorized that CD86 more potently activated T cells than CD80. Kinetic differences between CD28 and CTLA-4 for the same ligands convinced researchers CD86 more naturally stimulated CD28. APCs often express both ligands at varying relative surface densities suggesting additional mechanosensing investigations varying relative ligand surface densities could elucidate how differential ligand mechanosensitivity could impact the overall integrated mechanical signal.

4.4.6 Conclusion

Collectively, the findings within this work provide a foundation for additional mechanistic studies into CD28 and its immunological relevance. Receptor-ligand interaction 2D kinetics and force-dependent lifetimes clearly distinguish CD28 ligands with potential consequences shaping actin cytoskeletal and co-stimulation calcium signalling dynamics. The findings presented require more thorough experimental

validation but correlate well with previous investigations into TCR dependent and independent CD28 signalling. Mechanistically, its well appreciated that CD28 signalling profoundly influences immunity, but few investigations probed into differences between CD28 ligands and how those differences could influence key mechanisms shaping antigen specific immune responses. This work's single molecule and cell methodologies provided sensitivity and specificity lacking in other CD28 signalling investigations. Additional experiments perturbing Lck and actin cytoskeletal dynamics could provide more insight into differences between CD28 signalling induced by either CD80 or CD86. Improving BFP instrumentation could enable additional insights by mapping specific binding events with downstream receptor signalling events.

Molecular catches likely occur in other Ig superfamily (IgSF) receptors on T cells. Collectively, IgSF superfamily receptors could integrate information through mechanosensing towards diverse signalling outcomes. Previous work from our group showed this integration influenced thymocyte negative selection where Lck dependent dynamic catch bonds resulted from CD8 and TCR trimolecular bonds (232). Given similarities between IgSF family members, lateral interactions could exist between CD28 and other IgSF family members especially given Lck interacts with CD28 through both SH2 and SH3 domains. Researching crosstalk and lateral interactions between IgSF family members should elucidate key mechanistic processes governing immune receptor signal integration and how those processes could differentially influence T cell activation and fate.

Utilizing the insights within this work could potentially enhance clinical immunosuppression and immunotherapy. In a cell therapy context, differentially

modulating CD28 signalling and thus T cell stimulation strength prior to administering *in-vitro* treated T cells could shape T cell fates. Optimally controlling the relative amounts of memory and effector T cells could enhance cancer elimination effectiveness and decrease therapeutic complications. Additionally, insights within this work could provide a foundation for evaluating ICB and immunosuppression. ICB primarily functions by enhancing CD28 co-stimulation by blocking inhibitory receptors such as PD-1 and CTLA-4. CTLA-4-Ig/Fc chimeric proteins block CD28 co-stimulation through competitive inhibition. Hypothetically, T cells acquired from patients undergoing ICB or CTLA-4-Ig/Fc immunosuppression could differentially respond to CD28 ligation and co-stimulation. Quantifying differences in T cell morphological changes, CD28 mechanosensing, and intracellular calcium fluctuations could elucidate T cell CD28 responsiveness. CD28 signalling responsiveness could direct therapy decision making therapies more personalized for patient needs and hopefully avoiding devastating therapeutic complications.

CHAPTER 5. COMPARING TCR BIOPHYSICS ON DIFFERENT T CELL SUBTYPES ISOLATED FROM SPLEEN AND LIVER

5.1 Introduction

Immunity requires a coordinated effort among immune cells both innate and adaptive. T cells must respond differently to self and non-self-antigens. T cells must also use information about past exposures to prevent infections or respond more effectively against threats. As the largest lymphatic organ in the body, the spleen plays a crucial role in filtering and presenting pathogens and abnormal cells. Downstream the splenic vein lies the hepatic portal vein, a large vein also receiving venous blood from mesenteric and gastric veins and supplying the liver. Despite their proximity, T cells within the spleen and liver receive different immunological cues. Livers contain unique APCs known to promote tolerance, but also must facilitate immune reactivity against pathogens and abnormal cells. Moreover, the immune system also balances its capacity to eliminate threats immediately and enhance future immune responses. Given different immunological cues T cells receive in the spleen and liver, this work examined how these cues influence TCR biophysics among different CD8+ T cell subtypes. The experiments featured within this work reflect a collaboration between Dr. Cheng Zhu's and Dr. Arash Grakoui's laboratories towards providing additional perspectives into viral immune responses and how T cell presence within the spleen or liver influences T cell function. Clinically, hepatitis immune responses within the liver shape can result in acute or chronic disease with chronic disease potentially resulting in end-stage liver disease. The insights from this work suggested differences in TCR biophysics distinguish CD8+ T cells from both spleen and liver. Moreover,

modulating TCR biophysics might influence T cell memory development by shaping stimulation strength and impacting T cell homeostasis. Collectively, these insights inform vaccine and immunotherapy development suggesting modulating T cell response strength can influence immunity through shaping CD8+ T cell memory and effector function development. Influencing hepatitis immunity specifically could prevent liver fibrosis and cirrhosis, chronic liver disease sequela.

5.1.1 Significance of Investigating T Cell Subsets

T cells comprise many different subsets (65). Moreover, T cells also reside within different tissues where they must respond to differentially presented antigen and cytokine environments (19). Cell diversity shapes immunity by enabling T cells to function differentially based on information integrated by APCs (348). Diversity within T cells occurs by two major axes related to memory and polarization (85, 349, 350). After antigen exposure, T cells develop within a spectrum of functional and self-renewal capacity. Memory T cells exhibit more stem-like properties while effector T cells more readily perform T cell functions (85). T cell polarization refers to T cells adopting differential functionality usually related to cytokine expression profiles shaped by transcription factors (349). In the context of CD8+ T cells, the prototypical CD8+ T cell functions to cytotoxically destroy cells displaying specific antigens (350). Differential proliferation and functional capacity among CD8+ T cells enable the immune system to effectively clear cells displaying abnormal antigens, but also mount future responses more readily if the same abnormal antigen presents itself again (85).

Differential proliferation and function characterize a spectrum of T cells ranging from memory to effector phenotypes. Memory T cells originate from a small population of antigen experienced T cells surviving the T cell contraction phase that undergo differentiation enabling them to form a faster and stronger secondary immune response. Two major memory T cell populations include effector memory and central memory distinguished by their CD127 and KLRG1 expression. Higher KLRG1 or CD127 expression denotes more effector or memory like functionality among memory T cells (85, 351). This work examined TCR biophysics in CD8+ T cells acquired from spleen and liver.

Given their importance in secondary immune responses, many questions remain about how memory T cells mechanistically arise after antigen exposure and how their subpopulations shape secondary responses. Several models seek to characterize memory T cell development after antigen exposure. One theory describes memory T cell development originating from differential antigen stimulation duration and intensity possibly arising from differential APC stimulatory conditions shaped by antigen presentation, cytokines, and co-stimulatory ligands. Another model suggests that effector T cells adopt differential states based on a cumulative history of similar signals encountered during an infection (351). Most recently, single T cell fate mapping and *in-vivo* cell cycle analysis towards revealing early proliferative differences among T cells shaped by antigenic and inflammatory stimuli during clonal expansion. Notably central memory precursors retained more proliferative sensitivity dependent on antigen exposure rather than the inflammatory signals that shaped effector cell proliferation (352). Insights within this work provide additional perspectives into naïve, memory, and effector T cell biology

through TCR biophysical measurements using T cells acquired from organs with distinct immunological cues.

5.1.2 Immunologic Motivation for Investigating Spleen and Liver

As the largest lymphatic organ within the body the spleen functions to filter blood pathogens and abnormal cells. Anatomically spleens contain both red and white pulp. Within red pulp an open circulatory system and mechanical filtration enables abnormal cell (primarily RBCs) phagocytosis by macrophages. Humoral and cell-mediated immunity occurs within white pulp that resemble lymph nodes. Collectively, the red and white pulp work together immunologically to mount immune responses to hematogenous pathogens and abnormal cells. Asplenia, splenic function loss, enhances patient susceptibility to encapsulated bacteria through a lack of IgM memory B cells (353). During homeostasis APCs within the spleen clear debris including apoptotic cells enabling splenic self-antigen tolerance induction. Upon infection or host damage pattern recognition receptors (PRR) on myeloid cells induce T cell activation signals on APCs, cytokine secretion, and pathogen clearance. T and B lymphocytes within the spleen segregate into different anatomic regions based upon chemokine signals. T and B lymphocyte anatomic segregation shapes humoral and cell-mediated immunity development (354). CD8+ memory and effector T cell subsets localize within the red pulp and white pulp's T cell zone, respectively (355). The spleen's pivotal role in pathogen responses necessitates additional investigations into factors that shape T cell antigen recognition within the spleen as well as correlations with T cell memory and effector function.

The liver's metabolic functions within the body necessitate receiving 25% resting cardiac output blood with most of the blood supplied by the hepatic portal vein (70-75%). The hepatic portal vein circulation stems from a collection of gastric and mesenteric veins providing digested nutrients and toxins. The liver also receives many antigens from the gastrointestinal tract necessitating a tolerogenic and hyporesponsive environment to prevent immune activation against oral and self-antigens. The gut contains different microorganisms and their composition impacts intestinal inflammation, a process associated with liver disease (356). Portal shunting can reverse oral antigen hyporesponsiveness while antigen injection into the hepatic portal vein induces tolerance (357-359), T cell cytotoxic responses enable pathogen clearance. Hepatitis viruses primarily infect hepatocytes with different subtypes correlated with infection chronicity and end-stage organ disease. Given the presence of many gastrointestinal pathogens and viral hepatitis infections, immunologically T cells must also respond and eliminate hepatic infections to prevent hepatic disease. Understanding CD8+ T cell antigen recognition within the liver could provide insights into how hepatitis infections escape immunity and how modulating antigen responsiveness within the liver could enhance immunity against pathogens.

Responding against intracellular pathogens requires CD8+ T cell cytotoxicity. Depleting CD8+ T cells in hepatitis B infected chimpanzees causes viremia resurgence (360). Cytotoxic CD8+ T cell activation leads to clonal expansion and antigen responsiveness, but a robust infection response requires memory and effector function development, a process shaped by interactions between CD8+ T cells and other immune cells. CD4+ T cells can influence CD8+ T cell memory and effector function development

through cytokine secretion and licensing APCs. Licencing refers to a rare sequential interaction between antigen-specific CD4+ T cells and then subsequently antigen-specific CD8+ T cells with APCs (356). DCs within spleens and livers express both MHC class I and class II molecules enabling the potential for licensing to occur in both organs. Examining T cell subsets before and after a resolved infection provides perspective into how immunological processes such as differential cytokine expression and licencing influence T cell function and immunity.

Given their proximity and shared circulation, dynamic processes between spleen and liver immune cells likely influence each other. Moreover, differences between homeostatic antigen presentation spleen and liver favour different immune responses. Given their immunologic relevance to viral responses, this work focuses on CD8+ T cell subsets isolated from spleen and livers. Capturing information about CD8+ T cell antigen recognition before and after infections within the spleen and liver could provide perspectives into viral immunity. This work uses *in-situ* CD8+ T cell TCR biophysical measurements towards defining how differential TCR biophysics with the spleen and liver could regulate T cell responsiveness. The insights provided within this work address mechanistically how TCR biophysics could influence observed CD8+ T cell hyporesponsiveness within the liver with implications that impact effector and memory function development.

5.1.3 Motivation From Previous Anatomic Compartmentalization Investigations

Previous investigations involving a similar collaboration demonstrated splenic local cellular and cytokine environments influenced CD8+ T cell antigen affinity, function,

and cell fate (333). This past research into acute LCMV viral responses revealed uncoupling in TCR 2D effective affinity between CD8+ T cells in splenic red and white pulp anatomic compartments during the immune contraction phase. They observed increased effective 2D TCR affinity correlated with cytotoxicity and could be influenced by microenvironmental factors. They also demonstrated that memory precursors yielded lower effective 2D affinity than effector memory cells isolated from splenic red pulp. Moreover, adoptive transfer of CD8+ memory precursors T cells from red and white pulp yielded cells with differential gene expression and proliferative capacity (333).

5.1.4 Liver Induced T cell Tolerance, Hyporesponsiveness, and Apoptosis

The liver microenvironment provides a unique environment for immune cells generally associated with immunosuppression. Liver anatomy plays a role in shaping T cell immunity and antigen responses. The liver generally features activated CD4+ and CD8+ T cells localized near the portal track (361). Tolerance mechanisms in liver involve CD4+ T regulatory cell development and CD8+ T cell apoptosis (362). Among CD8+ T cells, naïve CD8+ T cells within the liver become activated and die potentially through passive or activation mediated mechanisms (363, 364). Investigations demonstrated that CD28 co-stimulation could prevent hepatocyte mediated activation and passive death (365). Antigen presentation within the liver can also be mediated by specialized macrophages called Kupffer cells as well as myeloid and lymphoid dendritic cells that induce tolerance within the liver (362, 366).

Researchers describe T cells from the liver as hyporesponsive referring to diminished responsiveness to antigens through TCR signalling. Researchers previously

found splenic and hepatic DCs produce proinflammatory cytokines or IL-10 in response to TLR4 stimulation, respectively. Additionally, CD4+ T cells demonstrated less allogenic proliferation and increased regulatory T cell development when stimulated by liver DCs (367). Similarly, activated hepatic stellate cells with enhanced PD-L1 expression supressed thymidine uptake, normal T cell proliferation, and enhance T cell apoptosis in TCR stimulated T cells (364). Recently, researchers demonstrated liver metastasis supressed activated CD8+ T cells from the systemic circulation that underwent apoptosis upon interacting with $FasL^{+}$ $CD11b^{+}F4/80^{+}$ positive monocyte-derived macrophages a process that reduced peripheral T cells numbers and decreased tumoral T cell diversity and function (368). Moreover, tissue resident memory CD8+ T cells promoted fibrosis resolution through hepatic stellate cell apoptosis in non-alcoholic steatohepatitis (NASH) (369).

This work focuses on TCR biophysical measurements on CD8+ T cells acquired from mouse spleen and liver towards examining how these *in-vivo* microenvironments impact TCR biophysics among different T cell subsets. Given how CD8+ T cell responses within the liver influence health and disease impacting both liver disease and extrahepatic disease resolution, understanding differences between CD8+ T cells in the liver and spleen could provide insights into how TCR biophysics influences hepatic T cell hyporesponsiveness and how those consequences shape viral responses.

5.1.5 Summary of Chapter Findings and Relevance

This work expands upon current knowledge about memory and effector T cell development with TCR biophysical measurements acquired from different T cell subtypes

in the spleen and liver. TCR biophysics impact T cell antigen recognition and processes that regulate TCR biophysics would shape immunological responses. Within the context of this work, TCR biophysics refers to 2D effective affinity and force-dependent dissociation kinetics. TCR-pMHC biophysical interaction measurements reflect lateral interactions between the TCR and other immunologic receptors and signalling machinery. Immunologic cues within anatomic compartments influence TCR biophysics (333) and could also influence TCR biophysics within the liver warranting an investigation.

Micropipette adhesion frequency assay (MAFA) and BFP experiments characterized CD8+ T cells within different subsets isolated from spleen and liver microenvironments before and after an acute LCMV infection (LCMV-armstrong). Spleen and liver microenvironments influenced CD8+ T cell 2D effective TCR affinity regardless of T cell subtype. Moreover, this work demonstrated central memory T cell TCR 2D effective affinity correlated with previous findings illustrating lower 2D effective TCR affinity in memory precursors than effector cells. TCR force-dependent off rate measurements also differed between naïve CD8+ T cells isolated from spleen and liver microenvironments with liver cells lacking a molecular catch. Furthermore, TCR interactions mediated molecular catch loss suggesting molecular catch loss might reflect cellular feedback to T cell stimulation. These findings illustrated the importance of characterizing both 2D kinetics and force-dependent off-rates when evaluating TCR biophysics and provided insights into hepatic viral immunity. Dysfunctional TCR-pMHC correlated with presumed CD8+ hepatic T cell hyporeactivity. TCR biophysics could reflect T cell responsiveness potential. Hepatic mediated CD8+ T cell death could enable liver activated T cells pruning during viral responses. CD8+ T cell pruning could provide selection pressure towards

memory T cell development where reduced 2D effective affinity might protect T cell responsiveness.

5.2 Background

5.2.1 Animal Infection Models in Immunologic Investigations

Animal models play an essential role in immunologic research providing insights into complex immune mechanisms resulting from communication between immune and non-immune cells. Unfortunately, cancer cell lines provide limited insights into immunologic cell functions given cancers demonstrate abnormal homeostatic functions allowing themselves to grow uncontrollably without appropriate cellular cues. Immunologic animal models comprise many different species ranging from zebrafish to non-human primates each with distinct advantages and disadvantages. Researchers generally accept that non-human primate models retain the most similarity with humans, but their inherent costs and procedural difficulty often encourage researchers to develop murine disease models.

This work employs a murine viral infection model involving P14 transgenic TCR mice. Transgenic animals models comprise genetically altered organisms produced for the purpose of studying health and disease. Transgenic TCR mice feature genetically altered TCR genes that enable researchers to influence T cell antigen responsiveness towards studying immunity. Murine transgenic TCR models demonstrate additional overlap with human immunity. Moreover, advanced transgenic humanized mouse models can enhance translatability (370-372). As an established viral immune model, the P14 transgenic model works well for studying complex processes shaping viral immunity but with limitations towards human translatability. Among inherent limitations include antigen presentation

involves unique MHC genes differing between organisms, organism anatomic differences, and the inability to reproduce complex environmental factors that influence human disease within animal models. Despite these limitations, transgenic murine TCR models still empower seminal immunologic insights eventually impacting patient care.

5.2.2 P14 Transgenic TCR Infection Model

P14 transgenic mice carry altered TCRA and TCRB genes resulting in transgenic TCR expression. P14 TCR specifically interacts with MHC class I ($H2\text{-}D^b$) presented glycoprotein 33 peptide residues 33-41 ($gp33_{33\text{-}41}$). The P14 transgenic TCR mice enable studying viral responses. P14 transgenic TCR mice can develop acute and chronic LCMV viral infections based on LCMV variants LCMV-armstrong and LCMV-clone 13, respectively (373, 374). P14 transgenic mice can also be RAG-1-deficient towards developing monoclonal TCR T cells (333). This work employed RAG-1 deficient P14 transgenic TCR mice and thus observed differences in TCR biophysics within this work stem from immunologic cues and not genetic differences.

5.2.3 Tumour Microenvironments Shape T Cell Function

T cells integrate information from signalling pathways towards coordinating their immunological functions. Defining microenvironmental characteristics include tissue extracellular matrix, vascular structures, the parenchymal cells mediating tissue function, stromal cells that provide structure within tissues, and tissue resident immune cells (375). Tumour microenvironments (TME) influence infiltrating T cells through many different mechanisms potentially resulting in T cell dysfunction that could prevent T cells from

effectively clearing tumours. T cell dysfunction induced by tumour microenvironments result from anergic, exhausted, and senescent T cells (376).

Immunosuppression within the TME results from the interactions between tumour and immune cells. Immune cells in the TME can secrete immunomodulatory cytokines that influence infiltrating T cells. Specialized APCs found within the TME include tumour associated macrophages (TAM) and myeloid-derived suppressor cells (MDSC). TAMs and MDSCs secrete anti-inflammatory cytokines such as IL-6, IL-10, and TGF-β. TAMs, MDSCs, and tumour cells can also express co-inhibitory ligands that supress infiltrating T cell proliferation and function. Tregs can also exist within the TME differentiated externally and internally within the TME (377). Mounting evidence about how TMEs influence immunity encourages research into how other microenvironments influence immune cells. Its possible microenvironmental influences within the liver overlap with the TME given both microenvironments promote immunosuppression and tolerance.

5.2.4 Exhausted T Cells

T cell exhaustion describes T cell function resulting from chronic antigen stimulation, a process that occurs during viral infections and cancer. Exhausted T cells lose their functional characteristics becoming unable to proliferate and produce inflammatory cytokines. Exhausted CD8+ T start by losing IL-2 and TNF-α production capacity, can then exhibit impaired cytotoxicity, and finally during terminal exhaustion lose IFN-γ production (378). CD8+ T cell exhaustion correlates with high viral loads occurring during an infection (379). Exhausted T cells express high levels of co-inhibitory receptors such as CTLA-4 and PD-1 that shape T cell function (380). Exhausted T cells cannot recover

and differentiate into memory CD8+ T cells and do not persist without antigen in mice (381). Given chronic antigen stimulation involves TCR signalling, TCR biophysics could relate to T cell antigen responsiveness and T cell exhaustion.

5.2.5 Relationships Between TCR Biophysics and Function

TCR-pMHC interactions mediates signalling through the TCR complex. Biophysical parameters such as affinity and half-life influence TCR complex signalling by shaping the nature of TCR ligation. Biophysical instruments that can measure TCR-pMHC interactions include SPR, FRAP, FRET, MAFA, and BFP. Based on the instrumentation system used to conduct biophysical measurements, measurements could 2D or 3D and mechanical or fluorescent (382). Interpreting 2D kinetic measurements offers broader affinity and on-rate values while interpreting the TCR-pMHC interactions. 2D affinity values strongly correlate with functional data generated using the same TCR-pMHC interactions while demonstrating a weaker relationship with off-rate. Comparing correlations between function and off-rates between 2D and 3D methods, 3D off-rates present an inverse correlation (382).

Previous TCR biophysics studies related TCR-pMHC interactions with T cell function. The OT1 transgenic mouse features inserts for TCRA-V2 and TCRB-V5 genes into a C57BL-6 background mouse. The resulting transgenic TCR receptor specifically interacts with MHC class I (H2-K^b) presented ovalbumin peptide residues 257-264 ($OVA_{257-264}$) (383, 384). Within the well-characterized OT1 transgenic TCR system, several pMHCs within the system exist in a spectrum between antagonist and agonist by varying amino acid residues within the $OVA_{257-264}$ sequence. OT1 associated H2-K^b

molecules include the original $OVA^{257-264}$ peptide sequence (OVA) and variants from this sequence described as agonists (G4, and A2 from lowest to highest) as well as the antagonists (V-OVA, R4 and E1) (384-386). Correlating 2D affinity and off rate between antagonists and agonists reveal among OVA pMHC variants display more agonism and less antagonism with increased 2D affinity and on-rate. Additionally, OVA pMHC variants with higher off rates demonstrate higher agonism than antagonism (251). Effective 2D affinity measurements within this work likely correlate with TCR agonism and antagonism.

5.2.6 Relationships Between TCR Mechanosensing and Function

Mechanosensitive TCRs form force-dependent catch bonds with pMHC demonstrating an optimal force that stabilizes interactions between TCR and pMHC effectively increasing the off-rate. Comparing agonists and antagonists using transgenic 2C human TCR demonstrate agonists form catch bonds while antagonists form slip bonds (9). Similarly, OVA agonists also produce catch bonds (235). The CD4+ 3.L2 TCR system specific for peptides presented by MHC class II also demonstrate the same catch bond relationship between agonists and antagonists (230). Force on TCR-pMHC bonds resulting in bond lifetime accumulation through catch bonds trigger calcium flux related to downstream TCR signalling (235). Dynamic catch bonds formed between trimolecular TCR-CD8-pMHC complexes regulate thymic negative selection through a mechanotransductive loop (9). Force-dependent dissociation kinetic investigations within this work could provide perspective into TCR-mediated antigen reactivity through observed molecular catch and slip bonds.

5.3 Experimental Data

5.3.1 Micropipette Adhesion Frequency Assay (MAFA) and Biomembrane Force Probe (BFP) Experimental Systems

Characterizing TCR biophysics on live cells required biophysical instrumentation setups specialized for *in-situ* measurements. Given our focus on viral immunity and previous work, all experiments involved RAG-1 deficient P14 transgenic TCR mice. The micropipette adhesion frequency assay enabled *in-situ* 2D effective affinity measurements. The BFP offered a live cell DFS instrument for bond lifetime measurements defining force-dependent dissociation kinetics. All experiments involved P14 transgenic TCR on CD8+ T cell surfaces and a CD8+ binding ablated gp33 (gp33mt) as shown in Figure 20. All experiments involved collaboration with Dr. Arash Grakoui's laboratory where Dr. Fengzhi Jin performed cell isolations and flow cytometric characterization enabling the biophysical measurements contained within this work.

Naïve CD8+ T cell isolated involved mechanically digesting mouse spleens and livers after portal vein perfusion and purifying cells using a naïve CD8+ T cell negative selection isolation kit. Experiments on central and effector memory cells required CD8+ T cell isolation kit using negative selection with subsequent fluorescence activated cell sorting (FACS). Central and effector memory population selection utilized differences in CD127 and KLRG1 expression. For MAFA experiments, biotinylated RBCs could be utilized towards presenting immobilized biotinylated gp33mt through surface immobilized SA. In BFP experiments, biotinylated RBCs treated with nystatin to enhance their stiffness enabled affixing SA coated glass beads that feature immobilized gp33mt ligands resulting

in an RBC-based force transducer. Experiments involved using micropipettes to assemble cell-cell or cell-bead pairs to probe TCR and pMHC interactions.

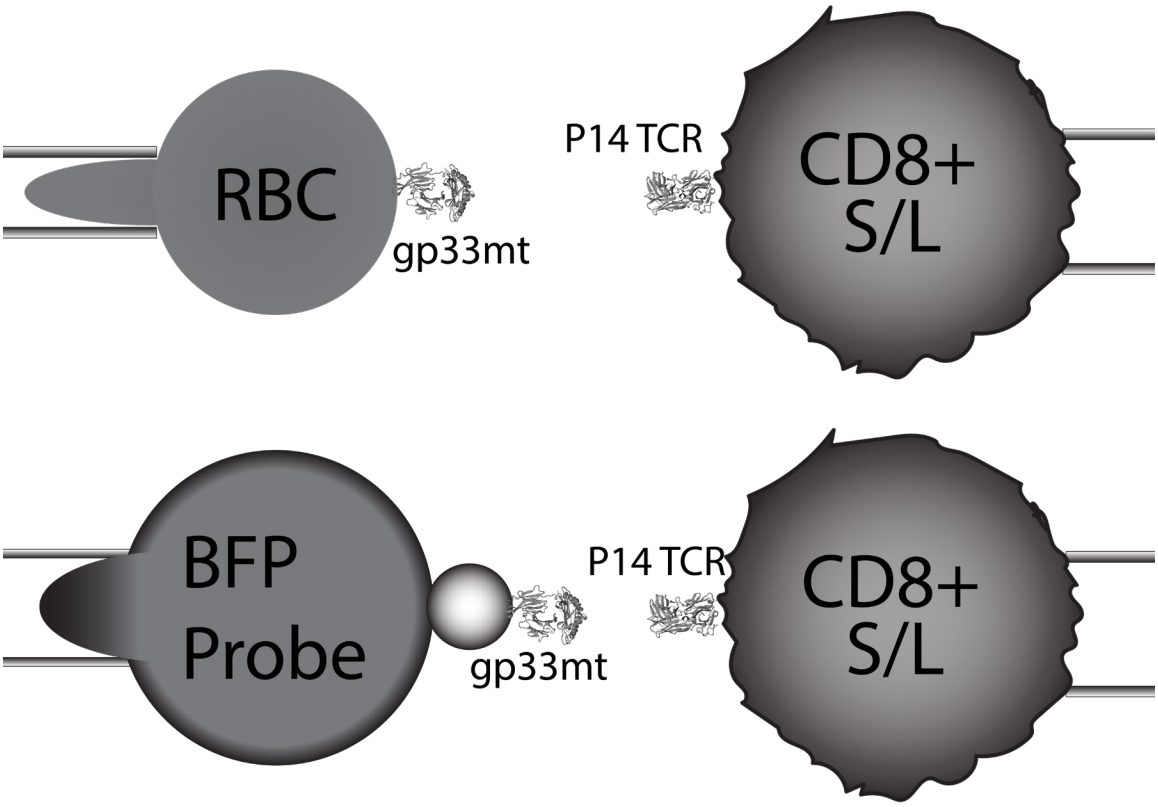

Figure 19 - Biophysical Instrumentation Systems Used in P14 Experiments. Experiments employed two different biophysical instrumentation setups. The micropipette adhesion frequency assay (MAFA) enabled resolving 2D effective affinities between P14 CD8+ T cell surface TCRs and gp33 unable to bind CD8 (gp33mt) (top). Biomembrane force probe (BFP) instrumentation quantified relationships between bond lifetime and force for the same P14 TCR and gp33mt (bottom). BFP experiments utilized SA coated beads featuring immobilized gp33mt ligands (bottom) while MAFA experiments immobilized gp33mt ligands on biotinylated RBC surfaces with SA.

5.3.2 P14 CD8+ Naïve T cells Isolated from Spleen and Liver Demonstrate Different 2D Effective Affinity

MAFA experiments characterized TCR 2D effective affinity differences between spleen and liver CD8+ T cell subsets. Preliminary experiments involved naïve CD8+ T cells. Focusing on the spleen and liver CD8+ T cells extended previous insights demonstrating TCR 2D effective affinity differences between red and white pulp CD8+ T cells (333) that captured the influence of distinct immunologic cues that shape immune responses in health and disease. Although MAFA experiments could resolve 2D kinetics by determining adhesion frequency at varying contact times, 2D effective affinity measurements enabled characterizing differences between CD8+ T cell populations with greater statistical power. Initial measurements focused on comparing spleen and liver naïve CD8+ T cell 2D effective affinity. Naïve CD8+ T cell measurements provided a strong baseline for demonstrating TCR 2D effective affinity differences between central and effector memory T cells. Using similar isolation steps involving an initial Percoll density separation ensured observed differences occurred irrespective of cell handling.

Pairing splenic and hepatic T cells together involved conducting adhesion frequency measurements with the same ligand coated RBC. Adhesion frequency measurements involved 50 contact cycles using a saturating contact time (2s). Flow cytometry quantified receptor and ligand surface densities by extrapolating molecular density from PE calibration bead. Flow cytometry staining required saturating PE conjugated antibodies against TCR and H2-D^b (Section 3.5). Calculating 2D effective affinity used a previously published mathematical model employing Equation 2 and Equation 4 (Section 3.6).

Flow cytometry provided by Dr. Fengzhi Jin revealed consistently lower TCR expression on CD8+ T cells from the liver compared the spleen. A representative flow cytometry from an experiment comparing naïve CD8+ T cells isolated from the liver

displayed around half as strong fluorescence in TCR staining for CD8+ T cells (Figure 21A) suggesting a substantial difference TCR expression. Exploring potential activation using the cell activation marker CD44 showed slightly higher CD44 expression in CD8+ T cells from the liver, but not a substantial difference (Figure 21A). CD8+ T cells from liver produced similar adhesion frequencies (data not shown) between spleen and liver, but 2D effective affinity calculations unexpectedly demonstrated statistically higher 2D effective affinity in naïve CD8+ T cells from liver compared to spleen using a paired two-sided t test on pooled data from five experiments (Figure 21B).

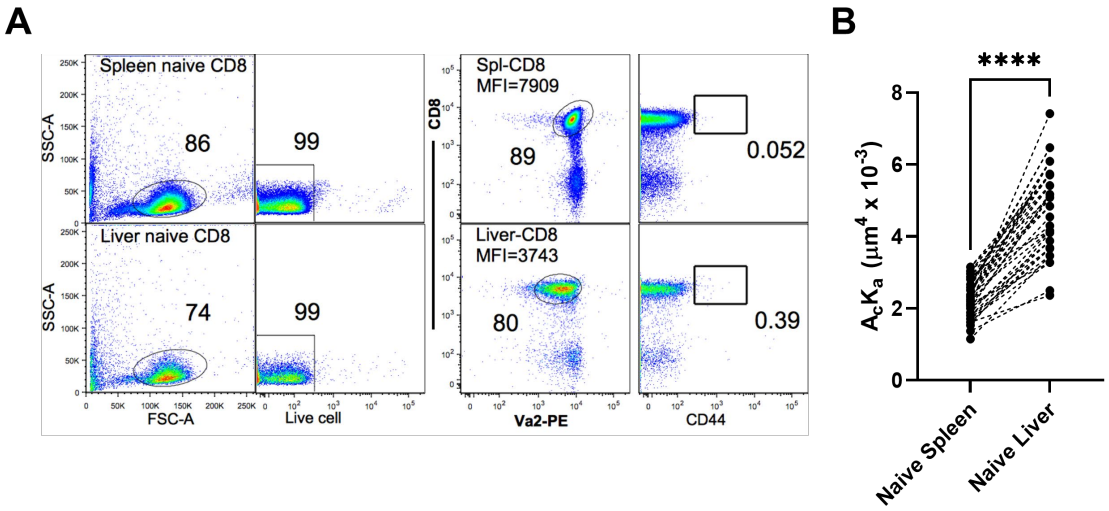

Figure 20 - Naive CD8+ T cells From Liver Show Higher 2D Effective Affinity. Isolating CD8+ naïve T cells from P14 mouse spleens and livers using similar processes ensured effective 2D effective affinity comparison between spleen and liver CD8+ T cells. Flow cytometry characterized naïve CD8+ T cells isolated from spleens and livers as well as determined TCR surface density. Panel A featured representative flow cytometry from an experiment. CD8+ T cells isolated from spleen expressed higher TCR levels suggesting naïve CD8+ T cells underwent antigen-independent activation (right middle A). Antigen independent activation did not result in substantial T cell activation marker CD44 expression (right most A). Pooling 2D effective affinity measurements from five pairing experiments allowed statistical comparisons using a paired two-sided t test. A plot representing

all the naïve CD8+ T cell paired comparisons between spleen and liver shows consistently higher values in liver cells (B). Each symbol represents a single cell-cell pair (n=37). Statistical comparison symbols featured on graph included: ** ($p < 0.0001$).**

5.3.3 Naïve CD8+ T cells Reveal Altered Mechanosensing Through Bond Lifetime Measurements

Unexpected differences between 2D effective affinity measurements in naïve CD8+ T cells isolated from spleen and liver inspired exploring potential differences in force-dependent dissociation kinetics using bond lifetime under force measurements. Bond lifetime under force measurements allowed identifying molecular catch or slip bond relationships. Identifying molecular catch and slip relationships allowed characterizing receptor mechanosensitivity with previous publications associating molecular catches and slips with TCR agonism and antagonism, respectively.

Bond lifetime measurements using the BFP in a force clamping mode targeted an adhesion frequency around 20% to prevent contributions from multiple bonds. For each lifetime signal, bond lifetime measurement reflects the time between peak force and clear bond dissociation. Naïve CD8+ T cells isolated from spleen and liver presented P14 TCR to gp33mt coated probes. Organizing bond lifetimes into force bins enabled visualizing relationships between bond lifetime and force (Figure 22A). Comparing naïve CD8+ T cells from spleen and liver revealed differences between the two groups at forces below 15 pN. For naïve CD8+ T cells from the spleen, analysis showed an increase in bond lifetime under force until a force bin between 6-12pN with proceeding decreasing bond lifetime trend. This relationship between bond lifetime and force matched other TCR data acquired from splenic naïve CD8+ T cells published by our lab (235). Naïve CD8+ T cells from the

liver demonstrated a continuously decreasing bond lifetime under progressive force. Bond survival analysis using the force bin with the greatest difference between naïve CD8+ T cells from spleen and liver illustrated the profound force-dependent kinetic differences (Figure 22B). Our survival analysis highlighted clear differences between naïve CD8+ T cells from spleen and liver in both the fast dissociation phase (initial linear trend between bond survival and lifetime) and the slower dissociation phase (later linear trend featuring a less step descent).

Validating insights from force-binned bond lifetime curves required kernel regression on the same bond lifetime data obtained for both naïve CD8+ T cells from spleen (Figure 22C) and liver (Figure 22D). A scatter plot for all bond lifetime under force measurements with bond lifetimes distributed into an ascending phase (red circles) and descending phase (blue squares) allowed visualizing kernel regression effectiveness (black line). The spleen experimental group demonstrated a kernel regression peak around 8.29 pN with a lifetime value around 0.322s. The liver kernel regression revealed a decreasing relationship between bond lifetime and force among regions with reasonable measurement density.

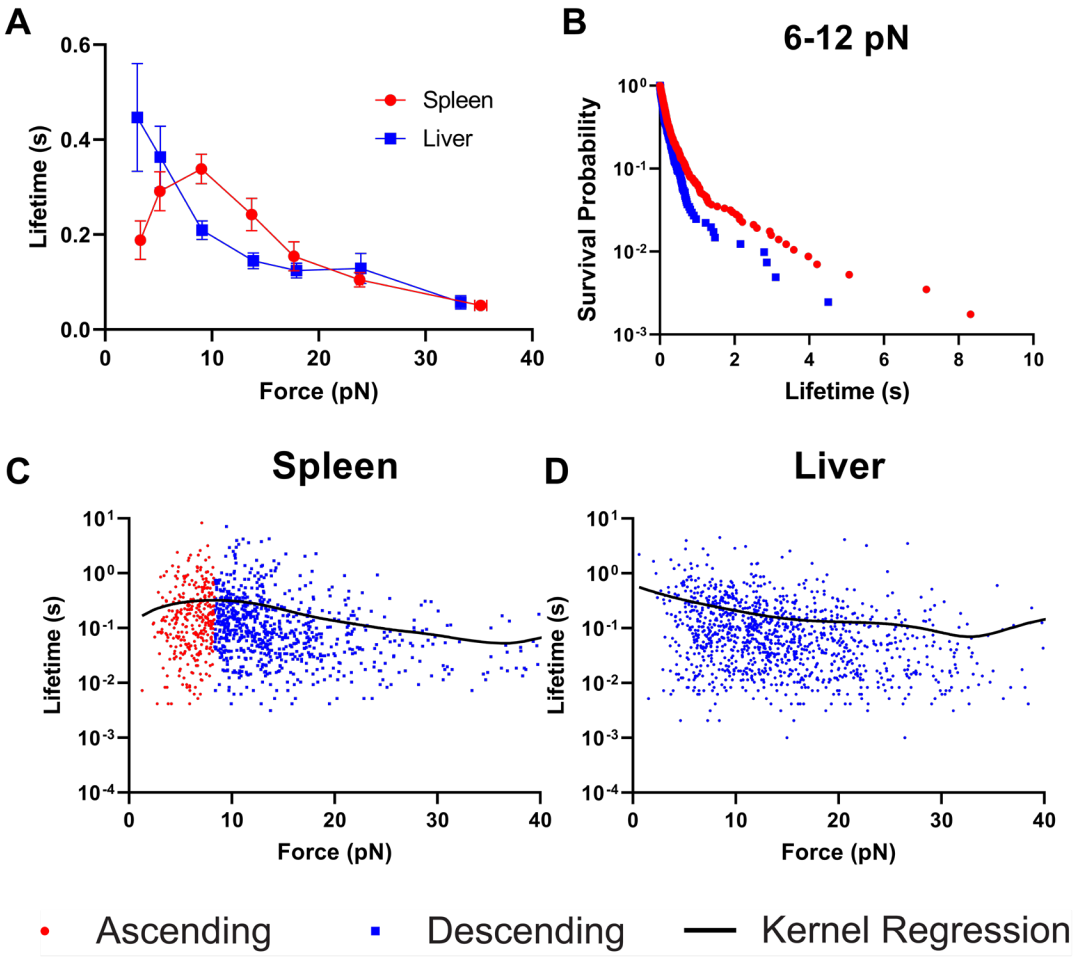

Figure 21 - Bond Lifetime Comparison Between Naïve CD8+ T Cells From Spleen and Liver Reveal Altered Mechanosensing. BFP bond lifetime under force measurements enabled characterizing differences between naïve CD8 T cell TCR mechanosensitivity. Organizing bond lifetime under force data into force bins reflected relationship between force and lifetime (A). Naïve CD8+ T cells from the spleen displayed an increased lifetime under force until a moderate force while naïve CD8+ T cells from the liver showed decreased lifetime under force. Using a bond survival analysis with 6-12 pN force bin data also illustrated force-dependent off rate differences between spleen and liver (B). Survival analysis revealed an early divergence between the spleen (n=571) and liver (n=406) experimental groups suggesting different dissociation rates. Kernel regression created another representation of the bond lifetime under force for both naïve CD8+ T cells from the spleen (C) and liver (D). Kernel regressions for both experimental groups reflected the same relationships demonstrated by force bins. Dividing the ascending (red circles) and descending (blue squares) phases based on peak detection from the kernel regression model (black line) visualized differences between molecular catch and slip trends. Lifetimes in the spleen's model peaked at 0.322s at 8.29 pN.

Lifetimes in the liver's model did not peak. Each symbol corresponded with a single bond lifetime measurement for spleen (n=1126) and liver (n=1187).

5.3.4 Splenic Naïve CD8+ T cells Display TCR Contact Dependent Changes in Bond Lifetime

The differences in bond lifetime under force measurements between naïve CD8+ T cells motivated us to consider if some TCR ligation related changes could produce a similar bond lifetime under force findings as found in hepatic cells. TCR ligation induced signalling could potentially regulate feedback mechanisms within the cell involving Lck signalling with changes in TCR mechanosensitivity corresponding with T cell activation. Relating TCR ligation with changes in mechanosentivity offered support that non-antigen dependent hepatic T cell activation dysregulated an important feedback mechanism involved in antigen-dependent responses.

Splitting lifetime measurements conducted before and after 100 full contact cycles enabled kernel regressions that described bond lifetime under force relationships. Kernel regression analysis revealed differences between the first and last 100 full contact cycles in spleen. Spleen CD8+ T cell bond lifetimes before 100 full contact cycles increased in bond lifetime under force before reaching a similar, but higher peak (0.374s and 7.84 pN) (Figure 23A) as the combined data set featured in Figure 22. In comparison, the spleen group after the first 100 contact cycles only showed a decreasing bond lifetime under force (Figure 23B). Moreover, the liver naïve CD8+ T cells displayed decreasing trends for bond lifetime under force whether the lifetimes came from before or after 100 full contact cycles (Figure 23C-D) illustrating the significance of the before and after contributions to the pooled data set (Figure 22C).

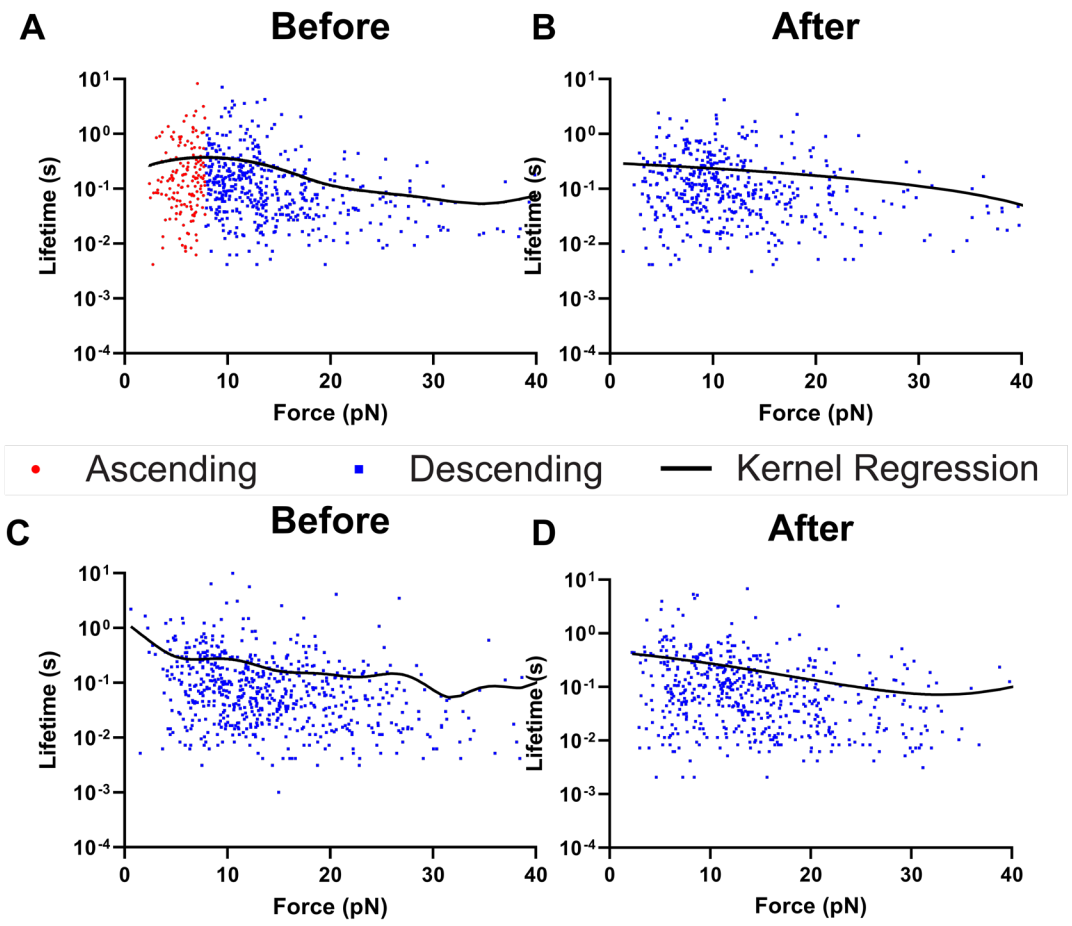

Figure 22 - Kernel Regression Revealed TCR Ligation Dependent Influences on Splenic Naïve CD8+ T cell Mechanosensitivity. Kernel regression analysis of bond lifetime data from Figure 22 segregated into subgroups representing the before and after 100 full contact cycles elucidated TCR ligation dependent effects on TCR mechanosensitivity. Kernel regression examined the relationship between force and bond lifetime. Splenic CD8+ T cell TCR bond lifetime measurements demonstrated an ascending bond lifetime trend (red circles) till a peak (0.374s and 7.84 pN) before 100 full contact cycles (A) and decreasing bond lifetime (blue squares) trend after (B) using the kernel regression model output (black line). Liver naïve CD8+ T cells both before (C) and after (D) revealed decreasing bond lifetime under more force through kernel regression model output. Each symbol represented a single bond lifetime measurement with sample sizes: spleen before (n=623), spleen after (n=473), liver before (n=634), and liver after (n=563).

5.3.5 CD8+ T Cell Memory Subsets Isolated from Spleen and Liver Display Different 2D Effective Affinities and Potential Mechanisms Contributing to 2D Effective Affinity Differences Between Anatomic Compartments

Differences between 2D effective affinity among T cell central and effector memory subsets provided additional insights into how memory T cell development regulated TCR biophysics. Conducting 2D effective affinity measurements involved isolating T cell central and effector memory subsets at least 30 days after an acute LCMV infection (Figure 24). After adoptively transferring P14 naïve CD8+ T cells from RAG1 deficient mice an LCMV-Armstrong infection induction caused an acute viral illness that resolved normally and generated central and effector memory T cell subsets. After 30 days post infection, spleen and liver CD8+ T cell isolations provided cells for FACS separations. FACS gating selected lymphocytes by forward and side scattering signal, live cells using live/dead staining, T cells by CD3 staining cells, adoptively transferred cells by Thy1.1 stating, and finally central and memory subsets based on CD127 and KLRG1 expression. Central memory CD8+ T cells expressed high CD127 and low KLRG1 while effector memory CD8+ T cells expressed low CD127 and high KLRG1.

MAFA instrumentation measured 2D effective affinity in CD8+ central and effector memory T cells subsets from the spleen and liver as previously characterized in Section 5.3.2, but paired spleen or liver T cells by T cell memory subset. Comparing CD8+ central memory (Figure 24A) and effector memory (B) T cells showed the same relationship between 2D effective affinity as with the naïve CD8+ T cells with cells from liver showing consistently higher 2D effective affinity. Contrasting CD8+ T cells from effector memory subsets between spleen and liver demonstrated statistically higher 2D effective affinity in

liver cells. Given TLR signalling induces cytokine expression as well as costimulation and coinhibition ligand expression as a response to gut bacteria draining into the liver's portal circulation, additional experiments probes into TLR9 influences on naïve CD8+ T cell 2D effective affinity. Naïve CD8+ T cells isolated from TLR9 knockout mice crossed with the same P14 transgenic TCR RAG1 knockout mice (Figure 24C) showed a similar increase in TCR 2D effective in liver over spleen cells.

Statistically comparing TCR 2D effective among CD8+ central and effector memory T cell subsets with their naïve CD8+ T counterparts from the same organ illustrated how differentiation into central and memory subtypes regulated 2D effective affinity (Figure 24D). Naïve CD8+ T cells and effector memory subsets from the same anatomic compartment showed no statistical difference. Central memory T cells demonstrated lower 2D effective affinity than their naïve counterparts from the same anatomic compartment with a more dramatic difference between liver cells. Comparing CD8+ central and effector memory cells from the same anatomic compartment revealed a statistically higher effector memory 2D effective affinity. TLR9 knockout mice showed no differences in splenic TCR 2D effective affinity compared to wild-type mice, but lower hepatic 2D effective affinity. Collectively, the data suggested spleen and liver microenvironments impacted TCR 2D effective affinity regardless of T cell subtype and TLR9 signalling contributed to the increased 2D effective affinity among liver CD8+ T cells.

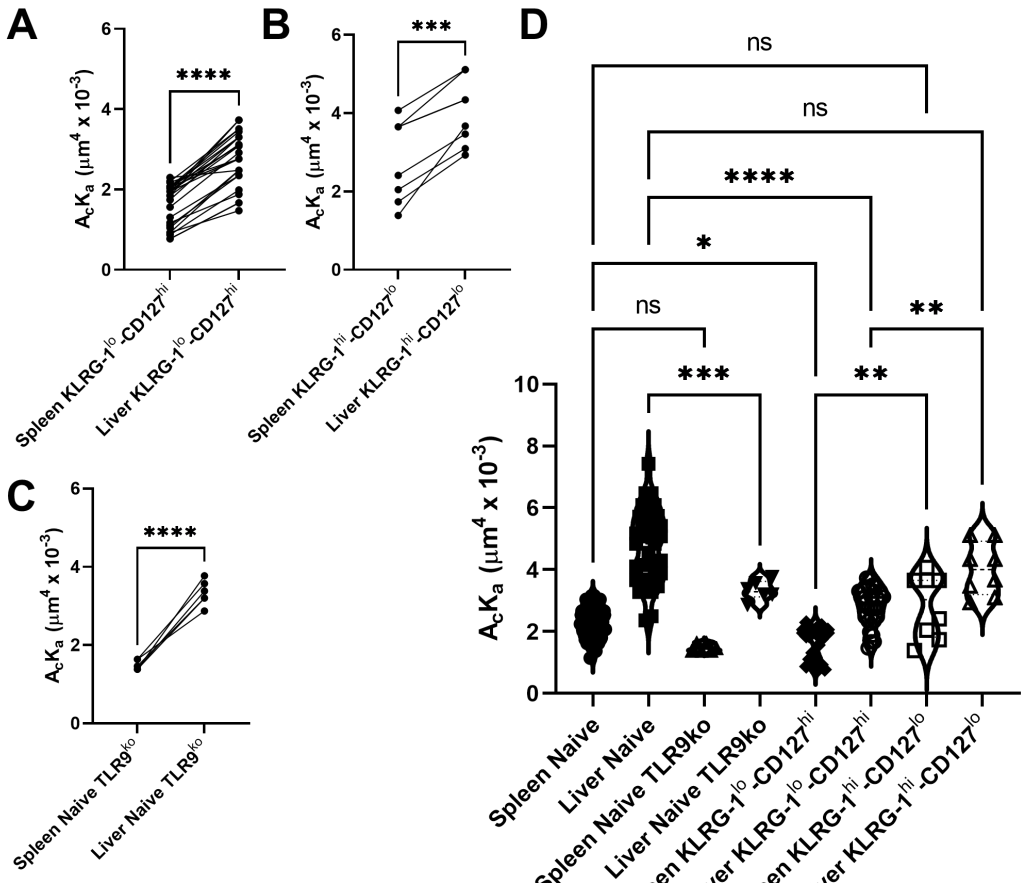

Figure 23 - Memory T Cell Subsets Display Different 2D Effective Affinity. MAFA experiments characterized TCR 2D effective affinity CD8+ T cell subsets isolated from spleen and liver. FACS separated central memory (CD127^{hi}-KLRG-1^{lo}) and effector memory (CD127^{lo}-KLRG-1^{hi}) CD8+ T cells 30 days post adoptive transfer and LCMV-Armstrong infection. Pairing spleen and liver CD8+ T cells for central (A) and effector memory (B) CD8+ T cells revealed a consistently higher 2D effective affinity in liver cells over spleen cells using a paired two-sided t test. TLR9 knockout mice evaluated TLR9 signaling contributions to 2D effective affinity measurements (C). TLR9 knockout naïve CD8+ T cells also demonstrated the same relationship between spleen and liver cells with the liver showing higher 2D effective by paired two-sided t test. Brown-Forsythe and Welch one-way ANOVA multiple comparison tests with Dunnett's correction using the same 2D effective affinity data illustrated statistical differences among CD8+ T cell subtypes isolated from spleen and liver (D). Comparing splenic and hepatic naïve CD8+ T cells with splenic central and effector memory subsets isolated from spleen showed statistically lower 2D effective affinity with central memory and no statistically significant difference in 2D effective affinity with effector memory. Similar comparisons between hepatic naïve CD8+ T cells with hepatic central and effector memory subsets isolated from

liver displayed substantially decreased 2D effective affinity in central memory cells and no difference with effector memory cells. Comparisons between CD8+ T cell central memory precursors and effector memory cells from the same anatomic compartment revealed higher 2D effective affinity for effector memory regardless from both organs. Comparing naïve CD8+ T cells with TLR9 knockout naïve CD8+ T cells from the same anatomic compartment exhibited no difference between spleen, but lower 2D effective affinity in TLR9 knockout naïve CD8+ T cells. Each plotted symbol represented a single 2D effective affinity measurement from one RBC-cell pair. Lines connecting symbols in A-C graphed pairing between spleen and liver anatomic compartments during 2D effective affinity measurements. Sample sizes for CD8+ T cell subsets shown: Naïve (n=37), Naïve TLR9^{ko} (n=6), CD127^{hi}-KLRG-1^{lo} (n=28), and CD127^{lo}-KLRG-1^{hi} (n=8). Statistical comparisons symbols shown included: ns (no significance), * ($p < 0.05$), ** ($p < 0.01$), * ($p < 0.001$), and **** ($p < 0.0001$).**

5.4 Discussion

TCR signalling contributes to T cell activation, development, and differentiation shaping immune responses mediated by T cells (258). Given TCR signalling's relevance to T cells, many investigators sought to correlate TCR-pMHC biophysical kinetic measurements with an observable functional outcome. Specifically, transgenic TCRs demonstrated cognate pMHC dependent affinity, on-rates, and off-rates correlated with pMHC placement within a spectrum from strong agonists to antagonists (251). Moreover, researchers also found perplexing that TCRs could observe both sensitivity and specificity despite kinetic dissimilarities with antibodies which observe strong affinities and slow dissociations. To explain how TCRs signalling could be sensitive and specific, several models sought to bridge molecular to cellular findings together (162). This work sought to understand how immunological cues from spleen and liver shape different CD8+ T cell subtypes TCR biophysics. *In-situ* live-cell TCR biophysical measurements reflect interactions between the TCR complex, lateral receptors, and signalling machinery that shape signal integration. In an immunologic context, understanding how the spleen and

liver microenvironments alter CD8+ T cell TCR biophysical measurements provides insights into how organ specific immunologic cues shape antigen recognition. This work desired insights into associations between TCR biophysics, microenvironment, as well as memory and effector T cell function with hopes those insights could influence vaccines and patient care.

5.4.1 Understanding TCR Biophysics in Physiologic and Pathophysiologic Contexts

Functional differences between transgenic TCRs and their pMHC ligands inspired investigations attempting to correlate TCR and pMHC interaction kinetics with functional outcomes from TCR ligation. Many of these investigations involved SPR measurements, but the relationships between measured kinetics and function remained poorly understood until examining the interactions with the MAFA and BFP demonstrated correlations between various OT1 pMHC agonists and antagonists clearly correlating increased 2D affinity with increased function and force-independent off-rate inversely with function (251, 382). More recently, employing similar techniques demonstrated 2D effective affinity between TCR and pMHC changed during immunological responses reflecting environmental immunologic cues associated with T cell functional characteristics within memory spectrum (333). Given these findings, this work investigated if immunologic cues within the liver historically considered tolerogenic shaped 2D effective affinity with clear functional influences on T cells.

The spleen and liver play different immunologic roles despite their proximity because circulatory differences. The liver receives a considerable amount of cardiac output (25%) and upstream circulatory organs provide the liver with both self and non-self-

antigens that the liver's APCs present under hyporesponsive (CD8+) and tolerogenic conditions (CD4+). Clinically, liver disease pathologically causes hepatocyte acute phase protein expression over normal protein expression with cirrhosis hallmarks including hypoalbuminemia and decreased coagulation factor expression. The liver delicately balances attenuating immunity preventing deleterious immune reactivity and empowering infection immune responses. Likewise, the spleen downstream the liver's circulation must filter hematologic antigens while also balancing tolerance and clearance. Physiologically, the spleen contributes to encapsulated bacteria responses and its absence increases infection risks against hematogenous pathogens. Understanding T cell biology within these two distinct immune environments remains a great interest among researchers primarily because immunity within these environments influences immune responses against infections, transplanted organs, autoantigens, and cancers.

Among infections with considerable interest include hepatitis with hepatitis variants ranging from acute to chronic infections. Understanding how splenic and liver microenvironments differentially influence TCR biophysics remains crucial in developing vaccines against chronic infections. This work provided unique insights into TCR biophysics among hepatic CD8+ T cells suggesting naïve subset dysregulation through altered TCR expression and molecular catch absence (Figure 22). Previously, research suggested molecular catch presence and absence related primarily to pMHC agonism and antagonism. This work provided evidence that immunological cues with the spleen and liver shaped TCR catch bond presence and absence. Although the results reflected only one TCR-pMHC interaction, immunologic cues potentially shape TCR catch bond presence and absence in TCR-pMHC interaction contexts. Additional experiments focused

on characterizing the immunologic cues associated with this transition and how such cues influence molecular catch presence or absence among pMHC agonists and antagonists could yield insights into how immunological cues regulate antigen responsiveness. Possibly, overlap between liver immunologic cues with other physiological and pathophysiologic microenvironments exist.

5.4.2 The Molecular Catch and Its Possible Relation to TCR Triggering

A key strength in the 2D effective affinity acquired within this work stemmed from measurements conducted immediately after isolations allowing our data to reflect endogenous TCR signalling within splenic and hepatic microenvironments. Environmental cues within spleen and liver influenced T cell metabolism and expression patterns enabling measurements that captured information about the TCR's functional state. Logically, the TCR biophysical measurements made could be influenced by TCR spatial organization, lateral immune receptors, signalling state, and signalling machinery interactions. TCR-pMHC interactions by influencing TCR ligation state also modulate feedback mechanisms that enable TCR sensitivity and specificity (TCR triggering).

In-situ live-cell biophysical instrumentation uniquely probed at the TCRs functional state using physiologically relevant pMHC surface densities that captured information about the receptor-ligand interactions, but importantly also molecular and cellular changes resulting from those interactions. This work illustrated using bond lifetime under force measurements that receptor ligation influenced TCR mechanosensitivity through catch bond loss (Figure 23). The observed changes likely relate to TCR triggering where balances between positive and negative feedback shape downstream TCR signalling.

Possible mechanisms shaping TCR triggering observed within naïve CD8+ T cells include positive and negative TCR signalosome feedback systems. Primary TCR triggering intracellular signalling proteins include Lck, CD45, and Zap70. Research into differences between central and effector memory subsets showed differences in constitutive Lck activity (387). Research into TCR signalosome feedback systems also suggest negative feedback distinguishes T cell subsets and influence pMHC responses shaping their placement within the agonism and antagonism spectrum. Negative feedback TCR signalosome regulators include: tyrosine-protein phosphatase non-receptor type 6 (SHP1), docking protein (DOK) 1, DOK2, hematopoietic progenitor kinase (HPK) 1, ubiquitin-associated and SH3 domain-containing protein B (STS1), and ubiquitin-associated and SH3 domain-containing protein A (STS2). Negative feedback regulators how quickly they influence the TCR signalosome enabling differential TCR signalosome function and antigen responses (388).

Additional work examining merging *in-situ* live cell biophysical measurements as well as their feedback system component compositions and their activation states could potentially yield important mechanistic insights into TCR signalosome regulation and how those regulation systems influence antigen responses. Immunologic cues could also differentially regulate TCR feedback systems among T cell subsets. Additional research defining the mechanistic process shaping altered TCR mechanosensitivity could yield insights into how to pharmacologically modulate TCR reactivity towards enhancing local tumour and infection responses while preventing off-target organ damage. These insights could be particularly important effector and central memory T cells differ in their feedback mechanisms enabling the desired clinical outcomes associated with memory T cells.

5.4.3 The Influence of Hepatic T Cell Antigen-Independent Activation on TCR Biophysics and Its Implications

Unexpectedly, MAFA paired comparisons between naïve CD8+ T cells from spleen and liver showed consistently higher 2D effective affinity in naïve liver CD8+ T cells uncoupling TCR 2D effective affinity (Figure 21). Interestingly, the increase in liver naïve CD8+ T cell 2D effective affinity occurred with decreased TCR surface density. These findings correlated with previous investigations into intrahepatic CD8+ T cells describing the liver as an activated CD8+ T cell "graveyard" (389). Several studies characterized CD8+ T cell activation proposing that the gut draining portal vein might stimulate immune cells or hepatic antigen presentation mediated CD8+ T cell death within the liver (362). TCR downregulation results from TCR activation and results in clonal anergy peripherally to mediate tolerance (390). Researchers also demonstrated TCR downregulation occurred through both direct engagement and engagement independent processes with engagement independent mechanisms shaped by Src kinase inhibition (391).

In the context of previous research, this work's findings suggested naïve CD8+ T cells underwent antigen-independent activation. Mechanistically this could result from dysregulated Src signalling and influenced by cholesterol synthesis within the liver. Specifically, LXR-dependent signalling in activated liver T cells might prevent T cell proliferation in a similar process as described previously (389) and alter T cell membrane fluidity and curvature like found within macrophage, liver, and intestinal cells (392, 393). LXR activation occurs from cholesterol synthesis intermediates and end product metabolites (394). LXR expression patterns vary between CD4+ T cell subtypes and LXR activation plasma membrane lipid order accelerating proximal T cell signalling molecule

activation (395). LXR their LXR expression suggesting that their Plasma membrane lipid raft biophysics influence T cell activation and T cell functional phenotypes (393, 396, 397). PPAR and LXR nuclear receptors influence inflammation and immunity through facilitating metabolism and immune system crosstalk influencing T helper cell differentiation (398). Within this work, hepatic CD8+ T cell plasma membranes sheared easily during micropipette aspiration causing cell fragility requiring careful handling. Hepatic T cell plasma membrane changes correlated with previous research suggesting that LXR activation among hepatic CD8+ T cells potentially contributed to observed antigen independent activation. LXR possibly influenced the TCR mechanosensing dysfunction. Additional experiments focusing on nuclear receptors and how their activation shapes immune synapse signalling machinery expression and activation could yield important insights into how TCR signalling can be modulated pharmacologically both *ex-vivo* and *in-vivo* with. Moreover, mechanistic research perturbing T cells with nuclear receptor agonists and antagonists could yield insights into how nuclear receptors seemingly shape T cell differentiation. Clinically, perturbing CD8+ T cell differentiation into memory subtypes could provide useful benefits during cancer immunotherapy, immunosuppression, and vaccine responses.

5.4.4 2D Effective Affinity Differences Among Splenic and Hepatic T Cell Subtypes and Their Implications

Examining if CD8+ T cells from different subsets differed in 2D effective affinity demonstrated similar differences between subtypes isolated from spleens and livers. TLR dependent influences potentially impacted 2D effective affinity measurements especially given the profound differences between splenic and hepatic APC cytokine expression

induced by their activation. Towards this end, this work investigated possible TLR dependent mechanisms using TLR9 (Figure 24). Hepatic CD8+ T cells showed increased 2D effective affinity regardless of T cell subset or TLR9 knockout. Interestingly, naïve CD8+ T cells demonstrated statistically greater 2D effective affinity over central memory T cells precursors with the largest difference between the hepatic T cells. The difference in 2D effective affinity could reflect central memory T cell homeostatic stability within liver microenvironments potentially protecting against TCR signalling dysregulation. This hypothesis aligns well with previous work examining TCR signalosome negative feedback and LXR activation influences on TCR signalling. Additionally, comparisons between naïve CD8+ T cells isolated from mice with similar cells from TLR9 knockout mice revealed smaller 2D effective affinity for TLR9 knockout naïve CD8+ T cells in the liver anatomic compartment. The observed differences could relate to immune signalling differences between spleen and liver with consequences that would influence T cell function and differentiation.

This work's findings left larger questions about why higher 2D effective affinity might not correlate with enhanced T cell antigen reactivity. Vaccine and immunotherapy researchers generally agree that stronger signals don't correlate with enhanced effectiveness with stronger and weaker signalling relating to effector and memory function, respectively. Given effector memory T cells susceptibility to exhaustion, increased TCR 2D effective affinity probably contributes to exhaustion observed experimentally during antigen responses. This work provides a foundation for characterizing how T cells regulate TCR biophysics during antigen sensing using signalling feedback systems. Feedback systems exist within many biological systems and especially shape TCR triggering.

Differences in TCR 2D effective affinity might reflect how T cells respond to stimulation using immunologic signalling feedback systems.

Clinically, differences in 2D effective affinity could be exploited during immunotherapy. During ICB T cells extracted from blood investigated using *in-situ* live cell biophysical instrumentation could provide insight into early therapy effectiveness using TCR 2D effective affinity to predict T cell subset population sizes. Moreover, measuring 2D effective affinity after stimulation and enrichment could map to T cell subset differentiation allowing researchers to shape memory function before administering CAR-T cell therapies hopefully towards enhancing effectiveness and preventing off-target immunity. Additional experiments with more sophisticated BFP instrumentation leveraging modalities like luciferase or fluorescence transcriptional activity could allow probing how mechanical stimulation shapes T cell differentiation through immunologically relevant transcription factors.

5.4.5 Conclusion

This work's findings expanded knowledge about how spleen and liver microenvironments shape TCR biophysics with implications that could shape immunotherapy and immunosuppression. This work could provide a foundation for understanding the relevance of hepatic immunologic cues beyond promoting CD8+ T cell death and hyporesponsiveness. Taken in context with other immunologic studies focused on characterizing central and effector memory CD8+ T cells, the results show that regulating TCR biophysics could influence antigen responsiveness. Hopefully, this work supports additional studies into how perturbing TCR signalling within the liver could

benefit patients clinically. Previous research associated hepatic immunologic cues with liver disease suggesting CD8+ T memory T cells targeting HSCs also shaped NASH (369). Moreover, liver metastasis restrained immunotherapy via macrophage-mediated T cell elimination (368). This work correlates well with these research findings and suggests the relevance of experimental findings within this work towards understanding and exploiting hepatic immunobiology. Future work should investigate TCR mechanosensitivity differences among T cell subsets. Such studies could elucidate increased TCR mechanosensitivity through preventing catch bond loss in memory T cells. This finding would correlate 2D effective affinity observations with TCR mechanosensitivity and provide additional evidence supporting hypotheses proposed within this work.

CHAPTER 6. INFLUENCE OF SHORT- AND LONG-TERM MEMORY ON TCR AND CD28 BIOPHYSICS AND BIOMECHANICS

6.1 Introduction

Cells employ dynamic systems while coordinating their functions. In T cells, dynamic processes shape T cell activation and signalling. T cell signalling involves coordinated biochemical changes in response to external environmental cues. Dynamic processes within T cells involve positive and negative feedback systems working through signal integration towards developing more complex cell behaviours (162). Antigen sensing remains most central to T cell function enabling antigen specific T cell responses toward mediating both humoral and cell-mediated immunity in CD4+ and CD8+ T cells, respectively (91). Moreover, antigen sensing involves processes occurring at both a molecular and cellular level. At a molecular level, T cell antigen sensing manifests from TCR conformational changes propagated through linked CD3 chains within the TCR complex (399). At a cellular system level, TCR complex signalling can drive TCR complex ITAM phosphorylation through Lck and ZAP70 activation eventually manifesting as global cellular changes influencing T cell function and fate (91).

Despite understanding these signalling outcomes from TCR triggering with agonist pMHCs in terms of biochemical changes and functional responses, mechanistic questions remain about how TCRs respond both sensitively and specifically towards antigens. Molecular level observations characterizing TCR-pMHC interaction kinetics using SPR

provided insights into both TCR sensitivity and specificity given associations between kinetics and agonist strength, but conflicting observations exist surrounding whether association or dissociation influence ligand strength (400, 401). Mechanical-based measurements for 2D kinetics provided meaningful correlations between kinetic rates and pMHC ligand agonism or antagonism (382). Key experimental observations demonstrating immune synapse structure and how agonist strength influenced immune synapse development provided the basis for many models seeking to describe TCR triggering. Collectively many believe that both receptor segregation and ligand binding kinetics shape TCR sensitivity and specificity (402).

This work employed mathematical modelling with biophysical instrumentation data towards expanding in-situ live cell biophysical instrumentation usefulness. The approaches used within this work could provide insights into mechanistic processes that shape immune receptor signalling. Moreover, this work provides a foundation for using *in-situ* biophysical instrumentation to probe at processes that shape the spatial and temporal dynamics

6.1.1 Significance of Mathematical Models Describing Memory

Feedback systems shape molecular and cellular systems through molecular level that influence cellular changes. Within the context of this work, memory refers to the idea that molecular and cellular systems retain information about past molecular interactions. Memory involves both irreversible and reversible changes that impact proceeding receptor-ligand interactions. Memory involves mechanisms occurring in time scales that range from seconds to hours. At a molecular level, memory could involve reversible changes like

phosphorylation and de-phosphorylation and irreversible changes such as proteolytic cleavage. At a cellular level, memory could influence receptor localization through internalization and recycling, internalization and degradation, and proteolytic shedding. Mathematical modelling biophysical data generated during *in-situ* live cell biophysical instrumentation revealed its utility in characterizing molecular and cellular system changes sensitively and specifically.

Resolving 2D kinetics involves transforming biophysical instrumentation data into a binary, discrete-time sequence and assuming the process retains same molecular interaction probability (Bernoulli process). Although this method allows kinetic rate calculations often the interpreted sequences demonstrate patterns inconsistent with the assumption that interactions occur with the same probability. Previously our laboratory characterized this as how a prior interaction could influence the proceeding interaction probability. Memory modelling demonstrated different molecular interactions could either promote or inhibit the proceeding interaction (Markov chain) (257). Similarly, interactions between molecular species could influence proceeding interactions if such an interaction removed or promoted the evaluated molecular interaction. Localization changes could influence *in-situ* biophysical measurements sensitively and specifically given experimentally how surface density relates to adhesion frequency.

Describing memory within molecular and cellular systems serves multiple purposes. Memory enhances how researchers interpret *in-situ* biophysical data and enabling studying spatially and temporally dependent mechanisms occurring at challenging time and spatial scales. This work focused on immunologic receptors revealing that common *in-situ* live cell measurement assumptions deviated from experimental data acquired while evaluating

CD28 and TCR receptor-ligand interactions. Given this work evaluated memory at different scales, mathematical modelling revealed effects potentially shaped by receptor-ligand feedback systems. This work provides a foundation for future work applying in-situ biophysical analysis towards biological research, clinical diagnostics, and drug development.

6.1.2 Feedback Systems and TCR Signalling Dynamics

Two models join both kinetic and organizational findings towards understanding TCR signalling dynamics. The serial engagement model postulates that TCR receptor ligand engagement can aggregate signalling through binding and unbinding between the TCR and pMHC enabling a single pMHC to successfully trigger T cell activation (403). The kinetic proofreading model focuses on downstream signalling occurring after TCR ligand engagement and how this engagement influences Lck activation through both positive and negative feedback mechanisms (401). Collectively these models agree that mechanistic manifestations from TCR-pMHC interactions must mediate internal signalling, but both provide limited insights into how T cells spatially and temporally regulate these interactions during antigen sensing providing the essential sensitivity and specificity needed to properly coordinate immunity at a cellular level.

Live cell biophysical measurements reveal that TCR genetics alone do not control TCR kinetics (333). Receptor-ligand interaction kinetics can be influenced strongly by their expression system, immobilization strategy (404), and environmental condition (405). At the most basic level these differences manifest from structural influences. For example, glycosylation alone can influence protein structure and often mammalian cell surface

proteins generated without glycosylation can lose their function (406, 407). Moreover, protein structure dynamically changes when proteins incur post-translational modifications (408) and engage their ligands (409, 410) or other signalling proteins (23). Given these structural differences, receptor-ligand biophysical characterization can differ between measurements conducted using only purified proteins and those natively expressed on cell surfaces. Experimental models recapitulating the most native interactions possible *ex-vivo* reveal important insights into internal signalling dynamics not possible with purified cell lines or proteins alone.

Demonstrating the necessity of measuring these interactions, experiments investigating LCMV viral responses revealed temporally dependent uncoupling between TCR 2D effective affinity measured in CD8+ T cells isolated from spleen red and white pulp during an acute infection contraction. This uncoupling related to differences in TCR affinity correlated with increased cytotoxic functionally perturbed experimentally by altering microenvironmental cues. Moreover, 2D effective affinity differences correlated with memory and effector cell population distributions (333). Biophysical measurements within this work provided evidence that *in-situ* live cell biophysical measurements could provide information reflecting microenvironmental influences on cells providing the basis that cellular systems can dynamically regulate receptor ligand interactions during physiologic and pathologic immunologic responses. This works findings could relate to feedback system signalling machinery differences previously found by researchers (387, 388). Moreover, experimental methodologies developed within this work could investigate molecular and cellular feedback systems that shape immune receptor signalling.

6.1.3 Summary of Chapter Findings

This works findings provided evidence that *in-situ* live-cell DFS measurements can capture information relating to memory and how memory could shape triggering and localization. Mathematically modelling memory captures information about receptor-ligand spatial and temporal dynamics beyond pervious 2D kinetics and bond lifetime under force measurements. This work suggested similar spatial and temporal dynamics influenced CD28 and TCR receptor-ligand interactions. Additionally, this work revealed splenic and liver microenvironments regulate measured immune receptor spatial and temporal dynamics. This work also employed a mathematical model describing binding accumulation and irreversibility towards showing findings consistent with immune receptor internalization. Collectively these findings provided insights into how spatial and temporal dynamics may influence immune receptor triggering.

6.2 Background

6.2.1 T Cell Polarization Morphological Features During Migration

Cell migration involves coordinated processes operating collectively within the cell controlling cell morphology. Cell polarization refers to differences manifesting in cells spatially concerning shape, structure, and function. Immune cell migration involves cell polarization with two spatially constrained and distinct morphological features described as the cell leading edge and uropod. During cell migration, the cell must extend its leading edge as well as contract its center and uropod in a coordinated process involving actin cytoskeletal rearrangement and actomyosin contraction within polarized features. Uropods contain specific organelles, receptors, and cytoskeletal proteins that aid in cell stabilization and enable quick contraction. Leading edges involve forming lamellipodia, filopodia,

blebs, and invadopoia plasma membrane protrusions. Leading edge structures commonly involved in T cell migration include transient lamellipodium (411). This work utilized biophysical instrumentation measurements involving live-cells and its likely receptor ligations influenced spatial and temporal distribution similarly like elucidated by other published research studies.

6.2.2 T cell Immunological Synapses and Kinapses: Relationships with Motility Structures

T cells migrating through lymphoid organs must dynamically regulate their migration to facilitate APC scanning. T cell APC scanning involves dynamically alternating between migration states forming both immunological kinapses and synapses with APCs (412). During this process T cells form dynamic protrusions that alternate between lamellipodium and pseudopodium (411). Immunological synapses involve lamellipodial structure extension over APCs (92, 413-415). During this process TCR microclusters peripherally formed migrate to the cSMAC through actin retrograde flow (242, 416, 417). Analogously to immune synapses, kinapses refer to dynamic immunological synapse like structures formed by migrating T cells (237). Within kinapses uropods feature aggregated TCR microclusters like the cSMAC (237). As previously discussed within this thesis, receptor ligation could induce morphological changes that generated force on receptor-ligand interactions. Although experimentally the morphological changes remained strongest during co-stimulation like conditions, its important to consider how receptor ligation during experiments might shape memory observations.

6.2.3 Modelling Memory Between Receptors and Ligands During Cell-Cell Interactions

Biophysical characterization of receptor-ligand interactions using the micropipette adhesion frequency assay involves instrument mediated contact cycles whereby each cycle becomes interpreted as a Bernoulli trial representing either an adhesive or non-adhesive event. The Bernoulli process within statistics describes discrete-time stochastic process resulting in binary outcomes. Bernoulli processes assume trail independence with an identical probability within the discrete-time sequence. However, this assumption might not necessarily remain true while evaluating a receptor-ligand system. Previous investigations into this assumption revealed that interactions between receptors and ligands could influence future interactions. This phenomenon termed memory involved evaluating the impact an adhesion event between a receptor ligand could enhance or diminish the chance for the proceeding event. Evaluation of three different interaction systems including LFA/ICAM-1, TCR/pMHC, or C-cadherin revealed differential memory with either no effect, enhancement, or diminishment, respectively (257). This research work incorporated this previously published model and added a mathematical model that captured long-term memory.

6.3 Experimental Data

6.3.1 Experimental System Used in Characterizing Adhesion Clustering and Irreversibility

Exploring memory accurately within molecular systems required *in-situ* live-cell DFS instrumentation. BFP instrumentation provided an ideal experimental setup for conducting live cell biophysical measurements generating signals for post-experiment

analysis. BFP chambers produced thermodynamically stable environments and cells could be monitored closely during experiments ensuring measurements reflected healthy cells.

Live-cell DFS using the BFP system generated bond lifetime data that described force-dependent off-rates. CD8+ T cells isolated from the spleen and liver expressed CD28 or TCR on their surface. SA beads featuring immobilized CD80, CD86, or gp33 pMHC featuring a CD8 binding ablation mutation (gp33mt) provided a probe surface for ligating T cell receptors (Figure 25). BFP experiments involved assembling a probe using treated RBCs pressurized according to mathematical model Evans and Richie to achieve a targeted force transducer stiffness. Computer vision enabled resolving 1D changes in bead position by using subpixel edge detection at the RBC-bead interface. Force transducer signals generated from bead position changes during piezoelectric controlled contact cycles. BFP instrumentation produced data that could be interpreted as adhesive or non-adhesive events. Previous data featured within this thesis enabled the analyses within this chapter.

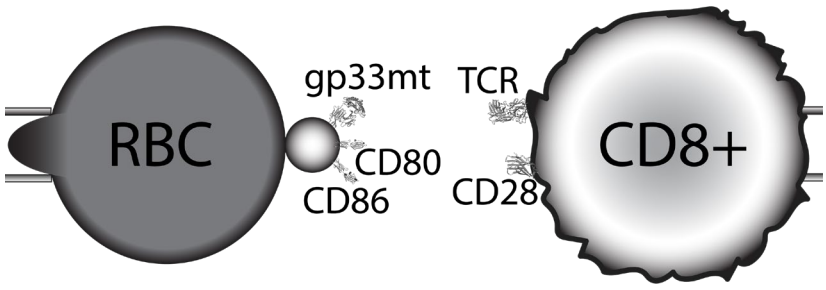

Figure 24 - Schematic of BFP Experimental Setup For Memory Calculations. BFP experiments utilized an assembled probe featuring an apical bead and pressurized RBC. Beads featured immobilized CD80, CD86, or gp33 pMHC unable to bind CD8 (left). Murine naïve CD8+ T cells isolated from spleen or liver presented TCR

or CD28. Piezoelectric controlled contact cycles enabled differentating between adhesive and non-adhesive events.

6.3.2 Interaction Specificity Within Experimental Data Groups

All biophysical experiments involving adhesion frequencies should demonstrate binding specificity between the probed receptor-ligand interactions. Ensuring the BFP data used for experimental analysis captured interactions specifically between the targeted receptors and ligands required annotating each contact cycle acquired when probing between probe-cell pairs. BFP experiments target an 20% adhesion frequency towards increasing statistical probability that adhesion events corresponded to single receptor-ligand interactions. Moreover, BFP experiments typically involve fast contact times to also both increase data acquisition rate and minimize multiple bond contributions.

Annotated BFP instrument cycle data generated discrete-time sequences with adhesive or non-adhesive events. Interpreting first 50 contact cycles for a cell-bead pair generated the pair's adhesion frequency (P_a). Comparing data generated from cell-bead pairs on one single experiment day demonstrated molecular system binding specificity (Figure 26). Non-ligand coated beads featuring just SA served as a negative control. CD80 and CD86 measurements involved naïve CD8+ T cells isolated from spleens. Gp33mt measurements utilized naïve CD8+ T cells isolated from spleen and liver. The presented data shows a mean $P_a \approx 0.2$ for all experimental groups other than SA beads without immobilized ligands which had a mean $P_a \approx 0$. Statistical comparisons between ligand-coated groups with the SA negative control revealed ligand-coated conditions presented ligands effectively with low non-specific contributions to the interpreted signals. Similar P_a between experimental conditions reflected experimental conditions optimized for single

receptor-ligand binding during lifetime measurements and do not reflect differences in 2D binding affinity.

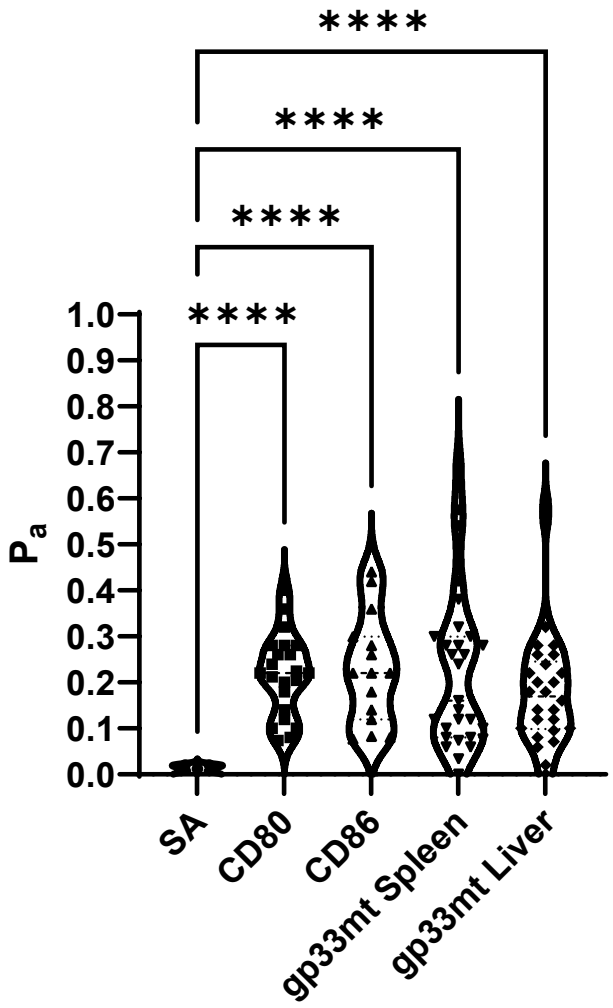

Figure 25 - Binding Specificity for Experimental System. BFP data generated from the first 50 contact cycles single cell-probe pairs on a single experimental day generated adhesion frequency (P_a) measurements for each experimental group displayed here as violin plot. Beads coated CD80, CD86, and gp33 without CD8 binding capacity (gp33mt) presented ligands during instrument cycles. SA beads without ligands served as a negative control. CD8+ T cells isolated from spleen presented CD28 and TCR for CD80, CD86, and gp33mt spleen experimental groups. CD8+ T cells isolated from liver presented TCR for the gp33mt liver experimental group. Each symbol represented a single cell-bead pair used during

experiments. Sample sizes for experimental groups: SA (n=5), CD80 (n=22), CD86 (n=15), gp33mt Spleen (n=29), and gp33mt Liver (n=26). ** illustrated an adjusted p value < 0.0001 using a Brown-Forsythe and Welch one-way ANOVA multiple comparisons test with Dunnet's multiple comparison correction.**

6.3.3 Representative Instrument Cycles Illustrating Adhesion Clustering

Identifying if BFP experimental data observed similar memory effects as previously published required examining changes in adhesion frequency and adhesion clustering throughout probe-cell contact cycles. Initially, visually inspecting running adhesion frequency and scaled adhesion events provided evidence supporting further analysis. Memory analyses reflected adhesion generated during evaluating probe-cell pairs.

Generating a comprehensive data set to show memory required pooling experimental data generated for CD80, CD86, gp33mt spleen, and gp33mt liver experimental groups from several experimental days together. The previously published memory model demonstrated a strong relationship between P_a and quantifying memory through adhesion clusters. Considering only probe-cell pairs with P_a above 20% and at least 150 instrument cycles interpreted as adhesive or non-adhesive events ensured analyses captured memory effects. Binary, discrete-time sequences allowed quantifying adhesion clusters within sequences as well as counting adhesion and non-adhesion events that occurred before and after prior adhesion or non-adhesion events (transition events).

Comparing running adhesion frequency versus contact cycle number for representative cell-bead pairs illustrated memory features within experimental data for all experimental groups (Figure 27). Running adhesion frequency represented a calculated P_a value evaluated from a contact cycle and all prior contact cycles. Running P_a plots visualized early periods where the P_a value varied widely and later where P_a appears to

converge. P_a scaled adhesion plots for the same probe-cell sequences demonstrated the clustering contributing to P_a fluctuations (Figure 28). P_a scaled adhesions represented binary events displayed as values calculated from the entire experimental sequence's P_a. Removing non-adhesion events within the sequence provided additional clarity. Given that values do not oscillate, visible overlapping symbols illustrated clustering within the sequences. Clustering within the displayed cell-bead pairs appeared similar between the experimental groups.

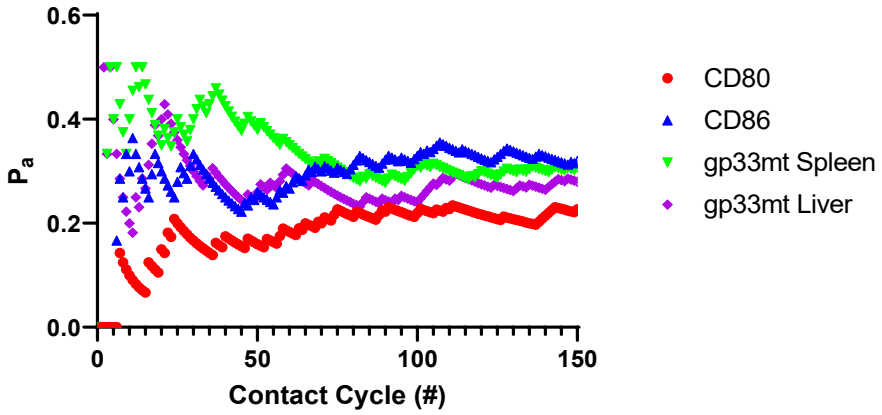

Figure 26 - Running Adhesion Frequency Plots Representing Data Used in Analysis. Single cell-bead pair from each experimental group represented relationships between running adhesion frequency (P_a) and the numer of contact cycles. Running adhesion frequency illustrated adhesion frequency calculations at every contact cycle. Experimental groups shown included: CD80 (red circle), CD86 (blue triangle), gp33mt (green inverted triangle), and gp33mt coated beads (purple diamond). Each running adhesion frequency plot captured 150 contact cycles. Over time running adhesion frequency appeared to converge.

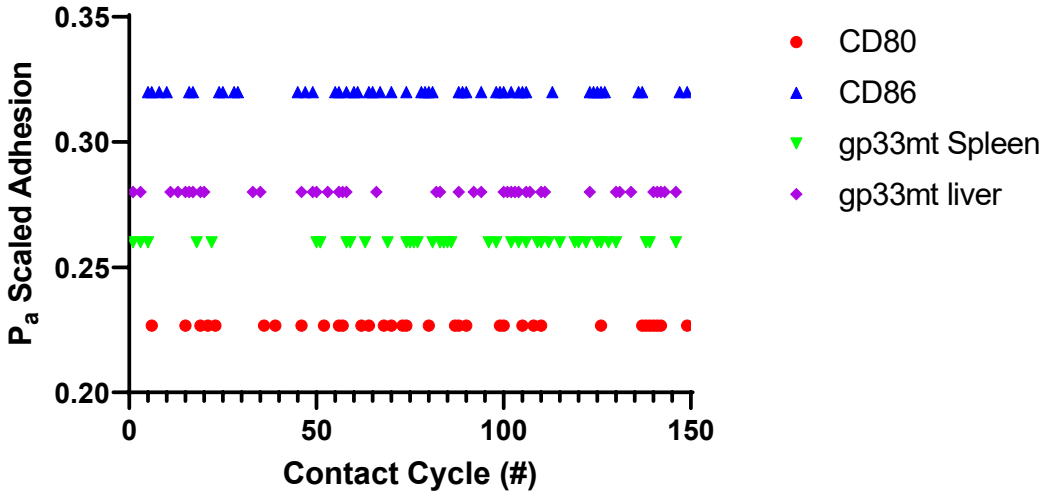

Figure 27 - P_a Scaled Adhesion Plot Generated From Representative Data Used in Analysis. From the same cell-bead pairs displayed in Figure 27 P_a scaled adhesion plots visualized clustering. P_a scaled adhesion represented adhesion events plotted using the sequences last running P_a value for a cell-bead pair. Experimental groups displayed included: CD80 (red circle), CD86 (blue trinagle), gp33mt spleen (green inverted triangle), and gp33mt liver (purple diamond). Plots enabled visualizing clusters within experimental data.

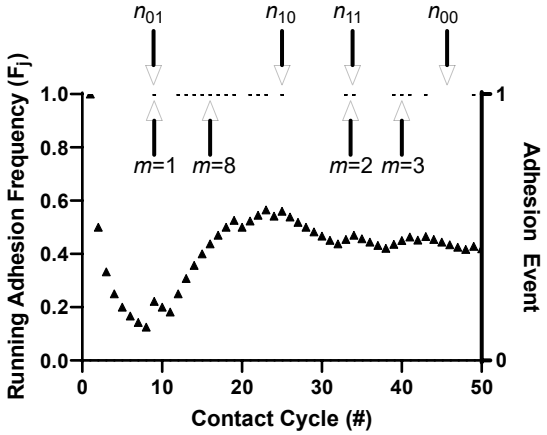

Figure 28 - Example Cluster Analysis and Transition Analysis. Graphing running P_a and adhesion events together showed relationships between adhesion clusters and running P_a fluctuations. Arrow indicated example adhesion cluster sizes (m) and transition groups (n_{ij}). All adhesion events existed within unique clusters defined by the amount of contiguous adhesion events. Assigning all adhesion events (j) into

transition groups depending on previous events (*i*) enabled directly calculating memory parameters from probe-cell pair sequences.

6.3.4 Cluster Analysis and Memory Model (M_M) Fitting

After validating clustering occurred within BFP experimental data additional analyses confirmed adhesion clusters existed within all experimental groups. Analyzing experimental groups required developing computational analysis routines towards accurately and reproducibility determining memory parameters. Memory parameters examined the adhesion probability (p) and adhesion probability following an immediate prior adhesion (Δp). Memory parameters corresponded with an effect induced by receptor ligation on immediately following events that reflected a probe's contact area spatial constraints and temporally the time between observing an adhesion and the proceeding contact cycle result.

Pooling sequences from CD80, CD86, gp33mt spleen, and gp33mt liver experimental groups enabled cluster analysis. Adhesion events occurring immediately after or before corresponded with independent and non-overlapping clusters. Adhesion counts within clusters determined cluster sizes (Figure 29). Grouping experimental groups cluster analyses together calculated statistics for cluster sizes between 1 (minimum cluster size) to 17 (maximum cluster size) creating cluster analysis histograms (Figure 30). Non-linear least squares fitting using the adhesion memory model (M_M) defined by Equation 16 (black line) generated memory parameters (p and Δp). Positive Δp values in all experimental groups indicated that adhesions increased the probability for consecutive adhesions for both TCR and CD28 bonds. Comparing Δp generated from pooled cluster analyses

demonstrated a statistically higher Δp for the CD86 experimental group compared to both spleen and liver gp33mt groups, but not CD80.

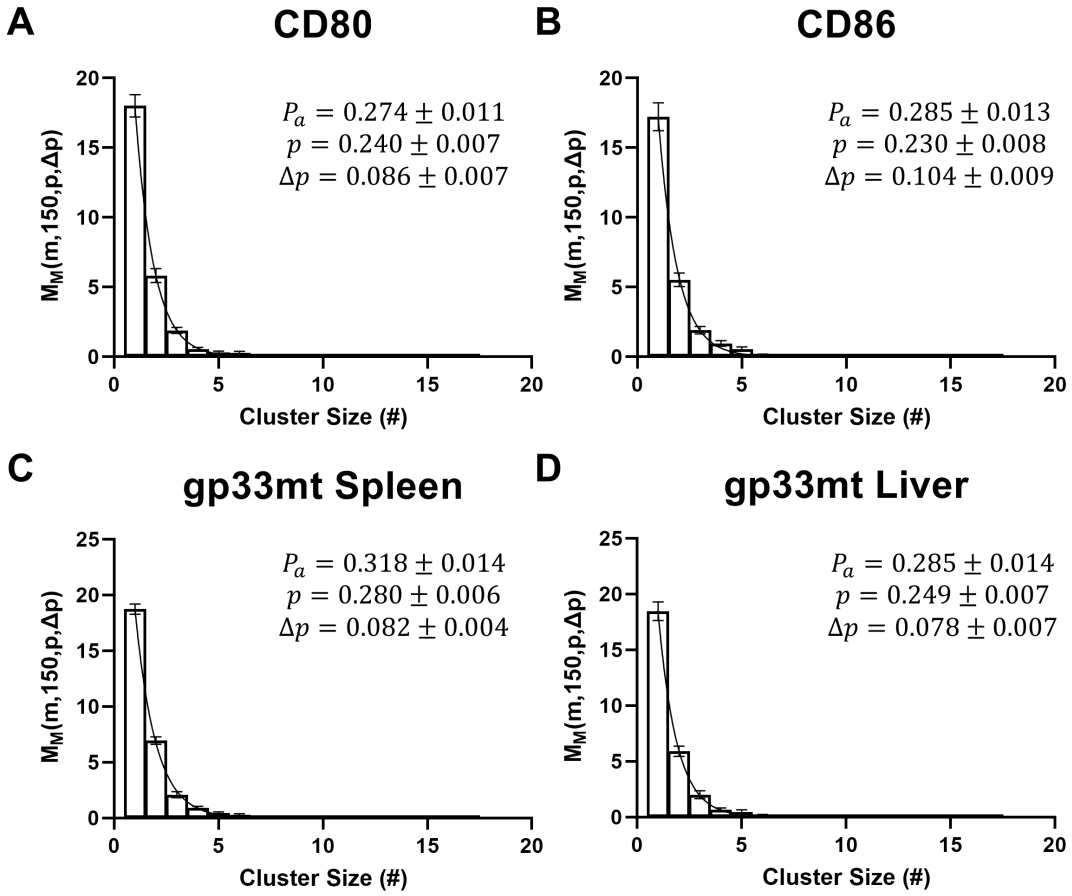

Figure 29 - Cluster Analysis and Memory Model Fit. Evaluating experiment sequences for clusters and their respective sizes enabled pooling cluster analyses together for experimental groups. Histograms showed pooled cluster analyses mean and SEM for cluster sizes between 1 and 17. Non linear least squares fitting using pooled cluster analyses determined memory parameters *p* and *Δp* for each experimental group (black line). Experimental groups analyzed embodied: CD80 (A), CD86 (B), gp33mt spleen (C), and gp33mt liver (D). Histograms also featured P_a mean ± SEM as well as non-linear fit parameter values ± SEM for *p* and *Δp*. Sample sizes for each experimental group included: CD80 (n=31), CD86 (n=24), gp33mt spleen (n=35), and gp33mt liver (n=21).

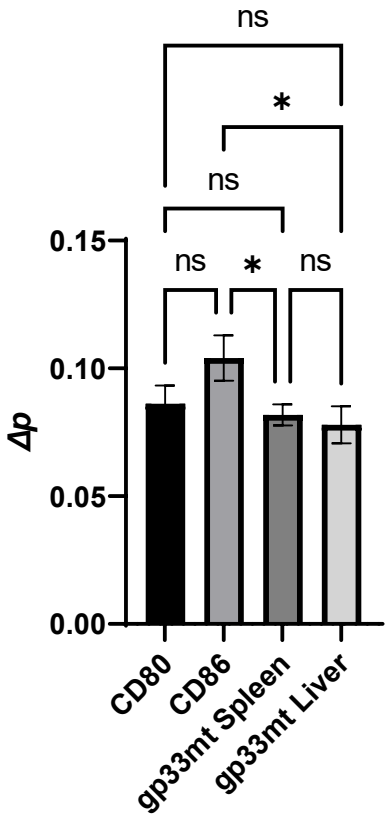

Figure 30 - Comparing Cluster Analyses *Δp* Fit. Comparing non-linear least squares fitting generated *Δp* parameters using a Brown-Forsythe and Welch one-way ANOVA multiple comparisons without correcting for multiple comparisons (unpaired t two-sided t test with Welch's correction) demonstrated a statistically higher *Δp* in CD86 compared spleen and liver gp33mt experimental groups. CD86 *Δp* lacked a statistical difference from the CD80 experimental groups. All other multiple comparisions failed to reveal statistical differences. Bar heigh represented fit parameter with error bars indicating fitting error. Statistical symbols shown included: * ($p < 0.05$) and ns (not significant).

6.3.5 Comparing Direct and Model Fit Memory Parameters

After establishing that nonlinear least squares fitting pooled experimental group cluster analyses described experimental groups well direct and fit memory methods needed validation. Different memory parameter calculation methods theoretically resembled each other, but practically the methods did not produce the same value. Ideally, nonlinear fitting

cluster analysis and direct memory calculations using transition probabilities within the same sequence should resemble each other. However, cluster analysis methodology remained susceptible to sequence edge effects whereby clusters could theoretically extend past sequence length.

Independently evaluating sequences from experimental groups produced cluster analyses and transition probabilities (Figure 29). Utilizing Equation 14 and Equation 15 allowed calculating memory parameters p and Δp directly from transition probabilities. Comparing direct and fitted memory parameters using scatter plots enabled comparing direct values (x-axis) and fitted values (y-axis) (Figure 32). Simple linear regressions analyzed relationships between memory methods using slopes and R^2. Δp slopes varied between 0.761 and 1.038 while *p values* between 0.710 and 1.079 demonstrating that fitted parameters tended be smaller than respective direct calculations. Δp R^2 values ranged between 0.634 and 0.823 while p values between 0.550 and 0.676. Overall, both methods overlapped well indicating analysis quality.

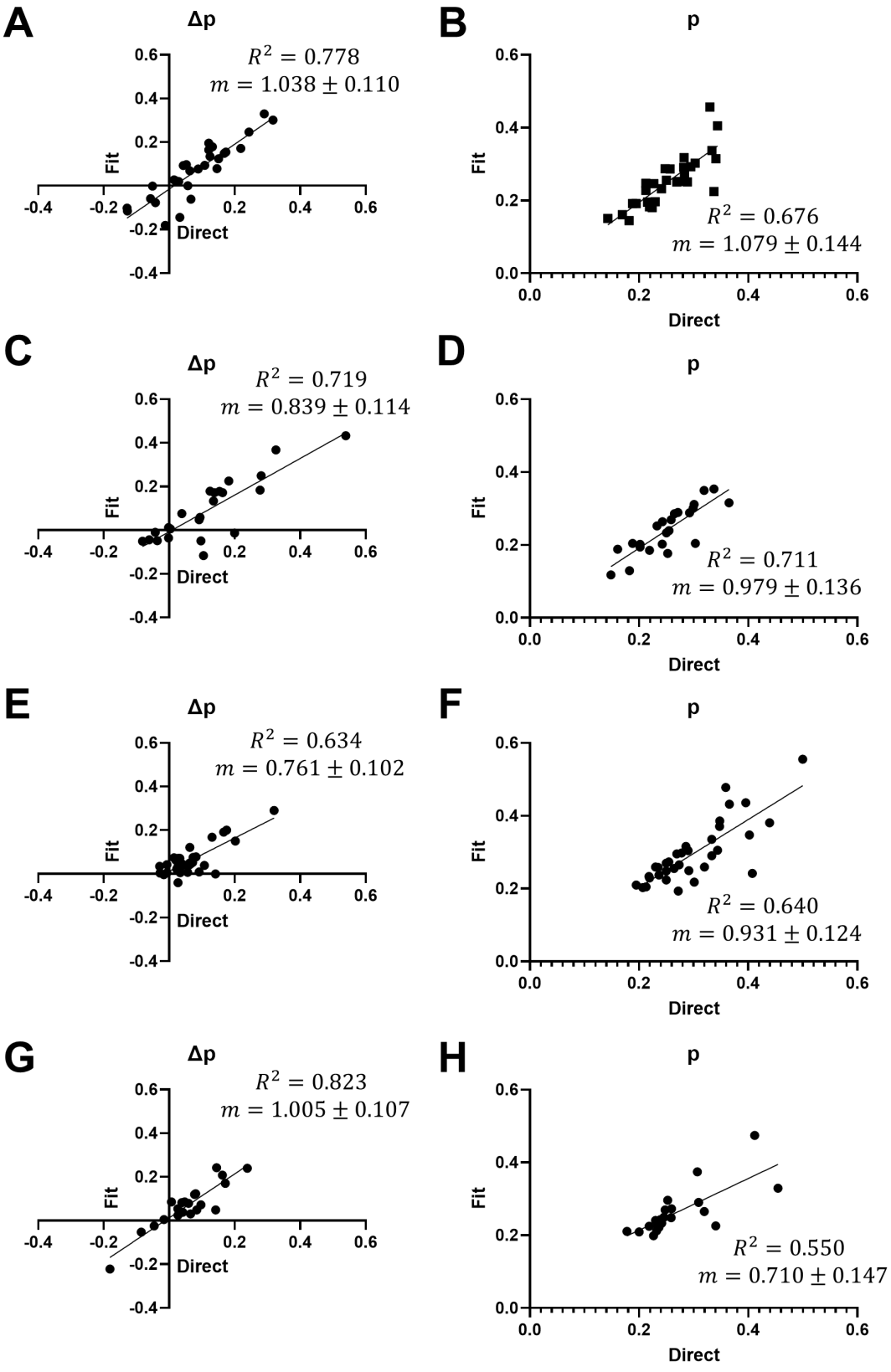
A
Δp
$R^2 = 0.778$
$m = 1.038 \pm 0.110$
Fit
Direct
B
p
$R^2 = 0.676$
$m = 1.079 \pm 0.144$
Fit
Direct
C
Δp
$R^2 = 0.719$
$m = 0.839 \pm 0.114$
Fit
Direct
D
p
$R^2 = 0.711$
$m = 0.979 \pm 0.136$
Fit
Direct
E
Δp
$R^2 = 0.634$
$m = 0.761 \pm 0.102$
Fit
Direct
F
p
$R^2 = 0.640$
$m = 0.931 \pm 0.124$
Fit
Direct
G
Δp
$R^2 = 0.823$
$m = 1.005 \pm 0.107$
Fit
Direct
H
p
$R^2 = 0.550$
$m = 0.710 \pm 0.147$
Fit
Direct

Figure 31 - Comparing Memory Parameters Generated by Direct Calculation and M_M Fitting. Sequences for each cell-bead pair enabled determining p and Δp using direct and M_M fitting. Experimental groups included: CD80 (A, B), CD86 (C, D), gp33mt Spleen (E,F), and gp33mt Liver (G,H). Scatter plots points represented the direct calculation on the x-axis and the model fit on the y-axis. Simple linear regressions for each scatter plot compared the calculation methods. R^2 and m parameters displayed derived from linear regression represent goodness of fit and slope, respectively, with the slope value including mean +/- fit error. Memory model parameters determined using both methods generally matched each other well, but the fit method Δp values tended to be lower than the direct method.

6.3.6 TCR and CD28 Receptors Demonstrate Similar Memory Parameters

After validating direct and fit memory parameter calculation methods further analyses focused on demonstrating memory parameters deviated statistically from a hypothetical zero mean. Specifically, Δp values that deviated significantly from zero would validate memory presence within our experimental groups. Zero Δp values corresponded with sequences that lacked deviation from a Bernoulli process meaning that each contact cycle's result retained an equal adhesion probability. Positive and negative Δp values reflected adhesion events increased or decreased adhesion probability in the following contact cycle, respectively.

Using the same calculations shown in Figure 32 to compare experimental groups direct or memory model fit methods with hypothetical zero means. In Figure 33, value distributions within violin plots showed memory parameter variability among experimental group sequences. The memory parameter Δp consistently deviated from a hypothetical zero mean statistically for all experimental groups regardless of calculation method. Comparing experimental group means among each other using a Brown-Forsythe and Welch one-way ANOVA multiple comparisons with Dunnet's multiple comparisons correction statistical test failed to show any consistent differences among the experimental

groups despite the CD86 experimental group's greater *Δp* (Figure 32A-B). Comparing *p* values experimental groups also revealed a lack of statistical differences among groups, but a consistent differences between CD86 and gp33mt Spleen (Figure 32C-D).

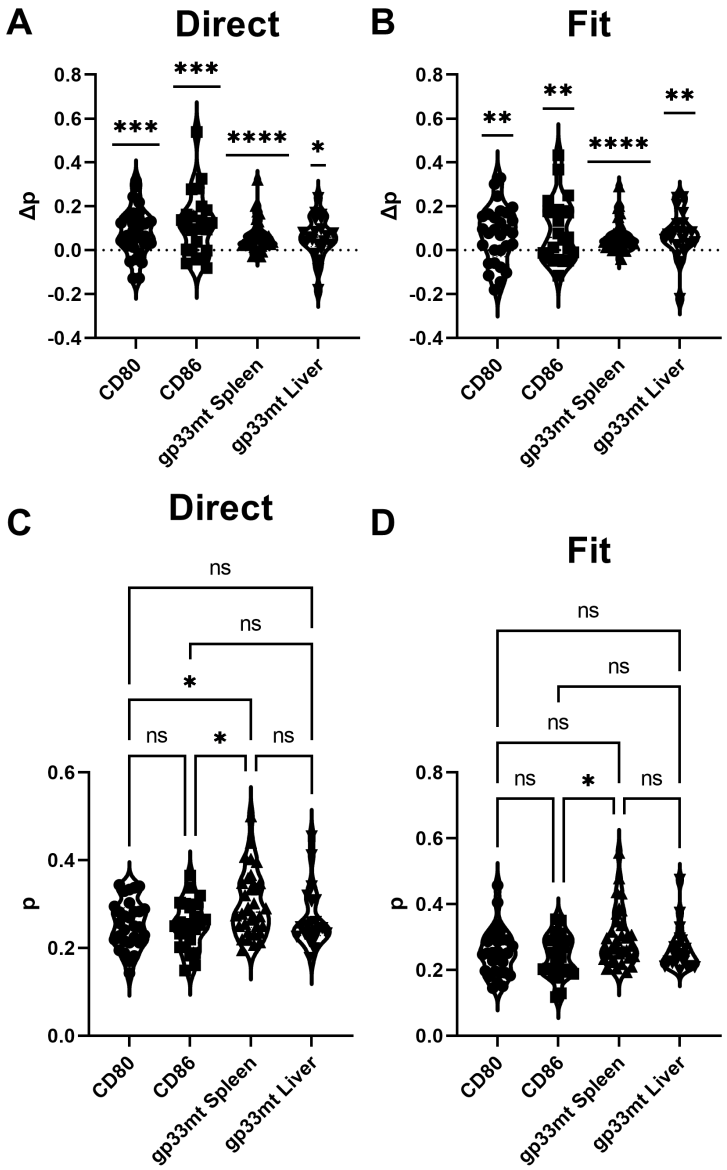

Figure 32 - *p* and *Δp* Comparisons for CD28 and TCR. Using the values calculated from experimental groups shown in Figure 32 statistical analyses for CD80, CD86, gp33mt spleen and gp33mt liver memory parameters validated memory within all

experimental groups. Direct and memory model fit methods Δp values demonstrated statistically significant deviations from a hypothetical zero mean with all mean values consistently being above zero. Comparing Δp values among experimental groups showed groups lacked statistical differences. Calculated p values did not experimentally differ much between groups statistically with the only consistent difference between CD86 and gp33mt spleen. Each symbol graphically represented one single cell-bead pair. Sample sizes for experimental groups comprised: CD80 (n=29), CD86 (n=23), gp33mt spleen (n=34) and gp33mt liver (n=21). Displayed statistical comparisons showed differences between Δp distributions and hypothetical zero mean (one sample t-test). Statistical comparisons between p values employed a Brown-Forsythe and Welch one-way ANOVA multiple comparisons with a Dunnet's multiple comparisons correction. Symbols for statistical comparisons shown included: ns ($p > 0.05$), $p < 0.05$ (*), $p < 0.01$ (**), $p < 0.001$ (***), and $p < 0.0001$ (****).

6.3.7 TCR Memory Shifts Over Time

After validating memory within experimental groups additional analyses sought see if memory parameters changed after multiple receptor-ligand interactions. Changes in short-term memory parameters showed how ligation dependent changes influenced memory. Changes in memory parameters could correspond with different ligation-dependent signalling responses. Moreover, memory dynamics could correspond with receptor localization differences.

Using the same sequences in previous memory parameter analyses, dividing sequences into the first and last 75 contact cycles allowed identifying differences between sequence halves (Figure 34). Using the direct method prevented differences between two sequences reflecting cluster splitting or edge effects as previously mentioned. Statistically, direct p and Δp for CD80 and CD86 experimental groups lacked differences between the first and last 75 contact cycles. Comparing gp33mt spleen and gp33mt liver groups revealed that gp33mt spleen and liver decreased and increased Δp, respectively. Direct p for gp33mt spleen and liver lacked a statistically significant difference.

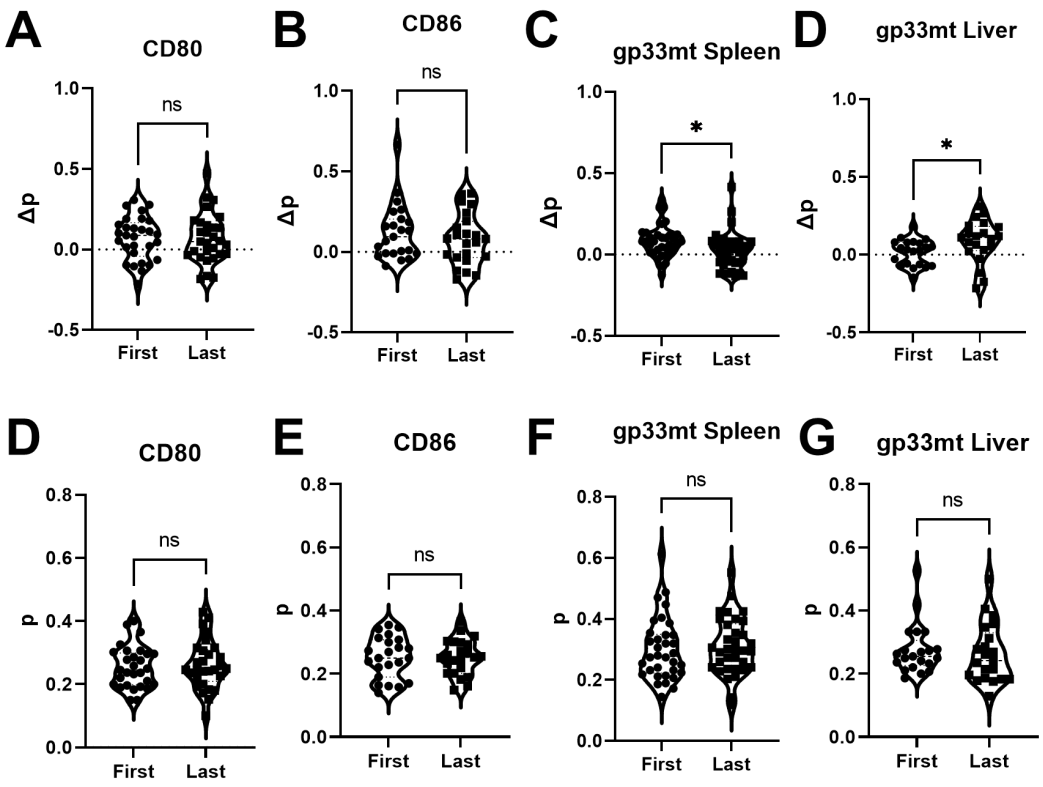

Figure 33 - Memory Parameters for First and Last 75 Contact Cycles. Sequences previously used for determining *p* and *Δp* split into the first and last 75 contact cycles allowed identifying ligation-dependent memory parameter changes. Using direct parameters prevented sequence edge influences given splitting sequences in half could split clusters unevenly. Statistical analyses revealed most experimental groups lacked differences in memory parameters between the first and last 75 contact cycles. However, gp33mt spleen and liver experimental groups showed statistically significant differences between first and last 75 contact cycle *Δp* values with decreases and increases, respectively. Sample size for experimental groups constituted: CD80 (n=29), CD86 (n=23), gp33mt spleen (n=34), and gp33mt liver (n=21). Every symbol within the violin plot represented a single cell-bead pair. Statistical comparisons utilized a paired t test between the first and last values acquired with the same cell-bead pair. Symbols for statistical analysis shown included: ns ($p > 0.05$) and * ($p < 0.05$).

6.3.8 TCR and CD28 Show Similar Irreversibility Modelling

Given previous memory analyses revealed short-term memory changes and ligation-dependent dynamics, demonstrating long-term memory could further illustrate that *in-situ* live-cell biophysical instrumentation captured ligation-dependent effects. Long-term memory referred to adhesion event impact on all proceeding events. Long-term memory mathematical modelling captured changes in receptor localization (receptor trafficking or proteolytic cleavage). Previous research reports characterized TCR activation resulted in receptor internalization (418-421) encouraging demonstrating similar findings through biophysical analysis.

The long-term memory model characterized binding changes as irreversibility (I_M) (Figure 35). Using the same 150 length sequences from the previous memory parameter analyses for CD80, CD86, gp33mt spleen, and gp33mt liver experimental groups provided evidence supporting identifying short and long-term memory with adhesion sequences. Irreversibility modelling nonlinear fitted $<n>$ and I_M by minimizing the MSDW (Equation 17) given running frequency observations f_i (Equation 18) and the irreversibility model F_i (Equation 19).

Graphing model graphed model Fi given hypothetical I_M values and a hypothetical $<n>$ demonstrated how I_M values influenced running P_a. The hypothetical model output emulated experimental group mean P_a (Figure 35A). Graphing nonlinear fitting results with running P_a demonstrated successful model fitting for a single CD80 experimental group cell-bead pair (Figure 35B). After validating that our model described our model well by visually expecting model fits with observed running adhesion frequency sequences, statistically comparing experimental group fitted I_M values against a hypothetical zero mean (one-sample t-test) and among each other resolved I_M significant long-term memory

effects and differences among experimental groups, respectively (Figure 35C). CD86 and gp33mt spleen experimental groups demonstrated statistically significant positive I_M values. CD80 and gp33mt liver did not show a statistical difference from a hypothetical zero mean. Experimental groups lacked statistically significant differences between groups.

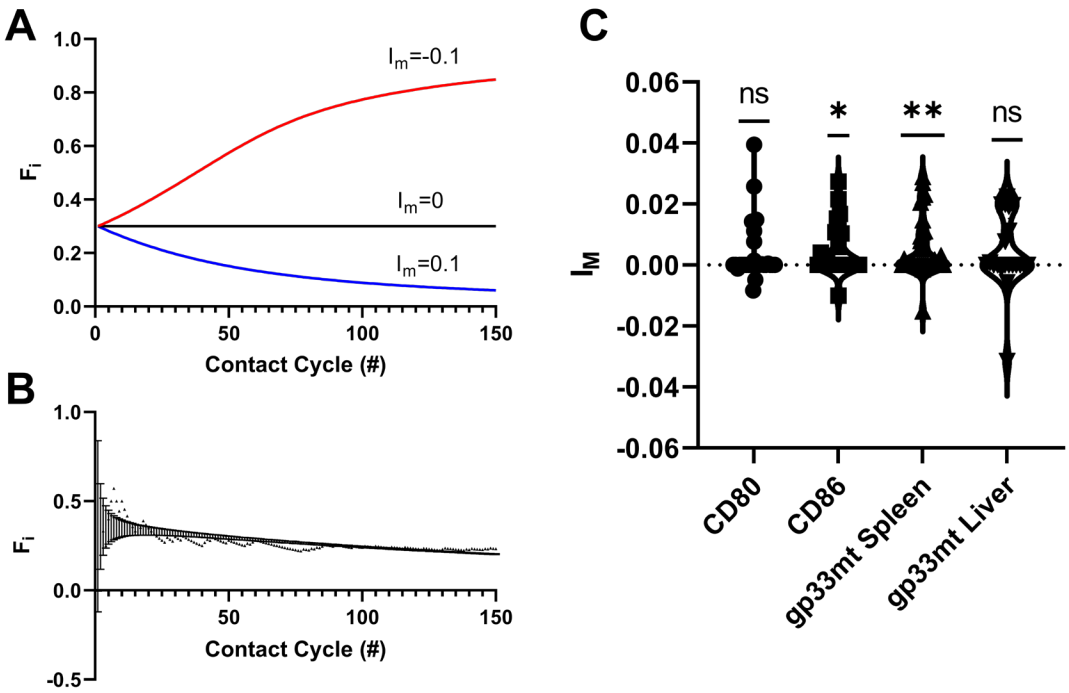

Figure 34 - Binding Irreversibility Resulting from CD28 and TCR Binding. Analyzing P_a changes within adhesion sequences using irreversibility modeling revealed potential long-term memory within experimental groups. Non-linear fitting minimized the MSWD (Equation 17) using the L-BFGS-B method to determine irreversibility parameters $<n>$ and I_M using binding irreversibility model F_i (Equation 19) and f_i (Equation 18). Demonstrating irreversibility hypothetically influenced P_a involved plotting F_i given hypothetical I_M values (-0.1, 0, and 0.1) and $<n>$ (P_a=0.3) (A). Illustrating a representative model nonlinear fit required plotting the final fitted F_i values and error for a CD80 cell-bead pair adhesion sequence (B). Statistically comparing the fitted I_M values for experimental groups CD80 (n=29), CD86 (n=23), gp33mt spleen (n=34), and gp33mt liver (n=21) determined their statistical significance against a hypothetical zero mean (one-sample t-test) and among each other (Brown-Forsythe and Welch one-way ANOVA multiple comparisons with Dunnet's multiple comparison correction) (C). Each symbol

within the violin plot represented a single cell-bead pair. Comparing values against hypothetical zero means showed larger I_M distributions derived for CD86 and gp33mt spleen experimental groups compared to a hypothetical zero mean. CD80 and gp33mt liver did not deviate from a hypothetical zero mean. Experimental groups lacked statistically significant differences among each other by one-way ANOVA multiple comparisons test. Symbols for statistical analysis as shown included: ns (not significant), * ($p < 0.05$), and ** ($p < 0.01$).

6.4 Discussion

TCR and CD28 receptors provide essential signals in mounting antigen specific immune responses. TCR and CD28 operate together when T cells and APCs contact each other shaping T cell activation and differentiation. APCs constitutively express CD28 ligands (CD80 and CD86) on their surfaces altering their expression based on their activation states (272). T cells must distinguish APC presented antigens both specifically and sensitively to appropriately coordinate immunity and prevent off-target effects (258). Given naïve T cells must quickly scan APC presented antigens within lymph nodes, research into the dynamics involved in cell-cell contacts between T cells and APCs demonstrated coordinated cytoskeletal processes shaping receptor localizations within immune synapses as well as dynamic cell-cell interaction called the kinapse formed by T cells migrating around APCs (411). Moreover, TCR activation drives receptor internalization a process that would also influence receptor localization on T cell surfaces. This work investigated if *in-situ* live-cell DFS experiments using BFP instrumentation captured information about the spatial and temporal dynamics influencing receptor-ligand interactions using mathematical modelling. In doing so, this work expanded the in-situ live-cell DFS instrumentation usefulness revealing its utility in demonstrating receptor-mediated mechanisms.

6.4.1 BFP Instrumentation Spatial and Temporal Resolution Uniquely Aligns with T cell Activation Microclusters

BFP experiments involve contact cycles between immobilized ligands and live cells. Compared to other biophysical instrumentation techniques like MAFA and HAFM BFP contact cycles involve small contact areas (< 1 μm). BFP contact areas resemble T cell activation microclusters (submicron-sized bodies) (422) suggesting other biophysical instrumentation techniques involving larger contact areas (MAFA and HAFM) possibly lack the spatial resolution required for capturing T cell activation microcluster dynamics. Moreover, BFP signal temporal resolution ensures contact cycles capture similar contact areas throughout evaluating probe-cell pairs and sensitively resolving adhesions, a important consideration given *in-situ* live-cell techniques such as MAFA rely upon instrument users to judge contact areas and adhesions. Additionally, BFP instrumentation allows users to control mechanical parameters that could influence receptor ligation such as receptor loading rates (423). In the context of our experiments, probes function as surrogate APCs presenting ligands that isolated CD8+ T cell surface receptors can bind enabling instrument data to reflect receptor-ligand interaction specificity. Given these considerations, BFP instrumentation measurements can go beyond receptor-ligand interactions biophysics and biomechanics towards capturing spatial and temporal changes due receptor ligation and activation. Although BFP probes still cannot substitute for endogenous APC surfaces, BFP instrumentation still captures

TCR and CD28 receptor ligation induces molecular and cellular changes known to influence receptor localization and activation state. Likely, BFP instrumentation captures similar localization and activation changes induced during probe-cell adhesion sequences.

Receptor localization and activation changes would mediate feedback mechanisms previously described within this work. Additional experiments should focus on perturbing receptor feedback systems to capture signalling mechanisms that mediate observed short and long-term memory. Additionally, understanding the feedback mechanisms regulating TCR and CD28 activation could provide a foundation for characterizing how mechanical force shapes receptor activation through short and long-term memory effects.

6.4.2 Validating Previous Memory Model and Validation Significance

Characterizing spatial and temporal dynamics required validating a previously published mathematical model that illustrated immediate differences in adhesion probability due to prior receptor-ligand interaction events (short-term memory) (257). Validating the prior memory model used data acquired from BFP experiments towards successfully showing similar memory effects in a different TCR-pMHC interaction system (P14 vs OVA). The analyses within this work more robustly illustrated memory effects using considerably larger probe-cell pair number and sequence length (previous publication used contact cycle # = 50 and sample size = 3-5 RBC-cell pairs). BFP and MAFA experiments importantly differ in receptor immobilization with RBC immobilized ligands freely diffusing across RBC surfaces and BFP ligands lacking diffusion. Short-term memory effects did not rely upon surface diffusion highlighting memory effects must correspond with T cell molecular and cellular changes.

All experimental groups possessed similarly positive Δp suggesting adhesion events occurring during cell-bead pair experiments impacted proceeding contact cycles. Memory modelling with the published mathematical model allowed quantifying memory and

comparing experimental group memory. This work's comparisons correlated with similar feedback systems regulating TCR and CD28 receptor-ligand interactions as previously reported in the literature (Lck, etc.). Memory effects also persisted despite reduced BFP contact cycles (0.1s) compared to usual conditions for interaction saturation (≥ 2s). Moreover, BFP experiments targeted single receptor-ligand interactions compared to possible multiple interactions present within MAFA contact cycles. Collectively, these distinguishing BFP features demonstrated memory at both temporal scales that could capture single receptor ligation induced feedback with temporal resolution difficult to achieve with imaging techniques.

Additional experiments should exploit in-situ live-cell BFP measurements towards elucidating signalling machinery feedback systems relate to memory observations. Perturbing intracellular signalling pathways with signalling machinery inhibitors such as Lck could elucidate mechanisms impacting short-term memory that likely reflect receptor molecular changes induced by receptor ligation. Moreover, examining how mechanical factors shape short-term memory could reveal mechanosensitivity mechanisms that would be particularly important at T cell-APC interfaces. This work provides a foundation for expanding BFP instrumentation usefulness in studying immune receptor mechanisms.

6.4.3 Significance of Short-Term Ligation-Dependent Dynamics

Although short-term memory observed could reflect mostly receptor molecular changes involving intracellular signalling machinery, differences in signalling machinery activation and localization could shape observed memory. TCR and CD28 ligation influences receptor localization as well as Lck interactions and activation as previously

mentioned within this work. Characterizing differences in short-term memory receptor ligation drives molecular and cellular changes within T cells offers perspectives into dynamic processes that shape T cell-APC interactions. Motivated by this potential this work featured additional analyses that captured potential memory effect differences within sequences.

Demonstrating receptor-ligation mediated memory effects required divided adhesion sequences into the first and last 75 contact cycles. CD80 and CD86 lacked statistically significant differences in the first and last 75 contact cycles, but unexpectedly found gp33mt spleen and liver experimental groups displayed opposing trends for the first and last 75 contact cycles. Interestingly, the CD86's experimental trend visually resembled gp33mt spleen, but this trend did not display a statistically significant difference between the first and last 75 contact cycles. Observed T cell receptor trends could correspond with receptor and signalling machinery localization changes observed by other researchers investigating T cell signalling.

Previous research found liver X receptor (LXR) activation shaped T cell activation by altering plasma membrane lipid order an effect that accelerated proximal T cell signalling molecule activation (424). As previously discussed within this work, liver T cells displayed dramatically different plasma membrane conditions. Moreover, T cells within livers receive many nuclear receptor activating ligands given the liver metabolizes lipids and synthesizes cholesterol. Given TCR receptor ligation drives signalling machinery activation, the memory differences between first and last 75 contact cycles likely reflects altered proximal signalling molecule activation correlating with quickly developing memory effects for liver cells compared to spleen cells. This illustrated that

analysing short-term memory dynamics could reveal mechanistic processes associated with signalling molecule activation. Potentially, observed differences between gp33mt spleen and liver groups reflect dysfunctional TCR signalling.

Additional experiments should expand upon these findings by conducting experiments with larger contact cycles and perturb proximal signalling machinery activation using kinase inhibitors and nuclear receptor agonists and antagonists. Insights generated from such studies could elucidate mechanisms that shape T cell receptor activation suggesting therapeutic strategies that could enhance immunotherapy effectiveness. Research into how statins shape immunotherapies highlight the significance of exploring how nuclear receptor modulation shapes T cell activation (425, 426). This work provides a foundation for mechanistic receptor signalling investigations.

6.4.4 Long-Term Modelling Significance

This work also featured long-term memory analyses that characterized adhesion-dependent changes that influenced all subsequent contact cycles using irreversibility modelling (I_M). Experimental groups lacked statistical differences when comparing experimental groups among each other. Interestingly, long-term memory modelling showed both CD86 and gp33mt spleen experimental groups possessed a statistically significant positive I_M while CD80 and gp33mt liver groups did not. Positive I_M illustrated mathematically adhesion sequences displayed downward running P_a trends possibly relating to receptor availability on T cell surfaces. Given the nature of BFP experiments, observed trends likely did not reflect ligand changes.

This work's long-term memory modelling could also reflect spatial and temporal dynamics influencing TCR-CD28 receptors that shape dynamic focal contacts between APCs and T cells. An important process that would influence TCR localization includes TCR internalization. TCR activation induces TCR internalization as previously discussed. Demonstrating TCR internalization within *in-situ* live-cell DFS measurements could provide an experimental methodology capable of resolving single receptor-ligand interaction dependent changes. Moreover, recapitulating previous mechanisms associated with TCR activation highlights BFP instrumentation physiologic relevance. As expected, TCR ligation within the gp33mt spleen experimental group drove decreasing running P_a trends ($I_M > 0$) that correlated with potential TCR internalization.

Interestingly, gp33mt liver lacked a statistically significant I_M compared with a hypothetical zero mean possibly indicating signalling dysfunction associated with CD8+ T cell hyporesponsiveness associated with liver-induced antigen-independent T cell activation. Given positive I_M values correlated with previous studies indicating TCR internalization following TCR activation, lacking statistically significant I_M could reflect hepatic CD8+ T cells could not activate the intracellular signalling, a finding that would correlate with catch bond absence demonstrated within this work.

CD86 and CD80 also differed in displaying statistically significant I_M values compared to hypothetical zero means. Assuming CD28 receptors on splenic T cells retain their physiologic functions, the lack of a statistically significant positive I_M value in the CD80 experimental group while the CD86 experimental group showed a statistically significant positive I_M might indicate differences between ligand activation capacity or

signalling differences. Such differences possibly relate to mechanosensitivity differences discussed within this work.

6.4.5 Potential Actin-Mediated Mechanisms and Potential Implications

Previous research indicates that TCR-pMHC interactions can trigger microcluster localization and that this localization shapes signalling (427). This work featured analyses that explored short-term memory and long-term changes shaped by receptor ligation. CD28 ligation appears to coordinate similar changes potentially relating to similar actin cytoskeletal processes that influence TCR-CD28 microcluster localization. Both receptors trigger Vav1 activation and Vav1 mediates the actin cytoskeletal processes involved in immune synapse formation (428). If observed short-term and long-term memory correlate with actin-mediated processes, the results within this work could potentially indicate that CD28 can trigger Vav1 activation towards actin cytoskeletal rearrangement independent from co-stimulation.

Focusing on short-term and long-term memory effects that would more likely correspond with both receptor and signalling machinery localization and activation, capturing memory effects could provide insights into how actin cytoskeletal changes influence T cell activation. The implications of this finding provide additional insight into observations made about T cell migration among APCs where T cells dynamically form interactions with APCs (237). CD28 potentially gets activated before and independently from TCR enabling T cells to recognize new potential antigen sources for antigen sensing. During experiments CD28 receptor activation corresponded with morphological changes

that shaped thermal fluctuation bond lifetime measurement forces as previously discussed within this work.

Additional experiments should examine how perturbing actin cytoskeleton dynamics influences short-term and long-term memory. Demonstrating that perturbing actin cytoskeleton dynamics influences memory effects could demonstrate that BFP instrumentation uniquely captures microcluster movement induced by T cell immune receptor activation. Actin cytoskeletal processes remain particularly important in that the potentially generate forces on TCR-pMHC bonds enabling physiologic TCR mechanosensing. Expanding upon current instrumentation towards characterizing actin-mediated process that influence immune receptors could elucidate additional mechanisms shaping immune receptor signalling and inspire novel therapeutic strategies that can enhance clinical outcomes.

6.4.6 Conclusion

This chapter's findings utilized mathematical modeling towards exploring receptor ligation-dependent changes that shape T cell receptor-ligand interactions. The work presented here validated a previous mathematical model describing TCR memory and demonstrated that CD28, another IgSF receptor, also exhibited similar memory. This work also examined memory dynamics that showed altered TCR memory dynamics in spleen and liver CD8+ T cells. Finally, this work utilized mathematical modelling towards showing receptor ligation could cause long-term effects with adhesion sequences. Collectively, these findings possibly related to immune receptor activation induced by receptor ligation.

The memory analyses contained within this work possibly provide methodology for examining immune receptor activation while minimally perturbing cells. The methodology developed within this chapter fills a gap in studying signaling. Unfortunately, understanding signaling often involves genetically modifying cells or tethering fluorescence indicators to receptors or signaling machinery, processes that potentially alter cell homeostasis and kinetics. Moreover, signal sensitivity and specificity constrain imaging methods hindering spatial and temporal resolution.

Utilizing memory as a receptor activation metric potentially could provide clinical diagnostic information quantifying immunotherapy or immunosuppression effectiveness. T cells isolated from blood could reflect immune system status allowing clinicians to examine antigen reactivity in additional flow cytometric immune cell population quantification. Hypothetically, BFP probes could feature a collection of relevant pMHC molecules using megapool approaches (429) and adhesion sequences generated with megapool probes could demonstrate ligation-dependent memory effects. As a diagnostic tool, increased or decreased antigen reactivity could inform therapy modifications that enhance clinical outcomes. This chapter's work hopefully inspires researchers to incorporate biophysical instrumentation techniques when studying receptor signaling mechanisms.

CHAPTER 7. CONCLUSIONS AND FUTURE DIRECTIONS

Characterizing receptor-ligand interaction biophysics provided many important historical insights into receptor signaling mechanisms. One of the most significant immunologic biophysics findings characterized differences between CD28 and CTLA-4 demonstrating CLTA-4 could effectively block CD28 co-stimulation through competitive inhibition. This insight motivated drug developments that blocked CTLA-4 using a monoclonal antibody that would enhance immunological responses (ipilimumab) as well as a chimeric protein drug featuring CTLA-4 that blocks immune responses (abatacept, belatacept) (295, 329).

Other IgSF family receptors like TCR remained more elusive until *in-situ* 2D kinetic measurements finally revealed measurements between TCR and pMHC that correlated with agonism and antagonism (251). This thesis work utilized live-cell *in-situ* biophysical measurements towards different experimental contexts: co-stimulatory receptor-ligand interactions, TCR and pMHC interactions in splenic and hepatic T cell subsets, as well as demonstrating functional changes in receptor-ligand interactions resulting from receptor engagement. *In-situ* live cell biophysical instrumentation techniques resolved information about molecular and cellular states that shape immune signaling. This thesis work desired providing a foundation for utilizing biophysical instrumentation techniques towards clinical diagnostics and therapies. Moreover, this thesis work aimed contribute TCR and CD28 biophysical insights that could be exploited towards clinical therapy effectiveness.

7.1.1 In-Situ Live-Cell Biophysical Instrumentation as an Engineering Approach to Understanding Signalling

In-situ live-cell biophysical experiments reflect a common methodology in science and engineering referred to as a black box. In the context of *in-situ* biophysical measurements cells function as black boxes. Stimulating cells through receptor ligand interactions provided black box inputs and force transducer signals captured outputs. Analyzing force transducer output generated information about 2D kinetics, force-dependent dissociation kinetics, ligation-mediated adhesion probability changes, ligation-mediated influences on force-dependent dissociation kinetics, and ligation-mediated generation. This thesis work highlighted the utility in such measurements for observing molecular and cellular changes mediated by receptor ligation.

Unfortunately, few experimental tools exist that can investigate molecular and cellular changes resulting from single receptor-ligand interactions. Moreover, few experimental techniques can concurrently extract information from single receptor-ligand interactions. Physiologically, TCR activation occurs both specifically and sensitively enabling T cell activation despite few suitable pMHC agonists present after proteolytically processing antigens. Towards measuring strong effects common experimental approaches involve large pMHC concentrations and sometimes even rely upon stimulation antibodies that kinetically differ from TCR-pMHC interactions. Continuing to investigate *in-situ* live-cell experimental and analysis approaches will potentially yield more information describing receptor-ligand interactions.

7.1.2 Enhancing BFP Instrumentation

Expanding immunologic signaling knowledge will require developing experimental approaches that match physiologic and pathophysiologic conditions. Likewise, BFP instrumentation enhancements should focus on increasing physiologic and pathophysiologic relevance. Current investigations rely upon assembling new BFP chambers every two hours before measurements become inconsistent. Developing BFP chamber conditions conducive to T cell homeostasis could enhance measurement throughput and quality. Current chamber conditions provide non-optimal temperature and oxygenation although current approaches exist for regulating chamber temperature. Although experimentally examining cells closely allows identifying cell death, focusing on optimizing conditions for T cell metabolism might enable identifying metabolism dependent mechanisms.

BFP instrumentation relies upon software to control cell position and measure force transducer signal. Current BFP instrumentation software utilizes LabView which unfortunately lacks optimization for computer vision applications at BFP instrument frame rates resulting in periodically dropped images and image analysis that lags behind image acquisition impacting instrument responsiveness when establishing bond lifetime clamping force. Incorporating FPGAs and high-performance computing techniques could dramatically enhance BFP instrumentation enabling force feedback systems for inducing more sophisticated force stimulation. Researchers already attempted enhancing BFP instrumentation software in developing the ultra-stable BFP that relied upon measuring multiple edge positions and force feedback (430), but did not specify instrument frame rate, a quantity influenced by camera ROI changes. Instrumentation software enhancements should focus on measuring bead position in two dimensions without losing imaging frames.

7.1.3 Challenges to BFP Experimental Approaches

As biological tool, *in-situ* live-cell biophysical instrumentation remains uncommon in biological laboratories. Given its limited use within biomedical research, BFP instrumentation could grow considerably from utilization by more research groups that could provide their unique insights into how to improve its instrumentation. BFP instrumentation retains unique benefits and drawbacks. Among things challenging its adoption in more laboratories includes the challenging nature of BFP experiments. As a biophysical instrument the BFP requires both engineering knowledge and instrumentation. Moreover, researchers using the BFP must also possess biological knowledge to interpret result significance. Hopefully as researchers continue to elucidate important biological phenomena using BFP instrumentation will generate more interest and result in a richer and more collaborative academic environment working towards enhancing its experimental use.

7.1.4 A Foundation for Investigating Immune Receptor Crosstalk

This thesis work revealed live cell *in-situ* biophysical characterization towards answering receptor signaling questions. This thesis work showed CD28 monovalency, characterized 2D kinetic differences that correlated with previous functional investigations, demonstrated conclusively that CD28 receptors form different catch bonds with their B7 ligands, and showed similarities between TCR and CD28. Collectively, these results suggested that co-stimulation and co-inhibition could involve mechanical information exchanged during T cell and APC interactions. CD28 results reflected similar findings to

other IgSF family receptors acquired within our laboratory (232, 235). Mechanical processes at T cell APC interfaces could potentially shape IgSF signal integration.

Future investigations into crosstalk between TCR and CD28 using *in-situ* live-cell biophysical instrumentation could yield important insights about T cell activation. This work provided a foundation for such work by initially characterizing CD28 and developing metrics that could be altered during crosstalk. Among possible crosstalk effects include altered receptor signaling feedback systems and receptor localization, processes that potentially contributed to observations made within this thesis work. Experimentally, kinases such as Lck can be perturbed towards altering TCR and CD28 2D kinetics, mechanosensitivity, and memory. Moreover, crosstalk could be differentially shaped by mechanical stimulation given both TCR and CD28 observe mechanosensitivity. Additional investigations into how mechanical stimulation shapes TCR and CD28 crosstalk could yield insights that improve immunotherapy.

7.1.5 Potential Antigen Sensing Implications

Comparing T cell subsets from different liver and spleen using 2D effective affinity and bond lifetime under force revealed unexpectedly a situation within hepatic T cells where a larger TCR 2D effective affinity and catch bond absence. Within the well-characterized hepatic CD8+ T cell population undergoing activation mediated cell death hepatic T cells demonstrated altered mechanosensing losing catch bonds they retained in the spleen. Reproducing the catch bond loss in splenic T cells by segregating data based on when during a cell-bead pair lifetime measurements occurred allowed correlating TCR ligation with potentially an activation effect. Memory analyses using splenic and hepatic

T cells also showed different dynamics in response to TCR ligation. Together findings among chapters possibly illustrated TCR receptor dysfunction, a finding that correlated with previous investigations demonstrating hepatic microenvironmental cues resulted in T cell hyporesponsiveness and altered antigen responses.

Possibly, T cells dynamically alter their ability to sense antigens and dysregulation in this process influences T cell activation and function. Further experiments should correlate differences demonstrated within this work with T cell functional differences. Exploring additional micronenvironments featuring different immunological cues and characterizing how such micronenvironments influence T cell function could reveal using the metrics developed within this work that certain immunological cues reduce or enhance TCR activation. This would enable T cells to respond differentially to antigens when infiltrating into infected or abnormal tissues. Such insights could prevent transplant rejection, enhance cancer elimination, or prevent chronic infections.

7.1.6 Immunotherapy Strategies Using Mechanical Stimulation

Hypothetically, this work supports the development of a mechanical system that simultaneously stimulates cells and interprets information about how cells received such stimulation. A mechanical system such features could activate T cells and provide different stimuli levels towards influencing cell function. Moreover, a mechanical system with such functionality could shape T cell development, activation, and differentiation towards recapitulating endogenous processes that occur during immune responses.

Current immunotherapies focus on altering immunity through pharmacological perturbations that systemically alter immunity or require genetic modifications that shape

antigen responsiveness. Although transformative within medicine, immunotherapies can result in harmful therapeutic sequela that can significantly reduce patient life quality. By developing potential TCR activation metrics, this work serves as a foundation for developing therapeutic strategies that incorporate biophysical instrumentation towards mechanically stimulated T cells and predicting T cell responsiveness. The mechanical system suggested within this work could engineer immunity in personalized ways specific for patient disease hopefully enhancing clinical outcomes and preventing harmful immunity.

7.1.7 Conclusion

This thesis work provided insights that possibly will shape future investigations and inspire translational medical advances. Recent medical advancements in pharmacologic immunotherapy and immunosuppression improved patient care and quality of life. Despite many therapeutic advancements, many fundamental questions about how the immune system works remain unanswered. The work presented within this thesis focused on biophysical measurements that retain their own strengths and weaknesses. The presented research recapitulated many established mechanisms towards narrowing the gap between biophysical measurements and T cell biology. Hopefully this work inspires and empowers future researchers seeking to answer questions about T cell immunology.

REFERENCES

1. Xia F, Qian CR, Xun Z, Hamon Y, Sartre AM, Formisano A, Mailfert S, Phelipot MC, Billaudeau C, Jaeger S, Nunes JA, Guo XJ, He HT. TCR and CD28 Concomitant Stimulation Elicits a Distinctive Calcium Response in Naive T Cells. Front Immunol. 2018;9:2864. Epub 2018/12/20. doi: 10.3389/fimmu.2018.02864. PubMed PMID: 30564247; PMCID: PMC6288997.

2. Rossy J, Williamson DJ, Benzing C, Gaus K. The integration of signaling and the spatial organization of the T cell synapse. Front Immunol. 2012;3:352. Epub 2012/11/29. doi: 10.3389/fimmu.2012.00352. PubMed PMID: 23189081; PMCID: PMC3504718.

3. Ledbetter JA, Imboden JB, Schieven GL, Grosmaire LS, Rabinovitch PS, Lindsten T, Thompson CB, June CH. CD28 ligation in T-cell activation: evidence for two signal transduction pathways. Blood. 1990;75(7):1531-9. Epub 1990/04/01. PubMed PMID: 2156582.

4. Janeway C. Immunobiology 5 : the immune system in health and disease. 5th ed. New York: Garland Pub.; 2001. xviii, 732 p. p.

5. Esensten JH, Helou YA, Chopra G, Weiss A, Bluestone JA. CD28 Costimulation: From Mechanism to Therapy. Immunity. 2016;44(5):973-88. Epub 2016/05/19. doi: 10.1016/j.immuni.2016.04.020. PubMed PMID: 27192564; PMCID: PMC4932896.

6. Judokusumo E, Tabdanov E, Kumari S, Dustin ML, Kam LC. Mechanosensing in T lymphocyte activation. Biophys J. 2012;102(2):L5-7. Epub 2012/02/22. doi: 10.1016/j.bpj.2011.12.011. PubMed PMID: 22339876; PMCID: PMC3260692.

7. Bashour KT, Gondarenko A, Chen H, Shen K, Liu X, Huse M, Hone JC, Kam LC. CD28 and CD3 have complementary roles in T-cell traction forces. Proc Natl Acad Sci U S A. 2014;111(6):2241-6. Epub 2014/01/29. doi: 10.1073/pnas.1315606111. PubMed PMID: 24469820; PMCID: PMC3926067.

8. Porciello N, Tuosto L. CD28 costimulatory signals in T lymphocyte activation: Emerging functions beyond a qualitative and quantitative support to TCR signalling. Cytokine Growth Factor Rev. 2016;28:11-9. Epub 2016/03/14. doi: 10.1016/j.cytogfr.2016.02.004. PubMed PMID: 26970725.

9. Wu P, Zhang T, Liu B, Fei P, Cui L, Qin R, Zhu H, Yao D, Martinez RJ, Hu W, An C, Zhang Y, Liu J, Shi J, Fan J, Yin W, Sun J, Zhou C, Zeng X, Xu C, Wang J, Evavold BD, Zhu C, Chen W, Lou J. Mechano-regulation of Peptide-MHC Class I Conformations Determines TCR Antigen Recognition. Mol Cell. 2019;73(5):1015-27 e7. Epub

2019/02/04. doi: 10.1016/j.molcel.2018.12.018. PubMed PMID: 30711376; PMCID: PMC6408234.

10. Ikeya T, Hanashima T, Hosoya S, Shimazaki M, Ikeda S, Mishima M, Guntert P, Ito Y. Improved in-cell structure determination of proteins at near-physiological concentration. Sci Rep. 2016;6:38312. Epub 2016/12/03. doi: 10.1038/srep38312. PubMed PMID: 27910948; PMCID: PMC5133543.

11. Minor DL, Jr. The neurobiologist's guide to structural biology: a primer on why macromolecular structure matters and how to evaluate structural data. Neuron. 2007;54(4):511-33. Epub 2007/05/25. doi: 10.1016/j.neuron.2007.04.026. PubMed PMID: 17521566; PMCID: PMC3011226.

12. Frueh DP, Goodrich AC, Mishra SH, Nichols SR. NMR methods for structural studies of large monomeric and multimeric proteins. Curr Opin Struct Biol. 2013;23(5):734-9. Epub 2013/07/16. doi: 10.1016/j.sbi.2013.06.016. PubMed PMID: 23850141; PMCID: PMC3805735.

13. Jensen EC. Use of fluorescent probes: their effect on cell biology and limitations. Anat Rec (Hoboken). 2012;295(12):2031-6. Epub 2012/10/13. doi: 10.1002/ar.22602. PubMed PMID: 23060362.

14. Bräuer M, Zich MT, Önder K, Müller N. The influence of commonly used tags on structural propensities and internal dynamics of peptides. Monatshefte für Chemie - Chemical Monthly. 2019;150(5):913-25. doi: 10.1007/s00706-019-02401-x.

15. Agbulut O, Coirault C, Niederlander N, Huet A, Vicart P, Hagege A, Puceat M, Menasche P. GFP expression in muscle cells impairs actin-myosin interactions: implications for cell therapy. Nat Methods. 2006;3(5):331. Epub 2006/04/22. doi: 10.1038/nmeth0506-331. PubMed PMID: 16628201.

16. Crivat G, Taraska JW. Imaging proteins inside cells with fluorescent tags. Trends Biotechnol. 2012;30(1):8-16. Epub 2011/09/20. doi: 10.1016/j.tibtech.2011.08.002. PubMed PMID: 21924508; PMCID: PMC3246539.

17. Snapp E. Design and use of fluorescent fusion proteins in cell biology. Curr Protoc Cell Biol. 2005;Chapter 21:21 4 1- 4 13. Epub 2008/01/30. doi: 10.1002/0471143030.cb2104s27. PubMed PMID: 18228466; PMCID: PMC2875081.

18. Mueller SN, Zaid A, Carbone FR. Tissue-resident T cells: dynamic players in skin immunity. Front Immunol. 2014;5:332. Epub 2014/08/01. doi: 10.3389/fimmu.2014.00332. PubMed PMID: 25076947; PMCID: PMC4099935.

19. Kumar BV, Connors TJ, Farber DL. Human T Cell Development, Localization, and Function throughout Life. Immunity. 2018;48(2):202-13. Epub 2018/02/22. doi: 10.1016/j.immuni.2018.01.007. PubMed PMID: 29466753; PMCID: PMC5826622.

20. Hunter MC, Teijeira A, Halin C. T Cell Trafficking through Lymphatic Vessels. Front Immunol. 2016;7:613. Epub 2017/01/10. doi: 10.3389/fimmu.2016.00613. PubMed PMID: 28066423; PMCID: PMC5174098.

21. Sasmal DK, Feng W, Roy S, Leung P, He Y, Cai C, Cao G, Lian H, Qin J, Hui E, Schreiber H, Adams EJ, Huang J. TCR-pMHC bond conformation controls TCR ligand discrimination. Cell Mol Immunol. 2020;17(3):203-17. Epub 2019/09/19. doi: 10.1038/s41423-019-0273-6. PubMed PMID: 31530899; PMCID: PMC7052167.

22. Xu X, Li H, Xu C. Structural understanding of T cell receptor triggering. Cell Mol Immunol. 2020;17(3):193-202. Epub 2020/02/13. doi: 10.1038/s41423-020-0367-1. PubMed PMID: 32047259; PMCID: PMC7052162.

23. Luo BH, Springer TA. Integrin structures and conformational signaling. Curr Opin Cell Biol. 2006;18(5):579-86. Epub 2006/08/15. doi: 10.1016/j.ceb.2006.08.005. PubMed PMID: 16904883; PMCID: PMC1618925.

24. Martino F, Perestrelo AR, Vinarsky V, Pagliari S, Forte G. Cellular Mechanotransduction: From Tension to Function. Front Physiol. 2018;9:824. Epub 2018/07/22. doi: 10.3389/fphys.2018.00824. PubMed PMID: 30026699; PMCID: PMC6041413.

25. Hargadon KM, Johnson CE, Williams CJ. Immune checkpoint blockade therapy for cancer: An overview of FDA-approved immune checkpoint inhibitors. Int Immunopharmacol. 2018;62:29-39. Epub 2018/07/11. doi: 10.1016/j.intimp.2018.06.001. PubMed PMID: 29990692.

26. June CH, Sadelain M. Chimeric Antigen Receptor Therapy. N Engl J Med. 2018;379(1):64-73. Epub 2018/07/05. doi: 10.1056/NEJMra1706169. PubMed PMID: 29972754; PMCID: PMC7433347.

27. Dotti G, Gottschalk S, Savoldo B, Brenner MK. Design and development of therapies using chimeric antigen receptor-expressing T cells. Immunol Rev. 2014;257(1):107-26. Epub 2013/12/18. doi: 10.1111/imr.12131. PubMed PMID: 24329793; PMCID: PMC3874724.

28. Teijaro JR, Farber DL. COVID-19 vaccines: modes of immune activation and future challenges. Nat Rev Immunol. 2021;21(4):195-7. Epub 2021/03/07. doi: 10.1038/s41577-021-00526-x. PubMed PMID: 33674759; PMCID: PMC7934118.

29. Pouzolles M, Oburoglu L, Taylor N, Zimmermann VS. Hematopoietic stem cell lineage specification. Curr Opin Hematol. 2016;23(4):311-7. Epub 2016/05/03. doi: 10.1097/MOH.0000000000000260. PubMed PMID: 27135980.

30. Rosales C, Uribe-Querol E. Phagocytosis: A Fundamental Process in Immunity. Biomed Res Int. 2017;2017:9042851. Epub 2017/07/12. doi: 10.1155/2017/9042851. PubMed PMID: 28691037; PMCID: PMC5485277.

31. Kondo M. Lymphoid and myeloid lineage commitment in multipotent hematopoietic progenitors. Immunol Rev. 2010;238(1):37-46. Epub 2010/10/26. doi: 10.1111/j.1600-065X.2010.00963.x. PubMed PMID: 20969583; PMCID: PMC2975965.

32. Kitamura Y, Oboki K, Ito A. Development of mast cells. Proc Jpn Acad Ser B Phys Biol Sci. 2007;83(6):164-74. Epub 2007/09/01. doi: 10.2183/pjab.83.164. PubMed PMID: 24367142; PMCID: PMC3855204.

33. McBrien CN, Menzies-Gow A. The Biology of Eosinophils and Their Role in Asthma. Front Med (Lausanne). 2017;4:93. Epub 2017/07/18. doi: 10.3389/fmed.2017.00093. PubMed PMID: 28713812; PMCID: PMC5491677.

34. Sasaki H, Kurotaki D, Tamura T. Regulation of basophil and mast cell development by transcription factors. Allergol Int. 2016;65(2):127-34. Epub 2016/03/15. doi: 10.1016/j.alit.2016.01.006. PubMed PMID: 26972050.

35. Rosales C. Neutrophil: A Cell with Many Roles in Inflammation or Several Cell Types? Front Physiol. 2018;9:113. Epub 2018/03/09. doi: 10.3389/fphys.2018.00113. PubMed PMID: 29515456; PMCID: PMC5826082.

36. Varol C, Mildner A, Jung S. Macrophages: development and tissue specialization. Annu Rev Immunol. 2015;33:643-75. Epub 2015/04/12. doi: 10.1146/annurev-immunol-032414-112220. PubMed PMID: 25861979.

37. Chistiakov DA, Sobenin IA, Orekhov AN, Bobryshev YV. Myeloid dendritic cells: Development, functions, and role in atherosclerotic inflammation. Immunobiology. 2015;220(6):833-44. Epub 2015/01/18. doi: 10.1016/j.imbio.2014.12.010. PubMed PMID: 25595536.

38. Bennstein SB. Unraveling Natural Killer T-Cells Development. Front Immunol. 2017;8:1950. Epub 2018/01/30. doi: 10.3389/fimmu.2017.01950. PubMed PMID: 29375573; PMCID: PMC5767218.

39. Pieper K, Grimbacher B, Eibel H. B-cell biology and development. J Allergy Clin Immunol. 2013;131(4):959-71. Epub 2013/03/08. doi: 10.1016/j.jaci.2013.01.046. PubMed PMID: 23465663.

40. Germain RN. T-cell development and the CD4-CD8 lineage decision. Nat Rev Immunol. 2002;2(5):309-22. Epub 2002/05/30. doi: 10.1038/nri798. PubMed PMID: 12033737.

41. Chistiakov DA, Orekhov AN, Sobenin IA, Bobryshev YV. Plasmacytoid dendritic cells: development, functions, and role in atherosclerotic inflammation. Front Physiol. 2014;5:279. Epub 2014/08/15. doi: 10.3389/fphys.2014.00279. PubMed PMID: 25120492; PMCID: PMC4110479.

42. Villadangos JA, Young L. Antigen-presentation properties of plasmacytoid dendritic cells. Immunity. 2008;29(3):352-61. Epub 2008/09/19. doi: 10.1016/j.immuni.2008.09.002. PubMed PMID: 18799143.

43. Hoogeboom R, Tolar P. Molecular Mechanisms of B Cell Antigen Gathering and Endocytosis. Curr Top Microbiol Immunol. 2016;393:45-63. Epub 2015/09/05. doi: 10.1007/82_2015_476. PubMed PMID: 26336965.

44. Nair S, Dhodapkar MV. Natural Killer T Cells in Cancer Immunotherapy. Front Immunol. 2017;8:1178. Epub 2017/10/12. doi: 10.3389/fimmu.2017.01178. PubMed PMID: 29018445; PMCID: PMC5614937.

45. Marshall JS, Warrington R, Watson W, Kim HL. An introduction to immunology and immunopathology. Allergy Asthma Clin Immunol. 2018;14(Suppl 2):49. Epub 2018/09/29. doi: 10.1186/s13223-018-0278-1. PubMed PMID: 30263032; PMCID: PMC6156898.

46. Zhang N, Bevan MJ. CD8(+) T cells: foot soldiers of the immune system. Immunity. 2011;35(2):161-8. Epub 2011/08/27. doi: 10.1016/j.immuni.2011.07.010. PubMed PMID: 21867926; PMCID: PMC3303224.

47. Swain SL, McKinstry KK, Strutt TM. Expanding roles for CD4(+) T cells in immunity to viruses. Nat Rev Immunol. 2012;12(2):136-48. Epub 2012/01/24. doi: 10.1038/nri3152. PubMed PMID: 22266691; PMCID: PMC3764486.

48. Hampton HR, Chtanova T. Lymphatic Migration of Immune Cells. Front Immunol. 2019;10:1168. Epub 2019/06/14. doi: 10.3389/fimmu.2019.01168. PubMed PMID: 31191539; PMCID: PMC6546724.

49. Capece T, Kim M. The Role of Lymphatic Niches in T Cell Differentiation. Mol Cells. 2016;39(7):515-23. Epub 2016/06/17. doi: 10.14348/molcells.2016.0089. PubMed PMID: 27306645; PMCID: PMC4959015.

50. McLachlan JB, Jenkins MK. Migration and accumulation of effector CD4+ T cells in nonlymphoid tissues. Proc Am Thorac Soc. 2007;4(5):439-42. Epub 2007/08/09. doi: 10.1513/pats.200606-137MS. PubMed PMID: 17684285; PMCID: PMC2647594.

51. Nolz JC, Starbeck-Miller GR, Harty JT. Naive, effector and memory CD8 T-cell trafficking: parallels and distinctions. Immunotherapy. 2011;3(10):1223-33. Epub 2011/10/15. doi: 10.2217/imt.11.100. PubMed PMID: 21995573; PMCID: PMC3214994.

52. Doulatov S, Notta F, Laurenti E, Dick JE. Hematopoiesis: a human perspective. Cell Stem Cell. 2012;10(2):120-36. Epub 2012/02/07. doi: 10.1016/j.stem.2012.01.006. PubMed PMID: 22305562.

53. Schwarz BA, Bhandoola A. Trafficking from the bone marrow to the thymus: a prerequisite for thymopoiesis. Immunol Rev. 2006;209:47-57. Epub 2006/02/02. doi: 10.1111/j.0105-2896.2006.00350.x. PubMed PMID: 16448533.

54. Serwold T, Ehrlich LI, Weissman IL. Reductive isolation from bone marrow and blood implicates common lymphoid progenitors as the major source of thymopoiesis. Blood. 2009;113(4):807-15. Epub 2008/10/18. doi: 10.1182/blood-2008-08-173682. PubMed PMID: 18927436; PMCID: PMC4123410.

55. North RJ. Importance of thymus-derived lymphocytes in cell-mediated immunity to infection. Cell Immunol. 1973;7(1):166-76. Epub 1973/04/01. doi: 10.1016/0008-8749(73)90193-7. PubMed PMID: 4540430.

56. Wilson A, Held W, MacDonald HR. Two waves of recombinase gene expression in developing thymocytes. J Exp Med. 1994;179(4):1355-60. Epub 1994/04/01. doi: 10.1084/jem.179.4.1355. PubMed PMID: 8145048; PMCID: PMC2191458.

57. Petrie HT, Livak F, Schatz DG, Strasser A, Crispe IN, Shortman K. Multiple rearrangements in T cell receptor alpha chain genes maximize the production of useful thymocytes. J Exp Med. 1993;178(2):615-22. Epub 1993/08/01. doi: 10.1084/jem.178.2.615. PubMed PMID: 8393478; PMCID: PMC2191132.

58. Kajita MK, Yokota R, Aihara K, Kobayashi TJ. Experimental and theoretical bases for mechanisms of antigen discrimination by T cells. Biophysics (Nagoya-shi). 2015;11:85-92. Epub 2015/01/01. doi: 10.2142/biophysics.11.85. PubMed PMID: 27493520; PMCID: PMC4736787.

59. Neefjes J, Jongsma ML, Paul P, Bakke O. Towards a systems understanding of MHC class I and MHC class II antigen presentation. Nat Rev Immunol. 2011;11(12):823-36. Epub 2011/11/15. doi: 10.1038/nri3084. PubMed PMID: 22076556.

60. Klein L, Hinterberger M, Wirnsberger G, Kyewski B. Antigen presentation in the thymus for positive selection and central tolerance induction. Nat Rev Immunol. 2009;9(12):833-44. Epub 2009/11/26. doi: 10.1038/nri2669. PubMed PMID: 19935803.

61. Klein L, Kyewski B, Allen PM, Hogquist KA. Positive and negative selection of the T cell repertoire: what thymocytes see (and don't see). Nat Rev Immunol. 2014;14(6):377-91. Epub 2014/05/17. doi: 10.1038/nri3667. PubMed PMID: 24830344; PMCID: PMC4757912.

62. Nishana M, Raghavan SC. Role of recombination activating genes in the generation of antigen receptor diversity and beyond. Immunology. 2012;137(4):271-81. Epub 2012/10/09. doi: 10.1111/imm.12009. PubMed PMID: 23039142; PMCID: PMC3530083.

63. Curotto de Lafaille MA, Lafaille JJ. Natural and adaptive foxp3+ regulatory T cells: more of the same or a division of labor? Immunity. 2009;30(5):626-35. Epub 2009/05/26. doi: 10.1016/j.immuni.2009.05.002. PubMed PMID: 19464985.

64. Perniola R. Twenty Years of AIRE. Front Immunol. 2018;9:98. Epub 2018/02/28. doi: 10.3389/fimmu.2018.00098. PubMed PMID: 29483906; PMCID: PMC5816566.

65. Golubovskaya V, Wu L. Different Subsets of T Cells, Memory, Effector Functions, and CAR-T Immunotherapy. Cancers (Basel). 2016;8(3). Epub 2016/03/22. doi: 10.3390/cancers8030036. PubMed PMID: 26999211; PMCID: PMC4810120.

66. Kanamori M, Nakatsukasa H, Okada M, Lu Q, Yoshimura A. Induced Regulatory T Cells: Their Development, Stability, and Applications. Trends Immunol. 2016;37(11):803-11. Epub 2016/09/14. doi: 10.1016/j.it.2016.08.012. PubMed PMID: 27623114.

67. Corthay A. How do regulatory T cells work? Scand J Immunol. 2009;70(4):326-36. Epub 2009/09/16. doi: 10.1111/j.1365-3083.2009.02308.x. PubMed PMID: 19751267; PMCID: PMC2784904.

68. Rudensky AY. Regulatory T cells and Foxp3. Immunol Rev. 2011;241(1):260-8. Epub 2011/04/15. doi: 10.1111/j.1600-065X.2011.01018.x. PubMed PMID: 21488902; PMCID: PMC3077798.

69. Wan YY. Multi-tasking of helper T cells. Immunology. 2010;130(2):166-71. Epub 2010/06/19. doi: 10.1111/j.1365-2567.2010.03289.x. PubMed PMID: 20557575; PMCID: PMC2878461.

70. Victora GD, Nussenzweig MC. Germinal centers. Annu Rev Immunol. 2012;30:429-57. Epub 2012/01/10. doi: 10.1146/annurev-immunol-020711-075032. PubMed PMID: 22224772.

71. St Paul M, Ohashi PS. The Roles of CD8(+) T Cell Subsets in Antitumor Immunity. Trends Cell Biol. 2020;30(9):695-704. Epub 2020/07/07. doi: 10.1016/j.tcb.2020.06.003. PubMed PMID: 32624246.

72. Yu Y, Ma X, Gong R, Zhu J, Wei L, Yao J. Recent advances in CD8(+) regulatory T cell research. Oncol Lett. 2018;15(6):8187-94. Epub 2018/05/29. doi: 10.3892/ol.2018.8378. PubMed PMID: 29805553; PMCID: PMC5950136.

73. Perdomo-Celis F, Taborda NA, Rugeles MT. Follicular CD8(+) T Cells: Origin, Function and Importance during HIV Infection. Front Immunol. 2017;8:1241. Epub 2017/11/01. doi: 10.3389/fimmu.2017.01241. PubMed PMID: 29085360; PMCID: PMC5649150.

74. Chen Y, Yu M, Zheng Y, Fu G, Xin G, Zhu W, Luo L, Burns R, Li QZ, Dent AL, Zhu N, Cui W, Malherbe L, Wen R, Wang D. CXCR5(+)PD-1(+) follicular helper CD8 T cells control B cell tolerance. Nat Commun. 2019;10(1):4415. Epub 2019/09/29. doi: 10.1038/s41467-019-12446-5. PubMed PMID: 31562329; PMCID: PMC6765049.

75. Yang Y, Ochando JC, Bromberg JS, Ding Y. Identification of a distant T-bet enhancer responsive to IL-12/Stat4 and IFNgamma/Stat1 signals. Blood. 2007;110(7):2494-500. Epub 2007/06/19. doi: 10.1182/blood-2006-11-058271. PubMed PMID: 17575072; PMCID: PMC1988915.

76. Chan WL, Pejnovic N, Lee CA, Al-Ali NA. Human IL-18 receptor and ST2L are stable and selective markers for the respective type 1 and type 2 circulating lymphocytes. J Immunol. 2001;167(3):1238-44. Epub 2001/07/24. doi: 10.4049/jimmunol.167.3.1238. PubMed PMID: 11466339.

77. Gattinoni L. Memory T cells officially join the stem cell club. Immunity. 2014;41(1):7-9. Epub 2014/07/19. doi: 10.1016/j.immuni.2014.07.003. PubMed PMID: 25035947; PMCID: PMC6377559.

78. Mueller SN, Gebhardt T, Carbone FR, Heath WR. Memory T cell subsets, migration patterns, and tissue residence. Annu Rev Immunol. 2013;31:137-61. Epub 2012/12/12. doi: 10.1146/annurev-immunol-032712-095954. PubMed PMID: 23215646.

79. Youngblood B, Hale JS, Ahmed R. T-cell memory differentiation: insights from transcriptional signatures and epigenetics. Immunology. 2013;139(3):277-84. Epub 2013/01/26. doi: 10.1111/imm.12074. PubMed PMID: 23347146; PMCID: PMC3701173.

80. Zhang N, Hartig H, Dzhagalov I, Draper D, He YW. The role of apoptosis in the development and function of T lymphocytes. Cell Res. 2005;15(10):749-69. Epub 2005/10/26. doi: 10.1038/sj.cr.7290345. PubMed PMID: 16246265.

81. Obar JJ, Lefrancois L. Memory CD8+ T cell differentiation. Ann N Y Acad Sci. 2010;1183:251-66. Epub 2010/02/12. doi: 10.1111/j.1749-6632.2009.05126.x. PubMed PMID: 20146720; PMCID: PMC2836783.

82. Martinez RJ, Evavold BD. Lower Affinity T Cells are Critical Components and Active Participants of the Immune Response. Front Immunol. 2015;6:468. Epub 2015/10/07. doi: 10.3389/fimmu.2015.00468. PubMed PMID: 26441973; PMCID: PMC4564719.

83. Patrick MS, Cheng NL, Kim J, An J, Dong F, Yang Q, Zou I, Weng NP. Human T Cell Differentiation Negatively Regulates Telomerase Expression Resulting in Reduced Activation-Induced Proliferation and Survival. Front Immunol. 2019;10:1993. Epub 2019/09/10. doi: 10.3389/fimmu.2019.01993. PubMed PMID: 31497023; PMCID: PMC6712505.

84. Gattinoni L, Speiser DE, Lichterfeld M, Bonini C. T memory stem cells in health and disease. Nat Med. 2017;23(1):18-27. Epub 2017/01/07. doi: 10.1038/nm.4241. PubMed PMID: 28060797; PMCID: PMC6354775.

85. Kaech SM, Wherry EJ, Ahmed R. Effector and memory T-cell differentiation: implications for vaccine development. Nat Rev Immunol. 2002;2(4):251-62. Epub 2002/05/11. doi: 10.1038/nri778. PubMed PMID: 12001996.

86. Woodland DL, Kohlmeier JE. Migration, maintenance and recall of memory T cells in peripheral tissues. Nat Rev Immunol. 2009;9(3):153-61. Epub 2009/02/26. doi: 10.1038/nri2496. PubMed PMID: 19240755.

87. Cui W, Kaech SM. Generation of effector CD8+ T cells and their conversion to memory T cells. Immunol Rev. 2010;236:151-66. Epub 2010/07/20. doi: 10.1111/j.1600-065X.2010.00926.x. PubMed PMID: 20636815; PMCID: PMC4380273.

88. Gebhardt T, Mueller SN, Heath WR, Carbone FR. Peripheral tissue surveillance and residency by memory T cells. Trends Immunol. 2013;34(1):27-32. Epub 2012/10/06. doi: 10.1016/j.it.2012.08.008. PubMed PMID: 23036434.

89. Dustin ML. The immunological synapse. Cancer Immunol Res. 2014;2(11):1023-33. Epub 2014/11/05. doi: 10.1158/2326-6066.CIR-14-0161. PubMed PMID: 25367977; PMCID: PMC4692051.

90. Davis SJ, van der Merwe PA. The kinetic-segregation model: TCR triggering and beyond. Nat Immunol. 2006;7(8):803-9. Epub 2006/07/21. doi: 10.1038/ni1369. PubMed PMID: 16855606.

91. Courtney AH, Lo WL, Weiss A. TCR Signaling: Mechanisms of Initiation and Propagation. Trends Biochem Sci. 2018;43(2):108-23. Epub 2017/12/23. doi: 10.1016/j.tibs.2017.11.008. PubMed PMID: 29269020; PMCID: PMC5801066.

92. Grakoui A, Bromley SK, Sumen C, Davis MM, Shaw AS, Allen PM, Dustin ML. The immunological synapse: a molecular machine controlling T cell activation. Science. 1999;285(5425):221-7. Epub 1999/07/10. doi: 10.1126/science.285.5425.221. PubMed PMID: 10398592.

93. Ritter AT, Angus KL, Griffiths GM. The role of the cytoskeleton at the immunological synapse. Immunol Rev. 2013;256(1):107-17. Epub 2013/10/15. doi: 10.1111/imr.12117. PubMed PMID: 24117816; PMCID: PMC4312978.

94. Kumari S, Curado S, Mayya V, Dustin ML. T cell antigen receptor activation and actin cytoskeleton remodeling. Biochim Biophys Acta. 2014;1838(2):546-56. Epub 2013/05/18. doi: 10.1016/j.bbamem.2013.05.004. PubMed PMID: 23680625; PMCID: PMC3877165.

95. Razvag Y, Neve-Oz Y, Sajman J, Yakovian O, Reches M, Sherman E. T Cell Activation through Isolated Tight Contacts. Cell Rep. 2019;29(11):3506-21 e6. Epub 2019/12/12. doi: 10.1016/j.celrep.2019.11.022. PubMed PMID: 31825832.

96. Hammer JA, Wang JC, Saeed M, Pedrosa AT. Origin, Organization, Dynamics, and Function of Actin and Actomyosin Networks at the T Cell Immunological Synapse. Annu Rev Immunol. 2019;37:201-24. Epub 2018/12/24. doi: 10.1146/annurev-immunol-042718-041341. PubMed PMID: 30576253.

97. Roy NH, Burkhardt JK. The Actin Cytoskeleton: A Mechanical Intermediate for Signal Integration at the Immunological Synapse. Front Cell Dev Biol. 2018;6:116. Epub 2018/10/05. doi: 10.3389/fcell.2018.00116. PubMed PMID: 30283780; PMCID: PMC6156151.

98. Garcia KC, Degano M, Stanfield RL, Brunmark A, Jackson MR, Peterson PA, Teyton L, Wilson IA. An alphabeta T cell receptor structure at 2.5 A and its orientation in the TCR-MHC complex. Science. 1996;274(5285):209-19. Epub 1996/10/11. doi: 10.1126/science.274.5285.209. PubMed PMID: 8824178.

99. Morath A, Schamel WW. alphabeta and gammadelta T cell receptors: Similar but different. J Leukoc Biol. 2020;107(6):1045-55. Epub 2020/01/30. doi: 10.1002/JLB.2MR1219-233R. PubMed PMID: 31994778.

100. Joachims ML, Chain JL, Hooker SW, Knott-Craig CJ, Thompson LF. Human alpha beta and gamma delta thymocyte development: TCR gene rearrangements, intracellular TCR beta expression, and gamma delta developmental potential--differences between men and mice. J Immunol. 2006;176(3):1543-52. Epub 2006/01/21. doi: 10.4049/jimmunol.176.3.1543. PubMed PMID: 16424183; PMCID: PMC1592528.

101. Wucherpfennig KW, Gagnon E, Call MJ, Huseby ES, Call ME. Structural biology of the T-cell receptor: insights into receptor assembly, ligand recognition, and initiation of signaling. Cold Spring Harb Perspect Biol. 2010;2(4):a005140. Epub 2010/05/11. doi: 10.1101/cshperspect.a005140. PubMed PMID: 20452950; PMCID: PMC2845206.

102. Dong, Zheng L, Lin J, Zhang B, Zhu Y, Li N, Xie S, Wang Y, Gao N, Huang Z. Structural basis of assembly of the human T cell receptor-CD3 complex. Nature. 2019;573(7775):546-52. Epub 2019/08/29. doi: 10.1038/s41586-019-1537-0. PubMed PMID: 31461748.

103. Mariuzza RA, Agnihotri P, Orban J. The structural basis of T-cell receptor (TCR) activation: An enduring enigma. J Biol Chem. 2020;295(4):914-25. Epub 2019/12/19. doi: 10.1074/jbc.REV119.009411. PubMed PMID: 31848223; PMCID: PMC6983839.

104. Jung D, Alt FW. Unraveling V(D)J recombination; insights into gene regulation. Cell. 2004;116(2):299-311. Epub 2004/01/28. doi: 10.1016/s0092-8674(04)00039-x. PubMed PMID: 14744439.

105. Roth DB. V(D)J Recombination: Mechanism, Errors, and Fidelity. Microbiol Spectr. 2014;2(6). Epub 2015/06/25. doi: 10.1128/microbiolspec.MDNA3-0041-2014. PubMed PMID: 26104458; PMCID: PMC5089068.

106. Schatz DG, Ji Y. Recombination centres and the orchestration of V(D)J recombination. Nat Rev Immunol. 2011;11(4):251-63. Epub 2011/03/12. doi: 10.1038/nri2941. PubMed PMID: 21394103.

107. Baxter AG, Hodgkin PD. Activation rules: the two-signal theories of immune activation. Nat Rev Immunol. 2002;2(6):439-46. Epub 2002/07/03. doi: 10.1038/nri823. PubMed PMID: 12093010.

108. Bernard A, Lamy, Alberti I. The two-signal model of T-cell activation after 30 years. Transplantation. 2002;73(1 Suppl):S31-5. Epub 2002/01/26. doi: 10.1097/00007890-200201151-00011. PubMed PMID: 11810059.

109. Buchbinder EI, Desai A. CTLA-4 and PD-1 Pathways: Similarities, Differences, and Implications of Their Inhibition. Am J Clin Oncol. 2016;39(1):98-106. Epub 2015/11/13. doi: 10.1097/COC.0000000000000239. PubMed PMID: 26558876; PMCID: PMC4892769.

110. Chen L, Flies DB. Molecular mechanisms of T cell co-stimulation and co-inhibition. Nat Rev Immunol. 2013;13(4):227-42. Epub 2013/03/09. doi: 10.1038/nri3405. PubMed PMID: 23470321; PMCID: PMC3786574.

111. Ward-Kavanagh LK, Lin WW, Sedy JR, Ware CF. The TNF Receptor Superfamily in Co-stimulating and Co-inhibitory Responses. Immunity. 2016;44(5):1005-19. Epub 2016/05/19. doi: 10.1016/j.immuni.2016.04.019. PubMed PMID: 27192566; PMCID: PMC4882112.

112. Martin PJ, Ledbetter JA, Morishita Y, June CH, Beatty PG, Hansen JA. A 44 kilodalton cell surface homodimer regulates interleukin 2 production by activated human T lymphocytes. J Immunol. 1986;136(9):3282-7. Epub 1986/05/01. PubMed PMID: 3082984.

113. Gray Parkin K, Stephan RP, Apilado RG, Lill-Elghanian DA, Lee KP, Saha B, Witte PL. Expression of CD28 by bone marrow stromal cells and its involvement in B lymphopoiesis. J Immunol. 2002;169(5):2292-302. Epub 2002/08/24. doi: 10.4049/jimmunol.169.5.2292. PubMed PMID: 12193694.

114. Rozanski CH, Arens R, Carlson LM, Nair J, Boise LH, Chanan-Khan AA, Schoenberger SP, Lee KP. Sustained antibody responses depend on CD28 function in bone marrow-resident plasma cells. J Exp Med. 2011;208(7):1435-46. Epub 2011/06/22. doi: 10.1084/jem.20110040. PubMed PMID: 21690252; PMCID: PMC3135367.

115. Woerly G, Decot V, Loiseau S, Loyens M, Chihara J, Ono N, Capron M. CD28 and secretory immunoglobulin A-dependent activation of eosinophils: inhibition of mediator release by the anti-allergic drug, suplatast tosilate. Clin Exp Allergy. 2004;34(9):1379-87. Epub 2004/09/07. doi: 10.1111/j.1365-2222.2004.02036.x. PubMed PMID: 15347370.

116. Venuprasad K, Parab P, Prasad DV, Sharma S, Banerjee PR, Deshpande M, Mitra DK, Pal S, Bhadra R, Mitra D, Saha B. Immunobiology of CD28 expression on human neutrophils. I. CD28 regulates neutrophil migration by modulating CXCR-1 expression. Eur J Immunol. 2001;31(5):1536-43. Epub 2001/07/24. doi: 10.1002/1521-4141(200105)31:5<1536::AID-IMMU1536>3.0.CO;2-8. PubMed PMID: 11465111.

117. Weng NP, Akbar AN, Goronzy J. CD28(-) T cells: their role in the age-associated decline of immune function. Trends Immunol. 2009;30(7):306-12. Epub 2009/06/23. doi: 10.1016/j.it.2009.03.013. PubMed PMID: 19540809; PMCID: PMC2801888.

118. Gross JA, Callas E, Allison JP. Identification and distribution of the costimulatory receptor CD28 in the mouse. J Immunol. 1992;149(2):380-8. Epub 1992/07/15. PubMed PMID: 1320641.

119. Evans EJ, Esnouf RM, Manso-Sancho R, Gilbert RJ, James JR, Yu C, Fennelly JA, Vowles C, Hanke T, Walse B, Hunig T, Sorensen P, Stuart DI, Davis SJ. Crystal structure of a soluble CD28-Fab complex. Nat Immunol. 2005;6(3):271-9. Epub 2005/02/08. doi: 10.1038/ni1170. PubMed PMID: 15696168.

120. van der Merwe PA, Bodian DL, Daenke S, Linsley P, Davis SJ. CD80 (B7-1) binds both CD28 and CTLA-4 with a low affinity and very fast kinetics. J Exp Med. 1997;185(3):393-403. Epub 1997/02/03. doi: 10.1084/jem.185.3.393. PubMed PMID: 9053440; PMCID: PMC2196039.

121. Collins AV, Brodie DW, Gilbert RJ, Iaboni A, Manso-Sancho R, Walse B, Stuart DI, van der Merwe PA, Davis SJ. The interaction properties of costimulatory molecules revisited. Immunity. 2002;17(2):201-10. Epub 2002/08/28. doi: 10.1016/s1074-7613(02)00362-x. PubMed PMID: 12196291.

122. Peach RJ, Bajorath J, Naemura J, Leytze G, Greene J, Aruffo A, Linsley PS. Both extracellular immunoglobin-like domains of CD80 contain residues critical for binding T cell surface receptors CTLA-4 and CD28. J Biol Chem. 1995;270(36):21181-7. Epub 1995/09/08. doi: 10.1074/jbc.270.36.21181. PubMed PMID: 7545666.

123. Lucas CR, Cordero-Nieves HM, Erbe RS, McAlees JW, Bhatia S, Hodes RJ, Campbell KS, Sanders VM. Prohibitins and the cytoplasmic domain of CD86 cooperate to mediate CD86 signaling in B lymphocytes. J Immunol. 2013;190(2):723-36. Epub 2012/12/18. doi: 10.4049/jimmunol.1201646. PubMed PMID: 23241883; PMCID: PMC3538926.

124. Girard T, El-Far M, Gaucher D, Acuto O, Beaule G, Michel F, Mourad W, Sekaly RP. A conserved polylysine motif in CD86 cytoplasmic tail is necessary for cytoskeletal association and effective co-stimulation. Biochem Biophys Res Commun. 2012;423(2):301-7. Epub 2012/06/05. doi: 10.1016/j.bbrc.2012.05.116. PubMed PMID: 22659416.

125. Tseng SY, Liu M, Dustin ML. CD80 cytoplasmic domain controls localization of CD28, CTLA-4, and protein kinase Ctheta in the immunological synapse. J Immunol. 2005;175(12):7829-36. Epub 2005/12/13. doi: 10.4049/jimmunol.175.12.7829. PubMed PMID: 16339518; PMCID: PMC1626532.

126. Koorella C, Nair JR, Murray ME, Carlson LM, Watkins SK, Lee KP. Novel regulation of CD80/CD86-induced phosphatidylinositol 3-kinase signaling by NOTCH1 protein in interleukin-6 and indoleamine 2,3-dioxygenase production by dendritic cells. J Biol Chem. 2014;289(11):7747-62. Epub 2014/01/15. doi: 10.1074/jbc.M113.519686. PubMed PMID: 24415757; PMCID: PMC3953285.

127. Soskic B, Jeffery LE, Kennedy A, Gardner DH, Hou TZ, Halliday N, Williams C, Janman D, Rowshanravan B, Hirschfield GM, Sansom DM. CD80 on Human T Cells Is Associated With FoxP3 Expression and Supports Treg Homeostasis. Front Immunol. 2020;11:577655. Epub 2021/01/26. doi: 10.3389/fimmu.2020.577655. PubMed PMID: 33488578; PMCID: PMC7820758.

128. Bhatia S, Edidin M, Almo SC, Nathenson SG. Different cell surface oligomeric states of B7-1 and B7-2: implications for signaling. Proc Natl Acad Sci U S A. 2005;102(43):15569-74. Epub 2005/10/14. doi: 10.1073/pnas.0507257102. PubMed PMID: 16221763; PMCID: PMC1266120.

129. Mongini PK, Tolani S, Fattah RJ, Inman JK. Antigen receptor triggered upregulation of CD86 and CD80 in human B cells: augmenting role of the CD21/CD19 co-stimulatory complex and IL-4. Cell Immunol. 2002;216(1-2):50-64. Epub 2002/10/17. doi: 10.1016/s0008-8749(02)00512-9. PubMed PMID: 12381350.

130. Hathcock KS, Laszlo G, Pucillo C, Linsley P, Hodes RJ. Comparative analysis of B7-1 and B7-2 costimulatory ligands: expression and function. J Exp Med. 1994;180(2):631-40. Epub 1994/08/01. doi: 10.1084/jem.180.2.631. PubMed PMID: 7519245; PMCID: PMC2191623.

131. Hewitt EW. The MHC class I antigen presentation pathway: strategies for viral immune evasion. Immunology. 2003;110(2):163-9. Epub 2003/09/27. doi: 10.1046/j.1365-2567.2003.01738.x. PubMed PMID: 14511229; PMCID: PMC1783040.

132. Roche PA, Furuta K. The ins and outs of MHC class II-mediated antigen processing and presentation. Nat Rev Immunol. 2015;15(4):203-16. Epub 2015/02/28. doi: 10.1038/nri3818. PubMed PMID: 25720354; PMCID: PMC6314495.

133. Barral DC, Brenner MB. CD1 antigen presentation: how it works. Nat Rev Immunol. 2007;7(12):929-41. Epub 2007/11/27. doi: 10.1038/nri2191. PubMed PMID: 18037897.

134. Rossjohn J, Gras S, Miles JJ, Turner SJ, Godfrey DI, McCluskey J. T cell antigen receptor recognition of antigen-presenting molecules. Annu Rev Immunol. 2015;33:169-200. Epub 2014/12/11. doi: 10.1146/annurev-immunol-032414-112334. PubMed PMID: 25493333.

135. Papavasiliou FN, Schatz DG. Somatic hypermutation of immunoglobulin genes: merging mechanisms for genetic diversity. Cell. 2002;109 Suppl:S35-44. Epub 2002/05/02. doi: 10.1016/s0092-8674(02)00706-7. PubMed PMID: 11983151.

136. Yuseff MI, Pierobon P, Reversat A, Lennon-Dumenil AM. How B cells capture, process and present antigens: a crucial role for cell polarity. Nat Rev Immunol. 2013;13(7):475-86. Epub 2013/06/26. doi: 10.1038/nri3469. PubMed PMID: 23797063.

137. Joffre OP, Segura E, Savina A, Amigorena S. Cross-presentation by dendritic cells. Nat Rev Immunol. 2012;12(8):557-69. Epub 2012/07/14. doi: 10.1038/nri3254. PubMed PMID: 22790179.

138. Boomer JS, Green JM. An enigmatic tail of CD28 signaling. Cold Spring Harb Perspect Biol. 2010;2(8):a002436. Epub 2010/06/11. doi: 10.1101/cshperspect.a002436. PubMed PMID: 20534709; PMCID: PMC2908766.

139. Harada Y, Tanabe E, Watanabe R, Weiss BD, Matsumoto A, Ariga H, Koiwai O, Fukui Y, Kubo M, June CH, Abe R. Novel role of phosphatidylinositol 3-kinase in CD28-mediated costimulation. J Biol Chem. 2001;276(12):9003-8. Epub 2000/12/23. doi: 10.1074/jbc.M005051200. PubMed PMID: 11113113.

140. King PD, Sadra A, Teng JM, Xiao-Rong L, Han A, Selvakumar A, August A, Dupont B. Analysis of CD28 cytoplasmic tail tyrosine residues as regulators and substrates for the protein tyrosine kinases, EMT and LCK. J Immunol. 1997;158(2):580-90. Epub 1997/01/15. PubMed PMID: 8992971.

141. Truitt KE, Hicks CM, Imboden JB. Stimulation of CD28 triggers an association between CD28 and phosphatidylinositol 3-kinase in Jurkat T cells. J Exp Med. 1994;179(3):1071-6. Epub 1994/03/01. doi: 10.1084/jem.179.3.1071. PubMed PMID: 7509360; PMCID: PMC2191424.

142. Watanabe R, Harada Y, Takeda K, Takahashi J, Ohnuki K, Ogawa S, Ohgai D, Kaibara N, Koiwai O, Tanabe K, Toma H, Sugamura K, Abe R. Grb2 and Gads exhibit different interactions with CD28 and play distinct roles in CD28-mediated costimulation. J Immunol. 2006;177(2):1085-91. Epub 2006/07/05. doi: 10.4049/jimmunol.177.2.1085. PubMed PMID: 16818765.

143. Harada Y, Ohgai D, Watanabe R, Okano K, Koiwai O, Tanabe K, Toma H, Altman A, Abe R. A single amino acid alteration in cytoplasmic domain determines IL-2 promoter activation by ligation of CD28 but not inducible costimulator (ICOS). J Exp Med. 2003;197(2):257-62. Epub 2003/01/23. doi: 10.1084/jem.20021305. PubMed PMID: 12538664; PMCID: PMC2193818.

144. Kim HH, Tharayil M, Rudd CE. Growth factor receptor-bound protein 2 SH2/SH3 domain binding to CD28 and its role in co-signaling. J Biol Chem. 1998;273(1):296-301. Epub 1998/02/07. doi: 10.1074/jbc.273.1.296. PubMed PMID: 9417079.

145. Rudd CE, Schneider H. Unifying concepts in CD28, ICOS and CTLA4 co-receptor signalling. Nat Rev Immunol. 2003;3(7):544-56. Epub 2003/07/24. doi: 10.1038/nri1131. PubMed PMID: 12876557.

146. Park SG, Schulze-Luehrman J, Hayden MS, Hashimoto N, Ogawa W, Kasuga M, Ghosh S. The kinase PDK1 integrates T cell antigen receptor and CD28 coreceptor signaling to induce NF-kappaB and activate T cells. Nat Immunol. 2009;10(2):158-66. Epub 2009/01/06. doi: 10.1038/ni.1687. PubMed PMID: 19122654; PMCID: PMC2768497.

147. Coudronniere N, Villalba M, Englund N, Altman A. NF-kappa B activation induced by T cell receptor/CD28 costimulation is mediated by protein kinase C-theta. Proc Natl Acad Sci U S A. 2000;97(7):3394-9. Epub 2000/03/15. doi: 10.1073/pnas.060028097. PubMed PMID: 10716728; PMCID: PMC16250.

148. Pfeifhofer C, Kofler K, Gruber T, Tabrizi NG, Lutz C, Maly K, Leitges M, Baier G. Protein kinase C theta affects Ca2+ mobilization and NFAT cell activation in primary

mouse T cells. J Exp Med. 2003;197(11):1525-35. Epub 2003/06/05. doi: 10.1084/jem.20020234. PubMed PMID: 12782715; PMCID: PMC2193906.

149. Muller MR, Rao A. NFAT, immunity and cancer: a transcription factor comes of age. Nat Rev Immunol. 2010;10(9):645-56. Epub 2010/08/21. doi: 10.1038/nri2818. PubMed PMID: 20725108.

150. Salazar-Fontana LI, Barr V, Samelson LE, Bierer BE. CD28 engagement promotes actin polymerization through the activation of the small Rho GTPase Cdc42 in human T cells. J Immunol. 2003;171(5):2225-32. Epub 2003/08/21. doi: 10.4049/jimmunol.171.5.2225. PubMed PMID: 12928366.

151. Bustelo XR. Vav proteins, adaptors and cell signaling. Oncogene. 2001;20(44):6372-81. Epub 2001/10/19. doi: 10.1038/sj.onc.1204780. PubMed PMID: 11607839.

152. Fischer KD, Kong YY, Nishina H, Tedford K, Marengere LE, Kozieradzki I, Sasaki T, Starr M, Chan G, Gardener S, Nghiem MP, Bouchard D, Barbacid M, Bernstein A, Penninger JM. Vav is a regulator of cytoskeletal reorganization mediated by the T-cell receptor. Curr Biol. 1998;8(10):554-62. Epub 1998/05/28. doi: 10.1016/s0960-9822(98)70224-6. PubMed PMID: 9601639.

153. Muscolini M, Camperio C, Porciello N, Caristi S, Capuano C, Viola A, Galandrini R, Tuosto L. Phosphatidylinositol 4-phosphate 5-kinase alpha and Vav1 mutual cooperation in CD28-mediated actin remodeling and signaling functions. J Immunol. 2015;194(3):1323-33. Epub 2014/12/30. doi: 10.4049/jimmunol.1401643. PubMed PMID: 25539813.

154. Saarikangas J, Zhao H, Lappalainen P. Regulation of the actin cytoskeleton-plasma membrane interplay by phosphoinositides. Physiol Rev. 2010;90(1):259-89. Epub 2010/01/21. doi: 10.1152/physrev.00036.2009. PubMed PMID: 20086078.

155. Tavano R, Contento RL, Baranda SJ, Soligo M, Tuosto L, Manes S, Viola A. CD28 interaction with filamin-A controls lipid raft accumulation at the T-cell immunological synapse. Nat Cell Biol. 2006;8(11):1270-6. Epub 2006/10/25. doi: 10.1038/ncb1492. PubMed PMID: 17060905.

156. Riha P, Rudd CE. CD28 co-signaling in the adaptive immune response. Self Nonself. 2010;1(3):231-40. Epub 2011/04/14. doi: 10.4161/self.1.3.12968. PubMed PMID: 21487479; PMCID: PMC3047785.

157. Yokosuka T, Kobayashi W, Sakata-Sogawa K, Takamatsu M, Hashimoto-Tane A, Dustin ML, Tokunaga M, Saito T. Spatiotemporal regulation of T cell costimulation by TCR-CD28 microclusters and protein kinase C theta translocation. Immunity. 2008;29(4):589-601. Epub 2008/10/14. doi: 10.1016/j.immuni.2008.08.011. PubMed PMID: 18848472; PMCID: PMC2950619.

158. Sanchez-Lockhart M, Graf B, Miller J. Signals and sequences that control CD28 localization to the central region of the immunological synapse. J Immunol. 2008;181(11):7639-48. Epub 2008/11/20. doi: 10.4049/jimmunol.181.11.7639. PubMed PMID: 19017952; PMCID: PMC3993010.

159. Hayashi K, Altman A. Filamin A is required for T cell activation mediated by protein kinase C-theta. J Immunol. 2006;177(3):1721-8. Epub 2006/07/20. doi: 10.4049/jimmunol.177.3.1721. PubMed PMID: 16849481.

160. Tan YX, Manz BN, Freedman TS, Zhang C, Shokat KM, Weiss A. Inhibition of the kinase Csk in thymocytes reveals a requirement for actin remodeling in the initiation of full TCR signaling. Nat Immunol. 2014;15(2):186-94. Epub 2013/12/10. doi: 10.1038/ni.2772. PubMed PMID: 24317039; PMCID: PMC3946925.

161. van der Merwe PA, Dushek O. Mechanisms for T cell receptor triggering. Nat Rev Immunol. 2011;11(1):47-55. Epub 2010/12/04. doi: 10.1038/nri2887. PubMed PMID: 21127503.

162. George AJ, Stark J, Chan C. Understanding specificity and sensitivity of T-cell recognition. Trends Immunol. 2005;26(12):653-9. Epub 2005/10/21. doi: 10.1016/j.it.2005.09.011. PubMed PMID: 16236548.

163. Irvine DJ, Purbhoo MA, Krogsgaard M, Davis MM. Direct observation of ligand recognition by T cells. Nature. 2002;419(6909):845-9. Epub 2002/10/25. doi: 10.1038/nature01076. PubMed PMID: 12397360.

164. Krogsgaard M, Davis MM. How T cells 'see' antigen. Nat Immunol. 2005;6(3):239-45. Epub 2005/02/18. doi: 10.1038/ni1173. PubMed PMID: 15716973.

165. Sewell AK. Why must T cells be cross-reactive? Nat Rev Immunol. 2012;12(9):669-77. Epub 2012/08/25. doi: 10.1038/nri3279. PubMed PMID: 22918468; PMCID: PMC7097784.

166. Jameson SC. T cell receptor antagonism in vivo, at last. Proc Natl Acad Sci U S A. 1998;95(24):14001-2. Epub 1998/11/25. doi: 10.1073/pnas.95.24.14001. PubMed PMID: 9826640; PMCID: PMC33920.

167. Stotz SH, Bolliger L, Carbone FR, Palmer E. T cell receptor (TCR) antagonism without a negative signal: evidence from T cell hybridomas expressing two independent TCRs. J Exp Med. 1999;189(2):253-64. Epub 1999/01/20. doi: 10.1084/jem.189.2.253. PubMed PMID: 9892608; PMCID: PMC2192976.

168. Cusick MF, Libbey JE, Fujinami RS. Molecular mimicry as a mechanism of autoimmune disease. Clin Rev Allergy Immunol. 2012;42(1):102-11. Epub 2011/11/19. doi: 10.1007/s12016-011-8293-8

10.1007/s12016-011-8294-7. PubMed PMID: 22095454; PMCID: PMC3266166.

169. Takeshima H, Ushijima T. Accumulation of genetic and epigenetic alterations in normal cells and cancer risk. NPJ Precis Oncol. 2019;3:7. Epub 2019/03/12. doi: 10.1038/s41698-019-0079-0. PubMed PMID: 30854468; PMCID: PMC6403339 patent for detecting rare point mutations using a small number of sequencing templates.

170. Nguyen DX, Massague J. Genetic determinants of cancer metastasis. Nat Rev Genet. 2007;8(5):341-52. Epub 2007/04/19. doi: 10.1038/nrg2101. PubMed PMID: 17440531.

171. Caspi RR. Immunotherapy of autoimmunity and cancer: the penalty for success. Nat Rev Immunol. 2008;8(12):970-6. Epub 2008/11/15. doi: 10.1038/nri2438. PubMed PMID: 19008897; PMCID: PMC2764117.

172. Welsh RM, Selin LK. No one is naive: the significance of heterologous T-cell immunity. Nat Rev Immunol. 2002;2(6):417-26. Epub 2002/07/03. doi: 10.1038/nri820. PubMed PMID: 12093008.

173. Kamradt T, Volkmer-Engert R. Cross-reactivity of T lymphocytes in infection and autoimmunity. Mol Divers. 2004;8(3):271-80. Epub 2004/09/24. doi: 10.1023/b:modi.0000036236.11774.1b. PubMed PMID: 15384420.

174. Sanjuan R, Nebot MR, Chirico N, Mansky LM, Belshaw R. Viral mutation rates. J Virol. 2010;84(19):9733-48. Epub 2010/07/28. doi: 10.1128/JVI.00694-10. PubMed PMID: 20660197; PMCID: PMC2937809.

175. Petrova G, Ferrante A, Gorski J. Cross-reactivity of T cells and its role in the immune system. Crit Rev Immunol. 2012;32(4):349-72. Epub 2012/12/15. doi: 10.1615/critrevimmunol.v32.i4.50. PubMed PMID: 23237510; PMCID: PMC3595599.

176. van der Merwe PA, Davis SJ. Molecular interactions mediating T cell antigen recognition. Annu Rev Immunol. 2003;21:659-84. Epub 2003/03/05. doi: 10.1146/annurev.immunol.21.120601.141036. PubMed PMID: 12615890.

177. Davis MM, Boniface JJ, Reich Z, Lyons D, Hampl J, Arden B, Chien Y. Ligand recognition by alpha beta T cell receptors. Annu Rev Immunol. 1998;16:523-44. Epub 1998/05/23. doi: 10.1146/annurev.immunol.16.1.523. PubMed PMID: 9597140.

178. Wooldridge L, van den Berg HA, Glick M, Gostick E, Laugel B, Hutchinson SL, Milicic A, Brenchley JM, Douek DC, Price DA, Sewell AK. Interaction between the CD8 coreceptor and major histocompatibility complex class I stabilizes T cell receptor-antigen complexes at the cell surface. J Biol Chem. 2005;280(30):27491-501. Epub 2005/04/20. doi: 10.1074/jbc.M500555200. PubMed PMID: 15837791; PMCID: PMC2441837.

179. Valitutti S, Lanzavecchia A. Serial triggering of TCRs: a basis for the sensitivity and specificity of antigen recognition. Immunol Today. 1997;18(6):299-304. Epub 1997/06/01. PubMed PMID: 9190117.

180. Valitutti S, Muller S, Cella M, Padovan E, Lanzavecchia A. Serial triggering of many T-cell receptors by a few peptide-MHC complexes. Nature. 1995;375(6527):148-51. Epub 1995/05/11. doi: 10.1038/375148a0. PubMed PMID: 7753171.

181. Rabinowitz JD, Beeson C, Lyons DS, Davis MM, McConnell HM. Kinetic discrimination in T-cell activation. Proc Natl Acad Sci U S A. 1996;93(4):1401-5. Epub 1996/02/20. doi: 10.1073/pnas.93.4.1401. PubMed PMID: 8643643; PMCID: PMC39950.

182. Bettini ML, Chou PC, Guy CS, Lee T, Vignali KM, Vignali DAA. Cutting Edge: CD3 ITAM Diversity Is Required for Optimal TCR Signaling and Thymocyte Development. J Immunol. 2017;199(5):1555-60. Epub 2017/07/25. doi: 10.4049/jimmunol.1700069. PubMed PMID: 28733484; PMCID: PMC5568475.

183. Stefanova I, Hemmer B, Vergelli M, Martin R, Biddison WE, Germain RN. TCR ligand discrimination is enforced by competing ERK positive and SHP-1 negative feedback pathways. Nat Immunol. 2003;4(3):248-54. Epub 2003/02/11. doi: 10.1038/ni895. PubMed PMID: 12577055.

184. Rossy J, Owen DM, Williamson DJ, Yang Z, Gaus K. Conformational states of the kinase Lck regulate clustering in early T cell signaling. Nat Immunol. 2013;14(1):82-9. Epub 2012/12/04. doi: 10.1038/ni.2488. PubMed PMID: 23202272.

185. Davis SJ, van der Merwe PA. Lck and the nature of the T cell receptor trigger. Trends Immunol. 2011;32(1):1-5. Epub 2010/12/31. doi: 10.1016/j.it.2010.11.003. PubMed PMID: 21190897.

186. Lodish HF. Molecular cell biology. 4th ed. New York: W.H. Freeman; 2000. xxxix, 1084 p. p.

187. Model MA, Omann GM. Ligand-receptor interaction rates in the presence of convective mass transport. Biophys J. 1995;69(5):1712-20. Epub 1995/11/01. doi: 10.1016/S0006-3495(95)80041-X. PubMed PMID: 8580315; PMCID: PMC1236405.

188. Charras GT, Yarrow JC, Horton MA, Mahadevan L, Mitchison TJ. Non-equilibration of hydrostatic pressure in blebbing cells. Nature. 2005;435(7040):365-9. Epub 2005/05/20. doi: 10.1038/nature03550. PubMed PMID: 15902261; PMCID: PMC1564437.

189. Oster GF, Perelson AS. The physics of cell motility. J Cell Sci Suppl. 1987;8:35-54. Epub 1987/01/01. doi: 10.1242/jcs.1987.supplement_8.3. PubMed PMID: 3503893.

190. Loitto VM, Karlsson T, Magnusson KE. Water flux in cell motility: expanding the mechanisms of membrane protrusion. Cell Motil Cytoskeleton. 2009;66(5):237-47. Epub 2009/04/07. doi: 10.1002/cm.20357. PubMed PMID: 19347962.

191. Keren K, Yam PT, Kinkhabwala A, Mogilner A, Theriot JA. Intracellular fluid flow in rapidly moving cells. Nat Cell Biol. 2009;11(10):1219-24. Epub 2009/09/22. doi: 10.1038/ncb1965. PubMed PMID: 19767741; PMCID: PMC2867054.

192. Feder TJ, Brust-Mascher I, Slattery JP, Baird B, Webb WW. Constrained diffusion or immobile fraction on cell surfaces: a new interpretation. Biophys J. 1996;70(6):2767-73. Epub 1996/06/01. doi: 10.1016/S0006-3495(96)79846-6. PubMed PMID: 8744314; PMCID: PMC1225256.

193. Cooper GM. The cell : a molecular approach. 2nd ed. Washington, D.C.

Sunderland, Mass.: ASM Press ;

Sinauer Associates; 2000. xxiv, 689 p. p.

194. Tominaga M, Ito K. The molecular mechanism and physiological role of cytoplasmic streaming. Curr Opin Plant Biol. 2015;27:104-10. Epub 2015/07/24. doi: 10.1016/j.pbi.2015.06.017. PubMed PMID: 26202096.

195. Andres V, Gonzalez JM. Role of A-type lamins in signaling, transcription, and chromatin organization. J Cell Biol. 2009;187(7):945-57. Epub 2009/12/30. doi: 10.1083/jcb.200904124. PubMed PMID: 20038676; PMCID: PMC2806284.

196. Hirokawa N, Noda Y, Tanaka Y, Niwa S. Kinesin superfamily motor proteins and intracellular transport. Nat Rev Mol Cell Biol. 2009;10(10):682-96. Epub 2009/09/24. doi: 10.1038/nrm2774. PubMed PMID: 19773780.

197. Loreng TD, Smith EF. The Central Apparatus of Cilia and Eukaryotic Flagella. Cold Spring Harb Perspect Biol. 2017;9(2). Epub 2016/10/23. doi: 10.1101/cshperspect.a028118. PubMed PMID: 27770014; PMCID: PMC5287073.

198. Petry S. Mechanisms of Mitotic Spindle Assembly. Annu Rev Biochem. 2016;85:659-83. Epub 2016/05/06. doi: 10.1146/annurev-biochem-060815-014528. PubMed PMID: 27145846; PMCID: PMC5016079.

199. Brakebusch C, Fassler R. The integrin-actin connection, an eternal love affair. EMBO J. 2003;22(10):2324-33. Epub 2003/05/14. doi: 10.1093/emboj/cdg245. PubMed PMID: 12743027; PMCID: PMC156003.

200. Dufrene YF. Atomic force microscopy, a powerful tool in microbiology. J Bacteriol. 2002;184(19):5205-13. Epub 2002/09/10. doi: 10.1128/jb.184.19.5205-5213.2002. PubMed PMID: 12218005; PMCID: PMC135344.

201. van Mameren J, Wuite GJL, Heller I. Introduction to Optical Tweezers: Background, System Designs, and Commercial Solutions. Methods Mol Biol. 2018;1665:3-23. Epub 2017/09/25. doi: 10.1007/978-1-4939-7271-5_1. PubMed PMID: 28940061.

202. Sarkar R, Rybenkov VV. A Guide to Magnetic Tweezers and Their Applications. Frontiers in Physics. 2016;4:48.

203. Evans E, Ritchie K, Merkel R. Sensitive force technique to probe molecular adhesion and structural linkages at biological interfaces. Biophys J. 1995;68(6):2580-7. Epub 1995/06/01. doi: 10.1016/S0006-3495(95)80441-8. PubMed PMID: 7647261; PMCID: PMC1282168.

204. Righini M, Volpe G, Girard C, Petrov D, Quidant R. Surface plasmon optical tweezers: tunable optical manipulation in the femtonewton range. Phys Rev Lett. 2008;100(18):186804. Epub 2008/06/04. doi: 10.1103/PhysRevLett.100.186804. PubMed PMID: 18518404.

205. Neuman KC, Nagy A. Single-molecule force spectroscopy: optical tweezers, magnetic tweezers and atomic force microscopy. Nat Methods. 2008;5(6):491-505. Epub 2008/05/31. doi: 10.1038/nmeth.1218. PubMed PMID: 18511917; PMCID: PMC3397402.

206. Weisel JW, Shuman H, Litvinov RI. Protein-protein unbinding induced by force: single-molecule studies. Curr Opin Struct Biol. 2003;13(2):227-35. Epub 2003/05/03. doi: 10.1016/s0959-440x(03)00039-3. PubMed PMID: 12727517.

207. Johnson KC, Thomas WE. How Do We Know when Single-Molecule Force Spectroscopy Really Tests Single Bonds? Biophys J. 2018;114(9):2032-9. Epub 2018/05/10. doi: 10.1016/j.bpj.2018.04.002. PubMed PMID: 29742396; PMCID: PMC5961468.

208. Gourier C, Jegou A, Husson J, Pincet F. A Nanospring Named Erythrocyte. The Biomembrane Force Probe. Cellular and Molecular Bioengineering. 2008;1(4):263. doi: 10.1007/s12195-008-0030-x.

209. Ju L, Zhu C. Benchmarks of Biomembrane Force Probe Spring Constant Models. Biophys J. 2017;113(12):2842-5. Epub 2017/12/21. doi: 10.1016/j.bpj.2017.10.013. PubMed PMID: 29262376; PMCID: PMC5771216.

210. Schwartz MA, DeSimone DW. Cell adhesion receptors in mechanotransduction. Curr Opin Cell Biol. 2008;20(5):551-6. Epub 2008/06/28. doi: 10.1016/j.ceb.2008.05.005. PubMed PMID: 18583124; PMCID: PMC2581799.

211. Chen Y, Ju L, Rushdi M, Ge C, Zhu C. Receptor-mediated cell mechanosensing. Mol Biol Cell. 2017;28(23):3134-55. Epub 2017/09/29. doi: 10.1091/mbc.E17-04-0228. PubMed PMID: 28954860; PMCID: PMC5687017.

212. Sachs F. Stretch-activated ion channels: what are they? Physiology (Bethesda). 2010;25(1):50-6. Epub 2010/02/06. doi: 10.1152/physiol.00042.2009. PubMed PMID: 20134028; PMCID: PMC2924431.

213. Sadler KE, Stucky CL. Neuronal transient receptor potential (TRP) channels and noxious sensory detection in sickle cell disease. Neurosci Lett. 2019;694:184-91. Epub 2018/12/07. doi: 10.1016/j.neulet.2018.11.056. PubMed PMID: 30508569; PMCID: PMC6389361.

214. Gillespie PG, Walker RG. Molecular basis of mechanosensory transduction. Nature. 2001;413(6852):194-202. Epub 2001/09/15. doi: 10.1038/35093011. PubMed PMID: 11557988.

215. Puklin-Faucher E, Gao M, Schulten K, Vogel V. How the headpiece hinge angle is opened: New insights into the dynamics of integrin activation. J Cell Biol. 2006;175(2):349-60. Epub 2006/10/25. doi: 10.1083/jcb.200602071. PubMed PMID: 17060501; PMCID: PMC2064575.

216. Hynes RO. Integrins: versatility, modulation, and signaling in cell adhesion. Cell. 1992;69(1):11-25. Epub 1992/04/03. doi: 10.1016/0092-8674(92)90115-s. PubMed PMID: 1555235.

217. Ruggeri ZM, Mendolicchio GL. Adhesion mechanisms in platelet function. Circ Res. 2007;100(12):1673-85. Epub 2007/06/23. doi: 10.1161/01.RES.0000267878.97021.ab. PubMed PMID: 17585075.

218. Chi Z, Melendez AJ. Role of cell adhesion molecules and immune-cell migration in the initiation, onset and development of atherosclerosis. Cell Adh Migr. 2007;1(4):171-5. Epub 2007/10/01. doi: 10.4161/cam.1.4.5321. PubMed PMID: 19262139; PMCID: PMC2634102.

219. Auton M, Zhu C, Cruz MA. The mechanism of VWF-mediated platelet GPIbalpha binding. Biophys J. 2010;99(4):1192-201. Epub 2010/08/18. doi: 10.1016/j.bpj.2010.06.002. PubMed PMID: 20713003; PMCID: PMC2920722.

220. Mikhailenko SV, Oguchi Y, Ishiwata S. Insights into the mechanisms of myosin and kinesin molecular motors from the single-molecule unbinding force measurements. J R Soc Interface. 2010;7 Suppl 3:S295-306. Epub 2010/04/02. doi: 10.1098/rsif.2010.0107.focus. PubMed PMID: 20356879; PMCID: PMC2943883.

221. Nakamoto RK, Baylis Scanlon JA, Al-Shawi MK. The rotary mechanism of the ATP synthase. Arch Biochem Biophys. 2008;476(1):43-50. Epub 2008/06/03. doi: 10.1016/j.abb.2008.05.004. PubMed PMID: 18515057; PMCID: PMC2581510.

222. Rodgers AJ, Wilce MC. Structure of the gamma-epsilon complex of ATP synthase. Nat Struct Biol. 2000;7(11):1051-4. Epub 2000/11/04. doi: 10.1038/80975. PubMed PMID: 11062562.

223. Welf ES, Naik UP, Ogunnaike BA. A spatial model for integrin clustering as a result of feedback between integrin activation and integrin binding. Biophys J. 2012;103(6):1379-89. Epub 2012/09/22. doi: 10.1016/j.bpj.2012.08.021. PubMed PMID: 22995511; PMCID: PMC3446678.

224. Wiseman PW, Brown CM, Webb DJ, Hebert B, Johnson NL, Squier JA, Ellisman MH, Horwitz AF. Spatial mapping of integrin interactions and dynamics during cell migration by image correlation microscopy. J Cell Sci. 2004;117(Pt 23):5521-34. Epub 2004/10/14. doi: 10.1242/jcs.01416. PubMed PMID: 15479718.

225. Shi Q, Boettiger D. A novel mode for integrin-mediated signaling: tethering is required for phosphorylation of FAK Y397. Mol Biol Cell. 2003;14(10):4306-15. Epub 2003/09/10. doi: 10.1091/mbc.e03-01-0046. PubMed PMID: 12960434; PMCID: PMC207021.

226. Goffin JM, Pittet P, Csucs G, Lussi JW, Meister JJ, Hinz B. Focal adhesion size controls tension-dependent recruitment of alpha-smooth muscle actin to stress fibers. J Cell Biol. 2006;172(2):259-68. Epub 2006/01/13. doi: 10.1083/jcb.200506179. PubMed PMID: 16401722; PMCID: PMC2063555.

227. Sokurenko EV, Vogel V, Thomas WE. Catch-bond mechanism of force-enhanced adhesion: counterintuitive, elusive, but ... widespread? Cell Host Microbe. 2008;4(4):314-23. Epub 2008/10/16. doi: 10.1016/j.chom.2008.09.005. PubMed PMID: 18854236; PMCID: PMC2610669.

228. Thomas WE, Vogel V, Sokurenko E. Biophysics of catch bonds. Annu Rev Biophys. 2008;37:399-416. Epub 2008/06/25. doi: 10.1146/annurev.biophys.37.032807.125804. PubMed PMID: 18573088.

229. Chen W, Lou J, Zhu C. Forcing switch from short- to intermediate- and long-lived states of the alphaA domain generates LFA-1/ICAM-1 catch bonds. J Biol Chem. 2010;285(46):35967-78. Epub 2010/09/08. doi: 10.1074/jbc.M110.155770. PubMed PMID: 20819952; PMCID: PMC2975219.

230. Hong J, Persaud SP, Horvath S, Allen PM, Evavold BD, Zhu C. Force-Regulated In Situ TCR-Peptide-Bound MHC Class II Kinetics Determine Functions of CD4+ T Cells. J Immunol. 2015;195(8):3557-64. Epub 2015/09/04. doi: 10.4049/jimmunol.1501407. PubMed PMID: 26336148; PMCID: PMC4592802.

231. Das DK, Feng Y, Mallis RJ, Li X, Keskin DB, Hussey RE, Brady SK, Wang JH, Wagner G, Reinherz EL, Lang MJ. Force-dependent transition in the T-cell receptor beta-subunit allosterically regulates peptide discrimination and pMHC bond lifetime. Proc Natl Acad Sci U S A. 2015;112(5):1517-22. Epub 2015/01/22. doi: 10.1073/pnas.1424829112. PubMed PMID: 25605925; PMCID: PMC4321250.

232. Hong J, Ge C, Jothikumar P, Yuan Z, Liu B, Bai K, Li K, Rittase W, Shinzawa M, Zhang Y, Palin A, Love P, Yu X, Salaita K, Evavold BD, Singer A, Zhu C. A TCR mechanotransduction signaling loop induces negative selection in the thymus. Nat Immunol. 2018;19(12):1379-90. Epub 2018/11/14. doi: 10.1038/s41590-018-0259-z. PubMed PMID: 30420628; PMCID: PMC6452639.

233. Rosetti F, Chen Y, Sen M, Thayer E, Azcutia V, Herter JM, Luscinskas FW, Cullere X, Zhu C, Mayadas TN. A Lupus-Associated Mac-1 Variant Has Defects in Integrin Allostery and Interaction with Ligands under Force. Cell Rep. 2015;10(10):1655-64. Epub 2015/03/17. doi: 10.1016/j.celrep.2015.02.037. PubMed PMID: 25772353; PMCID: PMC4567551.

234. Rossy J, Laufer JM, Legler DF. Role of Mechanotransduction and Tension in T Cell Function. Front Immunol. 2018;9:2638. Epub 2018/12/07. doi: 10.3389/fimmu.2018.02638. PubMed PMID: 30519239; PMCID: PMC6251326.

235. Liu B, Chen W, Evavold BD, Zhu C. Accumulation of dynamic catch bonds between TCR and agonist peptide-MHC triggers T cell signaling. Cell. 2014;157(2):357-68. Epub 2014/04/15. doi: 10.1016/j.cell.2014.02.053. PubMed PMID: 24725404; PMCID: PMC4123688.

236. Chen W, Zhu C. Mechanical regulation of T-cell functions. Immunol Rev. 2013;256(1):160-76. Epub 2013/10/15. doi: 10.1111/imr.12122. PubMed PMID: 24117820; PMCID: PMC3818107.

237. Dustin ML. T-cell activation through immunological synapses and kinapses. Immunol Rev. 2008;221:77-89. Epub 2008/02/16. doi: 10.1111/j.1600-065X.2008.00589.x. PubMed PMID: 18275476.

238. Zhu C, Chen W, Lou J, Rittase W, Li K. Mechanosensing through immunoreceptors. Nat Immunol. 2019;20(10):1269-78. Epub 2019/09/20. doi: 10.1038/s41590-019-0491-1. PubMed PMID: 31534240; PMCID: PMC7592628.

239. Zhu DM, Dustin ML, Cairo CW, Thatte HS, Golan DE. Mechanisms of Cellular Avidity Regulation in CD2-CD58-Mediated T Cell Adhesion. ACS Chem Biol. 2006;1(10):649-58. Epub 2006/12/16. doi: 10.1021/cb6002515. PubMed PMID: 17168569.

240. Hahn WC, Bierer BE. Separable portions of the CD2 cytoplasmic domain involved in signaling and ligand avidity regulation. J Exp Med. 1993;178(5):1831-6. Epub 1993/11/01. doi: 10.1084/jem.178.5.1831. PubMed PMID: 7901319; PMCID: PMC2191224.

241. Morikis VA, Masadeh E, Simon SI. Tensile force transmitted through LFA-1 bonds mechanoregulate neutrophil inflammatory response. J Leukoc Biol. 2020;108(6):1815-28. Epub 2020/06/13. doi: 10.1002/JLB.3A0520-100RR. PubMed PMID: 32531836.

242. Varma R, Campi G, Yokosuka T, Saito T, Dustin ML. T cell receptor-proximal signals are sustained in peripheral microclusters and terminated in the central supramolecular activation cluster. Immunity. 2006;25(1):117-27. Epub 2006/07/25. doi: 10.1016/j.immuni.2006.04.010. PubMed PMID: 16860761; PMCID: PMC1626533.

243. Katz SG, Rabinovich PM. T Cell Reprogramming Against Cancer. Methods Mol Biol. 2020;2097:3-44. Epub 2019/11/30. doi: 10.1007/978-1-0716-0203-4_1. PubMed PMID: 31776916; PMCID: PMC7063988.

244. Kim ST, Takeuchi K, Sun ZY, Touma M, Castro CE, Fahmy A, Lang MJ, Wagner G, Reinherz EL. The alphabeta T cell receptor is an anisotropic mechanosensor. J Biol Chem. 2009;284(45):31028-37. Epub 2009/09/17. doi: 10.1074/jbc.M109.052712. PubMed PMID: 19755427; PMCID: PMC2781503.

245. Feng Y, Brazin KN, Kobayashi E, Mallis RJ, Reinherz EL, Lang MJ. Mechanosensing drives acuity of alphabeta T-cell recognition. Proc Natl Acad Sci U S A. 2017;114(39):E8204-E13. Epub 2017/08/16. doi: 10.1073/pnas.1703559114. PubMed PMID: 28811364; PMCID: PMC5625899.

246. Bertani G. Studies on lysogenesis. I. The mode of phage liberation by lysogenic Escherichia coli. J Bacteriol. 1951;62(3):293-300. Epub 1951/09/01. doi: 10.1128/JB.62.3.293-300.1951. PubMed PMID: 14888646; PMCID: PMC386127.

247. Howarth M, Takao K, Hayashi Y, Ting AY. Targeting quantum dots to surface proteins in living cells with biotin ligase. Proc Natl Acad Sci U S A. 2005;102(21):7583-8. Epub 2005/05/18. doi: 10.1073/pnas.0503125102. PubMed PMID: 15897449; PMCID: PMC1129026.

248. Raymond C, Tom R, Perret S, Moussouami P, L'Abbe D, St-Laurent G, Durocher Y. A simplified polyethylenimine-mediated transfection process for large-scale and high-throughput applications. Methods. 2011;55(1):44-51. Epub 2011/05/05. doi: 10.1016/j.ymeth.2011.04.002. PubMed PMID: 21539918.

249. Baldi L, Hacker DL, Meerschman C, Wurm FM. Large-scale transfection of mammalian cells. Methods Mol Biol. 2012;801:13-26. Epub 2011/10/12. doi: 10.1007/978-1-61779-352-3_2. PubMed PMID: 21987244.

250. Fairhead M, Howarth M. Site-specific biotinylation of purified proteins using BirA. Methods Mol Biol. 2015;1266:171-84. Epub 2015/01/07. doi: 10.1007/978-1-4939-2272-7_12. PubMed PMID: 25560075; PMCID: PMC4304673.

251. Huang J, Zarnitsyna VI, Liu B, Edwards LJ, Jiang N, Evavold BD, Zhu C. The kinetics of two-dimensional TCR and pMHC interactions determine T-cell responsiveness. Nature. 2010;464(7290):932-6. Epub 2010/04/02. doi: 10.1038/nature08944. PubMed PMID: 20357766; PMCID: PMC2925443.

252. Chen W, Evans EA, McEver RP, Zhu C. Monitoring receptor-ligand interactions between surfaces by thermal fluctuations. Biophys J. 2008;94(2):694-701. Epub 2007/09/25. doi: 10.1529/biophysj.107.117895. PubMed PMID: 17890399; PMCID: PMC2157231.

253. Dennehy KM, Elias F, Zeder-Lutz G, Ding X, Altschuh D, Luhder F, Hunig T. Cutting edge: monovalency of CD28 maintains the antigen dependence of T cell costimulatory responses. J Immunol. 2006;176(10):5725-9. Epub 2006/05/04. doi: 10.4049/jimmunol.176.10.5725. PubMed PMID: 16670276.

254. Krummel MF, Allison JP. CD28 and CTLA-4 have opposing effects on the response of T cells to stimulation. J Exp Med. 1995;182(2):459-65. Epub 1995/08/01. doi: 10.1084/jem.182.2.459. PubMed PMID: 7543139; PMCID: PMC2192127.

255. Chingozha L, Zhan M, Zhu C, Lu H. A generalizable, tunable microfluidic platform for delivering fast temporally varying chemical signals to probe single-cell response

dynamics. Anal Chem. 2014;86(20):10138-47. Epub 2014/09/26. doi: 10.1021/ac5019843. PubMed PMID: 25254360; PMCID: PMC4204904.

256. Liu Y, Blanchfield L, Ma VP, Andargachew R, Galior K, Liu Z, Evavold B, Salaita K. DNA-based nanoparticle tension sensors reveal that T-cell receptors transmit defined pN forces to their antigens for enhanced fidelity. Proc Natl Acad Sci U S A. 2016;113(20):5610-5. Epub 2016/05/04. doi: 10.1073/pnas.1600163113. PubMed PMID: 27140637; PMCID: PMC4878516.

257. Zarnitsyna VI, Huang J, Zhang F, Chien YH, Leckband D, Zhu C. Memory in receptor-ligand-mediated cell adhesion. Proc Natl Acad Sci U S A. 2007;104(46):18037-42. Epub 2007/11/10. doi: 10.1073/pnas.0704811104. PubMed PMID: 17991779; PMCID: PMC2084292.

258. Hwang JR, Byeon Y, Kim D, Park SG. Recent insights of T cell receptor-mediated signaling pathways for T cell activation and development. Exp Mol Med. 2020;52(5):750-61. Epub 2020/05/23. doi: 10.1038/s12276-020-0435-8. PubMed PMID: 32439954; PMCID: PMC7272404.

259. Goswami R, Awasthi A. Editorial: T Cell Differentiation and Function in Tissue Inflammation. Front Immunol. 2020;11:289. Epub 2020/03/11. doi: 10.3389/fimmu.2020.00289. PubMed PMID: 32153592; PMCID: PMC7047510.

260. Bretscher PA. A two-step, two-signal model for the primary activation of precursor helper T cells. Proc Natl Acad Sci U S A. 1999;96(1):185-90. Epub 1999/01/06. doi: 10.1073/pnas.96.1.185. PubMed PMID: 9874793; PMCID: PMC15114.

261. Hutchcroft JE, Bierer BE. Activation-dependent phosphorylation of the T-lymphocyte surface receptor CD28 and associated proteins. Proc Natl Acad Sci U S A. 1994;91(8):3260-4. Epub 1994/04/12. doi: 10.1073/pnas.91.8.3260. PubMed PMID: 7512728; PMCID: PMC43556.

262. Hutchcroft JE, Tsai B, Bierer BE. Differential phosphorylation of the T lymphocyte costimulatory receptor CD28. Activation-dependent changes and regulation by protein kinase C. J Biol Chem. 1996;271(23):13362-70. Epub 1996/06/07. doi: 10.1074/jbc.271.23.13362. PubMed PMID: 8662792.

263. Kim JE, White FM. Quantitative analysis of phosphotyrosine signaling networks triggered by CD3 and CD28 costimulation in Jurkat cells. J Immunol. 2006;176(5):2833-43. Epub 2006/02/24. doi: 10.4049/jimmunol.176.5.2833. PubMed PMID: 16493040.

264. Parry RV, Olive D, Westwick J, Sansom DM, Ward SG. Evidence that a kinase distinct from protein kinase C and phosphatidylinositol 3-kinase mediates ligation-dependent serine/threonine phosphorylation of the T-lymphocyte co-stimulatory molecule CD28. Biochem J. 1997;326 (Pt 1):249-57. Epub 1997/08/15. doi: 10.1042/bj3260249. PubMed PMID: 9337876; PMCID: PMC1218662.

265. Tsuchida M, Manthei ER, Knechtle SJ, Hamawy MM. CD28 ligation induces rapid tyrosine phosphorylation of the linker molecule LAT in the absence of Syk and ZAP-70 tyrosine phosphorylation. Eur J Immunol. 1999;29(7):2354-9. Epub 1999/07/31. doi: 10.1002/(SICI)1521-4141(199907)29:07<2354::AID-IMMU2354>3.0.CO;2-P. PubMed PMID: 10427998.

266. Tuosto L. NF-kappaB family of transcription factors: biochemical players of CD28 co-stimulation. Immunol Lett. 2011;135(1-2):1-9. Epub 2010/09/25. doi: 10.1016/j.imlet.2010.09.005. PubMed PMID: 20863851.

267. Marinari B, Costanzo A, Marzano V, Piccolella E, Tuosto L. CD28 delivers a unique signal leading to the selective recruitment of RelA and p52 NF-kappaB subunits on IL-8 and Bcl-xL gene promoters. Proc Natl Acad Sci U S A. 2004;101(16):6098-103. Epub 2004/04/14. doi: 10.1073/pnas.0308688101. PubMed PMID: 15079071; PMCID: PMC395929.

268. Frauwirth KA, Riley JL, Harris MH, Parry RV, Rathmell JC, Plas DR, Elstrom RL, June CH, Thompson CB. The CD28 signaling pathway regulates glucose metabolism. Immunity. 2002;16(6):769-77. Epub 2002/07/18. doi: 10.1016/s1074-7613(02)00323-0. PubMed PMID: 12121659.

269. Herold KC, Lu J, Rulifson I, Vezys V, Taub D, Grusby MJ, Bluestone JA. Regulation of C-C chemokine production by murine T cells by CD28/B7 costimulation. J Immunol. 1997;159(9):4150-3. Epub 1997/10/31. PubMed PMID: 9379007.

270. June CH, Ledbetter JA, Gillespie MM, Lindsten T, Thompson CB. T-cell proliferation involving the CD28 pathway is associated with cyclosporine-resistant interleukin 2 gene expression. Mol Cell Biol. 1987;7(12):4472-81. Epub 1987/12/01. doi: 10.1128/mcb.7.12.4472. PubMed PMID: 2830495; PMCID: PMC368131.

271. Okkenhaug K, Wu L, Garza KM, La Rose J, Khoo W, Odermatt B, Mak TW, Ohashi PS, Rottapel R. A point mutation in CD28 distinguishes proliferative signals from survival signals. Nat Immunol. 2001;2(4):325-32. Epub 2001/03/29. doi: 10.1038/86327. PubMed PMID: 11276203.

272. Sharpe AH, Freeman GJ. The B7-CD28 superfamily. Nat Rev Immunol. 2002;2(2):116-26. Epub 2002/03/26. doi: 10.1038/nri727. PubMed PMID: 11910893.

273. Schneider H, Downey J, Smith A, Zinselmeyer BH, Rush C, Brewer JM, Wei B, Hogg N, Garside P, Rudd CE. Reversal of the TCR stop signal by CTLA-4. Science. 2006;313(5795):1972-5. Epub 2006/08/26. doi: 10.1126/science.1131078. PubMed PMID: 16931720.

274. Schmidt SV, Nino-Castro AC, Schultze JL. Regulatory dendritic cells: there is more than just immune activation. Front Immunol. 2012;3:274. Epub 2012/09/13. doi: 10.3389/fimmu.2012.00274. PubMed PMID: 22969767; PMCID: PMC3432880.

275. Li K, Cheng X, Tilevik A, Davis SJ, Zhu C. In situ and in silico kinetic analyses of programmed cell death-1 (PD-1) receptor, programmed cell death ligands, and B7-1 protein interaction network. J Biol Chem. 2017;292(16):6799-809. Epub 2017/03/09. doi: 10.1074/jbc.M116.763888. PubMed PMID: 28270509; PMCID: PMC5399126.

276. Hui E, Cheung J, Zhu J, Su X, Taylor MJ, Wallweber HA, Sasmal DK, Huang J, Kim JM, Mellman I, Vale RD. T cell costimulatory receptor CD28 is a primary target for PD-1-mediated inhibition. Science. 2017;355(6332):1428-33. Epub 2017/03/11. doi: 10.1126/science.aaf1292. PubMed PMID: 28280247; PMCID: PMC6286077.

277. Zhao Y, Lee CK, Lin CH, Gassen RB, Xu X, Huang Z, Xiao C, Bonorino C, Lu LF, Bui JD, Hui E. PD-L1:CD80 Cis-Heterodimer Triggers the Co-stimulatory Receptor CD28 While Repressing the Inhibitory PD-1 and CTLA-4 Pathways. Immunity. 2019;51(6):1059-73 e9. Epub 2019/11/24. doi: 10.1016/j.immuni.2019.11.003. PubMed PMID: 31757674; PMCID: PMC6935268.

278. Holdorf AD, Lee KH, Burack WR, Allen PM, Shaw AS. Regulation of Lck activity by CD4 and CD28 in the immunological synapse. Nat Immunol. 2002;3(3):259-64. Epub 2002/02/06. doi: 10.1038/ni761. PubMed PMID: 11828322.

279. Wei Q, Brzostek J, Sankaran S, Casas J, Hew LS, Yap J, Zhao X, Wojciech L, Gascoigne NRJ. Lck bound to coreceptor is less active than free Lck. Proc Natl Acad Sci U S A. 2020;117(27):15809-17. Epub 2020/06/24. doi: 10.1073/pnas.1913334117. PubMed PMID: 32571924; PMCID: PMC7355011.

280. Balagopalan L, Kortum RL, Coussens NP, Barr VA, Samelson LE. The linker for activation of T cells (LAT) signaling hub: from signaling complexes to microclusters. J Biol Chem. 2015;290(44):26422-9. Epub 2015/09/12. doi: 10.1074/jbc.R115.665869. PubMed PMID: 26354432; PMCID: PMC4646300.

281. Pivniouk VI, Geha RS. The role of SLP-76 and LAT in lymphocyte development. Curr Opin Immunol. 2000;12(2):173-8. Epub 2000/03/14. doi: 10.1016/s0952-7915(99)00068-0. PubMed PMID: 10712938.

282. Hwang W, Mallis RJ, Lang MJ, Reinherz EL. The alphabetaTCR mechanosensor exploits dynamic ectodomain allostery to optimize its ligand recognition site. Proc Natl Acad Sci U S A. 2020;117(35):21336-45. Epub 2020/08/17. doi: 10.1073/pnas.2005899117. PubMed PMID: 32796106; PMCID: PMC7474670.

283. Sibener LV, Fernandes RA, Kolawole EM, Carbone CB, Liu F, McAffee D, Birnbaum ME, Yang X, Su LF, Yu W, Dong S, Gee MH, Jude KM, Davis MM, Groves JT, Goddard WA, 3rd, Heath JR, Evavold BD, Vale RD, Garcia KC. Isolation of a Structural Mechanism for Uncoupling T Cell Receptor Signaling from Peptide-MHC Binding. Cell. 2018;174(3):672-87 e27. Epub 2018/07/28. doi: 10.1016/j.cell.2018.06.017. PubMed PMID: 30053426; PMCID: PMC6140336.

284. Raychaudhuri S, Thomson BP, Remmers EF, Eyre S, Hinks A, Guiducci C, Catanese JJ, Xie G, Stahl EA, Chen R, Alfredsson L, Amos CI, Ardlie KG, Consortium B,

Barton A, Bowes J, Burtt NP, Chang M, Coblyn J, Costenbader KH, Criswell LA, Crusius JB, Cui J, De Jager PL, Ding B, Emery P, Flynn E, Harrison P, Hocking LJ, Huizinga TW, Kastner DL, Ke X, Kurreeman FA, Lee AT, Liu X, Li Y, Martin P, Morgan AW, Padyukov L, Reid DM, Seielstad M, Seldin MF, Shadick NA, Steer S, Tak PP, Thomson W, van der Helm-van Mil AH, van der Horst-Bruinsma IE, Weinblatt ME, Wilson AG, Wolbink GJ, Wordsworth P, Consortium Y, Altshuler D, Karlson EW, Toes RE, de Vries N, Begovich AB, Siminovitch KA, Worthington J, Klareskog L, Gregersen PK, Daly MJ, Plenge RM. Genetic variants at CD28, PRDM1 and CD2/CD58 are associated with rheumatoid arthritis risk. Nat Genet. 2009;41(12):1313-8. Epub 2009/11/10. doi: 10.1038/ng.479. PubMed PMID: 19898481; PMCID: PMC3142887.

285. Wagner M, Sobczynski M, Karabon L, Bilinska M, Pokryszko-Dragan A, Pawlak-Adamska E, Cyrul M, Kusnierczyk P, Jasek M. Polymorphisms in CD28, CTLA-4, CD80 and CD86 genes may influence the risk of multiple sclerosis and its age of onset. J Neuroimmunol. 2015;288:79-86. Epub 2015/11/05. doi: 10.1016/j.jneuroim.2015.09.004. PubMed PMID: 26531698.

286. Chen S, Zhang Q, Shen L, Liu Y, Xu F, Li D, Fu Z, Yuan W, Pang D, Li D. Investigation of CD28 gene polymorphisms in patients with sporadic breast cancer in a Chinese Han population in Northeast China. PLoS One. 2012;7(10):e48031. Epub 2012/11/08. doi: 10.1371/journal.pone.0048031. PubMed PMID: 23133541; PMCID: PMC3485049.

287. Guzman VB, Yambartsev A, Goncalves-Primo A, Silva ID, Carvalho CR, Ribalta JC, Goulart LR, Shulzhenko N, Gerbase-Delima M, Morgun A. New approach reveals CD28 and IFNG gene interaction in the susceptibility to cervical cancer. Hum Mol Genet. 2008;17(12):1838-44. Epub 2008/03/14. doi: 10.1093/hmg/ddn077. PubMed PMID: 18337305; PMCID: PMC2536747.

288. Li Y, Jin L, Yan J, Zhang H, Zhang R, Hu C. CD28 Genetic Variants Increase Susceptibility to Diabetic Kidney Disease in Chinese Patients with Type 2 Diabetes: A Cross-Sectional Case Control Study. Mediators Inflamm. 2021;2021:5521050. Epub 2021/05/08. doi: 10.1155/2021/5521050. PubMed PMID: 33958973; PMCID: PMC8075672.

289. Gmyrek GB, Pingel J, Choi J, Green JM. Functional analysis of acquired CD28 mutations identified in cutaneous T cell lymphoma. Cell Immunol. 2017;319:28-34. Epub 2017/07/18. doi: 10.1016/j.cellimm.2017.07.002. PubMed PMID: 28711152; PMCID: PMC5667648.

290. Yoo HY, Kim P, Kim WS, Lee SH, Kim S, Kang SY, Jang HY, Lee JE, Kim J, Kim SJ, Ko YH, Lee S. Frequent CTLA4-CD28 gene fusion in diverse types of T-cell lymphoma. Haematologica. 2016;101(6):757-63. Epub 2016/01/29. doi: 10.3324/haematol.2015.139253. PubMed PMID: 26819049; PMCID: PMC5013939.

291. Gough SC, Walker LS, Sansom DM. CTLA4 gene polymorphism and autoimmunity. Immunol Rev. 2005;204:102-15. Epub 2005/03/26. doi: 10.1111/j.0105-2896.2005.00249.x. PubMed PMID: 15790353.

292. Schober T, Magg T, Laschinger M, Rohlfs M, Linhares ND, Puchalka J, Weisser T, Fehlner K, Mautner J, Walz C, Hussein K, Jaeger G, Kammer B, Schmid I, Bahia M, Pena SD, Behrends U, Belohradsky BH, Klein C, Hauck F. A human immunodeficiency syndrome caused by mutations in CARMIL2. Nat Commun. 2017;8:14209. Epub 2017/01/24. doi: 10.1038/ncomms14209. PubMed PMID: 28112205; PMCID: PMC5473639.

293. Mitsuiki N, Schwab C, Grimbacher B. What did we learn from CTLA-4 insufficiency on the human immune system? Immunol Rev. 2019;287(1):33-49. Epub 2018/12/20. doi: 10.1111/imr.12721. PubMed PMID: 30565239.

294. Perez CP, Patel N, Mardis CR, Meadows HB, Taber DJ, Pilch NA. Belatacept in Solid Organ Transplant: Review of Current Literature Across Transplant Types. Transplantation. 2018;102(9):1440-52. Epub 2018/05/23. doi: 10.1097/TP.0000000000002291. PubMed PMID: 29787522.

295. Wei SC, Duffy CR, Allison JP. Fundamental Mechanisms of Immune Checkpoint Blockade Therapy. Cancer Discov. 2018;8(9):1069-86. Epub 2018/08/18. doi: 10.1158/2159-8290.CD-18-0367. PubMed PMID: 30115704.

296. Robert C. A decade of immune-checkpoint inhibitors in cancer therapy. Nat Commun. 2020;11(1):3801. Epub 2020/08/01. doi: 10.1038/s41467-020-17670-y. PubMed PMID: 32732879; PMCID: PMC7393098.

297. Salter AI, Ivey RG, Kennedy JJ, Voillet V, Rajan A, Alderman EJ, Voytovich UJ, Lin C, Sommermeyer D, Liu L, Whiteaker JR, Gottardo R, Paulovich AG, Riddell SR. Phosphoproteomic analysis of chimeric antigen receptor signaling reveals kinetic and quantitative differences that affect cell function. Sci Signal. 2018;11(544). Epub 2018/08/23. doi: 10.1126/scisignal.aat6753. PubMed PMID: 30131370; PMCID: PMC6186424.

298. Ying Z, He T, Wang X, Zheng W, Lin N, Tu M, Xie Y, Ping L, Zhang C, Liu W, Deng L, Qi F, Ding Y, Lu XA, Song Y, Zhu J. Parallel Comparison of 4-1BB or CD28 Co-stimulated CD19-Targeted CAR-T Cells for B Cell Non-Hodgkin's Lymphoma. Mol Ther Oncolytics. 2019;15:60-8. Epub 2019/10/28. doi: 10.1016/j.omto.2019.08.002. PubMed PMID: 31650026; PMCID: PMC6804784.

299. Brown KE. Revisiting CD28 Superagonist TGN1412 as Potential Therapeutic for Pediatric B Cell Leukemia: A Review. Diseases. 2018;6(2). Epub 2018/05/23. doi: 10.3390/diseases6020041. PubMed PMID: 29783736; PMCID: PMC6023298.

300. St Clair EW. The calm after the cytokine storm: lessons from the TGN1412 trial. J Clin Invest. 2008;118(4):1344-7. Epub 2008/03/22. doi: 10.1172/JCI35382. PubMed PMID: 18357347; PMCID: PMC2269728.

301. Skokos D, Waite JC, Haber L, Crawford A, Hermann A, Ullman E, Slim R, Godin S, Ajithdoss D, Ye X, Wang B, Wu Q, Ramos I, Pawashe A, Canova L, Vazzana K, Ram P, Herlihy E, Ahmed H, Oswald E, Golubov J, Poon P, Havel L, Chiu D, Lazo M, Provoncha K, Yu K, Kim J, Warsaw JJ, Stokes Oristian N, Siao CJ, Dudgeon D, Huang T, Potocky T, Martin J, MacDonald D, Oyejide A, Rafique A, Poueymirou W, Kirshner JR, Smith E, Olson W, Lin J, Thurston G, Sleeman MA, Murphy AJ, Yancopoulos GD. A class of costimulatory CD28-bispecific antibodies that enhance the antitumor activity of CD3-bispecific antibodies. Sci Transl Med. 2020;12(525). Epub 2020/01/10. doi: 10.1126/scitranslmed.aaw7888. PubMed PMID: 31915305.

302. Wu L, Seung E, Xu L, Rao E, Lord DM, Wei RR, Cortez-Retamozo V, Ospina B, Posternak V, Ulinski G, Piepenhagen P, Francesconi E, El-Murr N, Beil C, Kirby P, Li A, Fretland J, Vicente R, Deng G, Dabdoubi T, Cameron B, Bertrand T, Ferrari P, Pouzieux S, Lemoine C, Prades C, Park A, Qiu H, Song Z, Zhang B, Sun F, Chiron M, Rao S, Radošević K, Yang Z-y, Nabel GJ. Trispecific antibodies enhance the therapeutic efficacy of tumor-directed T cells through T cell receptor co-stimulation. Nature Cancer. 2020;1(1):86-98. doi: 10.1038/s43018-019-0004-z.

303. Runcie K, Budman DR, John V, Seetharamu N. Bi-specific and tri-specific antibodies- the next big thing in solid tumor therapeutics. Mol Med. 2018;24(1):50. Epub 2018/09/27. doi: 10.1186/s10020-018-0051-4. PubMed PMID: 30249178; PMCID: PMC6154901.

304. Martins F, Sofiya L, Sykiotis GP, Lamine F, Maillard M, Fraga M, Shabafrouz K, Ribi C, Cairoli A, Guex-Crosier Y, Kuntzer T, Michielin O, Peters S, Coukos G, Spertini F, Thompson JA, Obeid M. Adverse effects of immune-checkpoint inhibitors: epidemiology, management and surveillance. Nat Rev Clin Oncol. 2019;16(9):563-80. Epub 2019/05/17. doi: 10.1038/s41571-019-0218-0. PubMed PMID: 31092901.

305. Brudno JN, Kochenderfer JN. Toxicities of chimeric antigen receptor T cells: recognition and management. Blood. 2016;127(26):3321-30. Epub 2016/05/22. doi: 10.1182/blood-2016-04-703751. PubMed PMID: 27207799; PMCID: PMC4929924.

306. Chapter 8 Kinetics and nature of antibody-antigen interactions. In: Tijssen P, editor. Laboratory Techniques in Biochemistry and Molecular Biology: Elsevier; 1985. p. 123-49.

307. Boger DL, Goldberg J. Cytokine receptor dimerization and activation: prospects for small molecule agonists. Bioorg Med Chem. 2001;9(3):557-62. Epub 2001/04/20. doi: 10.1016/s0968-0896(00)00276-5. PubMed PMID: 11310589.

308. Eastwood D, Findlay L, Poole S, Bird C, Wadhwa M, Moore M, Burns C, Thorpe R, Stebbings R. Monoclonal antibody TGN1412 trial failure explained by species differences in CD28 expression on CD4+ effector memory T-cells. Br J Pharmacol. 2010;161(3):512-26. Epub 2010/10/01. doi: 10.1111/j.1476-5381.2010.00922.x. PubMed PMID: 20880392; PMCID: PMC2990151.

309. Du X, Li Y, Xia YL, Ai SM, Liang J, Sang P, Ji XL, Liu SQ. Insights into Protein-Ligand Interactions: Mechanisms, Models, and Methods. Int J Mol Sci. 2016;17(2). Epub

2016/01/29. doi: 10.3390/ijms17020144. PubMed PMID: 26821017; PMCID: PMC4783878.

310. Borriello F, Sethna MP, Boyd SD, Schweitzer AN, Tivol EA, Jacoby D, Strom TB, Simpson EM, Freeman GJ, Sharpe AH. B7-1 and B7-2 have overlapping, critical roles in immunoglobulin class switching and germinal center formation. Immunity. 1997;6(3):303-13. Epub 1997/03/01. doi: 10.1016/s1074-7613(00)80333-7. PubMed PMID: 9075931.

311. Giraldo DM, Hernandez JC, Urcuqui Inchima S. Impact of in vitro costimulation with TLR2, TLR4 and TLR9 agonists and HIV-1 on antigen-presenting cell activation. Intervirology. 2015;58(2):122-9. Epub 2015/04/22. doi: 10.1159/000371765. PubMed PMID: 25896146.

312. Farina C, Theil D, Semlinger B, Hohlfeld R, Meinl E. Distinct responses of monocytes to Toll-like receptor ligands and inflammatory cytokines. Int Immunol. 2004;16(6):799-809. Epub 2004/04/21. doi: 10.1093/intimm/dxh083. PubMed PMID: 15096475.

313. Slavik JM, Hutchcroft JE, Bierer BE. CD80 and CD86 are not equivalent in their ability to induce the tyrosine phosphorylation of CD28. J Biol Chem. 1999;274(5):3116-24. Epub 1999/01/23. doi: 10.1074/jbc.274.5.3116. PubMed PMID: 9915850.

314. Elloso MM, Scott P. Expression and contribution of B7-1 (CD80) and B7-2 (CD86) in the early immune response to Leishmania major infection. J Immunol. 1999;162(11):6708-15. Epub 1999/06/03. PubMed PMID: 10352289.

315. Wahl A, Dinet C, Dillard P, Nassereddine A, Puech PH, Limozin L, Sengupta K. Biphasic mechanosensitivity of T cell receptor-mediated spreading of lymphocytes. Proc Natl Acad Sci U S A. 2019;116(13):5908-13. Epub 2019/03/10. doi: 10.1073/pnas.1811516116. PubMed PMID: 30850545; PMCID: PMC6442626.

316. Longo PA, Kavran JM, Kim MS, Leahy DJ. Transient mammalian cell transfection with polyethylenimine (PEI). Methods Enzymol. 2013;529:227-40. Epub 2013/09/10. doi: 10.1016/B978-0-12-418687-3.00018-5. PubMed PMID: 24011049; PMCID: PMC4012321.

317. Zhu C, Williams TE. Modeling concurrent binding of multiple molecular species in cell adhesion. Biophys J. 2000;79(4):1850-7. Epub 2000/10/12. doi: 10.1016/S0006-3495(00)76434-4. PubMed PMID: 11023890; PMCID: PMC1301076.

318. Girard T, Gaucher D, El-Far M, Breton G, Sekaly RP. CD80 and CD86 IgC domains are important for quaternary structure, receptor binding and co-signaling function. Immunol Lett. 2014;161(1):65-75. Epub 2014/05/23. doi: 10.1016/j.imlet.2014.05.002. PubMed PMID: 24845157.

319. Fricke F, Beaudouin J, Eils R, Heilemann M. One, two or three? Probing the stoichiometry of membrane proteins by single-molecule localization microscopy. Sci Rep.

2015;5:14072. Epub 2015/09/12. doi: 10.1038/srep14072. PubMed PMID: 26358640; PMCID: PMC4642553.

320. Sanchez-Lockhart M, Rojas AV, Fettis MM, Bauserman R, Higa TR, Miao H, Waugh RE, Miller J. T cell receptor signaling can directly enhance the avidity of CD28 ligand binding. PLoS One. 2014;9(2):e89263. Epub 2014/03/04. doi: 10.1371/journal.pone.0089263. PubMed PMID: 24586641; PMCID: PMC3933428.

321. Tian R, Wang H, Gish GD, Petsalaki E, Pasculescu A, Shi Y, Mollenauer M, Bagshaw RD, Yosef N, Hunter T, Gingras AC, Weiss A, Pawson T. Combinatorial proteomic analysis of intercellular signaling applied to the CD28 T-cell costimulatory receptor. Proc Natl Acad Sci U S A. 2015;112(13):E1594-603. Epub 2015/04/02. doi: 10.1073/pnas.1503286112. PubMed PMID: 25829543; PMCID: PMC4386406.

322. Raab M, Pfister S, Rudd CE. CD28 signaling via VAV/SLP-76 adaptors: regulation of cytokine transcription independent of TCR ligation. Immunity. 2001;15(6):921-33. Epub 2002/01/05. doi: 10.1016/s1074-7613(01)00248-5. PubMed PMID: 11754814.

323. Savitzky A, Golay MJE. Smoothing and Differentiation of Data by Simplified Least Squares Procedures. Analytical Chemistry. 1964;36(8):1627-39. doi: 10.1021/ac60214a047.

324. Murtaza A, Kuchroo VK, Freeman GJ. Changes in the strength of co-stimulation through the B7/CD28 pathway alter functional T cell responses to altered peptide ligands. Int Immunol. 1999;11(3):407-16. Epub 1999/04/30. doi: 10.1093/intimm/11.3.407. PubMed PMID: 10221652.

325. Williams JA, Hathcock KS, Klug D, Harada Y, Choudhury B, Allison JP, Abe R, Hodes RJ. Regulated costimulation in the thymus is critical for T cell development: dysregulated CD28 costimulation can bypass the pre-TCR checkpoint. J Immunol. 2005;175(7):4199-207. Epub 2005/09/24. doi: 10.4049/jimmunol.175.7.4199. PubMed PMID: 16177059; PMCID: PMC1343453.

326. Tai X, Cowan M, Feigenbaum L, Singer A. CD28 costimulation of developing thymocytes induces Foxp3 expression and regulatory T cell differentiation independently of interleukin 2. Nat Immunol. 2005;6(2):152-62. Epub 2005/01/11. doi: 10.1038/ni1160. PubMed PMID: 15640801.

327. Fuse S, Zhang W, Usherwood EJ. Control of memory CD8+ T cell differentiation by CD80/CD86-CD28 costimulation and restoration by IL-2 during the recall response. J Immunol. 2008;180(2):1148-57. Epub 2008/01/08. doi: 10.4049/jimmunol.180.2.1148. PubMed PMID: 18178855; PMCID: PMC2954438.

328. King CL, Stupi RJ, Craighead N, June CH, Thyphronitis G. CD28 activation promotes Th2 subset differentiation by human CD4+ cells. Eur J Immunol. 1995;25(2):587-95. Epub 1995/02/01. doi: 10.1002/eji.1830250242. PubMed PMID: 7875222.

329. Moreland L, Bate G, Kirkpatrick P. Abatacept. Nat Rev Drug Discov. 2006;5(3):185-6. Epub 2006/03/25. doi: 10.1038/nrd1989. PubMed PMID: 16557658.

330. Watanabe M, Lu Y, Breen M, Hodes RJ. B7-CD28 co-stimulation modulates central tolerance via thymic clonal deletion and Treg generation through distinct mechanisms. Nat Commun. 2020;11(1):6264. Epub 2020/12/10. doi: 10.1038/s41467-020-20070-x. PubMed PMID: 33293517; PMCID: PMC7722925.

331. Porciello N, Kunkl M, Tuosto L. CD28 between tolerance and autoimmunity: the side effects of animal models. F1000Res. 2018;7. Epub 2018/06/16. doi: 10.12688/f1000research.14046.1. PubMed PMID: 29904580; PMCID: PMC5981186.

332. Yu XZ, Albert MH, Martin PJ, Anasetti C. CD28 ligation induces transplantation tolerance by IFN-gamma-dependent depletion of T cells that recognize alloantigens. J Clin Invest. 2004;113(11):1624-30. Epub 2004/06/03. doi: 10.1172/JCI20940. PubMed PMID: 15173889; PMCID: PMC419490.

333. Seo YJ, Jothikumar P, Suthar MS, Zhu C, Grakoui A. Local Cellular and Cytokine Cues in the Spleen Regulate In Situ T Cell Receptor Affinity, Function, and Fate of CD8(+) T Cells. Immunity. 2016;45(5):988-98. Epub 2016/11/17. doi: 10.1016/j.immuni.2016.10.024. PubMed PMID: 27851926; PMCID: PMC5131716.

334. Majolini MB, Boncristiano M, Baldari CT. Dysregulation of the protein tyrosine kinase LCK in lymphoproliferative disorders and in other neoplasias. Leuk Lymphoma. 1999;35(3-4):245-54. Epub 2000/03/08. doi: 10.3109/10428199909145727. PubMed PMID: 10706447.

335. Yang W, Pan W, Chen S, Trendel N, Jiang S, Xiao F, Xue M, Wu W, Peng Z, Li X, Ji H, Liu X, Jiang H, Wang H, Shen H, Dushek O, Li H, Xu C. Dynamic regulation of CD28 conformation and signaling by charged lipids and ions. Nat Struct Mol Biol. 2017;24(12):1081-92. Epub 2017/10/24. doi: 10.1038/nsmb.3489. PubMed PMID: 29058713.

336. Li L, Guo X, Shi X, Li C, Wu W, Yan C, Wang H, Li H, Xu C. Ionic CD3-Lck interaction regulates the initiation of T-cell receptor signaling. Proc Natl Acad Sci U S A. 2017;114(29):E5891-E9. Epub 2017/07/01. doi: 10.1073/pnas.1701990114. PubMed PMID: 28659468; PMCID: PMC5530670.

337. Glinos DA, Soskic B, Williams C, Kennedy A, Jostins L, Sansom DM, Trynka G. Genomic profiling of T-cell activation suggests increased sensitivity of memory T cells to CD28 costimulation. Genes Immun. 2020;21(6-8):390-408. Epub 2020/11/24. doi: 10.1038/s41435-020-00118-0. PubMed PMID: 33223527; PMCID: PMC7785515.

338. Ueda H, Morphew MK, McIntosh JR, Davis MM. CD4+ T-cell synapses involve multiple distinct stages. Proc Natl Acad Sci U S A. 2011;108(41):17099-104. Epub 2011/09/29. doi: 10.1073/pnas.1113703108. PubMed PMID: 21949383; PMCID: PMC3193211.

339. Anvari B, Torres JH, McIntyre BW. Regulation of pseudopodia localization in lymphocytes through application of mechanical forces by optical tweezers. J Biomed Opt. 2004;9(5):865-72. Epub 2004/09/28. doi: 10.1117/1.1778178. PubMed PMID: 15447007.

340. Franko JL, Levine AD. Antigen-independent adhesion and cell spreading by inducible costimulator engagement inhibits T cell migration in a PI-3K-dependent manner. J Leukoc Biol. 2009;85(3):526-38. Epub 2008/12/20. doi: 10.1189/jlb.0808505. PubMed PMID: 19095735; PMCID: PMC2653947.

341. Munoz MA, Biro M, Weninger W. T cell migration in intact lymph nodes in vivo. Curr Opin Cell Biol. 2014;30:17-24. Epub 2014/06/08. doi: 10.1016/j.ceb.2014.05.002. PubMed PMID: 24907445.

342. Pielak RM, O'Donoghue GP, Lin JJ, Alfieri KN, Fay NC, Low-Nam ST, Groves JT. Early T cell receptor signals globally modulate ligand:receptor affinities during antigen discrimination. Proc Natl Acad Sci U S A. 2017;114(46):12190-5. Epub 2017/11/01. doi: 10.1073/pnas.1613140114. PubMed PMID: 29087297; PMCID: PMC5699024.

343. Siokis A, Robert PA, Demetriou P, Dustin ML, Meyer-Hermann M. F-Actin-Driven CD28-CD80 Localization in the Immune Synapse. Cell Rep. 2018;24(5):1151-62. Epub 2018/08/02. doi: 10.1016/j.celrep.2018.06.114. PubMed PMID: 30067972.

344. Riteau B, Barber DF, Long EO. Vav1 phosphorylation is induced by beta2 integrin engagement on natural killer cells upstream of actin cytoskeleton and lipid raft reorganization. J Exp Med. 2003;198(3):469-74. Epub 2003/07/30. doi: 10.1084/jem.20021995. PubMed PMID: 12885870; PMCID: PMC2194094.

345. Ma R, Kellner AV, Ma VP, Su H, Deal BR, Brockman JM, Salaita K. DNA probes that store mechanical information reveal transient piconewton forces applied by T cells. Proc Natl Acad Sci U S A. 2019;116(34):16949-54. Epub 2019/08/09. doi: 10.1073/pnas.1904034116. PubMed PMID: 31391300; PMCID: PMC6708336.

346. Dobbins J, Gagnon E, Godec J, Pyrdol J, Vignali DA, Sharpe AH, Wucherpfennig KW. Binding of the cytoplasmic domain of CD28 to the plasma membrane inhibits Lck recruitment and signaling. Sci Signal. 2016;9(438):ra75. Epub 2016/07/28. doi: 10.1126/scisignal.aaf0626. PubMed PMID: 27460989; PMCID: PMC5929992.

347. Lenschow DJ, Sperling AI, Cooke MP, Freeman G, Rhee L, Decker DC, Gray G, Nadler LM, Goodnow CC, Bluestone JA. Differential up-regulation of the B7-1 and B7-2 costimulatory molecules after Ig receptor engagement by antigen. J Immunol. 1994;153(5):1990-7. Epub 1994/09/01. PubMed PMID: 7519638.

348. Beier KC, Kallinich T, Hamelmann E. Master switches of T-cell activation and differentiation. Eur Respir J. 2007;29(4):804-12. Epub 2007/04/03. doi: 10.1183/09031936.00094506. PubMed PMID: 17400879.

349. Kapsenberg ML. Dendritic-cell control of pathogen-driven T-cell polarization. Nat Rev Immunol. 2003;3(12):984-93. Epub 2003/12/04. doi: 10.1038/nri1246. PubMed PMID: 14647480.

350. Mittrucker HW, Visekruna A, Huber M. Heterogeneity in the differentiation and function of CD8(+) T cells. Arch Immunol Ther Exp (Warsz). 2014;62(6):449-58. Epub 2014/06/01. doi: 10.1007/s00005-014-0293-y. PubMed PMID: 24879097.

351. Kaech SM, Cui W. Transcriptional control of effector and memory CD8+ T cell differentiation. Nat Rev Immunol. 2012;12(11):749-61. Epub 2012/10/20. doi: 10.1038/nri3307. PubMed PMID: 23080391; PMCID: PMC4137483.

352. Kretschmer L, Flossdorf M, Mir J, Cho YL, Plambeck M, Treise I, Toska A, Heinzel S, Schiemann M, Busch DH, Buchholz VR. Differential expansion of T central memory precursor and effector subsets is regulated by division speed. Nat Commun. 2020;11(1):113. Epub 2020/01/09. doi: 10.1038/s41467-019-13788-w. PubMed PMID: 31913278; PMCID: PMC6949285.

353. Cameron PU, Jones P, Gorniak M, Dunster K, Paul E, Lewin S, Woolley I, Spelman D. Splenectomy associated changes in IgM memory B cells in an adult spleen registry cohort. PLoS One. 2011;6(8):e23164. Epub 2011/08/11. doi: 10.1371/journal.pone.0023164. PubMed PMID: 21829713; PMCID: PMC3150402.

354. Lewis SM, Williams A, Eisenbarth SC. Structure and function of the immune system in the spleen. Sci Immunol. 2019;4(33). Epub 2019/03/03. doi: 10.1126/sciimmunol.aau6085. PubMed PMID: 30824527; PMCID: PMC6495537.

355. Jung YW, Rutishauser RL, Joshi NS, Haberman AM, Kaech SM. Differential localization of effector and memory CD8 T cell subsets in lymphoid organs during acute viral infection. J Immunol. 2010;185(9):5315-25. Epub 2010/10/06. doi: 10.4049/jimmunol.1001948. PubMed PMID: 20921525; PMCID: PMC4267692.

356. Grakoui A, Crispe IN. Presentation of hepatocellular antigens. Cell Mol Immunol. 2016;13(3):293-300. Epub 2016/03/01. doi: 10.1038/cmi.2015.109. PubMed PMID: 26924525; PMCID: PMC4856799.

357. Watanabe T, Kudo M, Chiba T, Wakatsuki Y. Molecular mechanisms of portal vein tolerance. Hepatol Res. 2008;38(5):441-9. Epub 2007/12/12. doi: 10.1111/j.1872-034X.2007.00313.x. PubMed PMID: 18070053.

358. Wrenshall LE, Ansite JD, Eckman PM, Heilman MJ, Stevens RB, Sutherland DE. Modulation of immune responses after portal venous injection of antigen. Transplantation. 2001;71(7):841-50. Epub 2001/05/15. doi: 10.1097/00007890-200104150-00004. PubMed PMID: 11349714.

359. Callery MP, Kamei T, Flye MW. The effect of portacaval shunt on delayed-hypersensitivity responses following antigen feeding. J Surg Res. 1989;46(4):391-4. Epub 1989/04/01. doi: 10.1016/0022-4804(89)90208-4. PubMed PMID: 2784839.

360. Thimme R, Wieland S, Steiger C, Ghrayeb J, Reimann KA, Purcell RH, Chisari FV. CD8(+) T cells mediate viral clearance and disease pathogenesis during acute hepatitis B virus infection. J Virol. 2003;77(1):68-76. Epub 2002/12/13. doi: 10.1128/jvi.77.1.68-76.2003. PubMed PMID: 12477811; PMCID: PMC140637.

361. Pruvot FR, Navarro F, Janin A, Labalette M, Masy E, Lecomte-Houcke M, Gambiez L, Copin MC, Dessaint JP. Characterization, quantification, and localization of passenger T lymphocytes and NK cells in human liver before transplantation. Transpl Int. 1995;8(4):273-9. Epub 1995/01/01. doi: 10.1007/BF00346880. PubMed PMID: 7546149.

362. Crispe IN. Hepatic T cells and liver tolerance. Nat Rev Immunol. 2003;3(1):51-62. Epub 2003/01/04. doi: 10.1038/nri981. PubMed PMID: 12511875.

363. Bertolino P, Trescol-Biemont MC, Rabourdin-Combe C. Hepatocytes induce functional activation of naive CD8+ T lymphocytes but fail to promote survival. Eur J Immunol. 1998;28(1):221-36. Epub 1998/03/04. doi: 10.1002/(SICI)1521-4141(199801)28:01<221::AID-IMMU221>3.0.CO;2-F. PubMed PMID: 9485202.

364. Qian S, Lu L, Fu F, Li Y, Li W, Starzl TE, Fung JJ, Thomson AW. Apoptosis within spontaneously accepted mouse liver allografts: evidence for deletion of cytotoxic T cells and implications for tolerance induction. J Immunol. 1997;158(10):4654-61. Epub 1997/05/15. PubMed PMID: 9144477; PMCID: PMC2954768.

365. Bertolino P, Trescol-Biemont MC, Thomas J, Fazekas de St Groth B, Pihlgren M, Marvel J, Rabourdin-Combe C. Death by neglect as a deletional mechanism of peripheral tolerance. Int Immunol. 1999;11(8):1225-38. Epub 1999/07/28. doi: 10.1093/intimm/11.8.1225. PubMed PMID: 10421780.

366. Zheng M, Tian Z. Liver-Mediated Adaptive Immune Tolerance. Front Immunol. 2019;10:2525. Epub 2019/12/04. doi: 10.3389/fimmu.2019.02525. PubMed PMID: 31787967; PMCID: PMC6856635.

367. Bamboat ZM, Stableford JA, Plitas G, Burt BM, Nguyen HM, Welles AP, Gonen M, Young JW, DeMatteo RP. Human liver dendritic cells promote T cell hyporesponsiveness. J Immunol. 2009;182(4):1901-11. Epub 2009/02/10. doi: 10.4049/jimmunol.0803404. PubMed PMID: 19201843; PMCID: PMC3254024.

368. Yu J, Green MD, Li S, Sun Y, Journey SN, Choi JE, Rizvi SM, Qin A, Waninger JJ, Lang X, Chopra Z, El Naqa I, Zhou J, Bian Y, Jiang L, Tezel A, Skvarce J, Achar RK, Sitto M, Rosen BS, Su F, Narayanan SP, Cao X, Wei S, Szeliga W, Vatan L, Mayo C, Morgan MA, Schonewolf CA, Cuneo K, Kryczek I, Ma VT, Lao CD, Lawrence TS, Ramnath N, Wen F, Chinnaiyan AM, Cieslik M, Alva A, Zou W. Liver metastasis restrains immunotherapy efficacy via macrophage-mediated T cell elimination. Nat Med. 2021;27(1):152-64. Epub 2021/01/06. doi: 10.1038/s41591-020-1131-x. PubMed PMID: 33398162; PMCID: PMC8095049.

369. Koda Y, Teratani T, Chu PS, Hagihara Y, Mikami Y, Harada Y, Tsujikawa H, Miyamoto K, Suzuki T, Taniki N, Sujino T, Sakamoto M, Kanai T, Nakamoto N. CD8(+)

tissue-resident memory T cells promote liver fibrosis resolution by inducing apoptosis of hepatic stellate cells. Nat Commun. 2021;12(1):4474. Epub 2021/07/24. doi: 10.1038/s41467-021-24734-0. PubMed PMID: 34294714.

370. Li Y, Teteloshvili N, Tan S, Rao S, Han A, Yang YG, Creusot RJ. Humanized Mice Reveal New Insights Into the Thymic Selection of Human Autoreactive CD8(+) T Cells. Front Immunol. 2019;10:63. Epub 2019/02/20. doi: 10.3389/fimmu.2019.00063. PubMed PMID: 30778347; PMCID: PMC6369192.

371. Obenaus M, Leitao C, Leisegang M, Chen X, Gavvovidis I, van der Bruggen P, Uckert W, Schendel DJ, Blankenstein T. Identification of human T-cell receptors with optimal affinity to cancer antigens using antigen-negative humanized mice. Nat Biotechnol. 2015;33(4):402-7. Epub 2015/03/17. doi: 10.1038/nbt.3147. PubMed PMID: 25774714.

372. Wagar LE, DiFazio RM, Davis MM. Advanced model systems and tools for basic and translational human immunology. Genome Med. 2018;10(1):73. Epub 2018/09/30. doi: 10.1186/s13073-018-0584-8. PubMed PMID: 30266097; PMCID: PMC6162943.

373. Moskophidis D, Lechner F, Pircher H, Zinkernagel RM. Virus persistence in acutely infected immunocompetent mice by exhaustion of antiviral cytotoxic effector T cells. Nature. 1993;362(6422):758-61. Epub 1993/04/22. doi: 10.1038/362758a0. PubMed PMID: 8469287.

374. Zajac AJ, Blattman JN, Murali-Krishna K, Sourdive DJ, Suresh M, Altman JD, Ahmed R. Viral immune evasion due to persistence of activated T cells without effector function. J Exp Med. 1998;188(12):2205-13. Epub 1998/12/22. doi: 10.1084/jem.188.12.2205. PubMed PMID: 9858507; PMCID: PMC2212420.

375. Wang M, Zhao J, Zhang L, Wei F, Lian Y, Wu Y, Gong Z, Zhang S, Zhou J, Cao K, Li X, Xiong W, Li G, Zeng Z, Guo C. Role of tumor microenvironment in tumorigenesis. J Cancer. 2017;8(5):761-73. Epub 2017/04/07. doi: 10.7150/jca.17648. PubMed PMID: 28382138; PMCID: PMC5381164.

376. Xia A, Zhang Y, Xu J, Yin T, Lu XJ. T Cell Dysfunction in Cancer Immunity and Immunotherapy. Front Immunol. 2019;10:1719. Epub 2019/08/06. doi: 10.3389/fimmu.2019.01719. PubMed PMID: 31379886; PMCID: PMC6659036.

377. Maimela NR, Liu S, Zhang Y. Fates of CD8+ T cells in Tumor Microenvironment. Comput Struct Biotechnol J. 2019;17:1-13. Epub 2018/12/26. doi: 10.1016/j.csbj.2018.11.004. PubMed PMID: 30581539; PMCID: PMC6297055.

378. McLane LM, Abdel-Hakeem MS, Wherry EJ. CD8 T Cell Exhaustion During Chronic Viral Infection and Cancer. Annu Rev Immunol. 2019;37:457-95. Epub 2019/01/25. doi: 10.1146/annurev-immunol-041015-055318. PubMed PMID: 30676822.

379. Mueller SN, Ahmed R. High antigen levels are the cause of T cell exhaustion during chronic viral infection. Proc Natl Acad Sci U S A. 2009;106(21):8623-8. Epub 2009/05/13. doi: 10.1073/pnas.0809818106. PubMed PMID: 19433785; PMCID: PMC2688997.

380. Jubel JM, Barbati ZR, Burger C, Wirtz DC, Schildberg FA. The Role of PD-1 in Acute and Chronic Infection. Front Immunol. 2020;11:487. Epub 2020/04/09. doi: 10.3389/fimmu.2020.00487. PubMed PMID: 32265932; PMCID: PMC7105608.

381. Wherry EJ. T cell exhaustion. Nat Immunol. 2011;12(6):492-9. Epub 2011/07/09. doi: 10.1038/ni.2035. PubMed PMID: 21739672.

382. Edwards LJ, Zarnitsyna VI, Hood JD, Evavold BD, Zhu C. Insights into T cell recognition of antigen: significance of two-dimensional kinetic parameters. Front Immunol. 2012;3:86. Epub 2012/05/09. doi: 10.3389/fimmu.2012.00086. PubMed PMID: 22566966; PMCID: PMC3342060.

383. Kelly JM, Sterry SJ, Cose S, Turner SJ, Fecondo J, Rodda S, Fink PJ, Carbone FR. Identification of conserved T cell receptor CDR3 residues contacting known exposed peptide side chains from a major histocompatibility complex class I-bound determinant. Eur J Immunol. 1993;23(12):3318-26. Epub 1993/12/01. doi: 10.1002/eji.1830231239. PubMed PMID: 8258346.

384. Hogquist KA, Jameson SC, Heath WR, Howard JL, Bevan MJ, Carbone FR. T cell receptor antagonist peptides induce positive selection. Cell. 1994;76(1):17-27. Epub 1994/01/14. doi: 10.1016/0092-8674(94)90169-4. PubMed PMID: 8287475.

385. Hogquist KA, Jameson SC, Bevan MJ. Strong agonist ligands for the T cell receptor do not mediate positive selection of functional CD8+ T cells. Immunity. 1995;3(1):79-86. Epub 1995/07/01. doi: 10.1016/1074-7613(95)90160-4. PubMed PMID: 7621079.

386. Carreno LJ, Bueno SM, Bull P, Nathenson SG, Kalergis AM. The half-life of the T-cell receptor/peptide-major histocompatibility complex interaction can modulate T-cell activation in response to bacterial challenge. Immunology. 2007;121(2):227-37. Epub 2007/02/23. doi: 10.1111/j.1365-2567.2007.02561.x. PubMed PMID: 17313485; PMCID: PMC2265936.

387. Moogk D, Zhong S, Yu Z, Liadi I, Rittase W, Fang V, Dougherty J, Perez-Garcia A, Osman I, Zhu C, Varadarajan N, Restifo NP, Frey AB, Krogsgaard M. Constitutive Lck Activity Drives Sensitivity Differences between CD8+ Memory T Cell Subsets. J Immunol. 2016;197(2):644-54. Epub 2016/06/09. doi: 10.4049/jimmunol.1600178. PubMed PMID: 27271569; PMCID: PMC4935560.

388. Acuto O, Di Bartolo V, Michel F. Tailoring T-cell receptor signals by proximal negative feedback mechanisms. Nat Rev Immunol. 2008;8(9):699-712. Epub 2008/08/30. doi: 10.1038/nri2397. PubMed PMID: 18728635.

389. Bensinger SJ, Bradley MN, Joseph SB, Zelcer N, Janssen EM, Hausner MA, Shih R, Parks JS, Edwards PA, Jamieson BD, Tontonoz P. LXR signaling couples sterol

metabolism to proliferation in the acquired immune response. Cell. 2008;134(1):97-111. Epub 2008/07/11. doi: 10.1016/j.cell.2008.04.052. PubMed PMID: 18614014; PMCID: PMC2626438.

390. Rocha B, von Boehmer H. Peripheral selection of the T cell repertoire. Science. 1991;251(4998):1225-8. Epub 1991/03/08. doi: 10.1126/science.1900951. PubMed PMID: 1900951.

391. San Jose E, Borroto A, Niedergang F, Alcover A, Alarcon B. Triggering the TCR complex causes the downregulation of nonengaged receptors by a signal transduction-dependent mechanism. Immunity. 2000;12(2):161-70. Epub 2000/03/14. doi: 10.1016/s1074-7613(00)80169-7. PubMed PMID: 10714682.

392. Wang B, Tontonoz P. Liver X receptors in lipid signalling and membrane homeostasis. Nat Rev Endocrinol. 2018;14(8):452-63. Epub 2018/06/16. doi: 10.1038/s41574-018-0037-x. PubMed PMID: 29904174; PMCID: PMC6433546.

393. Robinson GA, Waddington KE, Pineda-Torra I, Jury EC. Transcriptional Regulation of T-Cell Lipid Metabolism: Implications for Plasma Membrane Lipid Rafts and T-Cell Function. Front Immunol. 2017;8:1636. Epub 2017/12/12. doi: 10.3389/fimmu.2017.01636. PubMed PMID: 29225604; PMCID: PMC5705553.

394. Spann NJ, Glass CK. Sterols and oxysterols in immune cell function. Nat Immunol. 2013;14(9):893-900. Epub 2013/08/21. doi: 10.1038/ni.2681. PubMed PMID: 23959186.

395. Waddington KE, Robinson GA, Rubio-Cuesta B, Chrifi-Alaoui E, Andreone S, Poon K-S, Ivanova I, Martin-Gutierrez L, Owen DM, Jury EC, Pineda-Torra I. LXR alters CD4⁺ T cell function through direct regulation of glycosphingolipid synthesis. bioRxiv. 2020:721050. doi: 10.1101/721050.

396. Luo C, Wang K, Liu DQ, Li Y, Zhao QS. The functional roles of lipid rafts in T cell activation, immune diseases and HIV infection and prevention. Cell Mol Immunol. 2008;5(1):1-7. Epub 2008/03/06. doi: 10.1038/cmi.2008.1. PubMed PMID: 18318989; PMCID: PMC4652918.

397. Kabouridis PS, Jury EC. Lipid rafts and T-lymphocyte function: implications for autoimmunity. FEBS Lett. 2008;582(27):3711-8. Epub 2008/10/22. doi: 10.1016/j.febslet.2008.10.006. PubMed PMID: 18930053; PMCID: PMC2596348.

398. Kidani Y, Bensinger SJ. Liver X receptor and peroxisome proliferator-activated receptor as integrators of lipid homeostasis and immunity. Immunol Rev. 2012;249(1):72-83. Epub 2012/08/15. doi: 10.1111/j.1600-065X.2012.01153.x. PubMed PMID: 22889216; PMCID: PMC4007066.

399. Minguet S, Swamy M, Alarcon B, Luescher IF, Schamel WW. Full activation of the T cell receptor requires both clustering and conformational changes at CD3. Immunity. 2007;26(1):43-54. Epub 2006/12/26. doi: 10.1016/j.immuni.2006.10.019. PubMed PMID: 17188005.

400. Stone JD, Chervin AS, Kranz DM. T-cell receptor binding affinities and kinetics: impact on T-cell activity and specificity. Immunology. 2009;126(2):165-76. Epub 2009/01/08. doi: 10.1111/j.1365-2567.2008.03015.x. PubMed PMID: 19125887; PMCID: PMC2632691.

401. Coombs D, Dembo M, Wofsy C, Goldstein B. Equilibrium thermodynamics of cell-cell adhesion mediated by multiple ligand-receptor pairs. Biophys J. 2004;86(3):1408-23. Epub 2004/03/03. doi: 10.1016/S0006-3495(04)74211-3. PubMed PMID: 14990470; PMCID: PMC1303978.

402. Chakraborty AK, Weiss A. Insights into the initiation of TCR signaling. Nat Immunol. 2014;15(9):798-807. Epub 2014/08/20. doi: 10.1038/ni.2940. PubMed PMID: 25137454; PMCID: PMC5226627.

403. Valitutti S. The Serial Engagement Model 17 Years After: From TCR Triggering to Immunotherapy. Front Immunol. 2012;3:272. Epub 2012/09/14. doi: 10.3389/fimmu.2012.00272. PubMed PMID: 22973273; PMCID: PMC3428561.

404. Vashist SK, Dixit CK, MacCraith BD, O'Kennedy R. Effect of antibody immobilization strategies on the analytical performance of a surface plasmon resonance-based immunoassay. Analyst. 2011;136(21):4431-6. Epub 2011/09/10. doi: 10.1039/c1an15325k. PubMed PMID: 21904732.

405. Jarmoskaite I, AlSadhan I, Vaidyanathan PP, Herschlag D. How to measure and evaluate binding affinities. Elife. 2020;9. Epub 2020/08/08. doi: 10.7554/eLife.57264. PubMed PMID: 32758356; PMCID: PMC7452723.

406. Marth JD, Grewal PK. Mammalian glycosylation in immunity. Nat Rev Immunol. 2008;8(11):874-87. Epub 2008/10/11. doi: 10.1038/nri2417. PubMed PMID: 18846099; PMCID: PMC2768770.

407. Brooks SA. Appropriate glycosylation of recombinant proteins for human use: implications of choice of expression system. Mol Biotechnol. 2004;28(3):241-55. Epub 2004/11/16. doi: 10.1385/MB:28:3:241. PubMed PMID: 15542924.

408. Rahimi N, Costello CE. Emerging roles of post-translational modifications in signal transduction and angiogenesis. Proteomics. 2015;15(2-3):300-9. Epub 2014/08/28. doi: 10.1002/pmic.201400183. PubMed PMID: 25161153; PMCID: PMC4297243.

409. Risueno RM, van Santen HM, Alarcon B. A conformational change senses the strength of T cell receptor-ligand interaction during thymic selection. Proc Natl Acad Sci U S A. 2006;103(25):9625-30. Epub 2006/06/13. doi: 10.1073/pnas.0601785103. PubMed PMID: 16766661; PMCID: PMC1480457.

410. Mobley DL, Dill KA. Binding of small-molecule ligands to proteins: "what you see" is not always "what you get". Structure. 2009;17(4):489-98. Epub 2009/04/17. doi: 10.1016/j.str.2009.02.010. PubMed PMID: 19368882; PMCID: PMC2756098.

411. Dupre L, Houmadi R, Tang C, Rey-Barroso J. T Lymphocyte Migration: An Action Movie Starring the Actin and Associated Actors. Front Immunol. 2015;6:586. Epub 2015/12/05. doi: 10.3389/fimmu.2015.00586. PubMed PMID: 26635800; PMCID: PMC4649030.

412. Valitutti S, Coombs D, Dupre L. The space and time frames of T cell activation at the immunological synapse. FEBS Lett. 2010;584(24):4851-7. Epub 2010/10/14. doi: 10.1016/j.febslet.2010.10.010. PubMed PMID: 20940018.

413. Dustin ML, Cooper JA. The immunological synapse and the actin cytoskeleton: molecular hardware for T cell signaling. Nat Immunol. 2000;1(1):23-9. Epub 2001/03/23. doi: 10.1038/76877. PubMed PMID: 10881170.

414. Bunnell SC, Kapoor V, Trible RP, Zhang W, Samelson LE. Dynamic actin polymerization drives T cell receptor-induced spreading: a role for the signal transduction adaptor LAT. Immunity. 2001;14(3):315-29. Epub 2001/04/06. doi: 10.1016/s1074-7613(01)00112-1. PubMed PMID: 11290340.

415. Tskvitaria-Fuller I, Rozelle AL, Yin HL, Wulfing C. Regulation of sustained actin dynamics by the TCR and costimulation as a mechanism of receptor localization. J Immunol. 2003;171(5):2287-95. Epub 2003/08/21. doi: 10.4049/jimmunol.171.5.2287. PubMed PMID: 12928373.

416. Campi G, Varma R, Dustin ML. Actin and agonist MHC-peptide complex-dependent T cell receptor microclusters as scaffolds for signaling. J Exp Med. 2005;202(8):1031-6. Epub 2005/10/12. doi: 10.1084/jem.20051182. PubMed PMID: 16216891; PMCID: PMC1373686.

417. Yokosuka T, Sakata-Sogawa K, Kobayashi W, Hiroshima M, Hashimoto-Tane A, Tokunaga M, Dustin ML, Saito T. Newly generated T cell receptor microclusters initiate and sustain T cell activation by recruitment of Zap70 and SLP-76. Nat Immunol. 2005;6(12):1253-62. Epub 2005/11/08. doi: 10.1038/ni1272. PubMed PMID: 16273097.

418. Martinez-Martin N, Fernandez-Arenas E, Cemerski S, Delgado P, Turner M, Heuser J, Irvine DJ, Huang B, Bustelo XR, Shaw A, Alarcon B. T cell receptor internalization from the immunological synapse is mediated by TC21 and RhoG GTPase-dependent phagocytosis. Immunity. 2011;35(2):208-22. Epub 2011/08/09. doi: 10.1016/j.immuni.2011.06.003. PubMed PMID: 21820331; PMCID: PMC4033310.

419. Crotzer VL, Mabardy AS, Weiss A, Brodsky FM. T cell receptor engagement leads to phosphorylation of clathrin heavy chain during receptor internalization. J Exp Med. 2004;199(7):981-91. Epub 2004/04/07. doi: 10.1084/jem.20031105. PubMed PMID: 15067034; PMCID: PMC2211883.

420. Alcover A, Alarcon B. Internalization and intracellular fate of TCR-CD3 complexes. Crit Rev Immunol. 2000;20(4):325-46. Epub 2000/12/02. PubMed PMID: 11100805.

421. Calleja E, Alarcon B, Oeste CL. Studying the Dynamics of TCR Internalization at the Immune Synapse. Methods Mol Biol. 2017;1584:89-99. Epub 2017/03/04. doi: 10.1007/978-1-4939-6881-7_7. PubMed PMID: 28255698.

422. Balagopalan L, Raychaudhuri K, Samelson LE. Microclusters as T Cell Signaling Hubs: Structure, Kinetics, and Regulation. Front Cell Dev Biol. 2020;8:608530. Epub 2021/02/13. doi: 10.3389/fcell.2020.608530. PubMed PMID: 33575254; PMCID: PMC7870797.

423. Ma Z, Discher DE, Finkel TH. Mechanical force in T cell receptor signal initiation. Front Immunol. 2012;3:217. Epub 2012/07/27. doi: 10.3389/fimmu.2012.00217. PubMed PMID: 22833746; PMCID: PMC3400889.

424. Waddington KE, Robinson GA, Rubio-Cuesta B, Chrifi-Alaoui E, Andreone S, Poon KS, Ivanova I, Martin-Gutierrez L, Owen DM, Jury EC, Pineda-Torra I. LXR directly regulates glycosphingolipid synthesis and affects human CD4+ T cell function. Proc Natl Acad Sci U S A. 2021;118(21). Epub 2021/05/20. doi: 10.1073/pnas.2017394118. PubMed PMID: 34006637; PMCID: PMC8166169.

425. Cantini L, Pecci F, Hurkmans D, Copparoni C, Aerts S, Belderbos RA, Cornelissen R, Dumoulin DP, Fiordoliva I, Rinaldi S, Aerts J, Berardi R. Statin treatment improves response to anti-PD1 agents in patients with malignant pleural mesothelioma and non-small cell lung cancer. Journal of Clinical Oncology. 2020;38(15_suppl):3074-. doi: 10.1200/JCO.2020.38.15_suppl.3074.

426. Rossi A, Filetti M, Taurelli Salimbeni B, Piras M, Rizzo F, Giusti R, Marchetti P. Statins and immunotherapy: Togetherness makes strength The potential effect of statins on immunotherapy for NSCLC. Cancer Rep (Hoboken). 2021:e1368. Epub 2021/04/01. doi: 10.1002/cnr2.1368. PubMed PMID: 33788420.

427. Yi J, Balagopalan L, Nguyen T, McIntire KM, Samelson LE. TCR microclusters form spatially segregated domains and sequentially assemble in calcium-dependent kinetic steps. Nat Commun. 2019;10(1):277. Epub 2019/01/19. doi: 10.1038/s41467-018-08064-2. PubMed PMID: 30655520; PMCID: PMC6336795.

428. Choi S, Schwartz RH. Impairment of immunological synapse formation in adaptively tolerant T cells. J Immunol. 2011;187(2):805-16. Epub 2011/06/21. doi: 10.4049/jimmunol.1003314. PubMed PMID: 21685322; PMCID: PMC3131438.

429. Glanville J, Huang H, Nau A, Hatton O, Wagar LE, Rubelt F, Ji X, Han A, Krams SM, Pettus C, Haas N, Arlehamn CSL, Sette A, Boyd SD, Scriba TJ, Martinez OM, Davis MM. Identifying specificity groups in the T cell receptor repertoire. Nature. 2017;547(7661):94-8. Epub 2017/06/22. doi: 10.1038/nature22976. PubMed PMID: 28636589; PMCID: PMC5794212.

430. An C, Hu W, Gao J, Ju BF, Obeidy P, Zhao YC, Tu X, Fang W, Ju LA, Chen W. Ultra-stable Biomembrane Force Probe for Accurately Determining Slow Dissociation Kinetics of PD-1 Blockade Antibodies on Single Living Cells. Nano Lett.

2020;20(7):5133-40. Epub 2020/06/13. doi: 10.1021/acs.nanolett.0c01360. PubMed PMID: 32530632.